Merger Induced Star Formation in The Antennae

and

The SPIFFI Near Infrared Integral Field Spectrometer

Dissertation der Fakultät für Physik

der Ludwig-Maximilians-Universität München

vorgelegt von
Sabine Mengel
aus Marburg
9. Februar 2001

.

Gutachter:	Prof. Dr. Reinhard Genzel
	Prof. Dr. Ralf Bender

Tag der mündlichen Prüfung:

CONTENTS

LIST OF FIGURES

LIST OF TABLES

1. ZUSAMMENFASSUNG

Wechselwirkende Galaxien wurden bereits vor mehreren Jahrzehnten entdeckt, jedoch lange Zeit als Kuriositäten betrachtet, die man um ihrer selbst willen zwar studieren kann, die jedoch für grundlegende astronomische oder kosmologische Fragen bedeutungslos sind.
Im Laufe der letzten Jahre hat sich diese Einschätzung drastisch gewandelt, denn merere verschiedene Beobachtungen legten den Schluß nahe, daß Verschmelzungen gasreicher Galaxien in den frühen Stadien des Universums wesentlich zahlreicher waren, und daß das, was wir in der näheren Umgebung der Milchstraße als elliptische Galaxien sehen, die Überreste solcher Begegnungen sein könnten.
In Fällen, wo die Ursprungsgalaxien große Mengen an Gas und Staub beherbergen, ist die Verschmelzung mit starken Sternentstehungsprozessen verbunden. Allerdings gestaltet es sich als extrem schwierig, detaillierte Informationen über den Ablauf solcher Wechselwirkungen zu erhalten, denn bei großen Rotverschiebungen gestattet die beschränkte räumliche Auflösung lediglich die Ableitung globaler Eigenschaften der Sternentstehung, und bei den resultierenden Galaxien in der Nähe der Milchstraße liegt die Entstehung bereits so lange zurück, daß es schwierig ist zu entscheiden, welcher der beobachteten Eigenschaften die Wechselwirkung zugrunde liegt.
Eine Möglichkeit, diesem Dilemma zu entgehen, bietet sich, wenn man nahegelegene verschmelzende Galaxien studiert. Der Prototyp der verschmelzenden Galaxien für die Frühphase der Wechselwirkung ist NGC 4038/4039, dessen Nähe die räumlich aufgelöste Untersuchung der Kollision gestattet. Die vorliegende Arbeit beschreibt eine Studie dieses Systems. Bevorzugt wurde der nahinfrarote Wellenlängenbereich, weil die großen Staubmengen eine hohe Extinktion bewirken, von der der optische Spektralbereich stärker betroffen ist als der infrarote.
Eine große Anzahl blauer, kompakter Sternhaufen zeigt bereits, daß die Wechselwirkung eine verstärkte Sternentstehung induziert hat. Diese Sternhaufen beinhalten jeweils eine Population gleichaltriger Sterne, deren Analyse anhand von verschiedenartigen Beobachtungen verschiedene Parameter der Sternentstehungsgeschichte in NGC 4038/39 liefert.
Nahinfrarote Feldspektroskopie wurde in sechs ausgewählten Regionen mit dem MPE-3D Spektrometer durchgeführt. Vier von ihnen decken Sternhaufen ab, die verschiedene Epochen der Sternentstehung repräsentieren sollen. Die restlichenliegen in den Galaxienkernen, in denen vermutet wird, daß die Sternentstehung deutlich früher begonnen hat. Um jedoch die gesamte Ausdehnung der verschmelzenden Galaxien abdecken zu können, wurden ergänzende abbildende Breit- und Schmalbandbeobachtungen durchgeführt, ebenfalls im Nahinfrarot. Die Schmalbandfilter wurden entsprechend ihres Nutzens für die Altersdiagnostik der Sternpopulationen ausgewählt. Ein dritter Satz von Beobachtungen erbrachte mittel- bis hochaufgelöste Spektren von stellaren Absorptionslinien und -banden im nahinfraroten und optischen Spektralbereich für ein paar der bei der jeweiligen Wellenlänge hellsten Haufen. Diese dienten dem Zweck der Ermittlung der dynamischen Masse der Haufen.
Diese Analyse liefert den zeitlichen Ablauf der Sternentstehung in den verschmelzenden Galaxien, von jüngster oder noch stattfindender Sternetstehung (3 - 10 Myrs) in dem Bereich, wo die beiden Galaxien zu überlappen scheinen, bis zu den ältesten heftigen Sternentstehungsausbrüchen in den Kernen (100 Myrs). Die Massen einzelner Sternhaufen, die durch Photometrie und hochauflösende Spektroskopie abgeleitet wurden, erreichen mehrere Millionen $M_{\odot}$.
Die 3D Daten enthüllen fortschreitende Sternentstehung auf kleinen räumlichen Skalen, denn ihre Datenkuben

zeigen junge Sternhaufen in direkter Nachbarschaft zu älteren Sternentstehungsregionen.
Dies macht den Hauptvorteil der abbildenden Spektroskopie gegenüber konventioneller Spaltspektroskopie deutlich: In nur einer einzigen Belichtung werden spektrale und räumliche Informationen simultan gewonnen. 3D, welches vom MPE gebaut wurde, is ein sehr erfolgreicher Repräsentant seiner Klasse. Da aber auch in den Nahinfrarotbereich in den letzten Jahren Detektoren der 1024^2pixel Klasse und Teleskope mit 8 m Durchmesser und Adaptiver Optik (die Beobachtungen an der Beugungsgrenze des Teleskps ermöglichen) Einzug gehalten haben, ist es möglich, mehrere Eigenschaften eines solchen Instrumentes entscheidend zu verbessern, wie z.B. die Zahl der räumlichen Pixel, die spektrale und räumliche Auflösung.
SPIFFI ist das Nachfolgeinstrument von 3D und wird, zusammen mit dem speziell für diesen Zweck vom European Southern Observatory entworfenen Adaptive Optik System MACAO, SINFONI bilden. Es wird im Juni 2002 am VLT-UT4 installiert werden. Die räumliche Auflösung liegt wählbar zwischen $0\farcs025$ and $0\farcs25$, wobei die große Pixelskala ein Feld von $8\farcs0 \times 8\farcs0$ abdeckt. Die spektrale Auflösung kann auch an die Quelle angepaßt werden und bei R = 2,200 oder R = 4,500 liegen. Der abgedeckte Wellenlängenbereich liegt bei 1.0 bis 2.5 μm. Eine Übersicht über das Instrument SPIFFI findet sich im zweiten Teil dieser Arbeit, zusätzlich eine etwas eingehendere Beschreibung einiger Teile und der Beschreibung eines Integrationszeitberechungsprogramms.

2. ABSTRACT

Interacting galaxies have been detected several decades ago, but have, for many years, been regarded as curiosities, worthy for study in their own right, but without any relevance for the more general questions in astronomy and cosmology. This attitude changed drastically over the last years, when several different observations and theory indicated that mergers of gas-rich galaxies could have been much more frequent in earlier epochs of the universe, and that what we observe as local elliptical galaxies could be the remnants of such early encounters.

However, it is extremely difficult to gain detailed information on the properties of such encounters, which are expected to be accompanied by violent events of star formation in cases where the progenitor galaxies host large amounts of gas and dust. At high redshifts, the limited spatial resolution allows us to derive only the global properties of the encounter, and in the remnants in the local universe, the interaction happened such a long time ago that it is difficult to unambiguously interpret the signatures that it imprinted on the resulting galaxy.

One way to overcome these limitations is to study ongoing galaxy mergers at small distances. The prototype merger in the early phases of merging is NGC 4038/4039, which due to its proximity allows to investigate the spatially resolved properties of the collision. This work describes the study of this system, mainly at near infrared wavelengths, because the large amounts of dust in the system lead to high extinction. Observing in the near infrared minimizes the impact of such high extinction. The triggering of intense star formation in NGC 4038/4039 is obvious from a large number of blue, compact star clusters. Different kinds of observations were performed to derive various parameters of the star formation history by analyzing the compact star clusters, each of them hosting a coeval population of stars.

Near infrared integral field spectroscopy was performed with the MPE-3D spectrometer on six fields. Four of them are star clusters intended to probe different epochs of the star formation, and two others are centered on the nuclei, where the star formation was suspected to have started considerably earlier. In order to cover the full spatial extent of the galaxies, these observations were supplemented by near infrared broad- and narrow band imaging. The narrow bands were selected to cover the diagnostic features useful for the age determination of stellar populations. A third set of observations obtained high resolution spectroscopy of the stellar features in some of the clusters, in the near infrared for the extinguished clusters and at optical wavelengths for optically bright clusters. The purpose of these high spectral resolution observations was to derive the virial masses of a few clusters.

The analysis yields the chronology of star formation in the merger, from recent or on-going star formation (3-10 Myrs) in the region where the two galaxies apparently overlap, to the oldest starbursts detected in the nuclei (100 Myrs). The masses of single clusters derived from photometry and high resolution spectroscopy are up to a few $\times 10^6 M_\odot$.

The 3D data also reveal propagating star formation on small spatial scales, because in their data cubes they show young starclusters in the direct vicinity of older starburst regions.

This demonstrates the main advantage of the integral field approach over conventional slit spectroscopy: In a single integration, spectral and spatial information is obtained simulateously. 3D, which was built by MPE, is a very successful representative of this type of instrument, but with the advent of new, bigger near-infrared detectors (1024^2 with respect to 256^2) and telescopes (8m vs. 4m) with adaptive optics, (allowing observations at the diffraction limit) it is possible to improve several characteristics of such an instrument, like the number

of spatial pixels, the spectral and spatial resolution.
SPIFFI is the successor to 3D and will, together with the dedicated adaptive optics system MACAO, which is built by the European Southern Observatory, form SINFONI. It will be installed at the VLT-UT4 telescope in June 2002. The spatial resolution can be chosen between $0\farcs025$ and $0\farcs25$ per pixel, where the large pixel scale covers a field of $8\farcs0$ on a side. The spectral resolution can also be adjusted to the nature of the target, either R=2200 or R=4500. The wavelength range covered is 1.0 to 2.5 μm. A general description of SPIFFI will be given, as well as a more thorough discussion of some of its constituents and a description of a performance estimator.

Part I

MERGER INDUCED STAR FORMATION IN THE ANTENNAE

3. NGC 4038/4039 – THE ANTENNAE

3.1 Introduction

The star formation activity in NGC 4038/39 – the "Antennae" – has been known from studies at various wavelengths, for example from Hα spectroscopy (Rubin et al., 1970) or the very blue colours observed in the HST images (Whitmore & Schweizer, 1995, called WS95 hereafter). Its relative proximity (19 Mpc assuming H_0=75km s^{-1}Mpc^{-1}) makes it the ideal candidate for the study of merger induced star formation on scales of single star clusters.

Each of these star clusters represents a coeval population of stars and allows us to derive the properties of the star formation process in that region fairly precisely. The Antennae are considered the nearby prototype for the merger of two gas-rich spiral galaxies. As will be explained in more detail in chapter 4.1, simulations suggest that this type of merger could result in the formation of elliptical galaxies (e.g. Toomre & Toomre (1972)). The remnants of these encounters would then be the ellipticals in the vicinity of the Milky Way. Part of their globular cluster system would originate from the survivors of the young star clusters formed during the tidal interaction, while the other part dates from the original galaxies.

However, some obvious dissimilarities in the two galaxy types require the verification of this hypothesis, which is one of the drivers for this analysis. For example, spiral galaxies have relatively large gas fractions of their total mass ($\sim$10 %) and are actively forming stars, whereas ellipticals have very little gas and generally low star formation rates.

The globular cluster frequency is twice as high in ellipticals (per unit luminous mass) (Harris & Racine, 1979; Harris & van den Bergh, 1981) as that in spirals, and the colours of the two cluster populations are very different. This has been interpreted as evidence against and in favour of the merger model. The luminosity- and mass functions of globular clusters in ellipticals are well known and characteristic. They are Gaussian in shape with a characteristic mass of $\sim 1-2\times10^5$ $M_\odot$, which corresponds to a turnover absolute magnitude of M = -7.2 mag. These characteristics are observed in all globular cluster systems, irrespective of environment. A general statement concerning the luminosity or mass functions of young cluster populations cannot yet be made, since the Antennae is one of the very few systems studied so far in that respect. But it shows a power-law luminosity-, and possibly also mass function (see Whitmore et al. (1999); Zhang & Fall (1999)), and more than just simple fading is required to obtain a Gaussian luminosity function after a Hubble time.

A full study of this problem would require to determine the fate of the gas in the interaction, the star formation properties of single clusters and the cluster population in general, and the future evolution to determine the appearance of the clusters at the age of the currently observed globular clusters ($>$ 10 Gyr).

This study concentrates on the latter aspects, because the gas interactions are best analyzed using computer simulations. The Antennae offer a large population of star clusters for this analysis: $\approx$800 compact clusters were identified by WS95 in optical HST observations, and with the refurbished telescope optics on HST, more that 14,000 pointlike objects were detected (Whitmore et al., 1999, W99 hereafter). However, many of the 14,000 are stars rather than faint clusters. The spectacular true-colour image composed from these observations is displayed in Figure 3.1. The most striking features in this image are probably the dust filaments distributed over the galaxies, obscuring some of the star formation regions.

It came as a surprise that the heavily extinguished region where the two disks apparently overlap ("overlap region") was revealed to be the most active star formation zone by radio observations (Hummel & Van der

Fig. 3.1: HST true colour image of NGC 4038/39, reproduced from Whitmore & Schweizer (1995). The most obvious features are the large number of bright, young, blue star clusters, the two bright nuclei and the dark dust lanes. The extinction is highest in the region where the two galaxies seem to overlap, eastward of the line connecting the two nuclei. To the north-west of the merger, there is a prominent loop of blue clusters which resembles a spiral arm (this will occasionally be called the "northwestern loop".

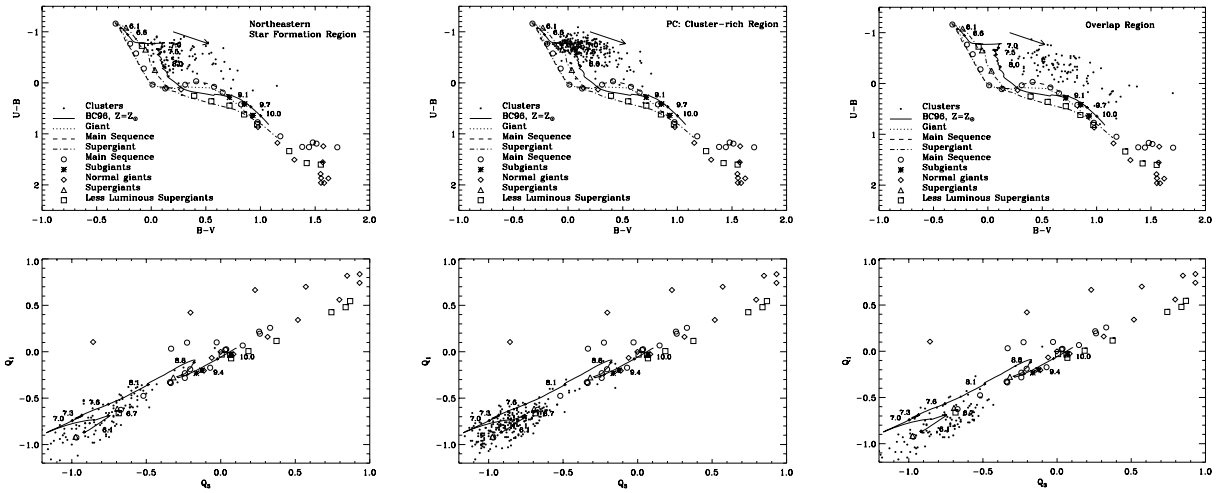

Fig. 3.2: Comparison of the Q parameters Q1 and Q3 with evolutionary synthesis models, taken from Whitmore et al. (1999)

Hulst, 1986), imaging and spectroscopy performed with ISO (Mirabel et al., 1998; Kunze et al., 1996; Fischer et al., 1996) and far infrared line emission observations (Nikola et al., 1998). The overlap region is relatively inconspicuous at optical wavelengths. The ISO results suggest very young ages for these clusters (few Myrs) and the presence of high mass (50-60 $M_{\odot}$) stars. Interestingly, a significant fraction of the total bolometric flux from the Antennae appears to originate in two clusters eastward of the NGC 4039 nucleus (numbers 86/87/88/89/90 in WS95), building up an optically bright knot, and number 80 in WS95, which is optically extinguished and declared a "very red object" by WS95. These two regions, which are the highest surface brightness features in the mid-infrared (12-17μm), contribute ≈25% of the total flux in this wavelength range (Mirabel et al., 1998), and ≈20% of the total emission from discrete radio sources (at 4.885GHz = 6cm) in NGC 4038/39 (Hummel & Van der Hulst, 1986). These large fractions suggest that these two regions must constitute a significant portion of the very recent or on-going star-formation within the Antennae. Understanding their properties within the perspective of the overall star formation history of the Antennae is of prime importance to understanding the bolometric output of these merging galaxies.

The last decades have seen an increasing number of publications focusing on NGC 4038/39, and they cover all wavelength ranges from radio to X-ray. Each of the observations was aimed to derive specific properties of the merger or its constituents. The following sections will summarize the findings of these observations and of the models which were performed to determine the dynamics of the system.

3.2 Optical imaging: Stars and ionized gas

The most intensive analysis of single star clusters in the Antennae so far was based on HST data which was the first data set to deliver the high spatial resolution required to study also faint single clusters. These analyses concentrated on the determination of the properties of the cluster population as a whole, including the cluster luminosity function (LF), and the cluster mass function (MF).

There had been three main publications based on HST observations, Whitmore & Schweizer (1995), Whitmore et al. (1999) and Zhang & Fall (1999). The first was based on observations taken before the correction of the telescope's optics, the other after the installation of COSTAR. The improvement in optical quality led to an increase in limiting magnitude by 3 mag in V and to an increase of the number of detected pointlike objects by a factor of 20. Both publications tried to estimate the burst ages and the cluster LF and MF. The first publication (Whitmore & Schweizer, 1995), however, need not to be taken into account, since the high level

of variable extinction was not considered for the analysis, only a constant extinction correction was applied for the whole galaxy. This led to suspiciously high values for the ages of the star clusters. These ages were derived from broadband optical colours, and since they were heavily affected by extinction, a mean age of 100 Myrs was erroneously derived. A proper luminosity function cannot be derived without a realistic extinction correction.

The second publication used the Q-parameter for the analysis. This parameter is constructed from four optical broadband colours in such a way that it becomes extinction insensitive. The technique will be described in more detail in section 5.5. Due to the increased spatial resolution of the refurbished telescope, around 14,000 pointlike sources were detected in the W99 images (compared to ∼700 in WS95). However, many of them are stars rather than clusters, and one of the challenging tasks in the data analysis was the separation of the two populations. Whitmore et al. applied four different techniques to achieve this, and all four gave similar results. The lower and upper limits to the number of clusters are 800 and 8000, respectively. The necessity of separating stars from clusters arises mainly from the desire to derive properties of the cluster population as a whole, like the luminosity function (LF), mean effective radius ($R_{\rm eff}$) and age distribution. The LF is one of the major results of their work. This analysis shows an apparent bend in the power-law shape. The location of the bend at M_V = -10.4 mag coincides with the typical mass of a globular cluster ($\approx 2 \times 10^5$ $M_\odot$), but only if an average extinction of $A_V = 1$ mag is assumed.

Another result concerns cluster sizes. The median effective radius was determined to be $R_{\rm eff} = 4 \pm 1$ pc, which is slightly larger than that of a typical Milky Way globular cluster (∼3 pc).

Using age estimates based on the Q-parameter in comparison with population synthesis models, four different populations were detected (see Figure 3.2): most of the clusters, which includes all of the brightest ones, belong to a population which is below 20 Myrs old. The youngest amongst these concentrate in the overlap region, and the brighter of the sligthly older ones form the loops which are obvious in the images. Two of these young clusters have ages which were confirmed spectroscopically (using the Goddard High Resolution Spectrograph, GHRS). They agree well with the ages determined via the Q-parameter. However, since they were selected to be very bright in U-band, they are in low extinction environments, where the Q-parameter technique is expected to work well.

Several members of a fainter ($\sim$ 1 mag fainter) population of around 100 Myrs were detected, mainly to the north-east of the merger, while some clusters of around 500 Myrs reside in the north-western extension, outward of the bright loop.

Very few members (11) of the globular cluster population of the progenitor galaxies were detected, all of them around the southern nucleus, where the surface brightness is low enough to detect the faint clusters (typical M_V = -7.2 mag for galactic globular clusters) against the background. However, according to a crude completeness correction, their actual number should be at least a factor of ten higher.

An Hα image reveals hydrogen recombination emission from many of the star clusters, which again confirms their young ages ($<$ 8 Myrs), because it requires the presence of young, hot, ionizing stars. Some of the clusters show extended, ionized shells/bubbles, traces of supernovae which ejected and ionized the cluster gas.

Zhang & Fall (1999) analyzed the same dataset in order to create a mass function (MF) from the luminosity function. They used the Q-parameters as above to estimate the intrinsic colour, extinction and expected luminosity of individual clusters. The mass of each cluster was then determined by comparison to the observed luminosity. As a result, they obtained a power law mass function $\Phi(M) \sim M^{-2}$, in contrast to the Gaussian mass function seen in globular cluster populations. It remains to be verified if the cluster ages are determined correctly by the Q analysis. They are a crucial part in this analysis, because they determine the expected cluster luminosities, which are compared to the observed absolute luminosities for the mass determination.

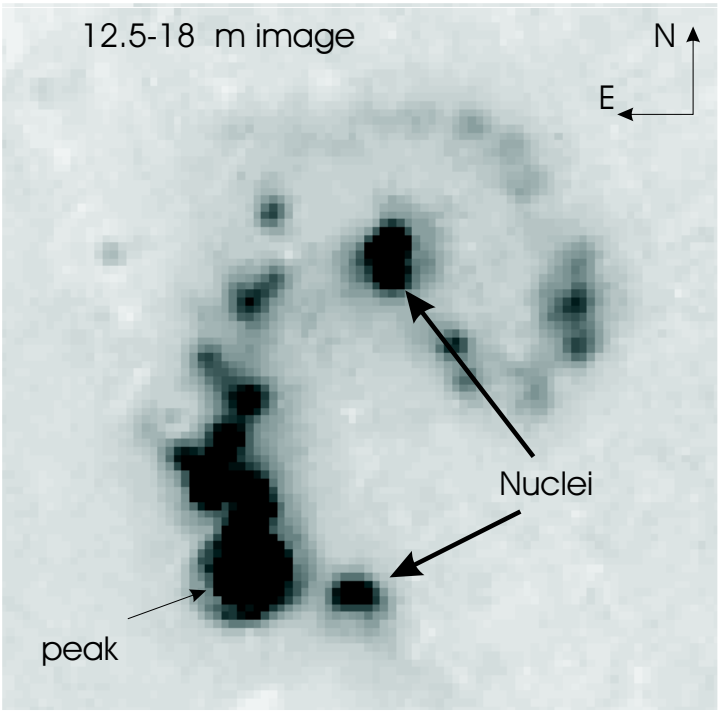

Fig. 3.3: ISO image between 12.5 and 18μm.

3.3 Mid-infrared Imaging and spectroscopy: Warm Dust

In 1996, several publications described the properties of NGC 4038/4039 in the mid- to far infrared. This wavelength range is sensitive to the thermal emission of warm dust and therefore to star formation regions where young stars heat up their surrounding medium. Also several forbidden line transitions are located in this wavelength regime, which can be exploited to derive some physical parameters of the environment. Observations were performed with the two spectrometers on-board the Infrared Space Observatory (ISO, Kessler et al. (1996)), the Short Wavelength Spectrometer (SWS, de Graauw (1996)) and the Long Wavelength Spectrometer (LWS, Clegg (1996)). Imaging was performed using the Infrared Space Observatory Camera (ISOCAM, Césarsky (1996)) in a spectrophotometric mode which used Circular Variable Filters (CVF).
The image obtained with the latter instrument in the wavelength range 12.5-18μm (see Figure 3.3, Mirabel et al. (1998) and Vigroux et al. (1996)) revealed the most intense star formation to be located in an extranuclear region. The location of the peak is a cluster which is inconspicuous at optical wavelengths.
Several other properties of the merger in general or special regions in particular were determined:

- Stars of masses as high as 60 $M_\odot$ are observed (mass from [NeIII]/[NeII] ratio) in highly obscured regions . This corresponds to effective temperatures of the ionizing stars of 39,500 K. $T_{\rm eff}$ in the nuclei is around 37,000 K (Kunze et al., 1996; Mirabel et al., 1998; Vigroux et al., 1996).

- High extinction in some regions, especially the interaction zone between the two nuclei: up to $A_V \approx 15$ mag (foreground screen extinction) or $A_V \approx 70$ mag (mixed stars and dust), from hydrogen recombination line ratios (Kunze et al., 1996). Fischer et al. (1996) derive $A_V = 1 - 4$ mag for some Brγ sources in the overlap region.

- 15% of the bolometric luminosity originate in an off-nuclear region smaller than 100 pc (obscured source in optical), (Mirabel et al., 1998)

- Displacement of dust lanes with respect to peak mid-infrared emission. Either due to a spatial separation of warm and cold dust, or due to projection effects, (Mirabel et al., 1998)
- Electron density in interaction region $\approx$ 300 cm^{-3} (from [SIII]18.71μm/33.48μm, Kunze et al. (1996))
- Young burst age in overlap region (7-8 Myrs), Fischer et al. (1996)

3.4 Millimeter Imaging: Molecular Gas

Using millimeter observations, CO emission can be mapped throughout the merger. Large concentrations of molecular clouds are birth places of stars and star clusters. At least two publications (Stanford et al., 1990; Wilson et al., 2000) determined the spatial distribution and densities of molecular clouds in the Antennae. The Wilson et al. (2000) data, obtained with the Owens Valley Millimeter Wave Interferometer, have the larger spatial coverage, therefore their results will be summarized briefly:

- The spatial distribution and concentration of CO gas correlates very well with ISO 15μm intensity, especially in the brightest regions. This means that stars are being formed from the fuel provided through the molecular clouds. But also the northwestern loop of star clusters is associated with some CO emission, in addition to the nuclei. The strongest peak of CO emission lies in the northern nucleus (NGC 4038).
- The most massive molecular gas complexes are unusually large (3-6 $\times 10^8$ M$_\odot$). Most of them are located in the region where the two galaxies apparently overlap.
- The most intensive 15μm peak hosts a star cluster which is not more massive or much younger than neighbouring clusters (see section 5.3.3). A possible explanation for the strongly rising mid-infrared (MIR) continuum is given by CO data. Two molecular cloud complexes with different velocities overlap at the location of the cluster. One of them could sweep small dust grains into the radiation field of older (few Myr) stars, which give rise to strong MIR emission.
- A table with molecular cloud masses is provided, which will be used in section 5.3.4 to test the correlation between gas and star formation rate density.

3.5 Dynamics

The first analysis of the dynamics of this system was performed by Toomre & Toomre (1972). Using simple models, they showed that the tidal features seen in this and other galaxies can be accounted for by tidal interactions and created an Antennae look-alike. Barnes (1988) used essentially the same initial conditions as described by Toomre & Toomre (1972) and added a dark mass halo, leading to two interacting spiral galaxies with bulge, disk and halo. Both galaxies are initially inclined by 60° with respect to the orbital plane. The pericentric arguments are -30°. A visualization of these initial conditions is displayed in Figure 3.4. Last pericenter, according to this model, was around 200 Myrs ago. The two disks are currently separating again. Roughly 100 Myrs later, the merger will be complete. Barnes (1988) points out that the appearance seems to be reproduced fairly well, however this is not the case for the velocity differences between the two galaxies. The observed value is around 30 km/s (Amram et al., 1992), in strong disagreement with the model predictions of Barnes (1988) (around 300 km/s). van der Hulst (1979) and Amram et al. (1992) point out that a simple rescaling of the model to the observed galaxy masses of around 4 $\times 10^{10}$M$_\odot$ will resolve most of this discrepancy.
The initial conditions suggested by Barnes (1988) were also used by Englmaier et al. (2000) in a simulation which included gas, stars and dark matter. It is very suggestive to think of the overlap region between the

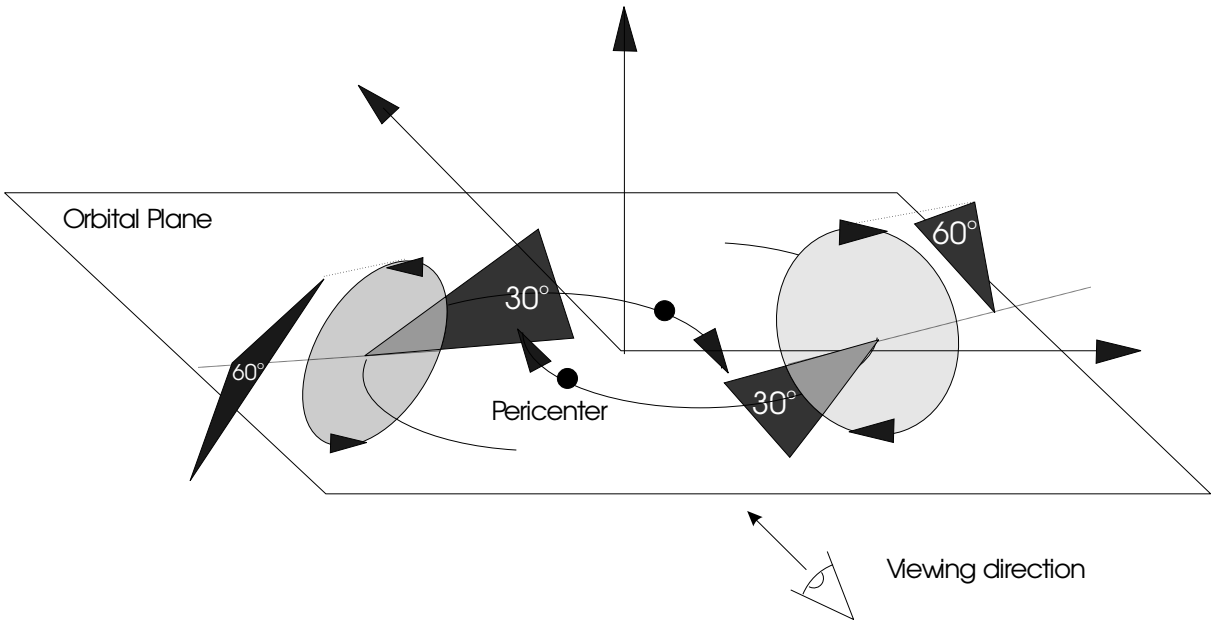

Fig. 3.4: This drawing (after Barnes (1988)) shows the initial conditions of the merger, as they were originally proposed by Toomre & Toomre (1972) and commonly used thereafter. The two galaxies start out on slightly eccentric elliptical orbits. Both galaxies are inclined by 60° with respect to the orbital plane. The pericentric argument is -30° for both galaxies. All of these angles are indicated in the drawing. For best match with the observed Antennae system, the model is seen from the direction indicated, a quarter of an orbit after pericenter.

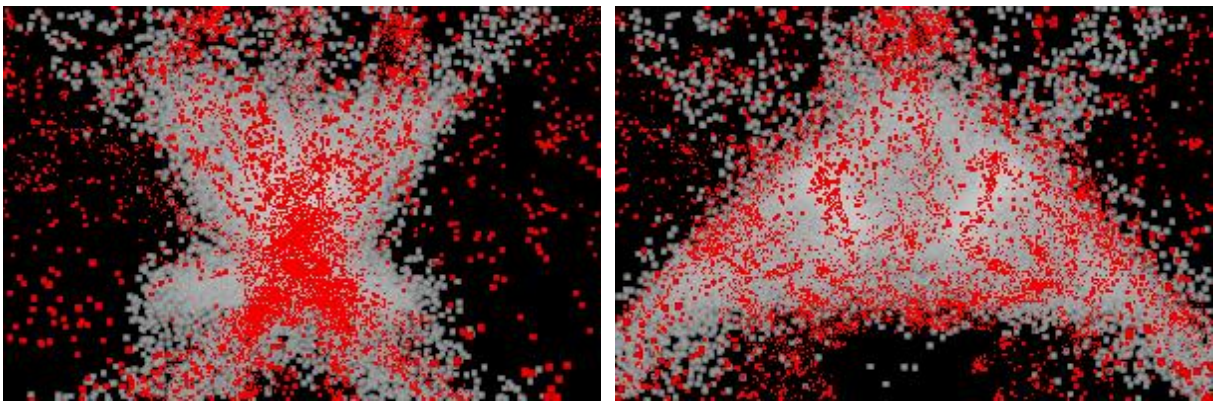

Fig. 3.5: Model computed by Englmaier et al. (2000). The two images are no time sequence, but a rotation of the modeled structure. Stars are shown in white, gas in red. The left panel shows the overlap region as a location of enhanced gas density. But if the model is rotated by 30°, this structure stretches out to form a long gaseous bridge.

two nuclei as the location where the disks actually collide, with the gas and dust being compressed and thus forced into strong star formation activity.
On the contrary, Englmaier et al.'s simulation rather suggests that region of enhanced optical depth is actually a projection effect. A gaseous bridge - or bar - forms between the two nuclei and its extent along the line of sight leads to the large extinction seen in this region. Figure 3.5 shows two views of the merger simulation: the view representing best the direction to the observer, and one at an angle of 30° to it, revealing the gaseous bridge.

4. MERGERS AND STAR CLUSTERS

4.1 An introduction to mergers

Two basic questions concerning the evolution of the universe are when galaxies formed, and when they formed their stars. Further, it needs to be determined, if these two events are closely linked or not. The last years have brought several observational insights into possible answers to these questions:
What had been suspected for years became evident with the deep observations of the Hubble Deep Field North (HDF-N): In the evolution of galaxies, mergers and other violent interactions between galaxies have played an important role in the early stages of the universe. Some of the well-known arguments for that fact were the pair density increasing as $(z+1)^m$ with $m \sim 3 \pm 1$ (Zepf & Koo, 1989; Abraham, 1999) already for studies with $z < 1$. Also, galaxies with peculiar shapes become more common with increasing redshift (van den Bergh et al., 1996). Theory also implicates merging as a driver of galaxy evolution, for example in the hierarchical clustering model by Layzer (1954), and in the Cold Dark Matter (CDM) model by Blumenthal et al. (1984), the merging of dark halos is an important characteristic of galaxy formation.
But the most convincing evidence came from the high redshift observations of galaxies in the Hubble Deep Field (HDF), which further supported the observation of increasingly common distorted galaxy shapes with increasing redshift, up to $z \sim 3$. Above that redshift, the cosmological dimming makes it difficult to identify features like tidal tails. But this population of HDF galaxies also shows strong starburst activity, where some of the galaxies appear to be forming stars at a rate of ~ 100 $M_\odot yr^{-1}$ (for comparison, the star formation rate of the Milky Way is ~ 1 $M_\odot yr^{-1}$). The galaxies forming stars at such an excessive rate emit most of their luminosity in the far infrared wavelength range, because the stellar radiation of these bursts is absorbed by dust and re-emitted. Due to these emission characteristics, these galaxies are called "Ultra Luminous Infrared Galaxies" (ULIRGs), and several examples are also observed at low redshifts. The Antennae belong to the slightly fainter group of otherwise similar properties, called LIRGs (Luminous Infrared Galaxies). The high redshift, heavily dust-obscured counterparts of ULIRGs are thought to have been identified at sub-mm wavelengths only recently (Hughes et al, 1998; Barger et al., 1999) and serve to argue that significant amounts of star formation took place at those epochs. At redshifts higher than $z \sim 5$, the Hubble types of galaxies seem to vanish completely (Barnes, 1999), the populations consist of objects that appear to be much smaller than present-day galaxies.
The properties of elliptical galaxies suggest that their formation included a violent relaxation process, and a very plausible suggestion for this violent process is the coalescence of multiple lumps. But if this merging process occurred only recently or earlier on, and how many objects were involved, or if the process occurred in several stages, is a topic that needs to be investigated (Barnes, 1999). Several studies (e.g., Schweizer & Seitzer (1992); Kaufmann, Charlot & White (1996); Schade et al. (1999)) with partially conflicting results suggest that a third to a half of the field ellipticals were already present at $z \sim 1$ and passively evolving from then on. These studies included the luminosity and colour observation of nearby ellipticals and deep photometric surveys. In general, it seems that merging started long before $z \sim 1$ and continued to the present for field ellipticals, while for cluster environments, the whole evolution started earlier and was basically finished at $z \sim 2$.

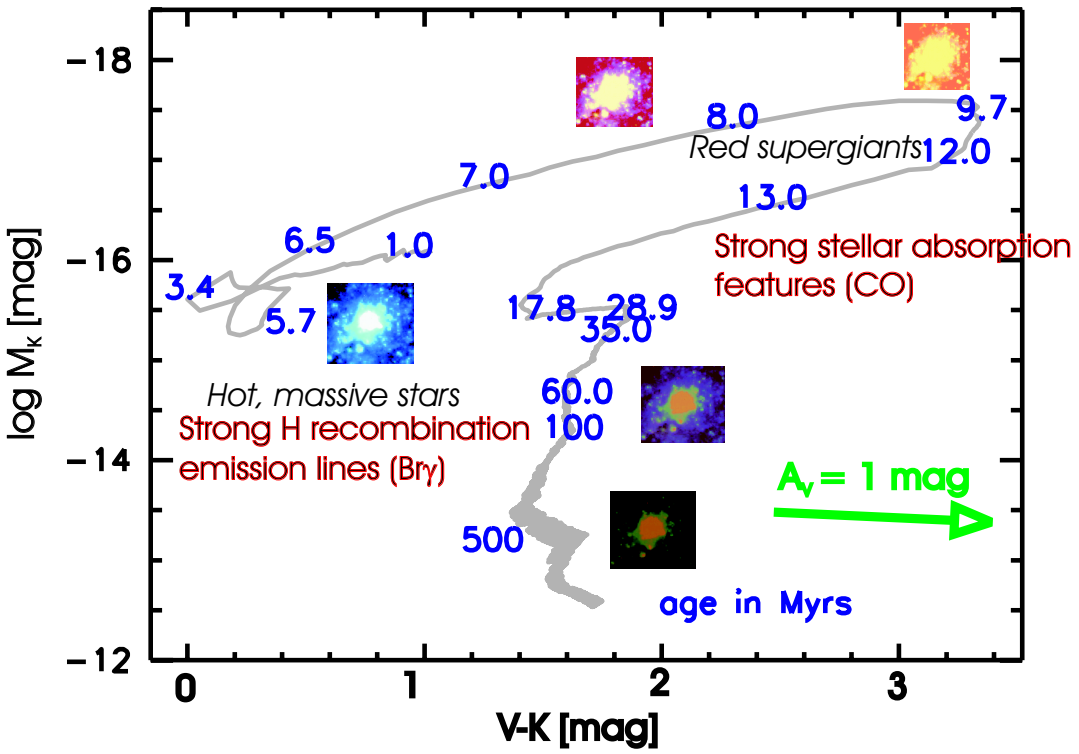

Fig. 4.1: Description of the evolution of a star cluster on a M_K/V-K diagram with characteristic phases indicated. At birth, the hot, massive, blue stars dominate the luminosity of the cluster and ionize their surrounding medium, giving rise to strong hydrogen recombination emission. As the cluster ages, these stars evolve into red supergiants. This evolutionary phase can easily be located in this diagram, and the supergiant spectral signatures detected in the near infrared. When the supergiants and giants die, the cluster colour stays more or less constant and it only fades away.

4.2 Star clusters and what they reveal

There are two basic ways to gain information about galaxy evolution: Either to observe them at the time when the action occurred, perhaps at the early stages of the universe, or to observe present day galaxies and to try to deduce from its components the evolution history of the host. A third approach that in a way combines the information already gained or provided by the two approaches is to observe present-day galaxies in which the processes that were important for the evolution are currently . As mentioned in section 4.1, mergers at high redshift are observed to have played an important role in galaxy evolution. But due to their distance, it is not possible to spatially resolve past and present star formation sites of these galaxies. Therefore it is useful to observe close templates in an approach to establish a scheme for this type of interaction.
This approach hosts some difficulties, because it is unclear how closely present day galaxies resemble the merger members at high redshifts, for example in gas content, metallicity, size and other properties. But since the other methods mentioned have difficulties, mainly of observational nature, the observation of a present day template seems a very reasonable approach.

These present-day templates, which means local mergers of spiral galaxies, are often observed to host a large population of bright blue star clusters that formed during the merger event (Lutz, 1991; Holtzman et al., 1992;

Schweizer, 1997). They have a property that makes them the perfect tool for the spatially resolved study of the starburst properties in a galaxy: usually, the spatial scale of these clusters is so small that it is safe to assume that the star formation occurred instantaneously. This means, that they are delta-burst probes, the ages of which can be determined using tracers suitable for that task. This age determination is generally possible, because, as a star cluster ages, different stellar populations dominate the luminosity of the cluster and imprint their spectral signature on the cluster as a whole. The colour-magnitude-evolution of such a cluster is shown in Figure 4.1. The curve was derived by a stellar population synthesis model (Starburst99 by Leitherer et al., 1999), while the cluster inset pictures serve to demonstrate the reddening and fading of a cluster.

The spectral evolution of a star cluster can be modelled using stellar population synthesis (for example by Leitherer et al. (1999); Sternberg (1998); Fioc & Rocca-Volmerange (1997)). These models create a star cluster according to an initial mass function with upper and lower mass cutoffs and then in discrete time steps follow the evolution of the cluster, producing as an output the synthesized spectrum at each time step. Some of these models - like the Starburst99 package - include also the nebular continuum emission from the ionized medium around hot stars.

These output spectra can then be used to establish tracers for the chronological evolution: spectral signatures that dominate only over certain age ranges. For example, the cluster colours can be determined by convolving the spectrum with the filter characteristics or equivalent widths of certain absorption or emission features predicted. Normalization to a total mass predicts absolute quantities like the luminosity in a given bandpass or the number of ionizing photons per unit mass.

Two main age discriminants lie in the near IR: Hydrogen recombination lines (Brγ will be used) and CO bandhead absorption features. Brγ emission is observed in star clusters below $\sim 8 \times 10^6$ yrs of age, when young hot, massive stars ionize their surroundings and lead to intense emission of hydrogen recombination lines. The CO bandhead is observed in any star cluster above that age limit, but with variable strength. It arises in the atmospheres of cool stars and is most prominent between 8 and 12 Myrs, when the red supergiants dominate the luminosity of a star cluster. See also section 4.4 for a more thorough discussion.

In addition to the equivalent width at Brγ, $W_{Br\gamma}$, and the equivalent width at the CO band head, W_{CO}, broadband colours like V-K or V-H can be used as an age diagnostic. They can be good age discriminants too, for the verification of the ages derived by other means, or to distinguish the age ranges of around 10 Myrs from those between 12 and 50 Myrs for the cases of high error bars. These two regimes can be quite well separated in the V-K colour. But it is affected by extinction, therefore an accurate extinction correction is required, for example by comparison of the Brγ / Hα - ratio with what is to be theoretically expected for case B recombination. The Paβ emission map can in principle be used for the same purpose. See chapter 5.3.6 for the creation of the extinction map for the Antennae.

The K-band and J-band HeI emission lines can be used as indicators for the hardness of the radiation field by comparison with the strength of the Brγ line. Shields (1993) studied the variation of the ratio HeI/(H recombination line) with the effective temperature of the ionizing stars. He showed that the J- and K-band lines are not the best possible tracers for that purpose, since the value of their ratio over Brγ does not show a monotonic behaviour with increasing temperature. The H-band line would be much more appropriate, since it is monotonic. However, the intensity is only 1/5 of the K-band line. So this ratio is used to derive a lower limit for the mass of the highest mass stars observed, and to compare this with the determined age of the cluster to check for consistency.

4.3 Stellar evolutionary synthesis modelling

4.3.1 Introduction

Stellar evolutionary synthesis modelling is used to derive the properties of a stellar population through its stages of evolution, from the birth of the first stars up to a Hubble time or longer. There have been numerous

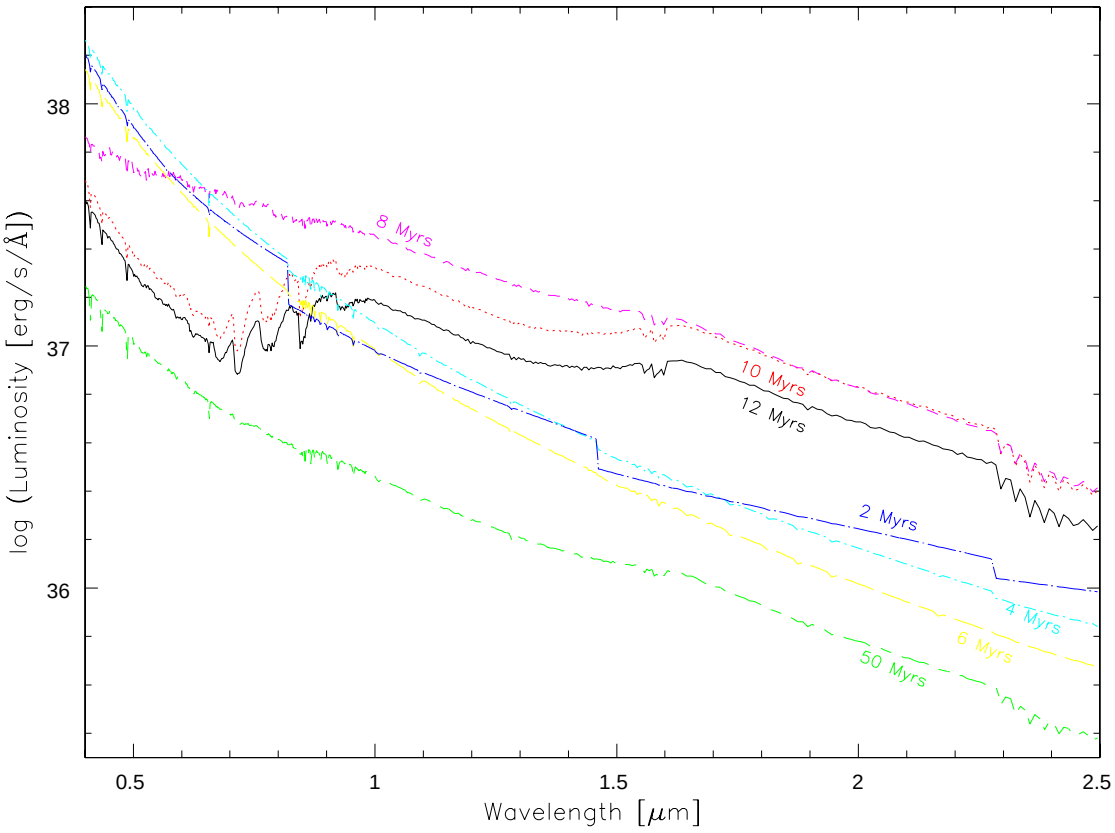

Fig. 4.2: Luminosity of a cluster of $10^6 M_\odot$ as a function of wavelength for different ages, derived from the Starburst99 models. Input parameters: instantaneous burst, Salpeter IMF between 1 and 100 $M_\odot$, solar metallicity. The SED includes the nebular continuum emission, but not the nebular emission lines.

approaches to this technique in the past (Tinsley, 1972; Huchra, 1977; Bruzual, 1983; Cerviño & Mas-Hesse, 1994; Fioc & Rocca-Volmerange, 1997; Sternberg, 1998; Leitherer et al., 1999). These approaches generally use a set of stellar evolution tracks, an initial mass distribution and a star formation rate as a function of time, and then follow the evolution of this stellar population. These models produce as output, for example, the spectral energy distribution (SED) of the whole population, often including the nebular emission, and/or they derive from this SED the time evolution of certain diagnostic features. The metallicity of the population is usually fixed (enrichment neglected) at a certain value, but some models were computed for several different abundances. Although much work on these types of models remains to be done, Starburst99 by Leitherer et al. (1999) is one of those considered substantially reliable. It has the advantage of presenting the results in a user-friendly way as a set of tables available electronically, and it also provides the source code and the possibility to run a model with user-defined parameters on one's own computer. The following section briefly describes some of its basic characteristics. In particular, we review what is known about the diagnostics that will be used subsequently to study the star formation properties of individual clusters. These include the equivalent widths of CO and Ca II absorption, and Brγ emission and broadband colours.

4.3.2 Starburst99

The Starburst99 package by Leitherer et al. (1999) is an evolutionary synthesis code that was explicitly developed to reproduce the properties of galaxies with active star formation. It uses an isochrone synthesis method (first introduced by Charlot & Bruzual (1991)), which does not have the discrete appearance of the classical method at late evolutionary stages that often occurs in other approaches. Interpolation between the tracks on the Hertzsprung-Russell-Diagram (HRD) on a variable mass grid leads to continuous isochrones. The output usually shows a smooth time evolution (their model time resolution being 0.1 Myr), with the exception of supernova-related quantities.

The package makes use of the synthetic model atmosphere grid of Lejeune et al. (1997) and the latest Geneva evolutionary tracks, complemented by the tracks with enhanced mass loss (Meynet et al., 1994, using Schmutz et al. (1992)) above a certain mass limit. The synthetic stellar spectra were calibrated to represent the average broadband colours of the respective stellar types. The Geneva tracks take into account the early asymptotic giant branch (AGB) evolution, but they omit the thermally pulsing AGB phase (TP-AGB). Binary evolution is also not considered, and chemical evolution is not treated self-consistently, the metallicity stays constant during the evolution of a population, and five different metallicities are available. Other input parameters include the slope of the IMF (exponent α of the power law dN/dM$\sim$M$^{-\alpha}$, say α = 2.35 Salpeter (1955) or α = 3.30 (weighted towards low-mass stars), for example. These mass distributions are valid between a lower and an upper mass cutoff ($M_{\rm lower}$ and $M_{\rm upper}$). While $M_{\rm lower}$ has little influence on the SED and contributes only to the stellar mass, making a simple scaling possible if it is to be changed, the choice of $M_{\rm upper}$ has strong influence on the output SED. The standard output tables have either $M_{\rm upper}$ = 30 or 100 $M_\odot$, but the possibility to run "tailored models" allows to select any values for $M_{\rm lower}$, $M_{\rm upper}$ and α.

The star formation rate is either instantaneous, also referred to as "single/simple stellar population", (the cluster mass is normalized to 10^6 $M_\odot$) or continuous with a SFR of 1 $M_\odot yr^{-1}$. This increase in stellar mass means that also the luminosity in a given wavelength range increases monotonically, as long as the death rate in the stellar population dominating that wavelength range has not reached an equilibrium with the corresponding birth rate. The Starburst99 code does not include the option of an exponentially decaying starburst.

The output of the code is the SED in time steps of 0.1 Myrs. All photons below 912 Å are converted to nebular continuum and line emission for the assumption of Case B recombination. This nebular emission is added to the SED, while generally, the emission below 912 Å is not removed. These SEDs were used, by convolution with a filter profile or similar techniques, to extract the evolution of a diagnostic feature in the star forming region. Some examples of the kinds of diagnostics that are built into the code are colour or magnitude evolution for standard optical and NIR filter sets.

The equivalent widths of stellar features are derived by applying the empirical formulae describing the quantity as a function of stellar effective temperature, gravity g and metallicity. The weighted average taking into account the contribution of each spectral type in the relevant wavelength range determines the value of the diagnostic for each time step. As an example, $W_{\rm CaT}$ (the equivalent width of the Calcium triplet absorption feature around 8600 Å, see section 4.4.1) is computed using the empirical relation of Díaz et al. (1989) $W_{\rm CaT}$ = 10.21 - 0.95 log(g) + 2.18 log($Z/Z_\odot$). $W_{\rm CaT}$ is insensitive to the stellar effective temperature.

The main drawbacks and uncertainties with the Starburst99 code and their relevance for this work are the following:

- Metallicities: The lack of a self-consistent treatment of the chemical evolution affects mainly the blue part of the spectrum for older stellar populations, because the youngest stars dominate that wavelength range and should be formed out of enriched ISM. Since most of the star clusters in this work are of small spatial extent (the effective radius is $R_{\rm eff}$= 4 pc), an instantaneous burst is appropriate, where after the initial delta-burst no stars are formed, the spectra and conclusions are not affected by the absence of metallicity evolution. In the nuclei and some of the largest clusters, however, this assumption might

not be correct, with an exponentially decaying burst possibly more appropriate. The NIR spectra should not be affected, and the UVES spectra were not taken in these regions.

- Binarity: Current estimates predict that roughly 50% of all stars form in binary pairs. However, it has not yet been extensively studied, how that affects the cluster spectra. Several investigations, most of them concerning the evolution of WR features, have been made (Cerviño & Mas-Hesse, 1994; Vanbeveren, Van Bever & de Donder, 1997; Schaerer & Vacca, 1998). Vanbeveren, Van Bever & de Donder (1997) state that binary star evolution "rejuvenates" a star cluster, because it populates via mass transfer parts of the Hertzsprung-Russel-diagram which had formerly been depleted. Only single star evolution was taken into account here, which could mean that the absolute age dating could date clusters too old. However, the relative dating between different clusters should be correct, unless binarity fraction or evolution varied significantly between them. The effect on the NIR data is quantitatively unknown, but qualitatively the cluster would look younger than its actual age in all the NIR age tracers.

- Mass loss and mixing: These processes, which occur at certain evolutionary stages, are only partially included in the models. While enhanced mass loss in the Wolf-Rayet (WR) and the AGB phase are included, the models for RGB stars do not reproduce the observed properties well for low metallicities. Since solar metallicities are likely to be appropriate in the case of the Antennae, this drawback does not affect the interpretation of the data. However, the omission of the TP-AGB phase has direct impact on the NIR part of the simulated spectra, as discussed recently by Oliva & Origlia (2000). They caution that the enhanced mass loss in the AGB phase and the inclusion of the TP-AGB phase directly influence the strength of the CO bandhead features. This effect is strongest in low metallicity environments above 50 Myrs and therefore has little impact on the data presented here. Nevertheless, instead of using Starburst99 for the age determination from the CO bandhead features, model predictions from STARS (Sternberg, 1998) were used. This code, also described thoroughly in Förster-Schreiber (1998), includes the TP-AGB phase.

The parameters which are most appropriate for the case of the star clusters in NGC 4038/39 are the following and will in the following chapters often be addressed as the *standard parameters*:

- instantaneous burst
  Cluster sizes are typically around $R_{\rm eff}$ = 4 pc. This small size, which corresponds to a dynamical timescale of $t_{\rm dyn}$ = few $\times 10^5$ yrs (also see chapter 4.5), does not allow star formation to proceed for durations comparable to the cluster ages of a few Myrs.

- solar metallicity (Z = 0.02)
  Given the fact that most of the bright clusters in the Antennae formed only recently and that the progenitor galaxies were gas-rich spirals, solar metallicity is the natural assumption. But this assumption is supported by the few metallicity determinations performed on similar objects (young star clusters in more advanced mergers, NGC 7252 and NGC 1275). Schweizer & Seitzer (1998) and Zepf et al. (1995) found metallicities of $\log(Z/Z_\odot)=0.00\pm0.15$. However, UVES spectroscopy of [W99]-2 suggested a metallicity higher than solar (see section 5.4.5), while the spectrum of [W99]-1 is compatible with $Z = Z_\odot$. Therefore, Z = 0.02 is assumed for all clusters except [W99]-2.

- Salpeter IMF (α = 2.35)
  most observations in starburst regions like the Antennae are compatible with a Salpeter IMF

- $M_{\rm lower} = 1\ M_\odot$, $M_{\rm upper} = 100\ M_\odot$
  the ISO data indicate the presence of high-mass stars in the overlap region for clusters with ages of several Myrs. At that age the highest mass stars have already evolved off the main sequence. The lower

mass cutoff is, somewhat arbitrarily, set to $1 M_\odot$. $M_{\rm lower}$ has no influence on relative properties like the equivalent widths, because stars below a few solar masses do not contribute to the total luminosity of the cluster at the age range considered here. Absolute quantities like luminosities can easily be scaled to a different $M_{\rm lower}$, if there is evidence that this is appropriate. See also chapter 5.4.3

The expected cluster SED for the whole wavelength ranges from the UV to the near infrared and for several different cluster ages, as they are derived for a cluster with the standard parameters and a total mass of 1 $\times 10^6$ $M_\odot$ are displayed in Figure 4.2.
If these parameters are inappropriate in certain cases (nuclei: exponentially decaying burst or continuous star formation, one cluster (see chapter 5.4.5): supersolar metallicity), other parameters will be considered and discussed in the corresponding chapters.

4.4 Diagnostics

In principle, the evolution of any diagnostic feature can be derived from the SED which is created as an output by the models, if the spectral resolution is high enough or not critical. As mentioned earlier, the evolution of line diagnostics is not derived from the SED, but calculated from empirical formulae. The most commonly used diagnostics are already published in tables or produced in the user-defined models that can be run independently. This is the case for the age diagnostics that will be used in the analysis of the star clusters in NGC 4038/39.

4.4.1 Equivalent widths

The relative strength of a spectral emission or absorption feature is conveniently measured as equivalent width (EW). It is defined as

$$W_\lambda = \int_{\lambda_1}^{\lambda_2} (1 - f_\lambda) {\rm d}\lambda \qquad (4.1)$$

with the integration limits λ_1 and λ_2, the normalized object spectrum f_λ with a flat continuum slope, and W_λ expressed in Å. The convenient property of the EW is the independence of extinction that arises from the continuum normalization. However, the equivalent widths used for the age diagnosis of the star clusters can be affected if the spectrum in that domain receives a contribution from the stellar population not currently considered. For example, if a young star cluster has an underlying older stellar population, that will, depending on the age, be the main contributor to the K-band continuum and thus lead to artificially low values for the $W_{\rm Br\gamma}$ (see also chapter 5.3.3). The equivalent widths have the disadvantage that they require a spectrum to be measured. Approximations to these values can be obtained by observations in narrow band filters, which means that within limited observing time a much larger spatial region can be covered. The EW determination from narrow-band imaging is less certain than the derivation of the EW from the spectrum, because the filters are relatively broad, so that they could include spectral features apart from the one being studied, and they are sensitive to redshift. However, if the object is within a redshift range that places the diagnostic feature within the filter bandpass (which is the case for the redshift of NGC 4038/39 of z≈1.005 and the commonly available narrow band filters), and a number of data points are available for the verification of the results, this method should yield useful values of the EW over a large region.

The Brγ equivalent width ($W_{\rm Br\gamma}$)

The Brγ line (rest wavelength $\lambda_0 = 2.166$ μm), like all the HI recombination lines in the young star clusters, arise from the ionized medium around young, hot, massive stars. This means that it is strong while these stars are still present and declines as the limiting mass for the main sequence evolution shifts to lower and lower

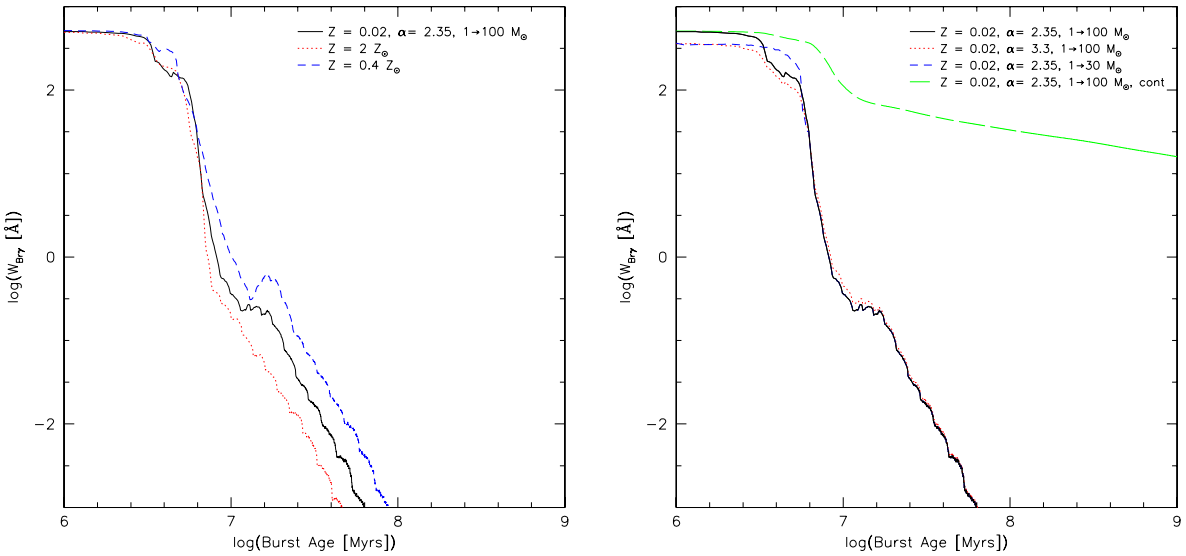

Fig. 4.3: Evolution of $W_{Br\gamma}$. The parameters that apply for each plot are indicated. In both plots, the *standard parameters* (p. 27) are displayed in black, solid lines. The left plot shows the variation with metallicity, in the right plot the IMF with respect to slope α and M_{upper} is varied. Moreover, the behaviour in case of continuous star formation is displayed. Only the duration of star formation has significant influence on $W_{Br\gamma}$ in the regime (between 10 and 200 Å) of interest.

masses. Above an age of $\sim$ 8 Myrs it is very weak for an instantaneous burst. The situation is somewhat different for the continuous star formation model, where $W_{Br\gamma}$ never drops below 10 Å, at least for the standard model (which is the model using the *standard parameters* from page 27) below 1 Gyr. Figure 4.3 shows the evolution of $W_{Br\gamma}$ up to a cluster age of 10^9 yr. The curve for the *standard parameters*, which will be mainly used for the analysis, is shown as a black, solid line, while variations of the input parameters have other linetypes and colours. Over the range of interest (between $W_{Br\gamma}$ = 10 and 200 Å) only little variations are observed, only the burst length has a dramatic influence on the evolution of $W_{Br\gamma}$. In the first panel, the metallicity affects the hydrogen recombination line by influencing the evolution timescales of the stars. Higher abundances lead to a slightly faster evolution of the hot, massive stars, while it is slower for sub-solar metallicity.

As expected, changing the upper mass cutoff from 30 to 100 $M_\odot$ has influence only up to $\approx$ 6 Myrs, the lifetime of a star of 30 $M_\odot$. The mass contribution of stars between 30 and 100 $M_\odot$ is low for a Salpeter IMF, therefore the evolutions for these two cases are virtually identical after 6 Myrs. For the steeper IMF with α=3.3, the still high M_{upper} of 100 $M_\odot$ balances $W_{Br\gamma}$ to be comparable to the Salpeter IMF and M_{upper} = 30 $M_\odot$ case. This IMF is biased towards low-mass stars, but their influence cannot be observed in this diagnostic, because only stars above $\approx$15 $M_\odot$ have a radiation field hard enough to significantly ionize the surrounding medium.

It has been observed (e.g. Mas-Hesse & Kunth (1999)) that very young star forming regions are never seen to reach the very high equivalent width in hydrogen recombination lines as they are predicted by the models. There have been two suggestions why this might be the case: Either dust destroys ionizing Lyman continuum photons, but has little effect on the corresponding optical or NIR continuum, thereby decreasing the observed equivalent width, or stellar evolution for the most massive stars (above 40 $M_\odot$) needs to be taken into account differently, because they might burn considerable amounts of their hydrogen already during the accretion phase and therefore effectively enter the main sequence at lower temperatures. If either of these

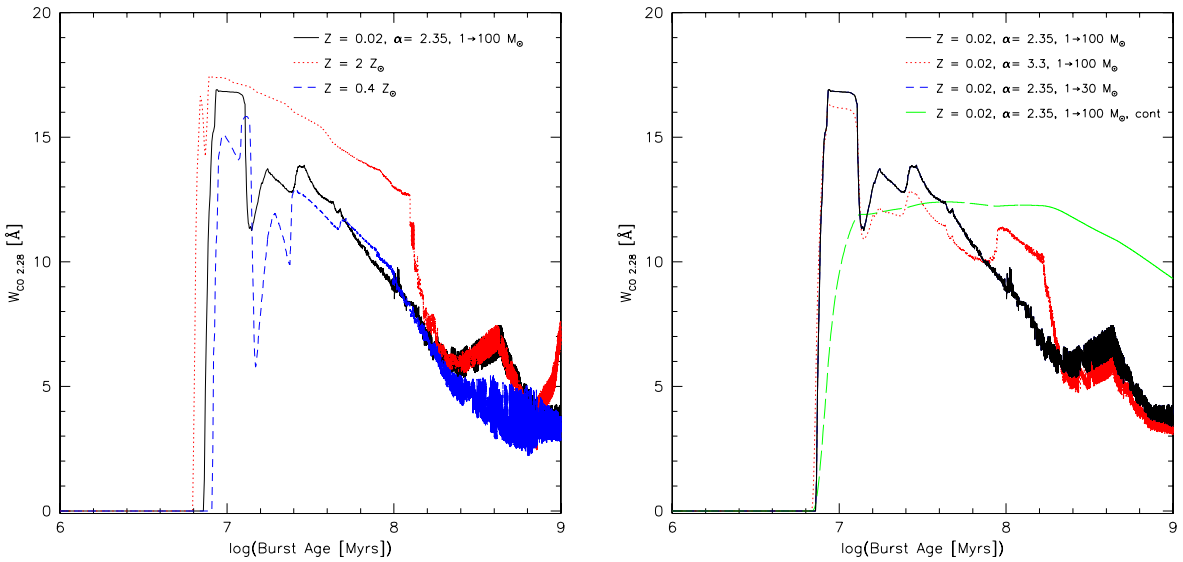

Fig. 4.4: Evolution of $W_{CO2.28}$. The parameters that apply for each plot are indicated. In both plots, the *standard parameters* are displayed in black, solid lines. The left plot shows the variation with metallicity, in the right plot the IMF with respect to slope α and M_{upper} is varied. Moreover, the behaviour in case of continuous star formation is displayed. Effects are most dramatic with variable burst length and variable metallicity. The evolution above ≈50 Myrs is somewhat uncertain, mainly for low metallicities. This arises from the non-inclusion of the TP-AGB phase in the stellar evolution models. For the interpretation of our observed diagnostic, the evolution predicted by the STARS code (Sternberg, 1998) is used instead (see Figure 4.5). These plots here are intended to show the dependence of the diagnostic on the various IMF parameters.

scenarios were applicable, an overestimation of the ages for clusters with very high values of $W_{Br\gamma}$ is possible.

The ^{12}CO(2-0) equivalent width (W_{CO})

The CO bandhead absorption features starting at a rest wavelength of 2.29μm have their origin in the atmospheres of cool stars, mainly red giants and supergiants. They represent ro-vibrational transitions of the CO molecule. The energy differences of the rotational states corresponding to a vibrational level are very small, they merge to a broad absorption feature with a so-called "bandhead" at the well-defined short wavelength edge that corresponds to the maximum energy of the vibrational-rotational transition (Herzberg, 1950). With the low resolution spectra obtained by 3D, the CO bandheads are unresolved. However, the higher resolution spectra observed with ISAAC resolve part of the absorption features. Close to the bandhead, the energy differences in the different rotational transitions are smallest, therefore they blend, but further away from the bandhead the energy differences increase, and show up as resolved “ripples” in the ISAAC spectra. See chapter 5.4.3 for a comparison of a stellar spectrum with the theoretical absorption features.

The bandhead corresponds to a rotational quantum number J=50, which implies excitation temperatures of $\sim$ 7000 K and therefore in an astrophysical context can only be formed in a stellar atmosphere. This explains why they are good tracers of the stellar population in environments that also contain hot gas, like for example the centres of galaxies or young stellar clusters. An analysis of the characteristics of the K-band CO absorption features (Persson et al., 1983; McWilliam & Lambert, 1984; Kleinmann & Hall, 1986; Lançon & Rocca-Volmerange , 1992) showed that their depth depends on stellar type (increasing towards later types), luminosity (increasing with increasing luminosity) and metallicity (increasing with metallicity). Metallicity in

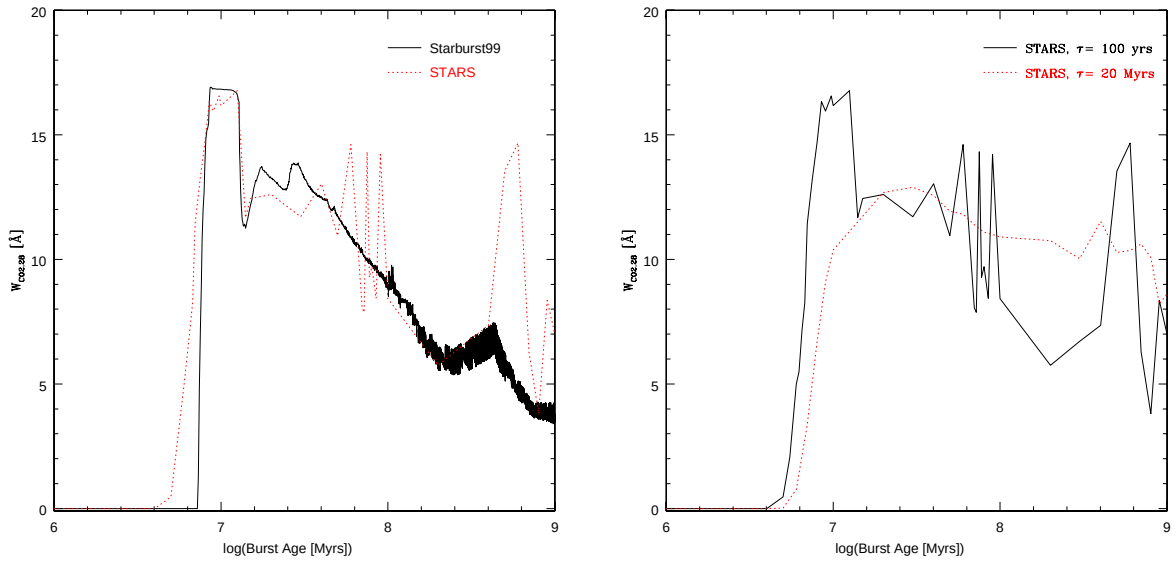

Fig. 4.5: Left panel: Evolution of $W_{CO2.28}$ calculated by two different evolutionary synthesis codes, Starburst99 (solid, black) and STARS (Sternberg, 1998) (dotted, red). Both models are compared for *standard parameters* (p. 27). For the STARS code, the instantaneous burst scenario was approximated by setting the timescale of the exponentially decaying burst to a very small number (100 yrs). The major difference between the two models is observed at ages between 40 and 100 Myrs and around 500 Myrs, where Starburst99 predicts a monotonically decreasing equivalent width, whereas the STARS predictions have several local maxima in these age ranges. This difference arises from the inclusion of the TP-AGB phase in STARS. The STARS predictions will be used for the analysis of the data presented in this work. However, most clusters will be found to have very young ages (below 12 Myrs), for which the difference in the models is insignificant. The right panel compares the evolution of W_{CO} predicted by STARS for the approximately instantaneous burst with that of an exponentially decaying burst with the timescale $\tau = 20$ Myrs.

Species	Vibrational band (v → v')	Bandhead [μm]
$^{12}C^{16}O$	2 → 0	2.2935
	3 → 1	2.3227
	4 → 2	2.3535
	5 → 3	2.3829
$^{13}C^{16}O$	2 → 0	2.3448
	3 → 1	2.3739
	4 → 2	2.4037

Tab. 4.1: Vacuum rest wavelengths of the CO bandheads

case of the Antennae is assumed solar (or twice solar in the case of one cluster, see chapter 5.4.5), but the other two dependencies mean that the bandheads are strongest in late type (K-M) supergiants, and still strong in late type giants (see the caption of Table 5.1 for some typical numbers for W_{CO}).
The rest wavelengths of the ^{12}CO and ^{13}CO bandheads that lie in the wavelength range accessible to the 3D spectra are listed in table 4.1.
When giants and/or supergiants dominate the luminosity of a star cluster, their features become evident in the integrated spectrum. The absorption is strongest in the supergiants, and since they dominate the luminosity between 8 and 12 Myrs, this is the age range where W_{CO} peaks. Figure 4.4.1 shows the evolution of W_{CO} for the *standard parameters* and with varied burst timescale, metallicity and IMF. The most extreme deviations from the "standard evolution" arise when the burst is continuous, but also when the metallicity varies. The dependency of the stellar evolution timescale on metallicity causes the massive stars to reach the RSG phase earlier or later than in the standard case. But also the maximum W_{CO} value reached differs for the three cases, and the transition from the RSG- to the giant dominated regime (10 vs. 50 Myrs). The evolution for the low metallicity case, as mentioned earlier, has to be used with caution, because theory for this case currently fails in reproducing the observed ratio of red- to blue supergiants.
A diagnostic which is basically identical to W_{CO} is the CO index, which is the difference in magnitude between a narrow band continuum filter and one centered on the second CO bandhead ($^{12}C^{16}O$(3-1) at 2.3227μm). This is the diagnostic which will be measured by the SOFI narrow band imaging, and for the sake of easy comparison, the CO index is converted into W_{CO} by using the empirical relationship (Oliva & Origlia, 2000; Kleinmann & Hall, 1986) CO_{phot} + 0.01)/0.57 = - 0.57 × 2.5 log(1 - W_{CO} / 53Å) - 0.01

The Calcium Triplet equivalent width (W_{CaT})

The evolution of the equivalent width of Ca II absorption (referred to as W_{CaT} and CaT, respectively, hereafter) is similar to that of W_{CO}, since it also arises from stellar atmospheres and is strongest in supergiants. W_{CaT}, as shown in empirical studies by Jones et al. (1984) and Díaz et al. (1989), is a strong function of metallicity, showing only fairly weak absorption at low metallicities. For a fixed metallicity, W_{CaT} is dominated by the influence of the stellar surface gravity and is strong for stars with low gravity like the red supergiants. This means that at ages when these stars dominate the luminosity of the cluster, just like in the W_{CO} case, W_{CaT} peaks, shows a second smaller increase during the TP-AGB phase and then declines. Figure 4.6 shows the evolution of the feature with the standard parameter set and for varied parameters. Since this diagnostic lies at much bluer wavelengths than W_{CO} it can be affected by contributions of other stellar types. Specifically, the contribution of higher Paschen lines from main sequence stars falls on top of the CaT and can still contribute mildly at ages less than 10 Myrs. This contribution does not affect the diagnostic plots presented here, because W_{CaT}, as described in the introduction to this chapter, is not derived from the synthesized spectrum, but

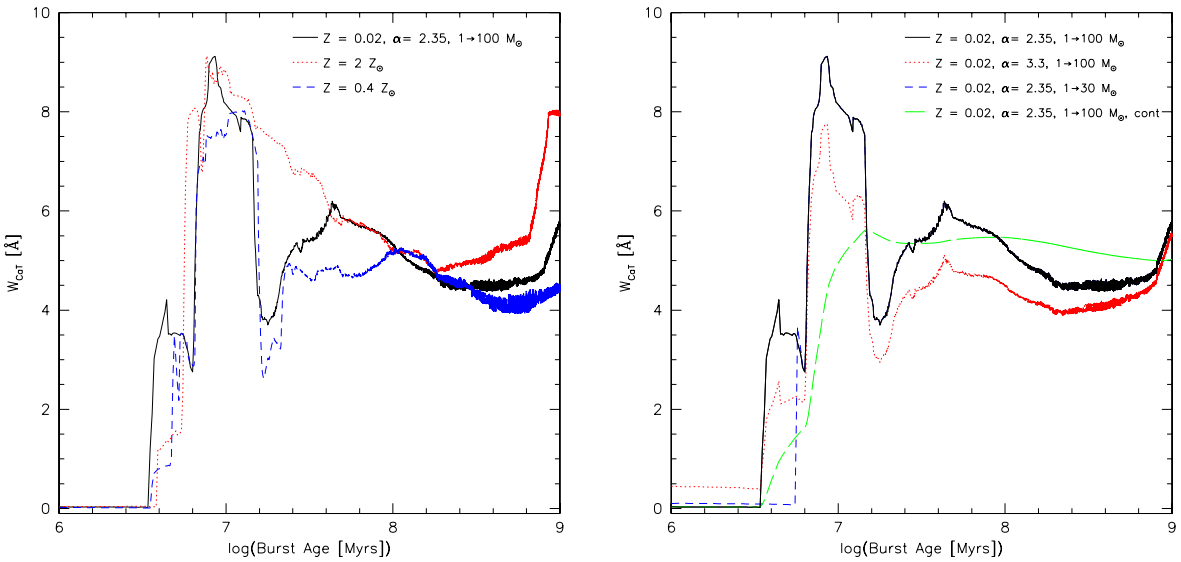

Fig. 4.6: Evolution of W_{CaT} for *standard parameters* (solid, black) and variations (left panel: metallicity, right panel: IMF and burst length).

for each star in the population from an empirical formula and then averaged. But since these stars can be present in cluster spectra, the Paschen absorption features have to be accounted for, as well as the continuum contribution of the main sequence stars.

Even though supergiants have the deepest CaT absorption and cause the maximum in the evolution track around 10^7 yrs, moderately hot main sequence stars also show this absorption feature to some extent (up to $W_{CaT} = 6$ Å, depending on metallicity), see Díaz et al. (1989) for some examples. This is the reason why the behaviour of W_{CaT} compared to W_{CO} differs most obviously below the age of ∼8 Myrs.

4.4.2 V-K colour

The colour evolution mirrors, like the equivalent widths, the influence of different star classes on the total luminosity of the cluster. As one example, the V-K colour evolution is shown, which displays one of the most extreme variations of any colour. Here, unlike with the EWs, extinction has a strong impact on the derivation of the colour. Figure 4.7 (left) shows the evolution of V-K colour with burst age for the *standard parameter* set and for variations in metallicity. The dip in the colour evolution between 50 and 100 Myrs is not nearly as deep as the one around 10 Myrs, and this can be used to differentiate the two age ranges, better than by using W_{CO} alone. According to the models, $W_{Br\gamma}$ at that age is already below 1 Å, below the noise level of the observations presented here. Figure 4.7 (right) shows the evolution of the V-K colour for variations in IMF, upper mass cutoff and burst length.

4.4.3 The HeI/Brγ line ratio

The K-band emission lines HeIλ2.058 μm and Brγ (at 2.166 μm) have different ionization potentials, but comparable critical densities. This would, in principle, make the ratio HeIλ2.058 μm over Brγ a sensitive tracer of the hardness of the radiation field. Since it is the hottest stars present, which contribute the largest fraction of the ionizing UV radiation field, their effective temperature T_{eff} could be determined.

However, as discussed by Shields (1993), the HeI2.058 emission is amplified by resonance flourescence due scattered Lyα photons which populate the upper level of the HeI2.058 line emission. This means that the

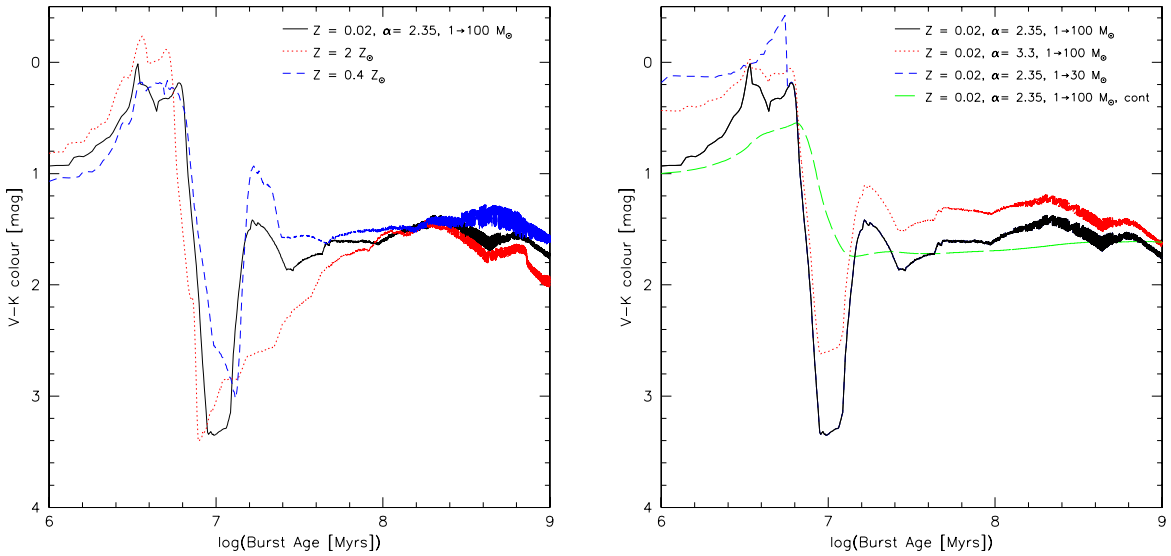

Fig. 4.7: Evolution of V-K colour for *standard parameters* (solid, black) and variations (left panel: metallicity, right panel: IMF and burst length)

strength of the line emission depends on the amount of scattered Lyα photons, and therefore on the nebular parameters line helium abundance, dust content, density etc.

For the environments studied here, this implies that the ratio HeIλ2.058μm/Brγ does not vary monotonically with increasing temperature $T_{\rm eff}$. For $T_{\rm eff} > 40,000$K, the ratio of HeI to HI decreases, thereby reducing the number of Lyα photons and HeIλ2.058μm/Brγ. Figure 4.8, calculated by Förster-Schreiber (1998) (which also includes a thorough discussion of the topic), shows the variation of this ratio with increasing effective temperature of the ionizing star for nebular parameters which are appropriate for the star clusters in NGC 4038/4039.

The ratio HeIλ1.701μm/Br10 is a much better indicator of the hardness of the radiation field. The HeIλ1.701μm line emission is insensitive to nebular parameters therefore HeIλ1.701μm/Br10 increases monotonically with increasing effective temperature of the ionizing stars. But unfortunately, the HeIλ1.701 line is extremely faint (roughly 10% of HeIλ2.058) and therefore not easily observed in faint sources or sources with a strong K-band continuum.

The ratio of HeIλ2.058μm/Brγ will nevertheless be analyzed for the 3D spectra, because the ISO data allow to set some constraints on the nebular parameters, like the density, with low spatial resolution (they suggested the presence of hot, massive stars in the overlap region (Kunze et al., 1996)). Therefore the HeIλ2.058/Brγ ratio should be useful in setting lower limits on the effective temperature of the hottest stars in the clusters, also in comparison with the [NeIII]/[NeII] ratio from the lower resolution ISOCAM CVF images (see chapter 3.3 for details).

4.4.4 Luminosities

Introduction

Absolute quantities for the clusters, like their luminosities in certain wavelength bands, or similarly the number of Lyman continuum photons $N_{\rm Lyc}$, are valuable tools for estimating the mass of the star cluster. The Starburst99 models are normalized to a cluster stellar mass of 10^6 $M_\odot$ (instantaneous burst), which has no effect on the relative properties in the previous section, but determines the scale of the properties described

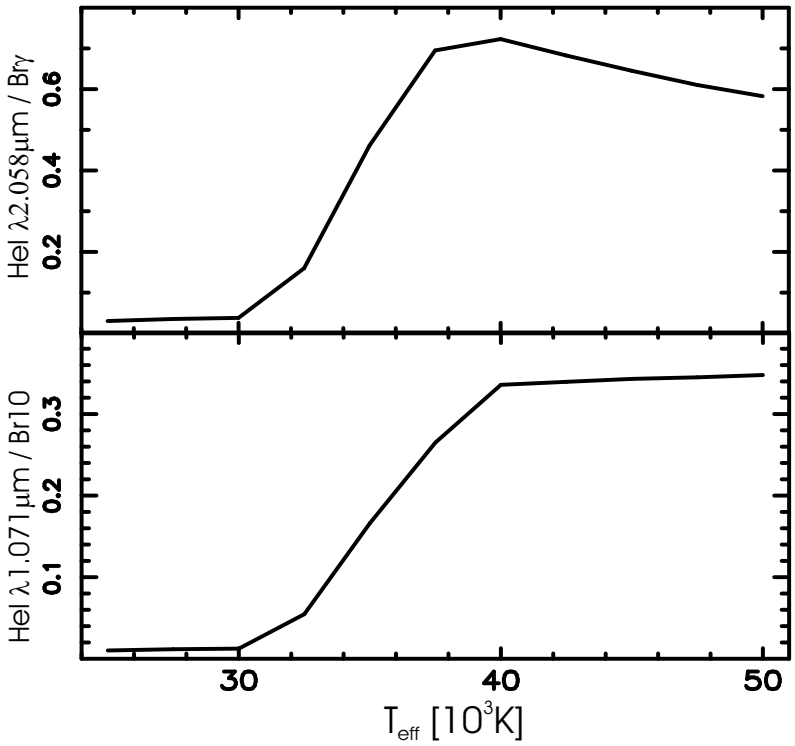

Fig. 4.8: Variation of HeIλ2.058μm/Brγ and HeIλ1.701μm/Br10 with $T_{\rm eff}$. The nebular parameters were density $n_H \approx n_e = 300$ cm^{-3}, radius of the HII region R = 25 pc and ionization parameter log(U) = -2.3 dex, solar gas abundance and dust grain depletion. The parameters apply to M82, but are comparable in the Antennae (Fischer et al., 1996). The electron density in a large aperture covering the overlap region of NGC 4038/39 was determined by Kunze et al. (1996) from ISO-SWS spectra to be $n_e = 300$ cm^{-3}. Förster-Schreiber (1998) used the CLOUDY photoionization code (Ferland, 1998) and theoretical computations by Smits (1991) to derive the above ratios. While HeIλ1.701μm/Br10 increases monotonically with $T_{\rm eff}$, the ratio HeIλ2.058μm/Brγ shows a maximum at around 40,000 K.

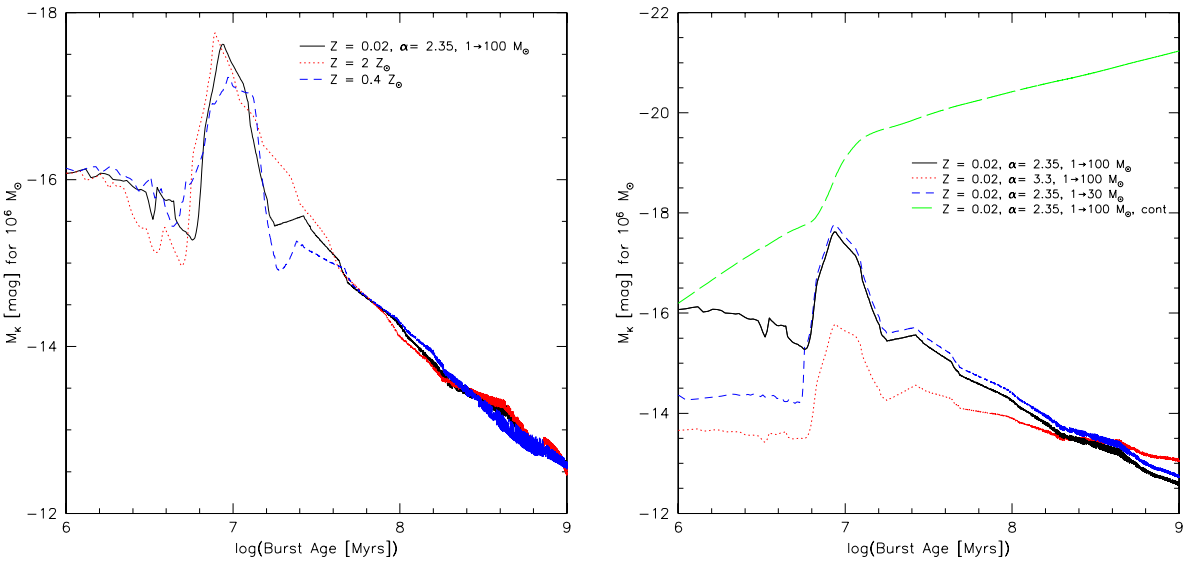

Fig. 4.9: Evolution of absolute K magnitude M_K for *standard parameters* (solid, black) and variations (left panel: metallicity, right panel: IMF and burst length).

in this section. These quantities are strongly dependent on the assumed IMF parameters, excluding M_{lower} (stars below 1 $M_\odot$ do not contribute significantly to the luminosity in any wavelength range below an age of 1 Gyr). So an extension of the IMF to masses below our assumed M_{lower} is done by simply scaling the output absolute quantities. For example scaling a Salpeter IMF with $M_{lower} = 1\ M_\odot$ to 0.1 $M_\odot$is done by *dividing* the linear quantity by 2.6 (distributing 10^6 $M_\odot$ over more low mass stars leaves less mass to the high mass stars which contribute to the luminosities).
All absolute quantities in this chapter require an assumption of the distance to NGC 4038/39. Lacking other measurements, the redshift of ∼1450 km/s is converted to a distance of 19.3 Mpc, assuming a Hubble constant of 75 km/s/Mpc. This corresponds to a distance modulus of m-M = 31.41.

K-band luminosity

The K band luminosity is easier to apply to the clusters in the Antennae, because it does not require a very accurate extinction estimate. For moderate extinctions ($A_V \approx 1$mag), the extinction in K-band is roughly 0.1 mag and therefore comparable to the photometric errors in our measurements. However, the spatial resolution in the near infrared images is low compared to the optical HST images. The luminosity increases monotonically in the continuous starburst scenario, because new stars are formed constantly. In this wavelength range, the newborn stars never reach an equilibrium luminosity state with the dying stars. The K-band luminosity peaks at $\sim 10^7$ years, when red supergiants dominate this wavelength range. It is obvious that it is crucial to differentiate clearly between clusters below 5 Myrs and those around 10 Myrs, because the luminosity both in K and in V band changes by two magnitudes in this age range.

V-band luminosity

Some of the considerations in the previous section also apply for the temporal evolution of the V-band magnitude. However, in V-band extinction is a severe problem in the Antennae, reaching $A_V = 5$ mag for some clusters. Before a comparison between measured and theoretical V-magnitudes is made, an extinction correction needs to be applied.

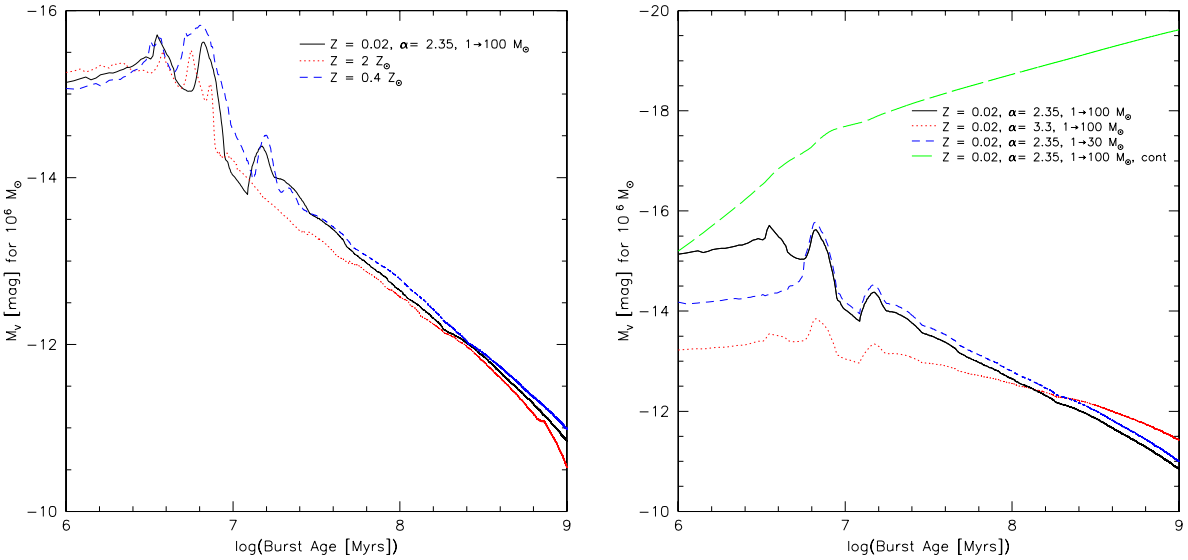

Fig. 4.10: Evolution of absolute V magnitude M_V for *standard parameters* (solid, black) and variations (left panel: metallicity, right panel: IMF and burst length).

Number of Lyman continuum photons (N_{Lyc})

The temporal evolution of the number of Lyman continuum photons (all photons with wavelengths below 912 Å, N_{Lyc}) is similar to that for $W_{Br\gamma}$. This is due to the fact that for a given recombination scenario (Starburst99 assumes case B recombination for the calculation of the nebular emission) there is a fixed ratio between N_{Lyc} and the number of Brγ photons. The only difference between the two properties is the normalization by the stellar and nebular continuum in case of $W_{Br\gamma}$. Also the determination of N_{Lyc} requires extinction calibration.

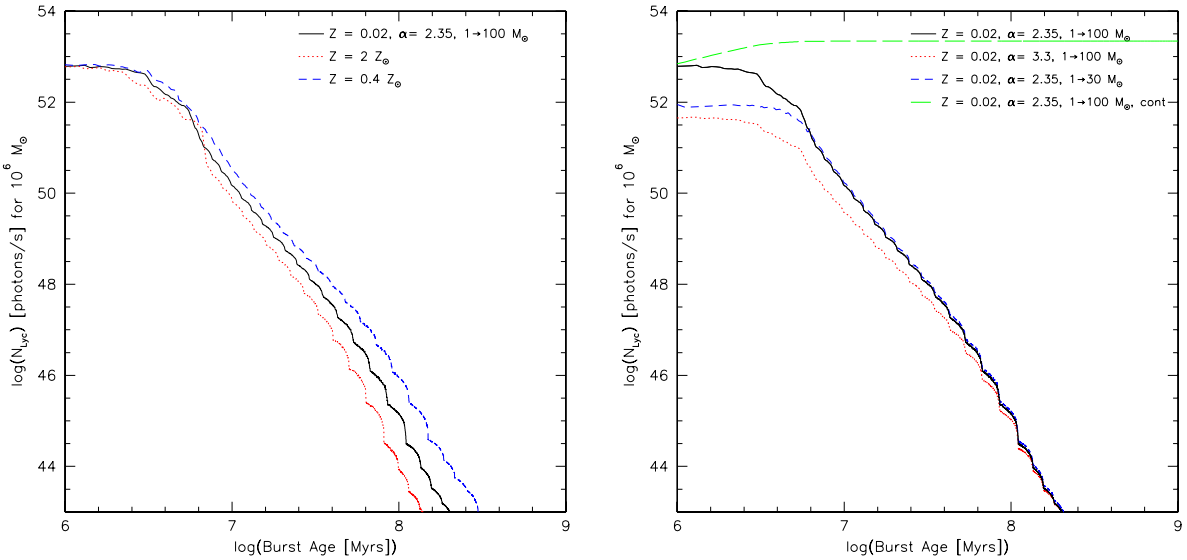

Fig. 4.11: Evolution of the number of Lyman continuum photons N_{Lyc} for *standard parameters* (solid, black) and variations (left panel: metallicity, right panel: IMF and burst length).

4.5 Cluster masses

There are three principle ways to estimate the mass of a stellar cluster:

- For a cluster which is close enough that it can be resolved into single stars, the mass of the total cluster and also the shape of the IMF can be determined by summing up the contributions from the single stars. However, crowding within the central region of the cluster and/or the faintness of the least massive stars can lead to difficulties in making these estimates. This method has been applied to Galactic star clusters (see Eisenhauer et al. (1998)) and some clusters in the Magellanic Clouds (Brandl et al., 1999).

- As mentioned in the previous sections, synthesis modelling techniques allow to estimate the mass of a star cluster from known absolute quantities, like the luminosity at the assumed age in a given band. This technique is also applicable to more distant star clusters. However, assumptions about the IMF, metallicity and star formation properties must be made and severely limit the accuracy of such an estimate.

- Stellar atmospheric features of the gravitationally bound stars in the cluster serve to trace the gravitational potential. Either radial velocities and proper motions of single stars are determined, or, for distant clusters, the superposition of the radial velocities of single stars lead to a broadening of the Doppler shifted stellar emission or absorption features. When proper motions cannot be obtained, due to a lack of spatial resolution, assumptions on the geometry, isotropy and dynamical properties of the cluster have to be made. Application of the Virial Theorem requires the knowledge of the cluster size for the determination of the mass. Usually, large errors are involved for distant clusters, because they are poorly resolved, so that their sizes and spatial profiles are difficult to determine.

In the case of the Antennae star clusters, we are restricted to the latter two techniques, because due to the large distance, the star clusters are barely resolved in the HST images, so they are clearly far from being resolved into single stars.
The second technique does not require any additional explanation, apart from what was said in section 4.4.4, but the third requires some explanation and justification of the basic assumptions (see Spitzer (1978)).
The star clusters in NGC 4038/39 are assumed to be gravitationally bound, because they have survived a minimum of 10-20 dynamical timescales $t_{\rm dyn}$:

$$t_{\rm dyn} = \frac{r_{\rm h}}{v} = \sqrt{\frac{r_{\rm h}^3}{0.4{\rm GM}}} = 2.43\sqrt{\frac{r_{\rm hp}^3}{\rm GM}} \tag{4.2}$$

$t_{\rm dyn}$ is the dynamical timescale, which corresponds to the time that it takes for a star to travel the distance of a cluster radius (see, for example, Gerhard (2000)). It takes very few dynamical timescales to dissolve a star cluster which is not gravitationally bound. $r_{\rm h}$ is the half mass cluster radius, v the average stellar velocity and M the total cluster mass. r_{hp} is the projected half mass radius (see also further down in this chapter). Expressing this in terms of the expected scales for M and r, equation 4.2 becomes:

$$t_{dyn} = 1.15 \times 10^5 \sqrt{\frac{(r_{\rm hp}\,[pc])^3}{M\,[10^5 M_\odot]}} \tag{4.3}$$

For our typical observed cluster sizes and masses (r_{hp} = 4pc, M = 10^6 $M_\odot$), $t_{\rm dyn}$ = 2.9 $\times 10^5$ yr, which justifies the assumption that the clusters are gravitationally bound.
Furthermore, we assume that in each of them the gravitational potential Φ is varying slowly with position. For a cluster where the stars themselves give rise to the potential and there are sufficiently large numbers of them,

so that the granularity of the cluster can be ignored, this should be valid and makes possible the existence of energetic equilibrium states. The contribution of the galactic potential is ignored.
Furthermore, we consider a steady state model, in which the gravitational potential Φ, the velocity distribution function f(r,v) and all other cluster properties are independent of time. This should be a reasonable assumption, unless the cluster was currently undergoing a collapse phase. This should not be the case in the age range that the clusters are expected to span.
The third basic assumption concerns the symmetry of the cluster, which is considered spherical ($\Phi = \Phi(r)$, f=f(r,v_r,v_t)). This generally holds for star clusters like these, except possibly for the outer regions where the galactic potential can cause deviations.
The first two assumptions are required if the Virial Theorem is to be applied. It says that for such a gravitationally stable system, total kinetic energy (T) and total gravitational energy (W) of the cluster are related through

$$2T = -W \qquad \text{(Virial Theorem)} \tag{4.4}$$

Replacing the kinetic energy by the total mass M and RMS 3-dimensional stellar velocity $\langle v^2 \rangle$, and expressing the gravitational energy in terms of total mass and half-mass radius $r_{\rm h}$ (this is the radius that includes half of the integrated mass of the cluster), the Virial Theorem becomes

$$M\langle v^2 \rangle \sim \frac{0.4GM^2}{r_{\rm h}} \tag{4.5}$$

The proportionality factor of 0.4 depends on the concentration of the cluster, ranging from 0.38 (core + halo) to 0.49 (uniform sphere). The value of 0.4 was empirically seen to be a good representation of most clusters, corresponding to a Plummer model with a denser core and a less dense halo (Spitzer, 1978).
However, as will be shown in chapter 5.5, the light profiles of clusters in NGC 4038/39 are in most cases better described by a King profile of concentration parameter c = 15 or 30 (corresponding to log(c) = 1.18 or 1.48, respectively). The corresponding proportionality factor is 0.42.
This is the 3-dimensional description of the cluster. For an isotropic velocity distribution, the projected 2-dimensional half-mass radius, $r_{\rm hp}$, is related to $r_{\rm h}$ by $r_{\rm hp}$ = 3/4 $r_{\rm h}$.
In a further step, we assume that light traces mass. It is unclear to what extent this assumption is justified. While the clusters are not expected to host dark masses, mass segregation, meaning the concentration of the most massive and luminous stars at the centres of the clusters, could be a potential problem. The dynamical redistribution of massive stars should happen on a relaxation timescale, $t_{\rm rlx}$ = N / (26 log(0.4 N)) × $t_{\rm dyn}$, which for our star clusters corresponds to several 100 Myrs (see Spitzer & Hart (1971)). However, there has been observational evidence (e.g. Brandl et al. (1996)) that young clusters, (like R136 in 30 Doradus, age ∼4 Myrs) show an unproportionally large concentration of massive stars near the centre. The reason for that is not clear yet. While Portegies Zwart (2000) could model some mass segregation within a few dynamical times for the case of R136 using N-body calculations, it is not clear if the same result could be obtained for other initial conditions. Other suggestions are a spatially variable IMF or delayed star formation in the cluster core (Meylan, 2000).
However, since in case of the Antennae we cannot resolve if mass segregation has already occurred in the clusters, it is assumed for the determination of the dynamical mass that this is not the case. However, if mass segregation was present, equation 4.7 would underestimate both the half mass radius and the RMS velocity dispersion and therefore the cluster mass.
The last assumption which will be used is the one already introduced as the third basic assumption, which is spherical symmetry. In such a system, the RMS 3-dimensional velocity of the stars can be described in terms of the velocity dispersion of the particles: $\langle v^2 \rangle = 3\sigma_r^2$. Thus the total cluster mass is:

$$M \approx \frac{9.5\sigma^2 r_{\rm hp}}{G} \tag{4.6}$$

Using the distance of NGC 4038/39 of 19.3 Mpc and expressing the mass in terms of solar masses, this becomes:

$$M \approx 2207 \left[\frac{\sigma}{km/s}\right]^2 \left[\frac{r_c}{pc}\right] \mathrm{M}_\odot \tag{4.7}$$

5. OBSERVATIONS AND DATA REDUCTION

5.1 Introduction

Four different sets of data were acquired to investigate the properties of merger induced star formation in NGC 4038/39. These different kinds of observations were necessary, because they aimed to investigate various properties of the merger.
One important point was to perform the observations in the NIR, because it was obvious from HST observations that the high level of extinction, especially in the overlap region, compromised the interpretation of optical data.
The coverage of the whole merger (excluding the large tidal tails) was the aim of NIR imaging observations using SOFI on ESO-NTT, since a census of the young cluster population is only possible if the properties of many clusters are determined. Narrow band imaging in emission and absorption features, as well as in NIR broad bands J, H and K, yields cluster age and extinction estimates.
The cluster properties in several selected smaller regions could be studied in greater detail and better accuracy using NIR integral field spectroscopy (with MPE-3D at the AAT). The selected wavelength range made it possible to study even clusters which are almost completely obscured at optical wavelengths, like the cluster corresponding to the luminosity peak in the ISO 15μm image (see section 3.3). It was selected as one of the target regions, together with three other young clusters in different parts of the merger, which, according to models, could be expected to have experienced different star formation histories. The three dimensional nature of the data, spatial and spectral resolution allow to study the star formation at small spatial scales (3D field of view is $6\farcs4$ on a side, corresponding to $\sim$600 pc).
From both mentioned data sets, with known ages and luminosities, photometric masses will be determined. However, the model dependence of these photometric masses drove the need for an independent mass measurement, which neither of the two sets of observations could provide, because it requires high resolution spectroscopy.
This task was performed by ISAAC on VLT1 and UVES on VLT2 on a small number of clusters, with high extinction for ISAAC and low extinction for UVES. Stellar atmospheric spectral signatures were observed in the K and I band, respectively, to determine the velocity dispersion. These wavelength ranges of these two instruments are very well suited for the task, because both K and I band are dominated by red supergiants and giants at a cluster age of $\sim 10^7$ yrs, the typical age of the Antennae clusters.
The ISAAC spectral resolution with the smallest slit width is just sufficient to resolve the expected dispersion. The high resolution of the Echelle spectrograph UVES is more than appropriate. The masses determined from these measurements are compared to the cluster masses derived using the photometric technique and allow some conclusions concerning the IMF.

5.2 3D NIR imaging spectroscopy

5.2.1 Cluster selection and observations

Models of the merger of two spiral galaxies (like that currently being observed in NGC 4038/4039) predict multiple bursts of star formation during the merger event (Mihos & Hernquist, 1996). Depending on the stage of the merger, these bursts can be in the region of overlap of the two galaxy disks, in the tidally shocked

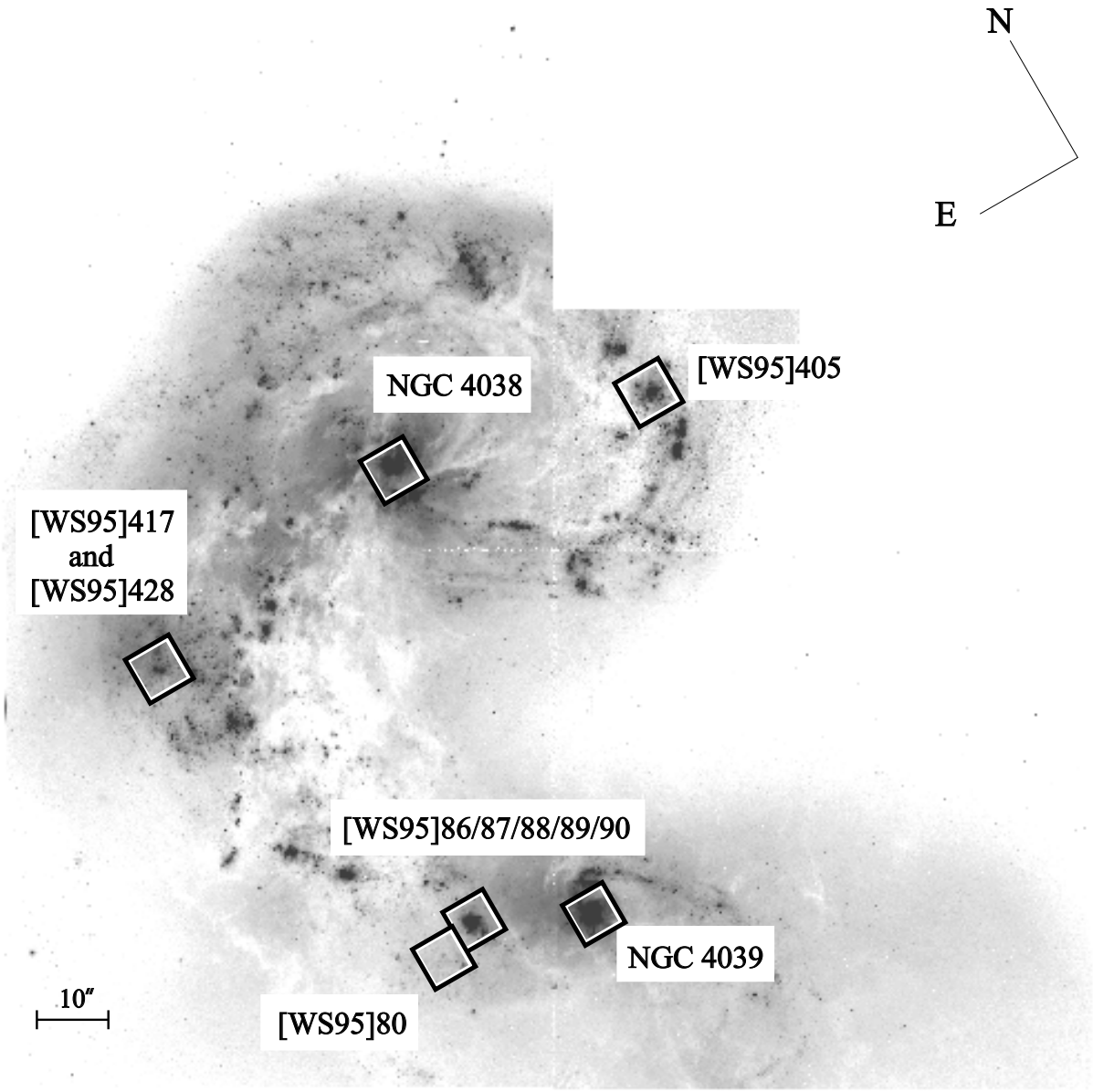

Fig. 5.1: The HST V-band image (Whitmore et al., 1999) displayed in a logarithmic grayscale with the 3D-fields and their numbering indicated (referring to Whitmore & Schweizer (1995)), as it is used in this work. The size scale is indicated in the image.

regions of the outer disks of each galaxy, or as significant quantities of gas fall in towards the two nuclei, in the nuclei of each galaxy.

We observed the two most prominent clusters within the interaction zone, two other IR bright clusters in the outer arms of NGC 4038/39 (likely to be tidally shocked regions), and the two nuclei. Such a selection would allow us (at a minimum) to probe the various regions of star-formation during the merger process within the inevitable constraint of only having a limited amount of observing time. While only observing six regions will not allow us to investigate the properties of the whole ensemble of compact clusters in the Antennae, our sample allows us to crudely investigate the possible range of ages across the Antennae. Figure 5.1 shows the two clusters in the interaction zone ([WS95]86 and [WS95]80), the two nuclei (NGC 4038 and NGC 4039) and two clusters in the outer loops ([WS95]417/[WS95]428 in the eastern and [W99]-2 in the western), indicated by boxes on the HST V-band image. These fields were observed with the 3D integral field spectrometer (Weitzel et al., 1996; Krabbe et al., 1995) in the K band.

For the observations, 3D was combined with the tip-tilt-guider ROGUE (Thatte et al., 1995) on the Anglo-Australian Telescope in February, 1998 and April, 1999. We used a K-band grism with a resolution of $\lambda/\Delta\lambda = 1000$ and a 256x256 NICMOS 3 array. 256 spectra were obtained simultaneously, arranged in a 16x16 pixel field on the sky. The detector integration time per exposure was 100 seconds. The on-source exposures were interleaved with off-source (offset 60″E or W of each cluster) exposures of identical integration time for the sky subtraction. To remove telluric features, the A2V star HD106819 was observed roughly once every hour. In order to Nyquist sample the spectra, we dithered in the spectral direction by half a pixel using a piezo-driven mirror. The spatial pixel scale of 0.″4 provided a field of view of 6.″4x6.″4.

The conditions were generally not photometric. The seeing during the observations of each individual region only showed moderate variation (<0.″2) but was significantly different for different objects. See the next section for details on single fields. The total on-source integration time was 6200s on the first field (hereafter abbreviated to [WS95]86), which is the optically bright star cluster, corresponding to the numbers 86/87/88/89/90 in WS95; 4200s on-source time for the second field (hereafter [WS95]80), which corresponds to the "very red object" number 80 in WS95; 3120s on-source time for the field in the eastern loop (numbers 417 and 428 in WS95); 3840s for the targets in the western loop (WS95 - number 405 and several fainter objects, hereafter [W99]-2). The nuclei of NGC 4038 and NGC 4039 were observed for 3360s and 2160s respectively. Due to a piezo failure, the spectrum of the nucleus of NGC 4039 is not Nyquist sampled.

5.2.2 Data reduction and analysis

Data reduction was performed using the 3D data reduction routines developed at MPE within the GIPSY (van der Hulst et al., 1992) data reduction environment. Single frames were dark subtracted, linearized and sky subtracted using the sky frame that was closest chronologically and had the right spectral dithering position. The wavelength calibration was accomplished by exposures of a neon discharge lamp. The re-binning of the spectrally interleaved data was performed onto a 600 pixel linear wavelength axis. Bad pixels and cosmic rays were removed from the 16x16x600 data cube, either by interpolation or by masking out. After spatial re-binning onto a 64x64 pixel grid, the single cubes were stacked by centering each on its K-band continuum peak or the Brγ peak for [WS95]86 and [WS95]80, respectively. Telluric features were removed by division by the atmospheric transmission profile obtained from the observations of the A2V star. The Brγ absorption line in the calibrator spectrum was interpolated linearly between the adjacent continuum. In the resulting cluster spectra, only the NGC 4038 nucleus spectrum shows a little remaining Brγ emission from the calibrator, which is not a worry, because it is at zero redshift and does not contaminate the Brγ emission from the object.
Object spectra were extracted using a square aperture centered on the continuum peak and sized to maximize the SNR of the resulting spectrum. The individual apertures and their sizes are shown in Figure 5.2. For fields which showed significant offsets between continuum and Brγ line emission peaks ([W99]-2 and the nucleus of NGC 4038), the aperture sizes were chosen so as to minimize contamination between the continuum and line emitting regions. The spectra were flux calibrated using the K_s-magnitudes from our flux calibrated SOFI image, obtained in May 99 at the NTT. The extracted spectra were normalized by dividing by the continuum value, estimated using a linear fit. From this we estimated the equivalent widths W_λ of the Brγ- and the He I-lines and the CO-band-heads. For the creation of linemaps, the linear fit was performed for each spatial pixel and subtracted. The spectra of all the regions (divided into subregions for some of the fields) are shown in Figure 5.2, together with the K_s-band images. Overlaid are the contours of Brγ or the H_2(1-0)S(1)-line (labelled in Figure 5.2).

5.2.3 3D results for young clusters

Results obtained from our data, incorporating results from publicly available HST data (Hα and V-band images - Whitmore et al., 1999), are listed in Table 5.1. [WS95]-86 was slightly resolved while [WS95]-80 was unresolved (both combined data sets had a final FWHM$\sim$1.″0). The FWHM of the seeing was $\sim$0.″8 during [WS95]417&428 observations, and the two clusters are marginally resolved into single components. During [W99]-2 observations, the seeing was poor (1.″6), but to the NE of the bright cluster, a fainter second cluster is visible. The tabulated values for [W99]-2-A and B refer to the bright cluster (A) and to the location of the Brγ peak (B).
We used the measured equivalent width of Brγ, $W_{\mathrm{Br}\gamma}$, and CO 2.29 μm band-head, W_{CO}, (Table 5.1), to determine the ages of the starbursts using stellar synthesis models (Leitherer et al., 1999; Sternberg, 1998). Assuming an upper mass cutoff M_{upper}=100$M_\odot$, Salpeter IMF slope and an instantaneous burst (see chapter 4.3.2 for justification of this choice), we derive ages of $3.7^{+1.0}_{-0.4} \times 10^6$yr for [WS95]-86 and $5.5^{+0.7}_{-0.8} \times 10^6$yr for [WS95]-80 (see Table 5.1 for details). Gilbert et al. (2000) derive a value of $\sim$4 Myrs for [WS95]-80, assuming the same starburst parameters, in reasonable agreement with our value (they do not provide and uncertainty for their measurement).
These fairly similar ages, with [WS95]-80 actually being older than [WS95]-86, does not explain (or only marginally) the pronounced peak seen in the 15 μm image. As the corresponding CVF spectra show, there is a steeply rising continuum seen in [WS95]-80, which neither in [WS95]-86, nor any of the other very young star formation sites (see also Wilson et al. (2000)) show. This continuum could arise from small dust grains heated by the presence of young, very massive stars. Presence of dust within the cluster could reconcile the 3D and ISO results: Dust destruction of Lyman continuum photons, as mentioned in chapter 4.4.1, lowers the observed equivalent width in hydrogen recombination lines and at the same time could provide the source

Property	Unit	[WS95]86	[WS95]80	[WS95]417 [WS95]428	[W99]-2-A [W99]-2-B	NGC 4039 nucleus	NGC 4038 A and B
R.A.	J2000	$12^h01^m54^s.5$	$12^h01^m54^s.8$	$12^h01^m55^s.8$	$12^h01^m50^s.6$	$12^h01^m53^s.4$	$12^h01^m53^s.0$
Dec.	J2000	$-18^\circ53'03''.2$	$-18^\circ53'06''.0$	$-18^\circ52'10''.3$	$-18^\circ52'11''.6$	$-18^\circ53'10''.3$	$-18^\circ52'04''.3$
Apert. size		$2''.2\times2''.2$	$2''.2\times2''.2$	$1''.4\times1''.4$ $1''.4\times1''.0$	$2''.2\times2''.2$ $2''.0\times1''.8$	$3''.8\times3''.8$	$3''.8\times2''.6$ $3''.0\times2''.2$
$W_{Br\gamma}$	Å	210 ± 10	116 ± 10	2 ± 2 7 ± 3.0	10.0 ± 2.5, 54 ± 5	2.9 ± 0.9	3.2 ± 0.9 11 ± 2 (58)
W_{CO}	Å	$0^{+2.0}_{-0.0}$	$0^{+2.0}_{-0.0}$	19 ± 4 15 ± 2	16.1 ± 1.0 0 ± 2	10.2 ± 0.9	10.0 ± 0.9 8.3 ± 0.9
Age	10^6yr	$3.7^{+1.0}_{-0.4}$	$5.5^{+0.7}_{-0.8}$	8.5...12.8 each	$8.1^{+2.0}_{-0.2}$	65 ± 15	65 ± 15 (5.9)
Hel/Brγ		0.47 ± 0.02	0.50 ± 0.02				0.17
T_{eff}	10^3K	36 ± 1	38 ± 1				33
m_K	mag	14.5 ± 0.2	14.8 ± 0.2	15.5 ± 0.3 each	13.9 ± 0.2	12.3 ± 0.2	12.9 ± 0.2 13.3 ± 0.2
m_V	mag	16.3 ± 0.15	18.8 ± 0.15	19.1 ± 0.3, 19.3 ± 0.3	16.8 ± 0.2	15.3 ± 0.2	16.1 ± 0.2, 16.6 ± 0.2
A_V	mag	1.4 ± 0.3	4.3 ± 0.3	0.3 ± 0.3	0.6 ± 0.3	0.2 ± 0.1	$0^{+0.2}_{-0.0}$, 0.5 ± 0.2
$F_{Br\gamma}$	10^{-16} erg $s^{-1}cm^{-2}$	83 ± 8	42 ± 8	1.5 ± 1	18 ± 3 (A+B)	20 ± 1	7 ± 2 21 ± 3
$F_{H\alpha}$	10^{-14} erg $s^{-1}cm^{-2}$	32 ± 3	2.3 ± 0.2	1.2 ± 0.2 (A+B)	10 ± 1 (A+B)	17 ± 1	8 ± 1 13 ± 1
Mass	$10^6M_\odot$	$1.6^{+1.2}_{-0.2}$	$3^{+3.6}_{-0.7}$	0.4-0.6	1.9 ± 0.3,		

Tab. 5.1: Col. (1) — Measured properties with 1σ uncertainties, not accounting for model uncertainties. Apert. size is the size of the apertures from which the values were derived. $W_{Br\gamma}$ indicates the equivalent width of the Brγ line, W_{CO} is the equivalent width of the ^{12}CO (2-0) bandhead feature, determined in the wavelength range 2.3060 - 2.3092 μm, which corresponds to the wavelength range given by Oliva & Origlia (1995), redshifted to the radial velocity of the Antennae. Its uncertainty was estimated from the neighbouring continuum. For comparison, a few values of W_{CO} for stars observed with 3D: K4.5 Ib: 15.3Å, M3.5 Iab: 19.6Å, K3 III: 9.1Å, M1 III: 12.1Å (Förster-Schreiber, 1998). Age is the model age that most closely matches the equivalent widths of Brγ and CO. Where the value for W_{CO} covered a range that did not behave monotonically with age, we gave an age range rather than a value $\pm\sigma$. T_{eff} of the most massive stars as indicated by the He I/Brγ ratio, He I/Brγ measured from the 3D spectroscopy, m_K from our spectroscopy, m_V from HST images (Whitmore et al., 1999), A_V from the flux ratio of Brγ/Hα, $F_{Br\gamma}$ as measured from our data, $F_{H\alpha}$ from HST images (Whitmore et al., 1999). The mass is estimated from the observed extinction corrected m_K in comparison with that expected from evolutionary synthesis models for a cluster of the given age. As model parameters we generally used the *standard parameters* described on page 27, except for [W99]-2-A, for which a metallicity of twice the solar value was assumed. Assuming solar metallicity there would give an age of 8.1 Myrs and corresponding mass of 1.1×10^6 $M_\odot$. Col. (2) — Unit in which the measurements in Cols. (3) to (8) are tabulated. Col. (3) to (8) — The measured properties (given in Col. (1)) of the six observed fields. The values for the properties of NGC 4038-B (Age, T_{eff} and the value for $W_{Br\gamma}$ in parentheses) make use of an assumption about the continuum level, see text for details.

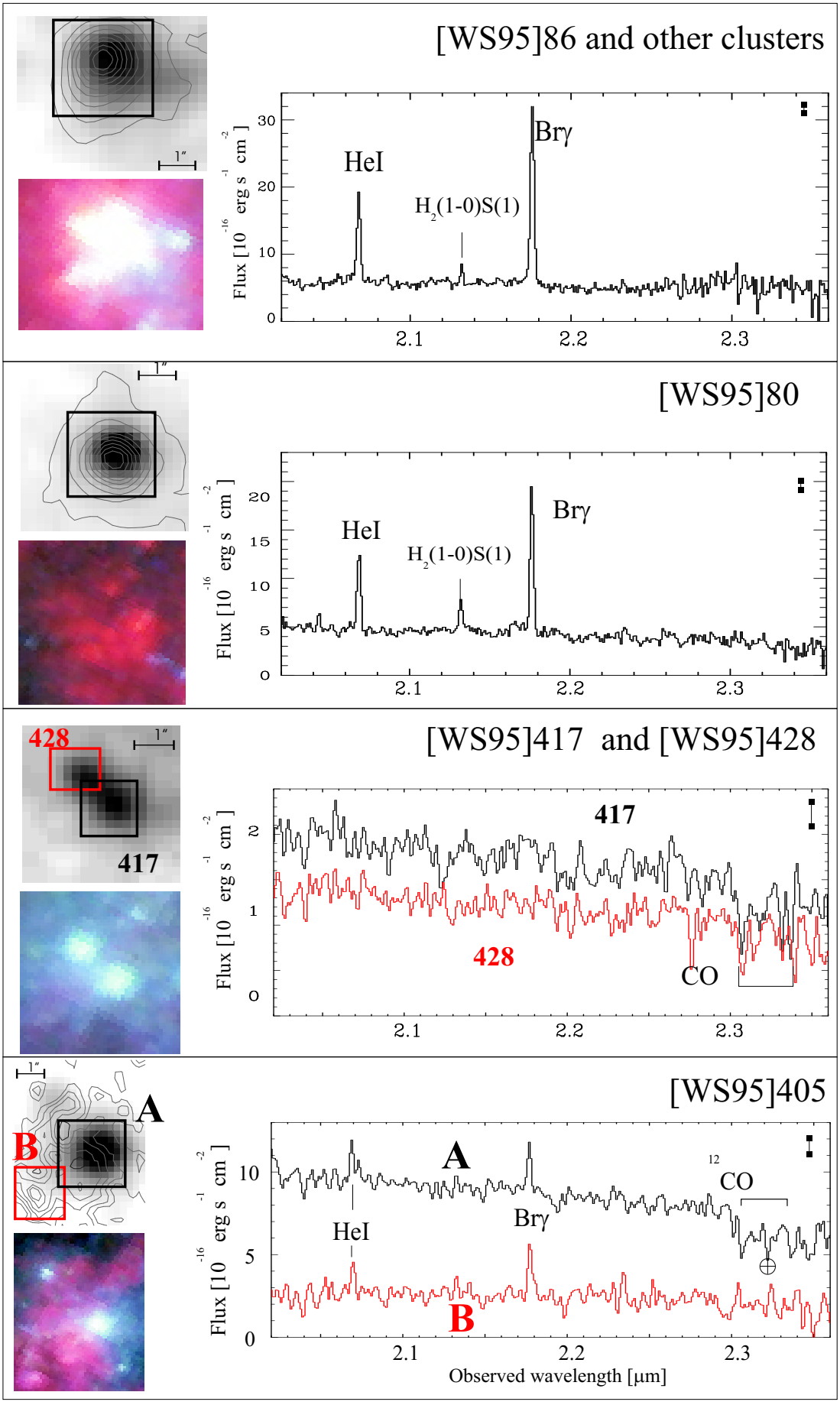
[WS95]86 and other clusters
1″
HeI
Brγ
H2(1-0)S(1)
Flux [10-16 erg s-1 cm-2]
[WS95]80
[WS95]417 and [WS95]428
428
417
CO
[WS95]405
A
B
12CO
Observed wavelength [μm]

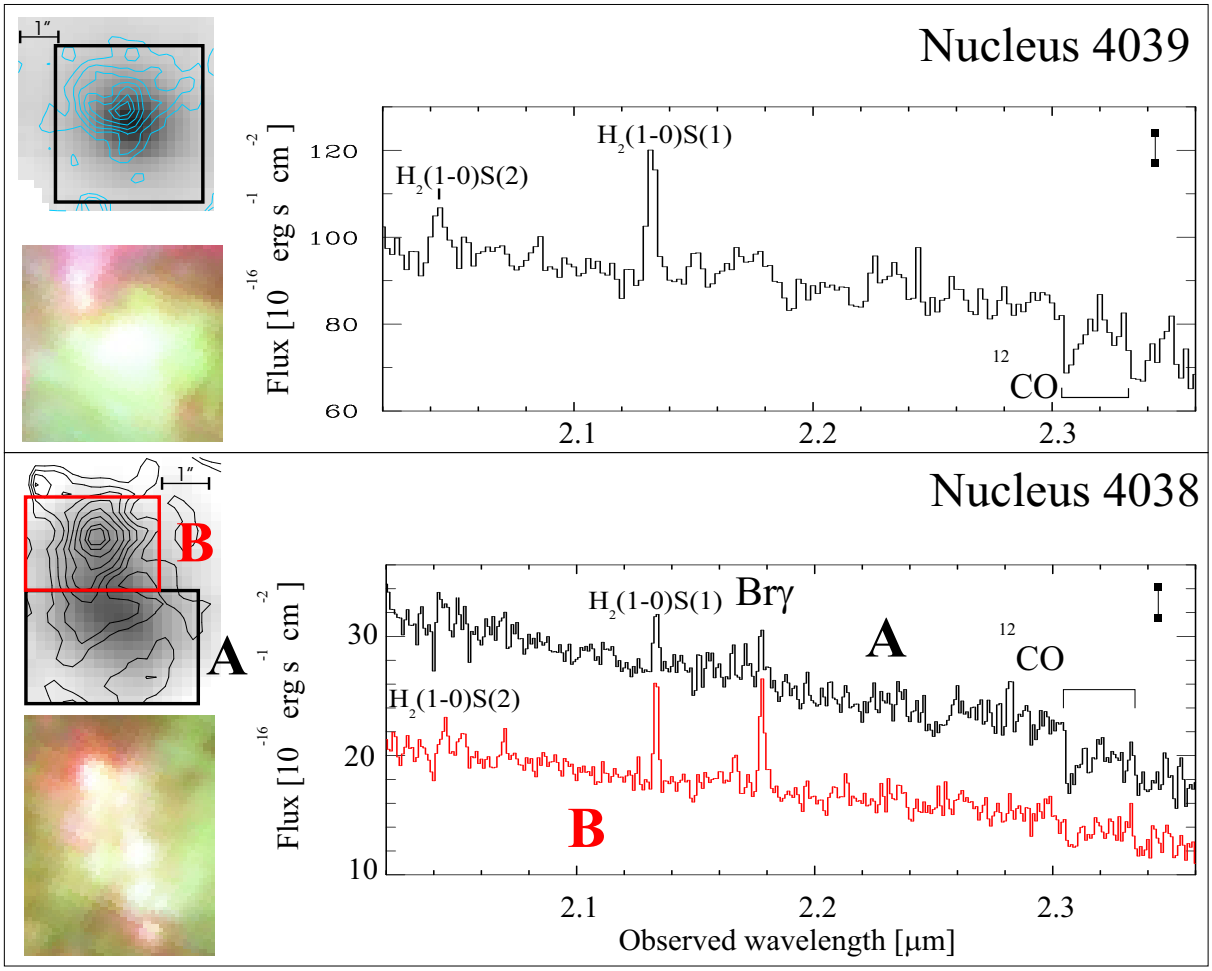

Fig. 5.2: K-band images of the observed fields with Brγ or H_2 contours, K-band spectra and the corresponding regions in color composite images taken from W99 (blue: U+B, green: V, red: Hα). The greyscale images in the left column (top) are created from the 3D data cubes by summation of the corresponding channels of the data cubes, continuum subtracted in the case of the emission line maps. They show the Brγ distribution in [WS95]86, [WS95]80, [WS95]417&428, [W99]-2 and nucleus of NGC 4038, and the H_2(1-0)S(1) distribution in the nucleus of NGC 4039. The highest contours represent 95% of the maximum flux, then from 90% continuing in steps of 10% downward. Maximum fluxes are 2.0 ([WS95]86), 1.7 ([WS95]80), 0.47 ([W99]-2), 0.59 (NGC 4039 nucleus) and 0.46 (NGC 4038 nucleus) $\times 10^{-16}$ erg s^{-1} cm^{-2}. The K magnitudes of the fields are given in Table 5.1. The spectra were extracted from the regions indicated in the K-band images. The fluxes are given in units of 10^{-16} erg s^{-1} cm^{-2} versus the wavelength in μm. The noise level is indicated in the top right corner of each spectrum. The images in the left column (bottom) show the corresponding regions of the HST multi-color image (W99) with U+B in the blue, V in the red and Hα in the red display. The scale is given as 1″ bars (the pixel size in all 3D images is 0.″2 x 0.″2). At the distance of the Antennae 1″ corresponds to 93 pc. N is up, E to the left in each image.

of strong mid infrared continuum emission. This would indicate a cluster age of far below 5.5 Myrs, rather around 2 Myrs, but a more reliable age dating is then not possible. $W_{Br\gamma}$ for cluster [WS95]-86 is actually higher than for [WS95]-80. This can indicate that $W_{Br\gamma}$ does not actually saturate at a dust destruction level (or it is above 200 Å), but that the amount of intra-cluster dust depends on environmental conditions, and [WS95]-86, as seen by the relatively moderate extinction, has smaller amounts of it.

The ages of the two clusters in [WS95]-417&428 are not very well constrained, due to the low S/N of the data and the bi-valued nature of the W_{CO} temporal evolution. The clusters in [WS95]417&428 are between 8.5 and 12.8 Myrs old. For the [W99]-2 spectra, it is not possible to get a consistent model age with the presence of both strong CO-band-heads and Brγ emission with an instantaneous burst. But given the size of the cluster (r_{hp}=4.6 pc) it is plausible to assume that the star-formation has a finite duration of a few $\times 10^5$ years (Efremov & Elmegreen, 1998). Other possibilities that might explain why these clusters have both CO absorption and Brγ emission are shock heating of the gas due to supernova explosions, the spatially seeing broadened Brγ emission from the region to the S-E of [W99]-2-A which contaminates the cluster spectrum, and possible gaps in our knowledge of stellar evolution and model atmospheres.

Another plausible explanation is shown in more detail in chapter 5.4.5. The high resolution optical spectra of this cluster suggest a supersolar metallicity for this cluster, and comparison of the evolutionary tracks for $W_{Br\gamma}$ and W_{CO} leads to a nice agreement in that case.

It is interesting to compare the 3D image and spectra of a region outside both [W99]-2 clusters with the multi-color HST image, since our data show a Brγ peak to the SE of the K-band continuum peak of cluster A. This coincides with a dust filament obvious in the HST image, and it could be the site of more recent star formation or of shock excitation in a more dusty environment.

The nuclear spectra differ from those of the young star clusters. W_{CO} (≈ 10Å) is lower here than in many of the star clusters, and only certain regions show fairly strong $W_{Br\gamma}$, while the general level is around 3 Å. If $W_{Br\gamma}$ was assigned to fainter examples of clusters like the one seen in the northern nucleus (see Fig. 5.2 and details in the next paragraph), and only W_{CO} is taken into account for the age determination, an instantaneous burst model suggest the same possible age range for both nuclei, 65±15 Myrs. Had star formation continued at a constant level, $W_{Br\gamma}$ would be higher than observed for the standard parameters. But a decaying burst of a timescale of a few million years which started $\sim$ 100 Myrs ago would lead to an agreement in both, W_{CO} and $W_{Br\gamma}$, as will be discussed in the next chapter.

The northern nucleus shows evidence for a more recent star forming activity to the north of the K-band peak, but it is difficult to estimate its age due to the underlying continuum contribution by the older background nuclear stellar population. But the presence of Brγ emission (no evidence for AGN activity was seen in other observations) requires the presence of O or B stars or recent shock excitation, thus implying that it is younger than ∼10-20 Myrs. Under the assumption that there is no intrinsic gradient in W_{CO} across the NGC 4038 nucleus, meaning that the observed lower W_{CO} at the location of the Brγ peak can be attributed to the additional continuum from the young stellar population, we estimate the young star light continuum to contribute about 1/5 of the total continuum, which increases the observed $W_{Br\gamma}$ to 58 Å. This then implies that the star cluster formed around 6 Myrs ago, consistent with the effective temperature of 33,000 K derived from the low ratio of He I/Brγ of 0.17.

The age uncertainties given in Table 5.1 only take into account uncertainties in the signal-to-noise of the data and do not take into account the systematic effects of selecting different IMF slopes, upper and lower mass cutoffs, abundances, or uncertainties in the models themselves.

The extinction was derived by comparing the theoretical ratio of Hα/Brγ (case B recombination ratio assuming T_e=10,000 K from Storey & Hummer, 1995) with the observed ratio. Using the extinction curve of Draine (1989) for a foreground screen model, we derived A_V of 1.4±0.2 and 4.3±0.2 for [WS95]86 and [WS95]80, respectively. They agree within the errors with the values we derived from the V-K color excess with the intrinsic color derived from the models for the respective cluster ages ($A_V = 1.6^{+0.6}_{-1.0}$ and $3.7^{+0.6}_{-1.0}$). For [WS95]417&428 and [W99]-2, we used the V-K colors not to confirm the extinction, but rather to further

constrain the age.

The ratio of He I λ2.058μm/Brγ is not an unambiguous tracer of the effective temperature of the highest mass stars present in a stellar population (Shields, 1993; Förster-Schreiber, 1998), but it was determined to investigate the ISO results at higher spatial resolution. The effective temperatures derived from the ratios of He I/Brγ=0.47 and 0.5 are 36,000 and 38,000K ([WS95]86 and [WS95]80, respectively), which corresponds to masses of roughly 28 $M_\odot$ and is below the 44,000K (50-60 $M_\odot$) derived from mid-infrared line ratios by Kunze et al. (1996). Given the sensitivity of the He I λ2.058μm line to nebular parameters (Shields, 1993) and the large aperture (14"$\times$27") used for the ISO measurement, some disagreement between our estimate and that obtained using ISO data for the temperature of the hottest stars is not surprising. Moreover, the relationship between temperature of the hottest stars and He I/Brγ is not monotonic and thus our estimates for the mass should be considered lower limits. These upper mass limits are consistent with our estimated ages of the [WS95]80 cluster, while the younger age of [WS95]86 would allow for the detection of higher mass stars. A qualitative comparison of the derived effective temperatures/ages of all fields agrees with the gradient in the [Ne III]/[Ne II] observed by Vigroux et al. (1996).

From the extinction corrected Brγ flux we can estimate the number of Lyman continuum photons, $N_{\rm Lyc}$. For this calculation, we used the extinction corrected Brγ flux, a distance of 19.2 Mpc for the Antennae, and recombination coefficients from Hummer & Storey (1987) and Storey & Hummer (1995). We find that $N_{\rm Lyc}$=3.1$\pm$0.3$\times10^{52}$ s^{-1} and 1.9$\pm$0.4$\times10^{52}$ s^{-1} for [WS95]86 and [WS95]80 respectively. This is somewhat lower than the value derived from the thermal radio continuum flux density estimated by Hummel & Van der Hulst (1986), which results in $N_{\rm Lyc} = 1.3 \pm 0.7 \times 10^{53}$ s^{-1} for the sum of [WS95]86 and [WS95]80. Given that our apertures are smaller, the difficulty in estimating the thermal contribution to the total radio emission, and that there is some diffuse radio emission, it is not surprising that there is a difference between the two estimates. It is also significantly less than the value of 1.0×10^{53} photons s^{-1} derived by Gilbert et al. (2000). Both our observed flux and estimated extinction are lower by factors of ~ 2 and both of these differences account for the discrepancy between our respective estimates of the Lyman continuum flux. However, Gilbert et al. (2000) caution that the extinction value they derived (A_K = 1.1mag) should be considered an upper limit.

Comparing our results ($M_K(0)$ and $N_{\rm Lyc}$) with the models of Leitherer et al. (1999, assuming a Salpeter IMF slope, M_{upper}=100 $M_\odot$, high mass stars have already evolved off the main sequence and are therefore not observed, and M_{lower}=1 $M_\odot$) for the age determined for each cluster in the previous section, the total mass of each cluster would be $1.6^{+1.2}_{-0.2}$ and $3.0^{+3.6}_{-0.7}\times10^6$ $M_\odot$ for [WS95]86 and [WS95]80 respectively. A lower mass limit equal to 0.1 $M_\odot$ (using Miller-Scalo slope for the lower mass end of the IMF) would imply masses a factor of 1.6 higher. For [WS95]417&428 and [W99]-2, we crudely estimated their masses using only their extinction-corrected K-magnitudes compared to the magnitudes expected from our derived ages. Their masses are lower than the masses of [WS95]86 and [WS95]80, and lie between 0.3 and 1.1 $\times10^6$ $M_\odot$.

This places each of the very massive [WS95]86 and [WS95]80 clusters into the same mass regime as M82A, which produces roughly the same amount of $N_{\rm Lyc}$, and has the same burst age (Förster-Schreiber, 1998). Their masses are more than a factor of ten higher than the average mass of a globular cluster (Mandushev et al., 1991). Even if they are expected to lose 60% of their mass over a Hubble time (Chernoff & Weinberg, 1990), they will still represent the top-end of the globular cluster mass function. The [WS95]417&428 and [W99]-2 clusters have masses which are more moderate and comparable to the average globular cluster mass. This mass range in the observed clusters is not surprising given that those two fields contribute a substantial amount of the bolometric luminosity of the Antennae. But a more accurate mass estimate of a larger fraction of the population of young star clusters is necessary to judge if the young clusters could evolve to form a part of the globular cluster population of an elliptical galaxy for example.

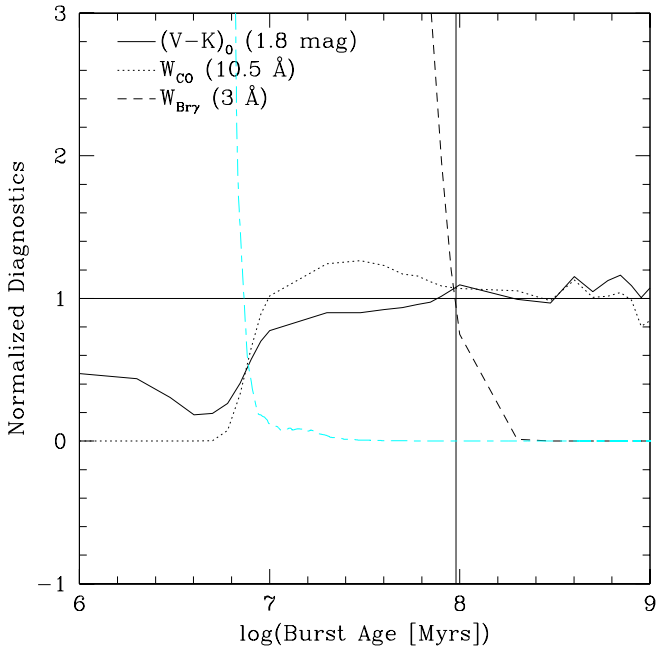

Fig. 5.3: The observed values for the age diagnostics W_{CO}, $W_{Br\gamma}$ and V-K colour (numbers given in the figure are almost exactly the same for both clusters) were used to normalize the corresponding diagnostic plots derived from STARS (Sternberg, 1998). The starburst parameters used were Salpeter IMF, solar metallicity, mass range 1-100 $M_{\odot}$ and an exponentially decaying burst with the timescale τ set to 21.5 Myrs. This provided the best fit to the data, and the derived burst age is 99 Myrs. Shown also as the long dash-short dashed line is the normalized $W_{Br\gamma}$ derived using Starburst99 for an instantaneous burst. The corresponding line for the Starburst99 continuous star formation model lies off the scale of this plot, never reaching below 5 on the vertical axis. This is also the case for a very low level of star formation, because stars are always formed due to the IMF provided.

5.2.4 3D results for the nuclei

Images and spectra of both nuclei were for convenience already shown in the previous section. But their properties differ significantly from those of the young clusters, therefore it seems justified to discuss them in a separate section.

Both nuclei show remarkable similarity in their properties concerning $W_{Br\gamma}$ and W_{CO} if the young star cluster, which formed in the northern cluster only $\sim 1\farcs5$ away from the K-band peak, is not taken into account. Both have values of W_{CO} around 10 Å, and a fairly low $W_{Br\gamma} = 3$ Å. These are the average values in the apertures indicated in Figure 5.2. Averaging over a larger aperture, within a radius of $5\farcs8$ from the respective K-band peaks, the influence of young star forming regions close to the nuclei becomes obvious. Performing these measurements on the SOFI data which will be described in the next chapter (5.3), leads to $W_{CO} = 8$ Å and $W_{Br\gamma} = 10$ Å. For the analysis of the nuclear starbursts, which are not resolved into single star formation regions in our 3D observations, the first pair of values will be used, and additionally the extinction corrected V-K colours, which is $(V\text{-}K)_0 \sim 1.8$ mag for both nuclei.

In the previous section, an age estimate for an instantaneous starburst in the nuclei was given, based on W_{CO} alone, assuming that the observed Brγ emission arises from a star cluster which spreads its light into the measured aperture due to the low spatial resolution. However, if this was not the case, an instantaneous starburst scenario would not agree with the observations. Models of galaxy interactions like Mihos & Hernquist

(1996); Barnes & Hernquist (1991) suggest a continuous fuelling of the nuclear regions starting shortly after pericenter. Therefore the equivalent widths will be compared to models with continuous or exponentially decaying star formation. The other parameters remain the same as the *standard parameters* from page 27. The derived starburst parameters are **burst ages of 100 Myrs** with a timescale for the exponential decay of τ = **21.5 Myrs**. These provided the best fit (see Figure 5.3) to the observations after an exploration of parameter space. However, if both parameters are varied at the same time, reasonable fits can be achieved in fairly large ranges for the burst age (±30 Myrs) and the timescale (±5 Myrs).
However, this does not affect the main conclusion, which is that in both nuclei star formation set in at the same time and continued with decreasing intensity for several Myrs. What we observe nowadays are the remnants of this old star formation episode, with some younger compact clusters forming in the vicinity of the nucleus. In order to estimate the average star formation rate in the nuclei, the extinction corrected K-band magnitudes in 5.″8 apertures around the K-band peaks of the nuclei, which includes most of the nuclear K-band emission, are compared to model predictions. This assumes that all of the K-band emission is contributed by the stars formed in the burst. For the star formation parameters described above, STARS predicts at an age of 100 Myrs that a burst which had a timescale of 21.5 Myrs will have an absolute K-band luminosity of M_K = -20.92 mag, (corresponding to m_K = 10.5 at the distance of the Antennae) for a total gas mass converted into stars of 2 $\times 10^8$ $M_\odot$.
The determined values are tabulated below.

Name	m_K [mag]	A_V [mag]	m_{K_0} [mag]	Stellar mass formed [$M_\odot$]	SFR [$M_\odot$/yr]
NGC 4038	9.85	0.25	9.6	5.5 $\times 10^8$	5.5
NGC 4039	10.38	0.25	10.1	2.9 $\times 10^8$	2.9

While these values indicate certainly an enhanced star formation rate (for comparison that of the Milky Way is around 1 $M_\odot$/yr) it is, as expected, not the dramatically increased star formation rate (SFR) which is seen in ULIRGs. See also the next section for further discussion.

Band	λ_{cen} [μm]	Width [μm]	DIT [s]	Total ON-source time [s]	Seeing
J	1.247	0.290	15	300	1.″0
H	1.653	0.297	15	300	0.″9
Ks	2.162	0.275	10	300	0.″7
Brγ	2.167	0.028	30	1500	0.″7
$CO_{2.32}$	2.336	0.030	30	7500	0.″7-1″
NB2.195	2.195	0.030	30	2280	0.″7-1″
NB2.28	2.280	0.030	30	1200	0.″7-1.″2
HeI λ2.058	2.058	0.028	30	840	1.″0
HeI λ1.083	1.038	0.0164	30	720	0.″7
Paβ	1.282	0.019	30	600	1.″0
NB1.215	1.215	0.018	30	960	1.″0
FeII (H)	1.644	0.025	30	450	1.″0

Tab. 5.2: Summary of the ESO-NTT NIR imaging observations.

5.3 NIR Broad- and Narrow Band Imaging

5.3.1 Observations

In the nights 11./12.05.99, NIR broad- and narrow band imaging was performed using the camera and spectrograph SOFI on the ESO-NTT 3.5m telescope. A total observing time of one night was dedicated to the project. Due to a light haze, the conditions were not photometric on any of the two nights, and the seeing varied throughout between 0.″6 and 1.″2, as measured in the optical. The large field objective with a field size of 4.″9×4.″9 was used, with a pixel size of 0.″29/pix. This gave the possibility to place the target NGC 4038/39 in one corner of the array and to shift it around in the four corners, making offset sky integrations unnecessary and thus saving 50% of integration time. All of the NIR broad bands were observed, and several diagnostic line filters with corresponding narrow band filters. The [FeII] line filter did not have a matching narrow band filter, so the broandband H filter needs to be used for continuum subtraction. Table 5.2 lists the observation descriptions for the run.

5.3.2 Data reduction and analysis

Reduction of the SOFI data was performed using the IRAF package. It included sky subtraction (either using the median of several images or, where this led to residuals, doing pairwise subtraction), flat fielding by a normalized median of all frames in an observing sequence. Due to a wrong setting of the "Pupil Rotation" switch, the object orientation varied from frame to frame, especially during the transit of the object. This had to be accounted for before the coaddition of the frames. They were rotated by the angle derived from the header information. Alignment and summation of the single integrations was performed using the REDUCE routine in the IRAF DIMSUM package. This also performs a dead/hot pixel correction and then interactively determines the relative shifts by identification of the same object in all frames. It is possible to tune the weights of single frames in the sum, but they were kept the same for all frames contributing to the sum.
The narrow band images were continuum subtracted by inter- or extrapolation of the narrow band continuum observations to the line filter region (in the K-band), or simple subtraction of an intensity-scaled narrow (J-band) or broad band (H-band) image. In the K-band, the observed narrow band filters were NB2.19μm and NB2.28μm, in the J-band NB1.215μm. For the H band, no narrow band continuum filter was available, so the broad band filter was used for the continuum subtraction of the [FeII]1.644μm image. Since the seeing

varied considerably between some pairs of line and continuum observations, the frames were broadened to the largest observed FWHM in the set before continuum subtraction. This applies to the Brγ, HeI λ2.058 μm and the CO images.
Flux calibration of the images was performed by bootstrapping from values in the literature for the J, H and K magnitudes (Bushouse & Stanford, 1992) and Hα fluxes (Keel et al., 1985) for Brγ/Hα. The K-band line fluxes were then determined and the corresponding continuum subtracted narrow band images flux calibrated by flux determination from the 3D observations of the six selected fields. This technique applies to the Brγ, HeI λ2.058 μm and the CO images. For the HeI λ1.083 μm and the [FeII] images it was not possible to perform a flux calibration, because no data are available in the literature. For the Paβ image, a crude flux calibration was performed relying on the case B recombination coefficients and the resulting ratio of Paβ/Brγ-flux, taking into account the extinction. However, the background subtracted images for the HeI lines and the Paβ emission showed an SNR which was fairly low compared to Brγ or Hα images. Four sources could be identified in the overlap region, but provided no new information. Therefore they will not be taken into account.

5.3.3 Ages from SOFI data

Cluster ages from SOFI data were determined by four different methods, only two of which were applicable for all clusters. The other two were feasible only for those clusters with the feature used present.
The four methods were described in section 4.4.
The most reliable age esitmates are obtained for those clusters with Brγ emission or CO absorption present. Therefore, Figure 5.4 shows a K-band image with contour overlays of Brγ emission with an equivalent width of 50 Å and higher, and with CO absorption of 15 Å and above. These two parameters are are also extracted from the table and converted to a plot with colour- and size coded symbols representing the observed equivalent widths (Figure 5.5).
These two plots reveal, as expected, that there is a region with many clusters of high Brγ emission, located in the overlap region.
Most of the clusters forming the nothwestern loop of clusters in NGC 4038 have a high equivalent width in CO. The photometrically determined values of $W_{Br\gamma}$, W_{CO}, extinction and broadband colours were combined to a common age estimate. This estimate is displayed in Figure 5.5, with symbols colour- and shape coding indicating the ages. In cases where, as mentioned in the caption of the figure, CO absorption and Brγ emission were both present in one cluster, which is not predicted by models for the *standard parameters*, the average value of the two age estimates was used. This can be justified by assigning this small discrepancy to uncertainties in the models. Also a finite very short duration of the starburst, which seems plausible at least for some of the larger clusters, or the assumption that the mechanical energy introduced by supernovae gives rise to line emission, leads to an agreement for both age indicators.
However, if the discrepancy arose rather from the presence of two or more clusters with sightly different ages which are unresolved in the K-band image, this could lead to problems. Not so much for the age estimate, where this kind of averaging would lead to a smoothening of the age distribution. But for the photometric cluster masses, which are determined from the absolute K-band magnitudes of the clusters in combination with the age estimates and evolutionary synthesis models, unresolved clusters could in the case of the Antennae clusters lead to an underestimate. An example will show this: Consider two clusters of 1×10^6 $M_\odot$ each, which are not resolved as two differnt sources in the K-band images. Using the Starburst99 predictions, their properties as single sources are determined to be the following:

Age	m_K	$W_{Br\gamma}$	W_{CO}
5.5 Myrs	16.11 mag	114 Å	0 Å
10 Myrs	14.04 mag	0.36 Å	16.8 Å

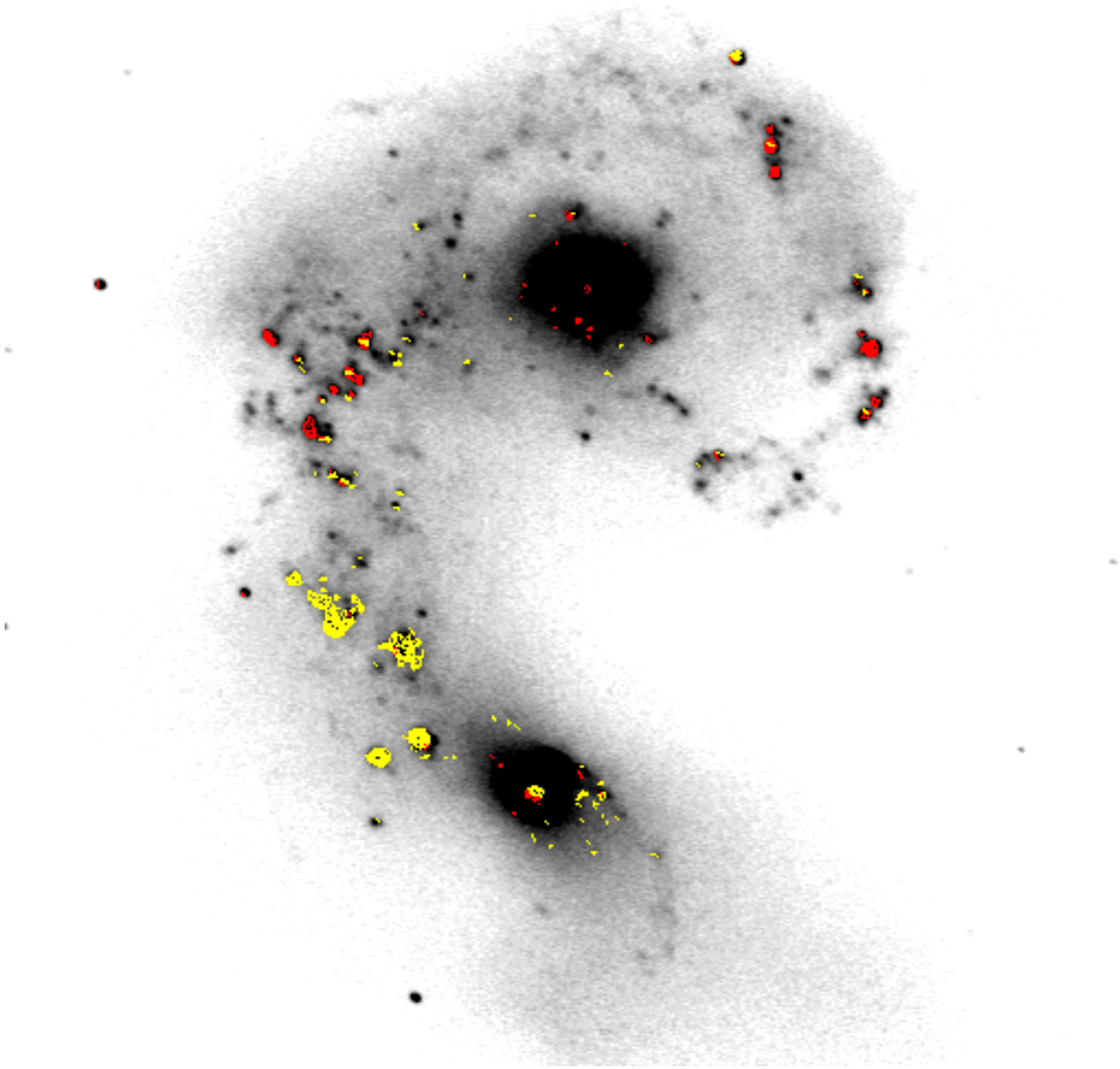

Fig. 5.4: K-band image with W_{CO} and $W_{Br\gamma}$ contour overlay. The contours (red: CO, yellow: Brγ) indicate the locations of a minimum equivalent width of $W_{CO} \geq 15$ Å and $W_{Br\gamma} \geq 50$ Å, respectively. In K band, 17% of the galaxy emission originates from the star clusters. However, from optical imaging it is clear that some contribution will originate from fainter clusters undetected in K.

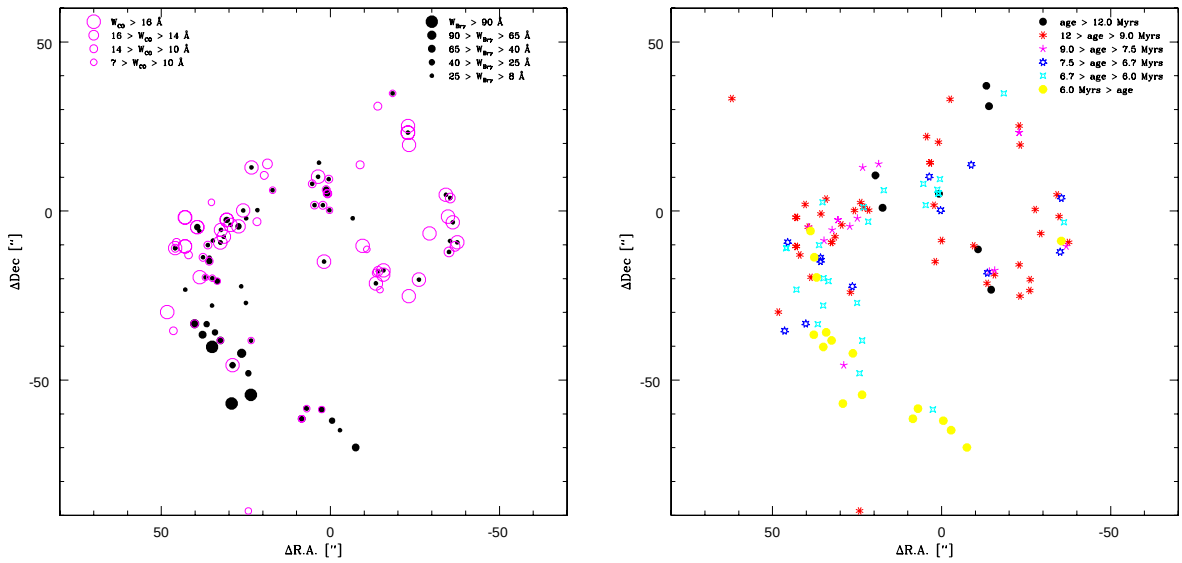

Fig. 5.5: Left panel: Colour- and size coded $W_{Br\gamma}$ and W_{CO} values of the detected clusters in NGC 4038/39. It is obvious that the youngest clusters (highest values of $W_{Br\gamma}$) are located in the overlap region of the two galaxies. Most of the clusters in the northwestern loop show high values of W_{CO}, indicating an age of around 10 Myrs. Many of the clusters with prominent CO absorption also show Brγ emission at a level above that predicted by models. Right panel: The information displayed on the left was converted into cluster ages from comparison with population synthesis models assuming the *standard parameters* defined on page 27. Note that cluster ages are given in Myrs, not log(age)! This means that almost all of the clusters are young (below 20 Myrs), and most of them around 10 Myrs. Two clusters have values of W_{CO} and V-K colour which are compatible with ages of 25 Myrs and above, and they show no Brγ emission. Two others have ages around 15 Myrs. The most recent star formation is seen to have taken place in the region where the two disks overlap. Ages of the clusters there are around 5 Myrs.

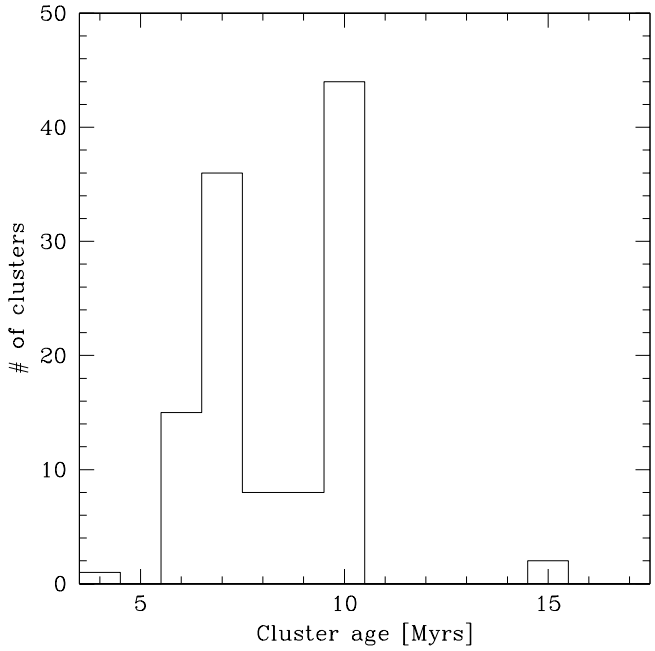

Fig. 5.6: Histogram of numbers of star clusters observed in each age bin. All clusters are young, and most clusters are either around 10 Myrs or around 7 Myrs old.

However, since they are not resolved, what is instead observed is m_K = 13.89 mag, $W_{Br\gamma}$ = 15 Å (corresponding age: 6.45 Myrs) and W_{CO} = 14.6 Å (corresponding age: 8.1 Myrs). The average age of the two estimates is 7.3 Myrs, fairly close to the actual average of 7.75 Myrs. But the mass determined from the comparison to m_K expected for a cluster of this age (m_K = 14.46 mag) leads to a total mass of 1.7 instead of 2.0 $\times 10^6$ $M_\odot$. Photometric cluster masses will nevertheless be determined, but one should bear in mind that a systematic error could lead to an underestimate of the photometric mass of up to ∼20%. Masses are determined too low because the observed ages are 10 Myrs or younger. If the ages could be erroneously dated too high above 10 Myrs, resulting mass estimates would be too high.

5.3.4 Photometric masses

Knowing the ages of the clusters is the presupposition for determining their photometric masses, M_{phot}, as described in section 4.4.4. The extinction corrected K-band magnitudes were compared to those expected for a cluster of a given age and mass for the model parameters described on page 27. The obtained masses for each cluster are given in Table A.1 in the Appendix. Figure 5.7 shows a histogram of the numbers of clusters per mass range. Masses of several million $M_\odot$ are rare, the bulk of detected clusters has masses around 1-2 $\times 10^5$ $M_\odot$. The SOFI data have neither the spatial resolution, nor the depth to identify a possible turnover below 1 $\times 10^5$ $M_\odot$, even if it was present.

The total mass produced in K-band detected star clusters amounts to $\mathbf{M}_{\mathrm{total,clusters}} = 1 \times 10^8$ $\mathbf{M}_\odot$. Since this mass was created over a period of 10^7 yrs, this makes the average SFR for the clusters throughout the Antennae $SFR_{clusters}$ = 10 $M_\odot$/yr. Adding to this the observed star formation rate of the two nuclei (see section 5.2.4) of 5.5 and 2.9 $M_\odot$/yr for NGC 4038 and 4039, respectively, this yields an overall star formation rate of 18.4 $M_\odot$/yr. Note that the mass in star clusters was only in those detected in K-band. The sheer number of clusters is higher in V-band by at least a factor of 5, but some of these clusters are not resolved as single sources in K-band, and therefore their combined luminosity is taken into account as the luminosity of

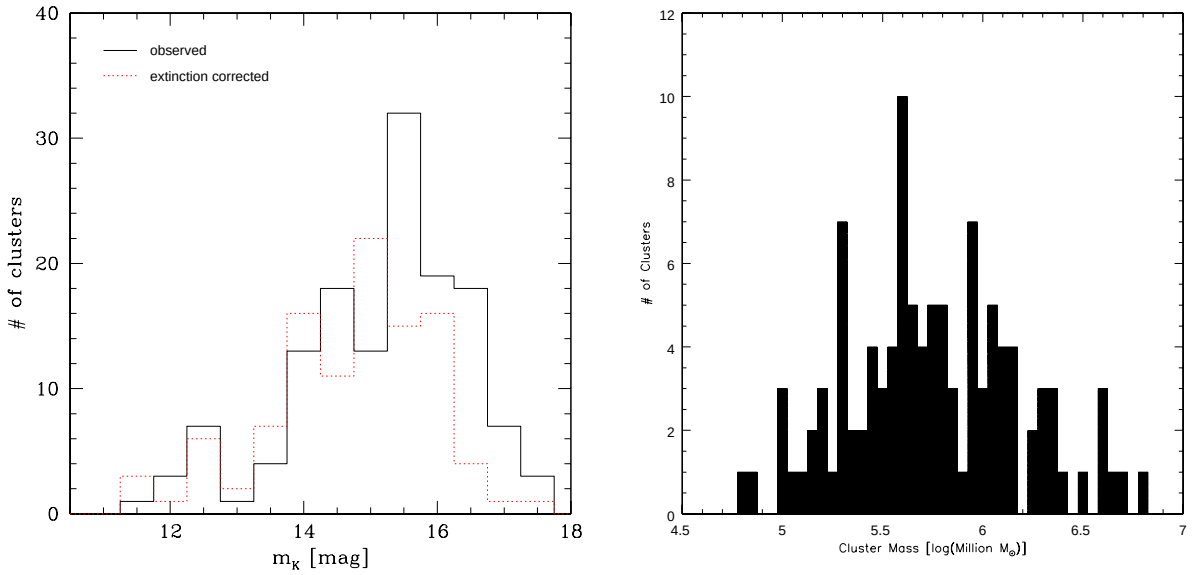

Fig. 5.7: K-magnitude (left) and mass histogram (right) of clusters detected in the SOFI K-band image. The values for the magnitudes are displayed both, as observed (solid line) and extinction corrected (dashed line). Masses are the photometric masses M_{phot} in 10^6 $M_\odot$, which are determined in comparison to evolutionary synthesis models using the *standard parameters* defined on page 27. Note that the masses could be underestimates for two reasons: low spatial resolution in the data can lead to and underestimate, as mentioned in the previous section, and the dynamical masses, as will be shown in chapter 4.5, are probably higher than the photometric masses, due to the presence of low mass stars which were not included in the model. The total mass produced in (detected) clusters is 1×10^8 $M_\odot$.

Identification	Diameter [kpc]	M_{mol} [10^8 $M_\odot$/yr] [10^8 $M_\odot$/yr]	$\Sigma_{SFR,theo}$ [$M_\odot$ yr^{-1} kpc^{-2}]	$\Sigma_{SFR,obs}$ [$M_\odot$ yr^{-1} kpc^{-2}]
NGC 4038	1.7	15	2.2	2.4
NGC 4039	1.4	5.0	0.8	1.9
SGMC 1	1.4	6.3	1.1	0.9
SGMC 2	< 1.1	3.9	1.1	0.8
SGMC 3	1.3	2.3	0.33	0.6
SGMC 4	1.1	3.7	1	0.67
SGMC 5	< 0.8	1.3	0.4	
TOTAL	Area 8.8 kpc^2	37.5	1.20	0.66

Tab. 5.3: Molecular cloud masses as they were determined by Wilson et al. (2000), together with the spatial (projected) extent of the cloud. They assumed the galactic conversion factor for the transition from CO fluxes to cloud masses, but caution that this assumption might not be correct for the NGC 4038 nucleus. From the cloud masses the expected SFR densities according to the Schmidt law (Equation 5.1) were calculated. The total number is compared for the overall star formation in the merger, but it will also be checked if the Schmidt law also holds for smaller scales.

the cluster, as mentioned in the previous section. Many of the other clusters are too faint to be identified in the K-band images, which will therefore most likely also be less massive. That will certainly be true if most of them are also in the age range of around 10 Myrs. To derive an absolute number for the stellar mass produced in *all* clusters, not only those detected in K-band, is difficult.
In an attempt to put this value of $\sim$18 $M_\odot$/yr into perspective, nevertheless, it is compared to the expected star formation rate if the gas density is taken into account. For the global star formation activity, there is a very tight relation between gas density and SFR density, which can be represented by a Schmidt power law. It holds over several magnitudes of both parameters and is described by, e.g. Kennicutt (1998).

$$\Sigma_{SFR} = (2.5 \pm 0.7) \times 10^{-4} \left(\frac{\Sigma_{gas}}{1 M_\odot pc^{-2}} \right)^{1.4 \pm 0.15} M_\odot yr^{-1} kpc^{-2} \qquad (5.1)$$

Σ_{SFR} and Σ_{gas} are the galaxy-averaged values for SFR and gas densities, respectively.
Using data from Wilson et al. (2000), who used millimeter observations to observe CO emission and derive gas masses in molecular cloud complexes (see section 3.4), this relation will be tested for the case of the Antennae. The relevant data from their tables are listed in Table 5.3, together with the estimated theoretical value for Σ_{SFR} derived from equation 5.1.
Figure 5.8 displays the results. The relation is tested for the overall relation between the gas and SFR densities, for which the empirical relation 5.1 was established, but also data points indicating the locations of single molecular cloud complexes are shown. To estimate the SFR density in the regions of the molecular clouds identified by Wilson et al. (2000), the respective masses of clusters identified in the K-band were summed. They always consisted of one main contributor of 2-5 $\times 10^6$ $M_\odot$ and only few low mass clusters.
As can be seen from Table 5.3 and form Figure 5.8, SFR density correlates very well with gas density, both globally *and* locally.

5.3.5 Discussion

The plot in the right panel of Figure 5.5 and the age histogram in Figure 5.6 show that essentially all star clusters seen in NGC 4038/39 are young, below $\sim$15 Myrs. This is extremely remarkable, because the whole merging process takes several 100 Myrs (300-400 Myrs according to models (Toomre & Toomre, 1972; Barnes,

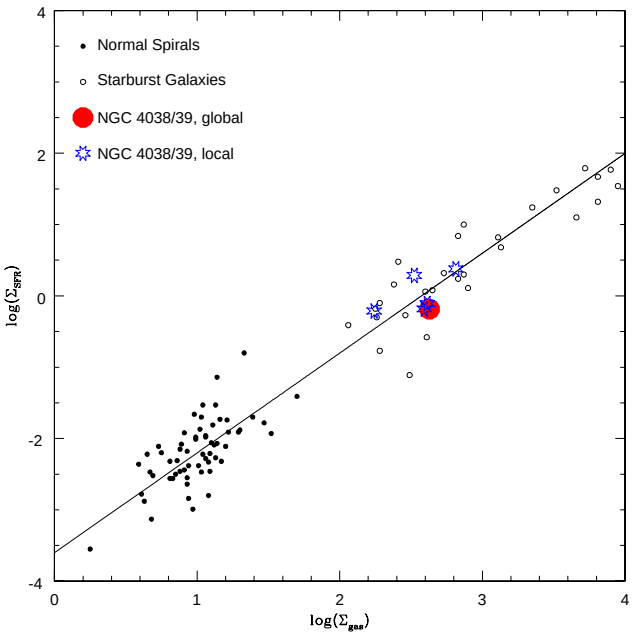

Fig. 5.8: The correlation between gas density (only molecular gas is taken into account) and SFR density is explored both globally (for which the applied empirical Schmidt law is usually obeyed) and locally. Gas density $\Sigma_{\rm gas}$ is in [$M_\odot$ pc^{-2}], SFR density $\Sigma_{\rm SFR}$ is in [$M_\odot$ yr^{-1} pc^{-2}]. Data points for normal spirals and starburst galaxies were taken from Kennicutt (1998). Gas densities were calculated from the molecular cloud masses and dimensions published by Wilson et al. (2000), the SFR density was calculated by determining the stellar mass and burst ages of the K-band detected clusters and scaling by the corresponding cloud size. It can be observed that not only globally the correlation between the two parameters can be expressed by the Schmidt law (Eq. 5.1), but also locally for the large molecular cloud complexes.

1988), and nevertheless a major star formation event was triggered in a time range of less than 10 Myrs over the whole extent of the galaxies, which is around 7 kpc. Just from the morphology of the merger and from the large gas and dust masses seen in the overlap region, one could have suspected that star formation was induced by an actual collision of the two disks, accompanied by a density increase and a shock wave running through the interstellar medium. However, this idea is refuted by several observations.

- A shock wave running through the interstellar medium (assumed speed 100 km/s) would require ~ 60 Myrs to cross the distance between the observed star forming regions and would therefore be unable to trigger starbursts within the observed narrow age range.
- Pericenter was around 200 Myrs ago (Barnes, 1988). The two galaxies are actually separating again in the configuration which is observed. Assuming that a density increase caused by collision of parts of the disks leads to the starburst would make it seem implausible why the onset of star formation was delayed by more than 100 Myrs
- Merger models like that performed by Englmaier et al. (2000), as mentioned in chapter 3, explain the large optical depths in the "overlap region" not as a collision region, but rather as a gaseous bridge connecting the two galaxies, therefore ruling out the mentioned seemingly obvious picture.

Dynamical processes which lead to an increase in density in various regions throughout both merging galaxies with considerable delay after pericenter are required to explain the observed age distribution. A plausible candidate for the relevant dynamical process is the self-gravitational response of the disks after the initial encounter: As the two galaxies separate, the influence of self gravity of each disk starts dominating again over the influence of the interaction partner. Tidal distortions can then be amplified into strong spiral or bar patterns (Mihos, 1999). This is just what is observed in NGC 4038/39, with the loop of young clusters to the north-west of the merger reminiscent of a spiral arm, just as its less pronounced counterpart emanating from the southern nucleus. See for comparison the fiducial merger described by Mihos & Hernquist (1996), which shows all the characteristics of the Antennae during their time steps 28.8 and 33.6, which corresponds to the self-gravitational response phase: long, prominent tidal tails, a gaseous/young stellar bridge connecting the two galaxies and spiral features consisting of gas and young stars in both galaxies.
The exact details of the gravitational response depend on the internal structure of the progenitor galaxies and the geometry of the encounter. For example, the absence of a bulge in merging galaxies consisting of disks and dark halos leads to strong bar or spiral formation shortly after the initial encounter. The bar is very efficient at driving gas into the nuclear regions to fuel a strong starburst. This, however, is not seen in NGC 4038/39. No strong bars are obvious (only a weak spiral structure) and the starburst in the nuclei is of a moderate level, which implies the presence of a small bulge that provides stability against bar formation.
Star formation in regions where the density was amplified by self-gravity sets in as the local gas density exceeds the Jeans limit. For regions where the initial conditions were comparable, like the spiral structures seen in the galaxy disks, this point can be reached at comparable times of the merger evolution, which gives an explanation for the coeval timing of the starbursts over large distances seen in the Antennae. It is also conceivable that in the overlap region, which corresponds to the gaseous bridge between the two galaxies, the initial gas densities were naturally lower than in the disks (having started at a lower density), and it took these gas masses slightly longer to reach the domain of gravitational instability and accompanying star formation. However, as can be seen in Figure 5.5, the age difference between the overlap region and the northwestern loop is only around 5 Myrs. This is far below anything that merger models with star formation included could resolve. Englmaier (2000) also created a merger model of NGC 4038/39 with star formation realized as a Schmidt law, converting to new stars all gas particles above a critical density. He was able to reproduce star formation activity in the nuclei, the northwestern loop and the overlap region, however the relative intensities were not quite as observed, and the timing cannot be resolved on a time scale fine enough. But in his model, in agreement with the observations, star formation in the nuclei started earlier than in the other two regions.

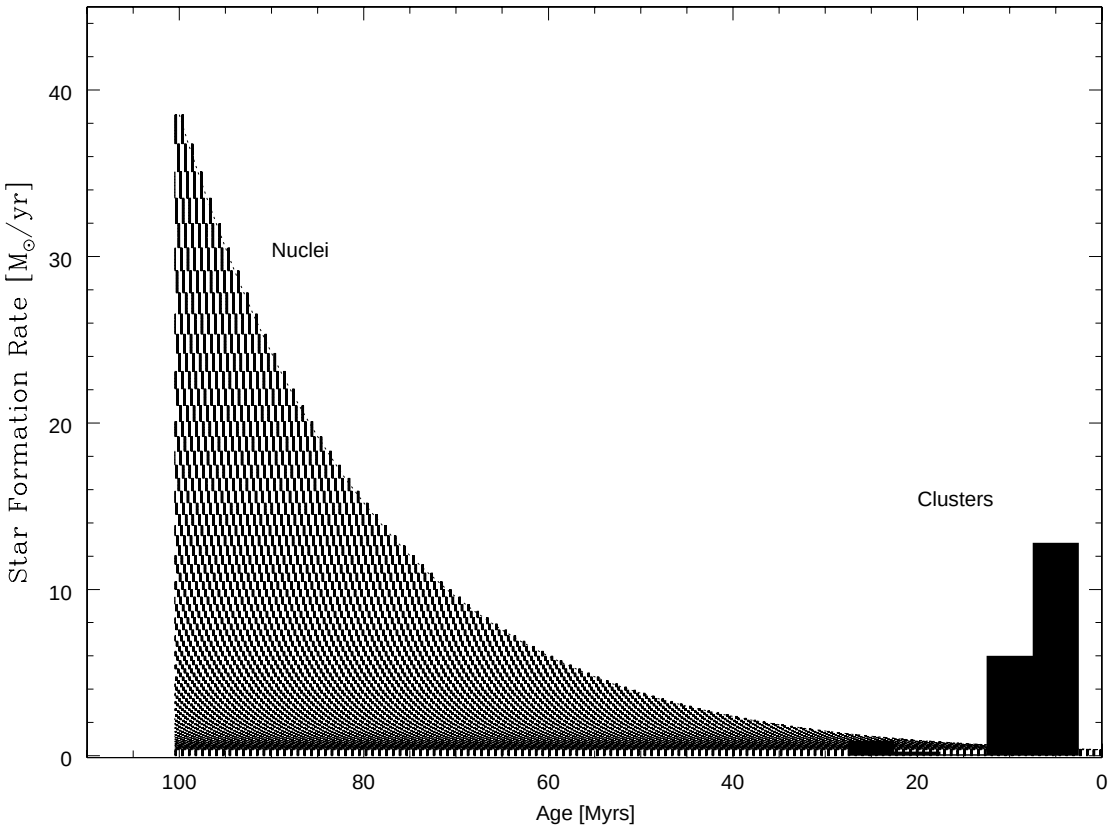

Fig. 5.9: This plot shows the starformation history of NGC 4038/39 as SFR(t). The star formation rate is measured in $M_\odot$/yr, time is in Mrys. Star formation in the two nuclei, which has almost the same time dependence, was summed and is displayed as the grey shaded area. Star formation in the young clusters is shown as the black histogram.

The early start of star formation in the nuclei (compare section 5.2.4) is due to the gravitational response during separation which creates the $m = 2$ instabilities (though not very prominent in the Antennae) that start shortly after the initial collision. While it takes the tidally distorted outer disks longer to reach critical gas densities in some regions, the gas funnelled into the two nuclei reaches that state comparatively early. However, these models (e.g. Barnes & Hernquist (1991), Mihos & Hernquist (1996)) predict a more or less continuous inflow towards the nuclei, which would imply continuous star formation.

However, this is not observed in the Antennae. As described in section 5.2.4, a continuous star formation scenario is not compatible with the observed age tracers. Even though star formation in the nuclei was not instantaneous, but rather exponentially decaying over ∼20 Myrs, and there are also star clusters seen which formed only recently, this cannot be described as continuous star formation. Simulations by Gerritsen (1997), which include feedback from star formation for merger models, predict that the star formation rate in the nuclei is decreased, because the starburst heats significant amounts of the inflowing material to temperatures of a few million degrees, which could be an explanation for the decay of the star forming activity, even though fuel might still be funnelled into the nuclear regions.

Several distinct, short bursts of star formation are also seen in other galaxies with induced star formation, like in M82 (Förster-Schreiber, 1998) or the large sample observed by Mas-Hesse & Kunth (1999). Star formation in NGC 4038/39 fits in well with the general pattern of short burst durations.

What was described so far only gave a possible explanation why star formation is triggered coevally in the whole merger, but not why the burst is so short. Locally, star formation may be terminated by the ignition of the most massive stars soon to be followed by the first supernova explosions. Stellar winds and shocks drive the medium between the stars out of the cluster. This is also shown by the very impressive Hα bubbles seen around almost every cluster except the very youngest in W99 (their Figure 4). The mechanical energy introduced into the surrounding medium then inhibits star formation in these regions for some time. However, if these shock waves encounter a region which was on the edge of the Jeans limit, the additional pressure introduced can trigger star formation. This is possibly observed in the region around cluster [W99]-2, as described in section 5.2.3. The Hα bubble around [W99]-2 extends just beyond a region of high extinction (see Figure 5.2 or W99), which has a high value of $W_{Br\gamma}$ and could therefore be a region with a newly formed, but not very luminous star cluster. Also the nuclei and some parts of the overlap region (as seen in Figure 5.5) show age differences between neighbouring clusters. This star formation, however, proceeds at a fairly low level. The large complexes which were most likely to form stars have already done so (apart from possibly some regions in the overlap zone), which leaves the smaller clouds to form stars, especially if triggered by external pressure.

If the youngest clusters in the overlap region had been dated too old (see remarks in sections 4.4.1, 5.2.3 and this section), this might indicate that star formation is actually still going on in this region and that the self-graviational response is not completed yet. Judging from the older star forming regions, where age differences between the star clusters are at most around 8 Myrs, new clusters might be forming for possibly another 2 Myrs. After this a next major starburst event will only occur when the gravitational potential has changed significantly, probably the next pericenter, which is still several $\times 10^7$ years ahead, and a still bigger nuclear starburst during the final merger (in around 100 Myrs), even though current star formation rates are probably high enough to ensure that the Antennae will not reach an extremely high luminosity (i.e., a ULIRG) even then.

Figure 5.9 visualizes the star formation history of NGC 4038/39 as it is derived for the clusters and the nuclei. After this speculative look into the future starburst activities in the Antennae: What about the past? Has there been a star formation event comparable to that currently seen in the recent history of the merger?

The SOFI K-band data show only two star clusters for which it is clear that the combination of W_{CO} $W_{Br\gamma}$ and colours suggests a cluster age of more than 15 Myrs. Clusters with large masses, as they are presently seen, up to a few million $M_\odot$, should be detected by the SOFI data as having a moderate CO equivalent width (12 Å) and J-K colours around 0.7, and the expected K magnitude of $\sim$ 16.5 is above the SOFI detection limit, even though in K band the cluster magnitude drops by 3 magnitudes between 10 and 20 Myrs. The less massive clusters of an older population quickly drop below the detection limit of around m_K =17.5 mag.

In the V band, older clusters should be much easier to detect, because in the age range mentioned before, they only fade by 1 mag. However, even though Whitmore et al. (1999) find some, though not many, clusters which seem to have ages of around 30-100 Myrs, they are 3-4 magnitudes fainter in V than the brightest clusters of 10 Myrs. This means that either no clusters with masses around 10^6 $M_\odot$ were formed, highest masses being rather a few $\times 10^5$ $M_\odot$, or that they were preferentially disrupted later.

The former explanation seems to be more likely. Had this earlier starburst been equally powerful as the current one, even the disruption of the most massive clusters would have left a few hundred less massive (10^5 $M_\odot$) clusters above the detection limit, which is clearly not observed. But if a burst 30-50 Myrs ago had produced fewer clusters, it is likely that due to statistical reasons, the cluster mass function was not sampled up to the very high end and the cluster masses did not exceed a few x 10^5 $M_\odot$.

5.3.6 Extinction

Interstellar extinction, the obscuration of light through absorption and scattering of media located between the source and the observer, is generally caused by dust grains of sizes between a few μm and a few mm. Their

composition and size distribution causes the wavelength dependence of the extinction, which was analyzed and described in empirical formulae by various authors (e.g., Mathis, Rumpl & Nordsieck (1977); Draine (1989)). In general, shorter wavelengths are affected more strongly by extinction, for example the extinction in the K-band is only a tenth of that in the V-band.
If the extinction is described as one homogeneous layer in front of a source, which is called the "uniform foreground screen model", the initial intensity I_0, the emergent intensity I and the optical depth τ of the extincting medium are related through:

$$I(\lambda) = I_0(\lambda)e^{-\tau_\lambda} \tag{5.2}$$

In the very common expression of extinction as the extinguished magnitudes in V-band (550nm), this becomes:

$$A_\lambda = 2.5log(e)\tau_\lambda = 1.086\tau_\lambda \tag{5.3}$$

For the wavelength dependence, the subsequent analysis will make use of the Draine extinction law:

$$\frac{A_\lambda}{A_V} = 0.351\lambda^{-1.75} \tag{5.4}$$

It was derived from observations in the Galaxy, but should be applicable to the environment encountered in NGC 4038/39.
There have been attempts to describe the extinction more realistically than with a uniform foreground screen, in the so-called "mixed model", which interleaves sources with the extincting dust grains. This should be a much more realistic approach for star clusters that form from molecular clouds, and where massive stars with intense winds or supernovae blow away and/or compress the dust in the regions between them. One indication that a mixed model is more appropriate than foreground screen is when the derived extinction A_V increases with the diagnostic wavelength, because then different wavelengths probe physically different environments. In the Antennae, there are no spatially resolved extinction measurements available so far. From the patchy appearance of the dust distribution, a mixed model seems appropriate for the description of the extinction seen in a large aperture, like in the ISO beam. However, it is still reasonable on the scale of single clusters to describe the extinction as a foreground screen, and therefore the extinction will be derived according to equation 5.3, using the Draine extinction law (Equation 5.4) for the wavelength dependence.
There are several techniques to determine the extinction in a given source.

- If spectra or narrow band filter observations are available, lines with a ratio that is determined by physical parameters, their actual ratios are determined by extinction if the physical parameters are known. This is, for example, the case for the HI recombination lines, the intrinsic ratios of which for the assumption of a case B recombination (large optical depths, every Lyman-line photon is scattered many times and converted into lower-series photons, see for example Osterbrock (1974)) mainly depend on the recombination coefficients and only weakly on environmental parameters like temperature and density. This fact will be used in the determination of the extinction for those clusters that show Brγ emission. The ratio of the Brγ narrow band image and that of the HST Hα image results in a two-dimensional extinction map, but the derived numbers will be reliable only for those clusters that show significant Brγ and Hα emission (see Fig. 5.10).

- If the intrinsic spectrum (or broadband colours, etc.) of a source is known, the additional wavelength dependent attenuation is caused by extinction. Fitting the spectrum or the data points for broadband colours with this colour excess gives an estimate for the extinction, and the quality of the estimate depends on the breadth of the wavelength coverage and the knowledge of the intrinsic spectrum. This method will be applied for all clusters. If the ages are known from $W_{Br\gamma}$ and/or W_{CO}, the corresponding spectrum is extracted from the population synthesis models and the broadband colours compared to those observed. The comparison with the extinction derived by the first method for clusters with

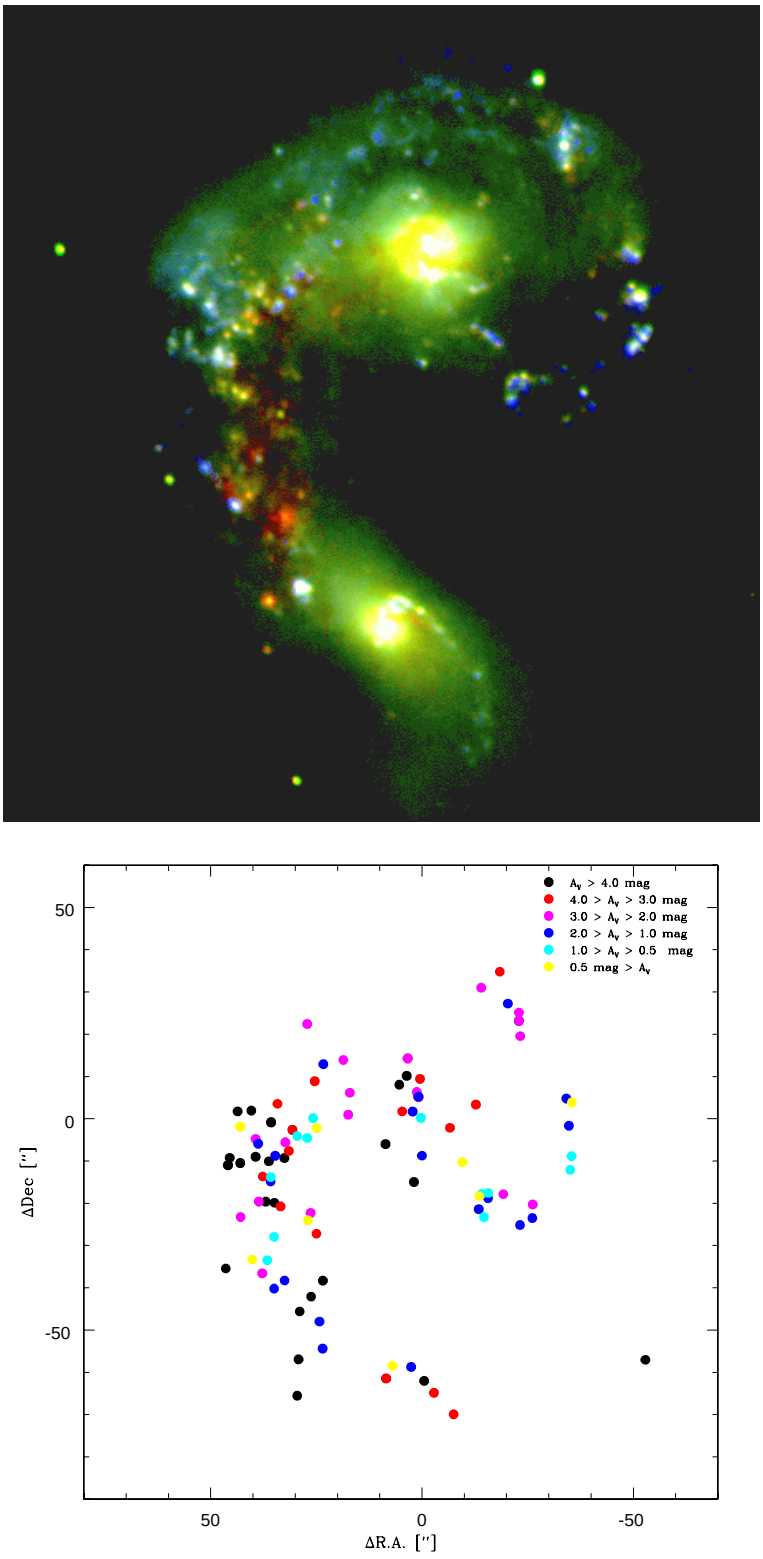

Fig. 5.10: False colour VJK-image of NGC 4038/39. Most of the reddening seen in the clusters in the overlap region is caused by extinction. The distribution of extinction towards the clusters, measured from the ratio of hydrogen recombination lines (Hα/Brγ), is displayed in the right hand panel with colour- and shape coded symbols. It lies between A_V=0.3 and 5 mag for the detected clusters.

Observations	Aperture/Resolution	A_V [mag]/Model	Comments
HST '95	Average for system	0.2 / f	
SWS	14″ x 20″ in overlap region	70 / m	from Brα/Brβ
Brγ	point sources in overlap region	1 - 4 / f	Brγ/ Hα
HST '99	clusters detected in HST	0.3 - 1.5 / f	Q analysis in comp. with pop. syn.

Tab. 5.4: Literature values of the extinction in NGC 4038/39. HST 95: Broadband imaging (Whitmore & Schweizer, 1995), SWS: Mid-infrared spectroscopy (Kunze et al., 1996), Brγ: Fabry-Perot imaging in Brγ, (Fischer et al., 1996), HST '99: Broadband imaging (Whitmore et al., 1999; Zhang & Fall, 1999), using extinction-insensitive Q parameter to determine the age and intrinsic colour of a cluster and from that the extinction. For the determination of the visual extinction A_V, either uniform foreground screen (f) or mixed sources and dust (m) were assumed.

Brγ emission also gives an estimate for the uncertainties in the method. For those clusters with no previous age estimate available, a two-parameter fit is applied to the observed colours, using the known wavelength dependence of the Draine extinction law and the spectra from Starburst99. The differences between model and observation are minimized for a combination of age and extinction.

No spatially resolved extinction measurements are available for the Antennae so far. From the optical HST data, Whitmore & Schweizer (1995) estimated an average value for the extinction, for their analysis of the new observations published in '99, they used the extinction-free Q parameters.
All other publications also used average values, either for the whole system, or for each galaxy separately, or for a large aperture within the galaxies. Table 5.4 lists the values published in the literature to date (late 2000) and the methods that were used for their determination.
The determination of the extinction requires the flux calibration of the Hα HST image, using the flux values published by Keel et al. (1985). The false colour image Figure 5.10 gives an impression on the level of extinction seen in the Antennae. All the clusters which appear very red lie in regions of high extinction. The levels measured by the Hα/Brγ ratio are indicated as coloured dots according to the legend. Measured values for A_V range from 0.2 to 5 mag. The visual appearance of the merger at optical values is reproduced by the numbers: Highest extinction, in Figure 5.10 marked by very red clusters, is seen in the overlap region, and some clusters, which appear blue in that image, indeed have low extinction.

5.4 NIR Medium- and Optical High Resolution Spectroscopy

As already mentioned, it is very important to derive the masses of the star clusters. Not only in their own right, but also in order to set the star clusters in relation with the model of hierarchical star formation in the early universe and to see whether they can really be the progenitors of a part of the globular star cluster populations observed in present day elliptical galaxies. The absolute quantities we derive in our other observations, like the K magnitude or the number of ionizing photons, can be used to estimate the cluster mass. However, this value is strongly model dependent and large uncertainties in the values lead to large errors in the mass. But, as will be discussed in chapter 5.4.3, we have derived these numbers for the clusters, and the masses turned out to be very high in some cases, a factor of 10 higher than the typical mass of a globular cluster in an elliptical galaxy. This would require further investigation, because it needs to be understood if these high-mass clusters then just represent the high-mass end of the distribution function of future globulars, or if they will be preferentially destroyed in the tidal field of the interaction, or if this young cluster population has characteristics that are in general incompatible with evolving into the globular cluster population.

The best method to derive masses independent from photometry is to use the velocity dispersion of the cluster. Using a stellar feature which is not contaminated by nebular emission, it is possible to derive the dispersion via Doppler broadening of the feature as observed in stars of the spectral type that best matches the strength of the feature of interest. This broadening results from the differing radial velocities of individual stars within the gravitational potential of the cluster. The spectroscopy requires moderate to high spectral resolution, and for the determination of the cluster sizes observations with high spatial resolution are necessary. Masses are determined by applying the virial theorem, which should be valid, because our cluster ages of a few million years generally correspond to many crossing times, and thus are gravitationally bound.

Two features which arise in stellar atmospheres are the CO absorption bandheads beyond 2.29 μm and the Calcium Triplet (CaT) at around 0.86 μm. The spectral resolution should be around R $\sim$ 9000 or higher, and the S/N ratio needs to be fairly high, around 15-20, if reliable mass estimates are to be obtained.

We performed spectroscopy in two different spectral domains, the optical and the near infrared.

Optical spectroscopy was performed using UVES on VLT-UT2. It delivers a spectral resolution of R$\sim$38,000 at a slit width of $0\farcs6$. The slit length is 12", so that 2 clusters could be included in the slit for each position. We observed two slit positions with two clusters each, and an additional setting with a very bright cluster for a shorter integration time when the seeing had degraded slightly.

The CaT spectroscopy requires a non-standard setup for UVES. It lies well within the region covered by the red chips in the dichroic mode, but there is a small gap between the two detectors that cover the red half of the spectrum. If the central wavelength of the red arm is not shifted a little bit, the CaT will end up exactly in that gap. For comparison with the cluster spectra, template spectra of the most probable contributors to the spectrum were obtained. For the CaT, these are the red supergiants, and at the ages estimated for the clusters, these should be around the M2I spectral type. But also the most massive main sequence stars present at that cluster age, which are late B- or early A stars, could contribute some fraction of the total emission. The comparison spectrum - composite, if necessary - will then be convolved with a Gaussian broadening function and compared with the cluster spectrum to derive the velocity dispersion.

Near infrared spectroscopy was performed using ISAAC on VLT-UT1. The maximum resolution it can deliver, at a slit width of $0\farcs3$, is R=9000. Simulations suggested that this should be sufficient to derive the velocity dispersion to a level of $\pm$10% for an SNR of 20.

Figure 5.11 shows the pointings for the two spectroscopy positions.

Position	Object	m_K	T_{int}	Total integration time	Comments
Slit 1	[W99]15	16.1	600s	15600s	Difficulties keeping both targets in slit
	[WS95]355	15.6	600s	15600s	
Slit 2	[W99]2	13.9	600s	2400s	
M3Iab	HD 303250	4.2	1.77s	∼70s	Active optics off, offset from slit by 0.″35

Tab. 5.5: Summary of ISAAC spectroscopy. The first slit position included two clusters, the second one cluster. The supergiant was observed as a template for the determination of the velocity dispersion. All targets were observed by nodding along the slit, always keeping the target(s) in the slit. The total integration time is the sum of several observing blocks, consisting of several integrations of duration T_{int}. In all cases, the slit width was 0.″3, resulting in a resolution $R = \lambda/\Delta\lambda$ of 9000.

5.4.1 Observations

ISAAC

ISAAC spectroscopy was performed on the 17th of April 2000 on VLT-UT1, using ISAAC with a 0.″3 slit and the central wavelength set to 2.31μm. The seeing as measured by the seeing monitor was between 0.″6 and 1.″0 during the Antennae cluster observations, 0.″9 during the spectroscopy of the M3 supergiant. The night was photometric. Atmospheric calibrators were observed several times during the night. As spectroscopic templates for the derivation of the velocity dispersion, four supergiants were observed, with the spectral types derived from the SIMBAD archive to be M0I, M0Ie, M3I and M5I. During the observations of the M0I star, the radical mis-estimate of the required exposure time (derived from m_V and intrinsic colour) already suggested a wrong colour and thereby classification, so the M0Ie, the only other suitable M0I-type star observable at that time of night with ISAAC, was also observed.

The selection of the template stars was not easy, because there were only very few supergiants that were not too bright to be observed by ISAAC and outside the Magellanic Clouds (which have sub-solar metallicity and are therefore not suitable). Unfortunately, it turned out that, of the stars observed, only one supergiant was classified correctly, the M3Iab star. The M5I was a giant star, most likely a K2III star, the others were completely misclassified. For the observations of the bright M3I star that will be used as a template, the active optics had to be switched off, and the target offset from the slit by 0.″35.

The selection of the star clusters made use of the imaging observations performed on the NTT using SOFI in large field imaging mode in May 99. They included narrow band imaging in the CO band head, making possible the selection of relatively extinguished clusters (A_V ∼5 mag) with substantial CO absorption. Amongst those fulfilling this criterion, the brightest ones in K-band were selected.

These were two clusters with a separation of $\sim 5''$ located in the overlap region. One of them has an optical counterpart, [W99]15, the other one is detectable only in I, therefore denoted a "Very Red Object (VRO)" by Whitmore & Schweizer (1995). Its number is [WS95]355. Their detectability in at least one band was a necessary constraint, since the cluster radii are to be determined from the HST data. They deliver the highest spatial resolution, and still are only marginally able to resolve these distant clusters. The two clusters [W99]15 and [WS95]355 were placed in one long slit (the ISAAC slit length is 120″) and the objects were nodded along the slit during the integrations, thereby not wasting time for sky background measurements.

Another pair of clusters had been selected, but the integration on the first setting took longer than expected: several re-acquisitions were required, because the objects drifted out of the narrow 0.″3 slit during the integration, especially during the transit of the target. It was necessary to do these re-acquisitions three times during the night. Therefore, when these integrations were done and an SNR sufficient for the purpose was obtained, there was not enough time left to perform the observations of the other selected set of clusters,

which were roughly as bright in K as the ones already observed. One of the brightest K-band clusters was observed instead, even though it is not highly extinguished. It is the cluster labelled [W99]2 and was observed in the same way as the first pair of clusters, in a 0.″3 slit with nodding. Table 5.5 summarizes the ISAAC observations.

UVES

UVES spectroscopy was performed in the night of the 18th of April 2000 on VLT-UT2. The instrument was set up to use a slit width of 0.″6, resulting in a resolution of around R = 38,000, depending on wavelength. The dichroic setup was chosen, using both the red and the blue channel of the spectrograph, but only the red part of the data will be discussed in this work. The red channel had the central wavelength shifted to 840nm. This was necessary, because part of the CaT (at NGC 4038/39 redshift of z∼0.005 located roughly at: 0.8540, 0.8585 and 0.8705 μm) would have fallen right into the small gap between the two arrays that cover the lower and the upper part of the spectra in the red channel. In order to maximize the efficiency, which is driven by the blaze angle of the grating, the blue camera had an additional tilt by 200 pixels. In order to maximize the SNR, an on-chip binning of 2x2 was applied. The 50kHz readout mode with high gain was selected, which provides best performance for the long integration times we anticipate for the clusters. In principle, it would have been possible to switch to the other read out mode for the stars, but in order to not introduce any change in the setup between the clusters and the template stars, and to avoid an additional set of calibration observations, all integration were performed in the same mode.

The clusters were selected using similar criteria to those used for ISAAC, only adjusted to the different wavelength range, selecting clusters with low extinction ($A_V \sim 0.3$ mag) and bright V magnitudes. An additional constraint was the desire to include more than one cluster in the slit. Due to the Echelle nature of the spectrograph, the slit length is only 12″, and the clusters selected are [W99]1 and [W99]43 in one position, [W99]10 and [W99]16 in the second position. These observations proceeded very smoothly, so that before the target set, some time was left to observe a third slit position including the cluster [W99]2. This bright cluster was also observed with ISAAC and thereby provides the possibility to compare the velocity dispersions derived from both instruments.

Observations of template supergiants was facilitated for UVES observations with respect to the ISAAC spectroscopy, because those stars are fainter in V by 4-5 mag, which means that many more stars are available without risk of saturating the detector. A large set of template stars was observed for the purpose of comparison with the cluster spectra. See Table 5.6 for details. The early type main sequence stars in the table were observed because it is anticipated that the spectrum in the V and I bands will be a composite of the late type supergiant and early type (B2V-B5V) main sequence stars. Additional calibration observations included atmospheric calibrators of various types (early type main sequence stars, white dwarfs).

The seeing during the night started out at around 0.″7, was at around 0.″85 during the second slit setting (9600s of integration), and degraded to 1.″1 when additional 1800s were taken on Slit 2. The degradation of the seeing also led us to observe on a third position of a bright, singular cluster for the rest of the night instead of going back to Slit 1. During the integration on Slit 3, the seeing degraded to 1.″4 and stayed at that level for the spectroscopy of most of the template and calibrator stars.

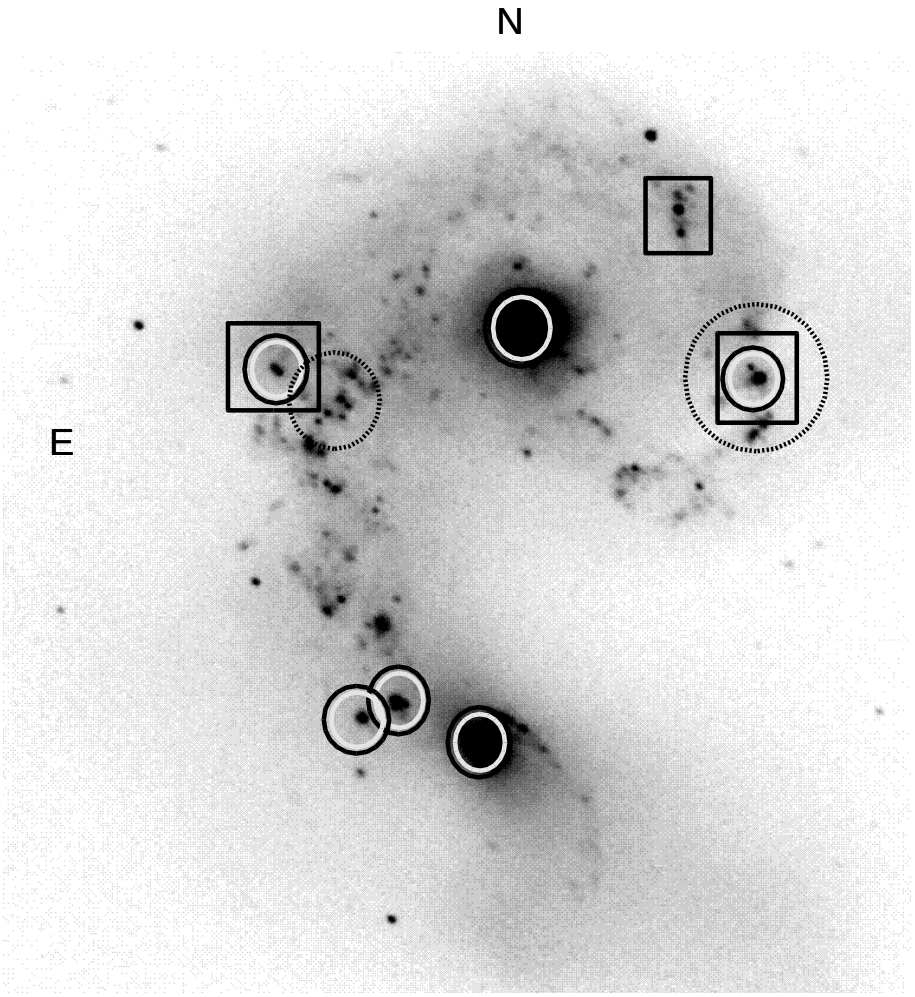

Fig. 5.11: SOFI Ks-band image with symbols indicating the location of the clusters selected for 3D integral field spectroscopy (black and whit small circles), ISAAC medium resolution spectroscopy (large, dashed circles) and UVES high resolution spectroscopy (squares).

Position	Object	m_V	T_{int}	Total integration time	Comments
Slit 1	[WS99]1	17.5	4800s	9600s	required pausing of integration due to A.O. software crash
	[WS95]43	20.0	4800s	9600s	
Slit 2	[WS99]10	19.1	4800s+1800s	11400s	required pausing of integration due to A.O. software crash
	[WS99]16	19.3	4800s+1800s	11400s	
Slit 3	[W99]-2	17.6	4600s	4600s	
M3Iab	HD 303250	8.69	20s/10s	20s/10s	
M5I	HD 142154	9.10	20s	20s	
B5V	HR 5914	5.94	4s/1s	4s/1s	
B2V	HR6028	4.59	4s/1s	4s/1s	
M1Ib	HR 6693	5.16	1s/4s	1s/4s	
K7IIa	HD 11475	6.96	20s/10s	20s/10s	
K5Ib	HR 7412	6.09	4s/15s	4s/15s	
K2Ib	BM Sco	7.00	10s/3s	10s/3s	
K0Ia	HR 6392	6.49	5s/20s	5s/20s	
K3II	HR 6842	5.28	4s/1s	4s/1s	
K2.5IIb	HR 7604	4.53	4s/1s	4s/1s	
K2II	HR 6498	4.33	4s/1s	4s/1s	
MIa-Ib	HR 4064	8.74	180s/180s	180s/180s	
K3Ib-IICN	HF6959	5.50	4s/1s	4s/1s	
K0.5IIb	HR 6392	5.49	4s/1s	4s/1s	
K5II	HR 7873	4.89	4s/1s	4s/1s	
B2V	HR 6946	5.72	1s/4s	1s/4s	
B5V	HR 5839	4.75	1s/4s	1s/4s	
WD	EG 274	11.4	600s	600s	atmospheric calibrator
O9V	HR 1996	5.1	1s/4s	1s/4s	atmospheric calibrator
O6V	HD 49798	8.5	50s	50s	atmospheric calibrator
O8.5V	HR 5664	5.09	4s/1s	4s/1s	atmospheric calibrator

Tab. 5.6: Summary of UVES spectroscopy of science targets (star clusters and template stars). Observations were performed with a slit width of $0\farcs6$, in dichroic mode. The central wavelength for the blue chip was set to 464nm, for the red arm to 840nm. Readout was performed at 50MHz, with 2×2 binning and high gain. The slit length was $12''$, and the achieved spectral resolution was roughly 19000. In the cases where two integration times are listed separated by a "/", the integration times in the two arms of the dichroic setup differ, listed first is the integration time in the blue.

5.4.2 Data reduction and analysis

ISAAC

The reduction of ISAAC data was performed in the standard way using the IRAF data reduction packages. It included dark subtraction and flatfielding (using a normalized flatfield created from dome flat observations) of the twodimensional array. Sky subtraction was performed pairwise, followed by a rejection of cosmics/bad pixels, replacing all pixels outside an allowed count range by median values. This procedure was repeated several times in order to be able to eliminate clusters of bad pixels, out of which only one pixel is detected at a time by the algorithm.

The spectra were then corrected for tilt and slit curvature in x and y direction. The displacement of the spectrum (running parallel to the x axis) was determined for each column. A polynomial was fit to this function and the spectra straightened accordingly. The same technique was applied to displacements in the spatial direction.

Single integrations were combined by first shifting the spectra in the spatial direction to the same pixel and then combining them using the median of the frames with rejection of highest and lowest pixels in the stack, in order to reject outlier pixels that might have survived the cosmic ray rejection procedure.

The object spectra were then extracted from user specified apertures. A linear fit to the background on both sides of the object spectrum was subtracted. Wavelength calibration was performed using observations of arc discharge lamps. Even though the spectral resolution was high and the observing times were long, OH night sky lines could not be used for this purpose, because the observed wavelength range does not show any OH emission lines. An atmospheric calibrator (B5V) was observed and reduced in the same way as the target and used to divide out the atmospheric absorption features.

Figure 5.12 shows the spectrum of an M3lab star, and overlaid are marks for the locations of the rotational transitions of the $^{12}C^{16}O$ 2-0 vibrational transition. It is obvious that the absorption features in the spectrum are matched very well. Since they are also resolved in the cluster spectra, they provide an excellent long baseline for the fitting technique.

Figure 5.13 displays the spectra of all the template stars observed with ISAAC, normalized and offset along the y-axis. Indicated are the regions used for the determination of W_{CO} (continuum and bandhead) with the corresponding numbers and the spectral types taken from the SIMBAD database.

The analysis of the data aimed at deriving the Doppler broadening of the stellar features in the cluster spectra. As mentioned above, the broadening has its origin in the different velocities of the stars along the line of sight and is assumed to be Gaussian in shape. The parameter σ of this Gaussian distribution was determined from the data for the three observed clusters by comparison with the spectra of the template star(s).

To obtain σ, we broadened the stellar spectrum with gaussian functions and compared it with the cluster spectrum in velocity space. To evaluate the quality of the fit, a χ^2_ν (ν is the number of degrees of freedeom which are taken into account for the calculation of the reduced χ^2) determination was performed and the parameter σ of the minimal χ^2_ν used as the result. Cluster- and stellar spectra are rebinned into equal velocity bins instead of equal wavelength steps. The template spectrum is redshifted by a recession velocity v_r and convolved with a Gaussian function of dispersion σ. χ^2_ν is determined for this pair of spectra in a wavelength range selected by the user. This means that the quadratic difference between the spectra χ^2 is normalized by the SNR of the spectra and the degrees of freedom. For a good fit, χ^2_ν is approximately 1.

The search for the global minimum of the function $\chi^2_\nu(v_r,\sigma)$ is performed using a simplex downhill algorithm for the tour through parameter space. The two variables are iterated until the minimum is found.

This technique is performed for a sequence of template supergiant star spectra or synthetic spectra compiled from several input supergiant spectra. Due to the complication mentioned in section 5.4.1, only one spectrum of a supergiant (M3lab) was observed during the dedicated observing run, but Linda Tacconi observed three more (K5Ib, M0Ib, M1lab, see Figure 5.13).

At an age of 10 Myrs, a cluster spectrum is expected to have substantial contributions also from hot main

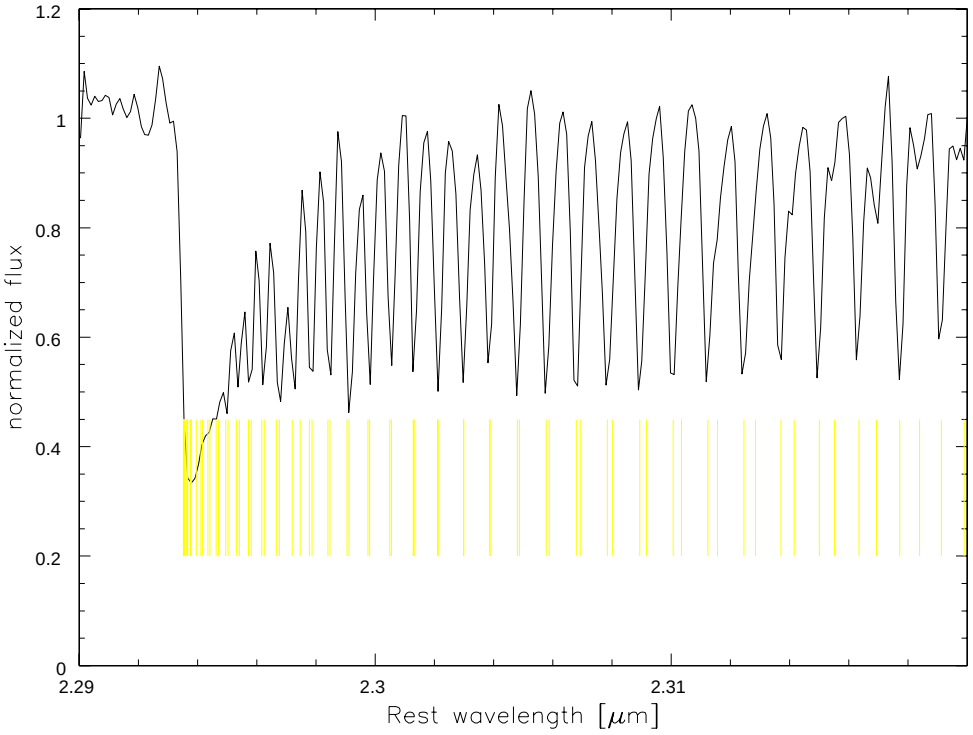

Fig. 5.12: Spectrum of an M3Iab supergiant. The vertical lines indicate the locations (not intensities) of rotational transistions of the $^{12}C^{16}O$ 2-0 vibrational transition. They are also resolved in the cluster spectra and provide a good reference signal for the fitting technique.

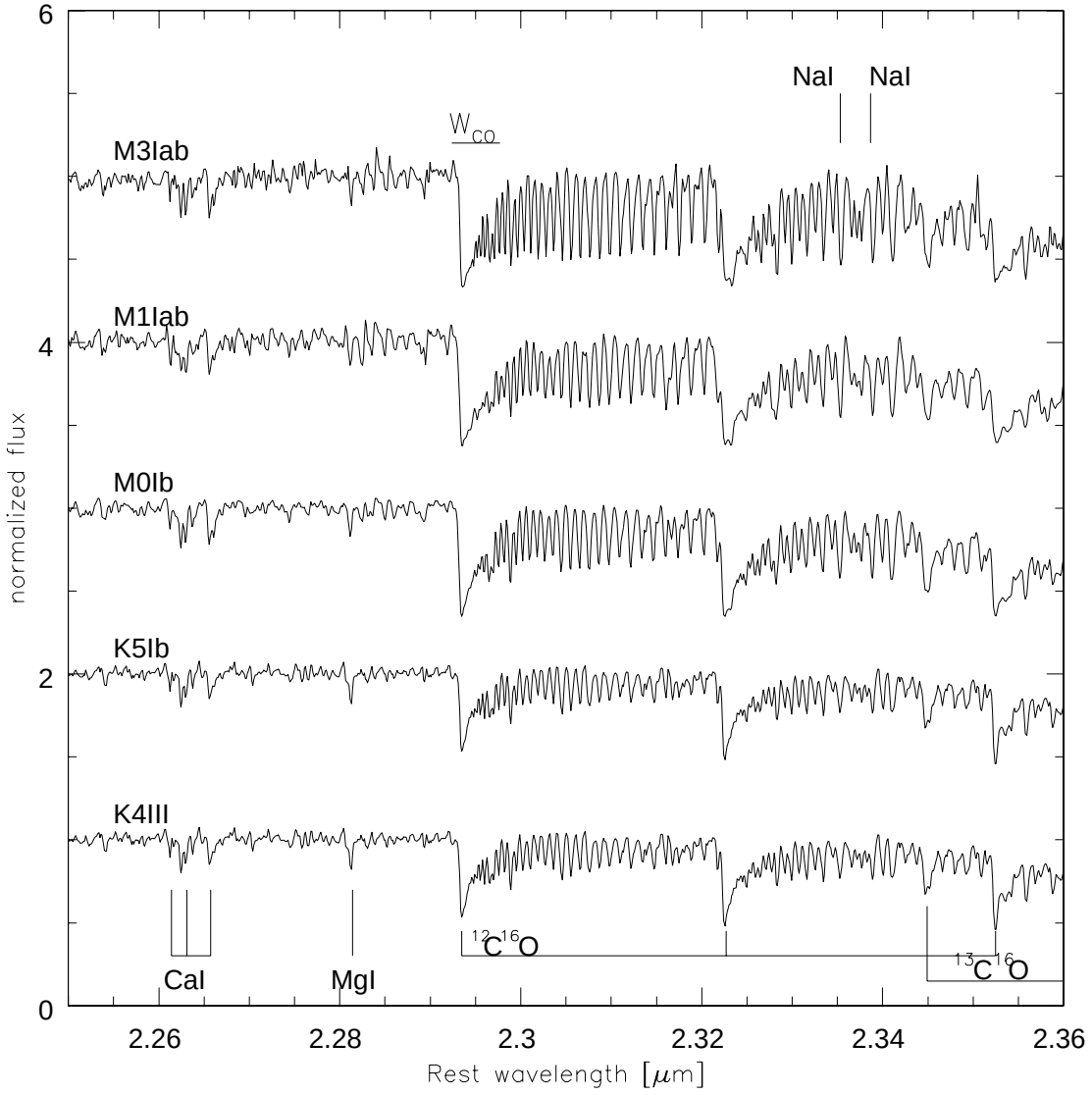

Fig. 5.13: Spectra of all supergiants observed with ISAAC, and an additional giant for comparison. The deepening of the absorption features with decreasing stellar temperature is obvious. Absorption features are labeled. The horizontal line above the top spectrum shows the wavelength range which was used to determine W_{CO}, according to the convention in Origlia et al. (1992).

sequence stars, mainly B type (see also chapter 5.4.4 and González Delgado and Leitherer (1999)). To simulate this contribution, a flat continuum is added to the supergiant spectrum and the result renormalized. This is appropriate, because hot main sequence stars have a flat continuum in that spectral regime.
This dilution with a continuum is tuned to match the equivalent width of the CO bandhead in the template spectrum with that of the cluster, and this artificial template is used to perform the fit. Other attempts include the creation of template spectra by adding a small contribution from a giant spectrum to that of a supergiant.

5.4.3 Masses from ISAAC and UVES spectroscopy

From ISAAC data

Three different star clusters were observed with ISAAC, [W99]-15, [WS95]-355 and [W99]-2. Their stellar velocity dispersions were determined by comparison with a stellar template spectrum, using the technique described in section 5.4.2.
Figures 5.14 and 5.15 give an overview over the tests performed with matching templates, which means that the same spectrum was used for both, the creation of the artificially broadened spectrum, and the redetermination of the velocity dispersion. It is found that the velocity dispersion is very well redetermined. Certainly for the high SNR (S/N = 100) case, but also for the lower SNR case (S/N = 20, which is approximately the level achieved by our observations), with only the uncertainties increased vs. the high-SNR case. Each data point in 5.14 is the average of 20 test runs, and the error bars are derived from the standard deviation of these 20 measurements. The parts of spectra in 5.15 show a noisy (S/N = 20), broadened ($\sigma_{\rm in}$ = 15 km/s) stellar spectrum (M3lab) together with the fit (also M3lab).
These tests, however, were not only aimed at getting an estimate for the uncertainties involved, but also were meant to show how to best find the matching template. It was seen, as expected, that a stellar template spectrum which does not match that of the dominant stellar type in the cluster spectrum has large impact on the derived velocity dispersion. For example, if the template type is too late for the cluster spectrum, which means that the amplitudes in the rotational transitions are too high, then the velocity dispersion needs to be higher in order to flatten them to the lower observed amplitude. This effect can be as large as ∼30% for our available template combinations.
Two criteria were dicovered by which to select the matching template:

- The actual qauality of the fit to the tip and the rising edge of the CO bandhead, since this regime is most sensitive to changes in stellar type. Compare Figure 5.19 for an example

- Independence of the fit on the selected wavelength range. Only for the correct template match does it become irrelevant for the final result if the bandhead itself, or just the overtones, or a wavelength range including also the start of the next bandhead are selected. With the correct template, the variations in the velocity dispersions are within ∼5%. With incorrect templates, the dispersions determined from different wavelength ranges vary by up to 30%. Figure 5.20 servers to illustrate this behaviour. While for one template the determined values for σ span only a narrow range, this range has broadened substantially if a slight mismatch is introduced.

Both of these criteria were considered in finding the templates for the observed three cluster spectra. The selection of templates included a range of supergiants from K4I to M3I spectral type.
For all three star clusters, the best match in the light of the above mentioned criteria was achieved for an M3lab spectrum, which, however, had to be diluted by a flat continuum for best results.
The choice of a flat continuum as a contributor to the cluster spectrum is not completely arbitrary. As mentioned in section 5.4.4, some contribution (∼10%) of hot main sequence stars is expected from evolutionary synthesis models for a cluster with an age of a few million years (e.g., González Delgado and Leitherer (1999)). These B2V-B5V stars have a spectrum which is essentially flat in the 2.3μm range.

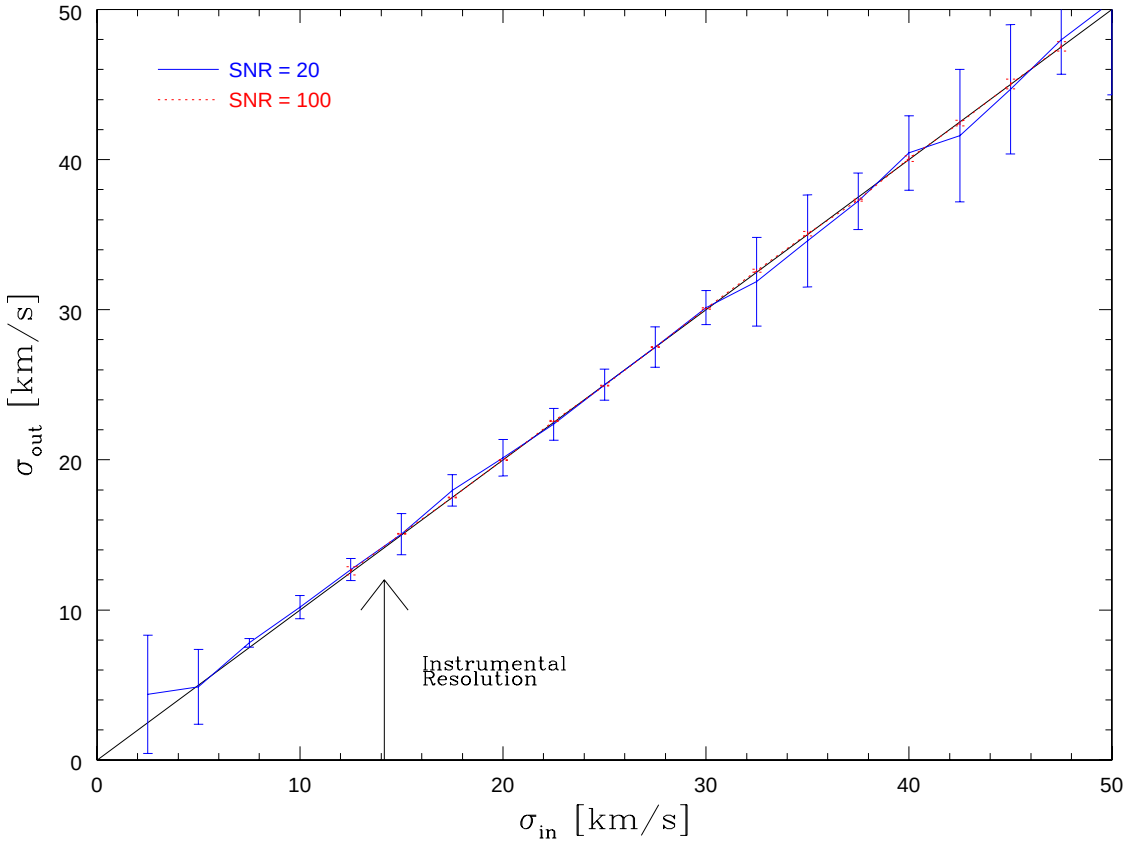

Fig. 5.14: Using a broadened template spectrum (M3Iab star) with added noise of SNR = 100 or 20, respectively, the input velocity dispersion ($\sigma_{\rm in}$) was redetermined using the same method as for the clusters within the wavelength range 2.29-2.318 μm. The resulting $\sigma_{\rm out}$ is plotted as a function of $\sigma_{\rm in}$, for the two different SNR. The expected flattening out can be observed below the instrumental resolution, which is indicated by a vertical line. Towards larger $\sigma_{\rm in}$, the errorbars grow somewhat surprisingly. This is caused by the large wavelength range used for the analysis, covering large parts of the rotational transistions, which are smeared out for high dispersions and contribute little information which is useful for the analysis. In that case it would be better to use the bandhead alone. The vertical line at 14.1 km/s indicates the instrumental resolution. This test shows that the velocity dispersion can be reliably determined to below that level, down to roughly half the instrumental resolution.

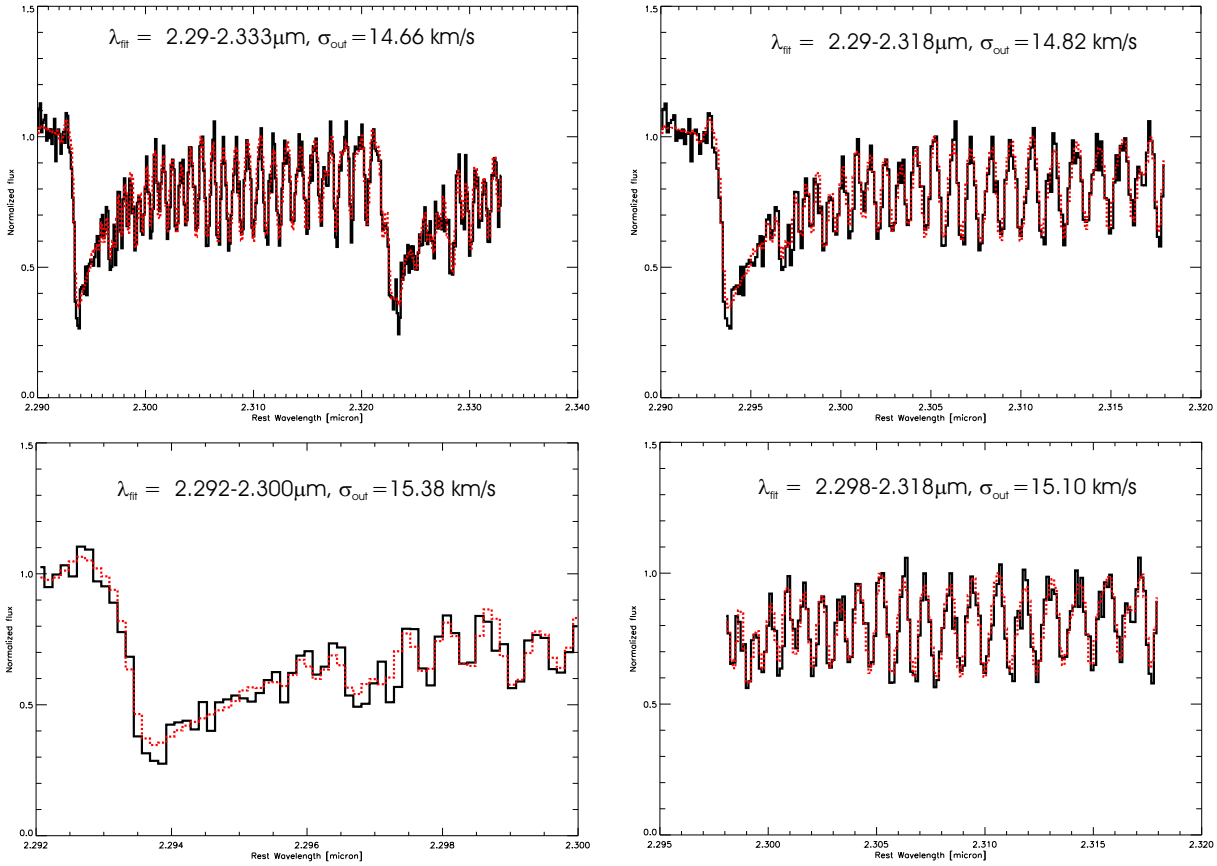

Fig. 5.15: For various input parameters, like σ, SNR and the fit wavelength range, tests have been performed to determine the reliability of the results obtained for the cluster spectra. In a first step, matching templates were used (meaning that the same star was used for the creation of the simulated noisy, broadened spectrum and the redetermination of the velocity dispersion. The applied broadening was $\sigma_{\rm in} = 15$ km/s. This value is reproduced fairly well in all wavelength ranges (average and 1-σ uncertainties: 15.0$\pm$0.3 km/s) with low scatter.

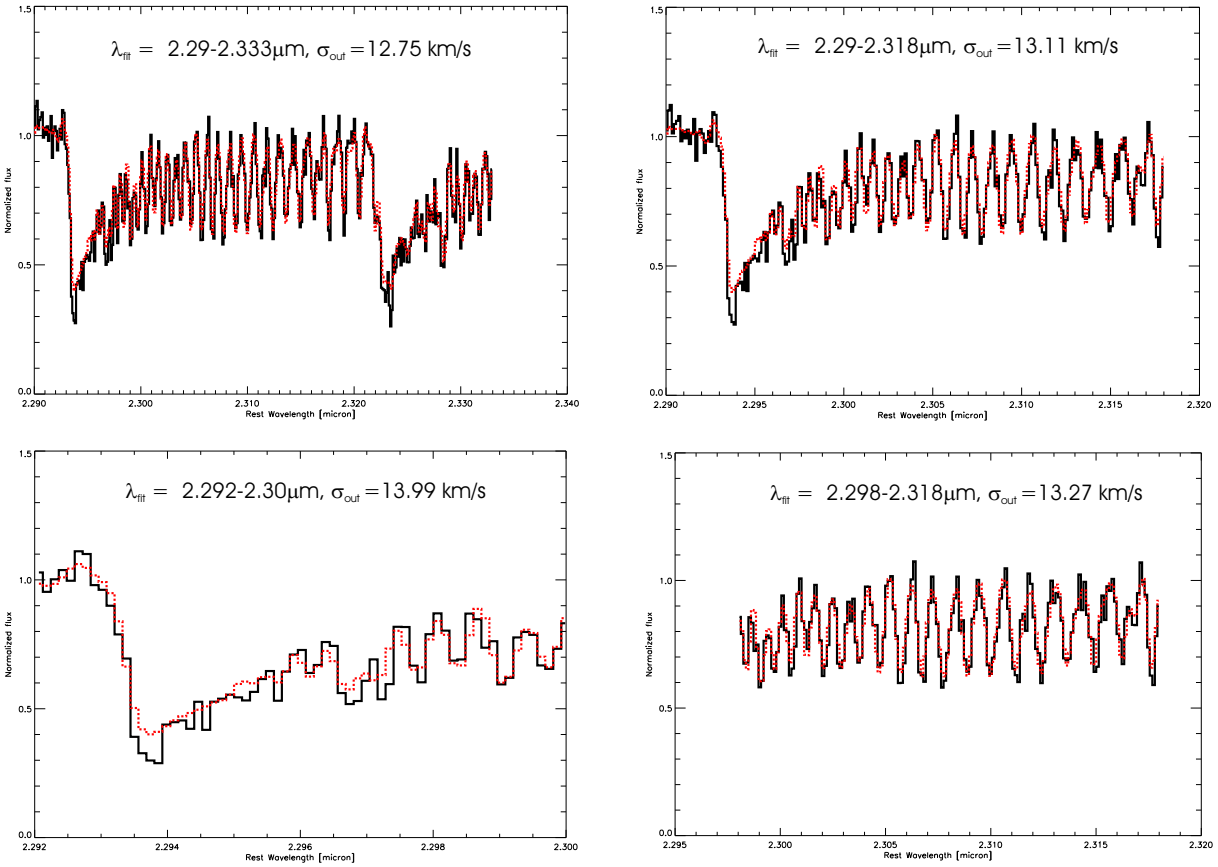

Fig. 5.16: This plot shows the results of tests similar to those shown in Figure 5.15. The same $\sigma_{\rm in} = 15$ km/s was used, and the same four wavelength ranges, but this time the simulated spectrum was created using an M3I star spectrum, while the template spectrum was an M3I spectrum, diluted by a constant continuum contribution of 10%. The continuum dilution decreased the amplitude of the rotational transitions and therefore led to a lower estimate of the velocity dispersion (average and 1-σ uncertainties: $\sigma = 13.3 \pm 0.5$ km/s). Comparing the lower left panel of this figure to that of Figure 5.15, the fit looks slightly too flat on the rising edge of the bandhead.

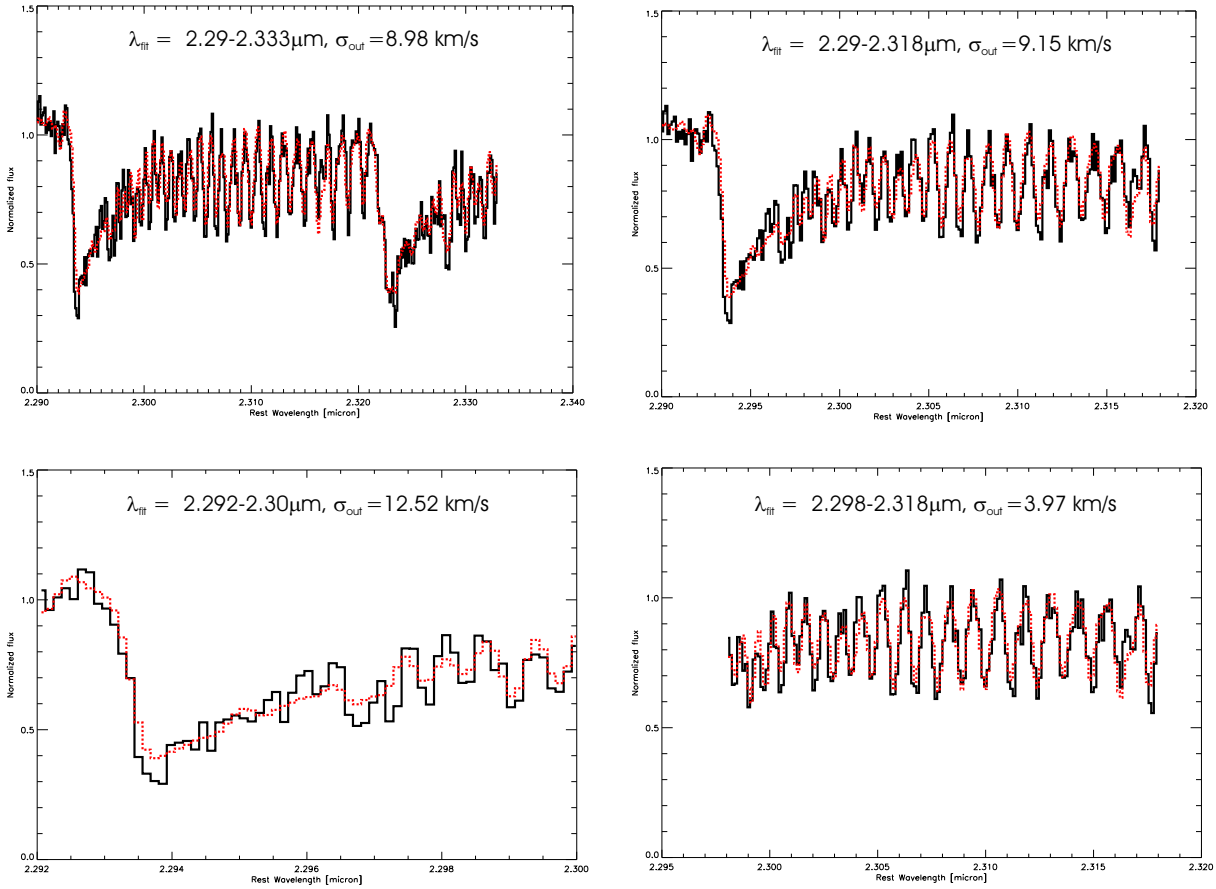

Fig. 5.17: These plots show the same trend as it was seen in Figure 5.16, but this time a real stellar template spectrum (M1I) was used to fit the same artificial spectrum as in Figures 5.15 and 5.16. For again the same $\sigma_{\rm in}$ and wavelengths ranges, the influence of the template mismatch is even more drastic, leading to an average value of $\sigma = 8.7 \pm 3.1$ km/s).

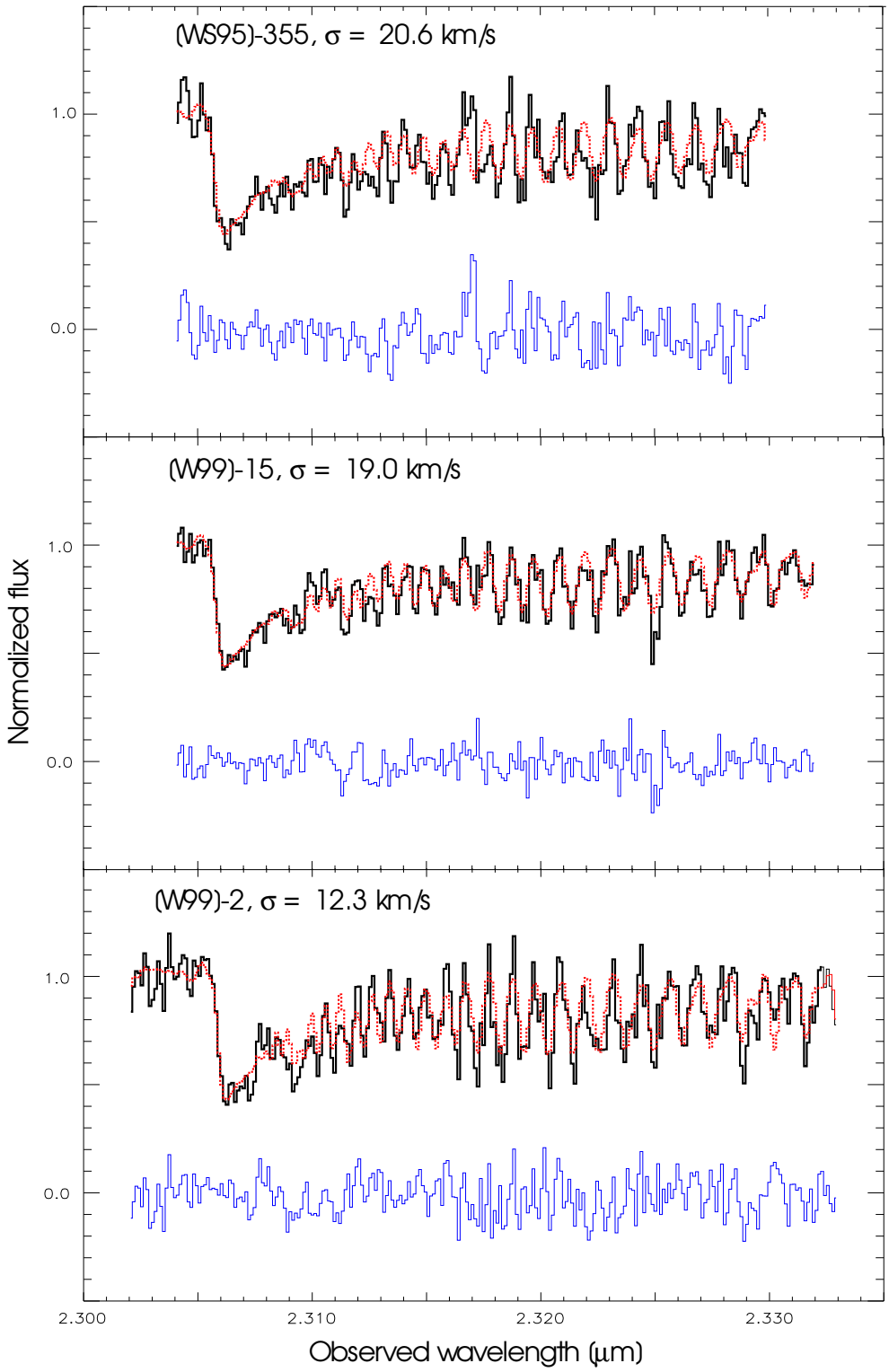

Fig. 5.18: Spectra of the three clusters [WS95]-355, [W99]-15 and [W99]-2 (top to bottom, solid, black) with the fits (dotted, red) and the residuals. The velocity dispersions given in the seperate panels are averages of fits within six different wavelength ranges. Clearly, [W99]-15 is reproduced best by the fit, and the residuals of [W99]-2 seem to show some non-white noise. With our selection of observed template stars, it was not possible to obtain a better fit.

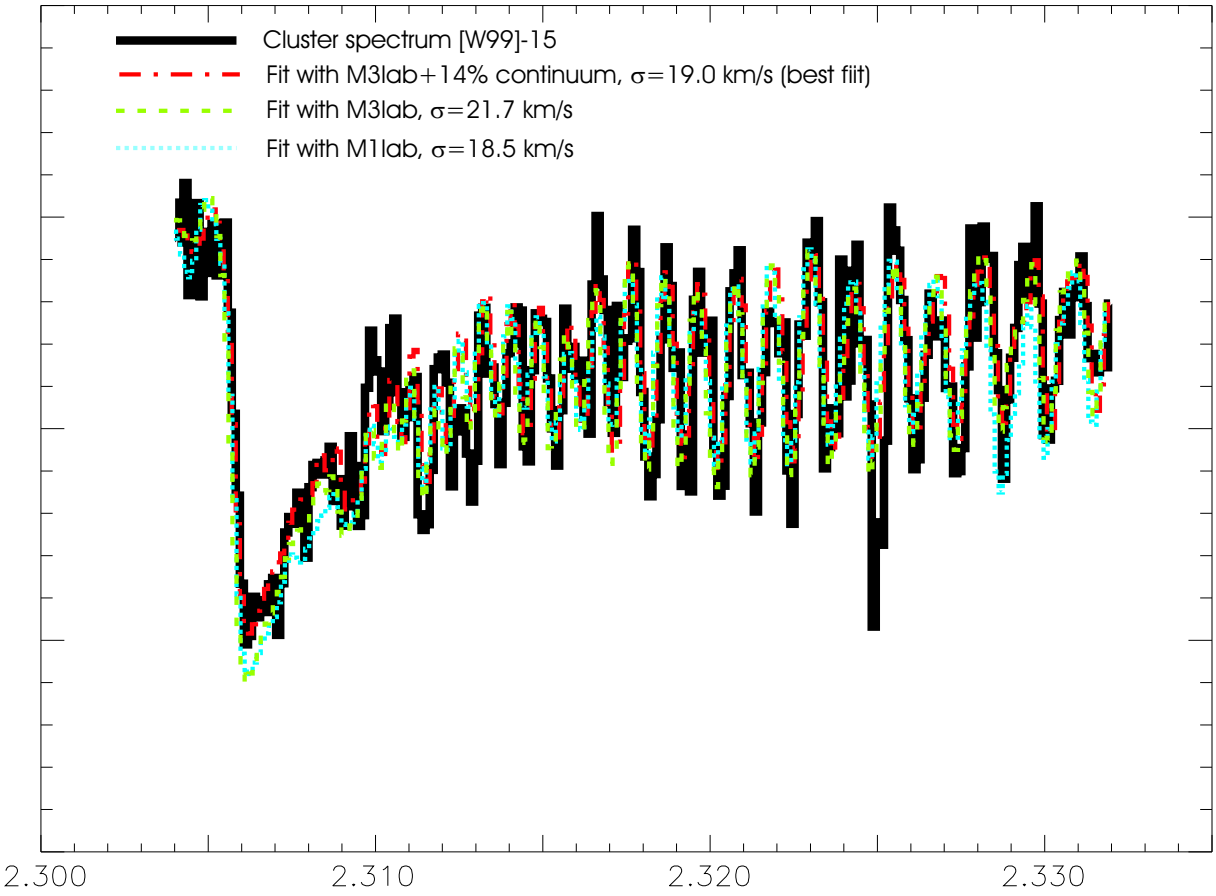

Fig. 5.19: Spectrum of W99-15 with different fits. The M3lab spectrum with the dilution of 14% fits best. Even though the overtones are matched fairly well by all three template spectra, the bandhead is missed substantially by the two other fits.

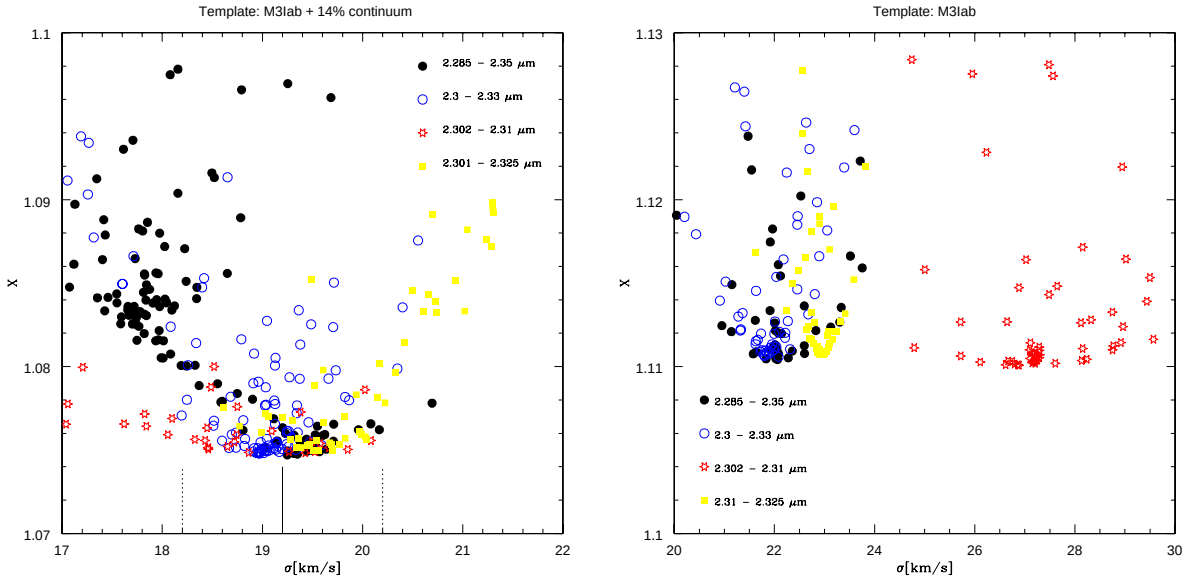

Fig. 5.20: Left panel: The reduced χ^2 values for fits to the spectrum of [W99]-15, using as a template an M3lab star with additional 14% continuum. The template spectrum was broadened by velocity dispersion σ. Different symbols indicate different fit wavelength ranges according to the legend. For all wavelength ranges, σ lies within the statistical uncertainties (mean value indicated by solid vertical line, uncertainties, as they are displayed in Figure 5.14, as dashed lines. The right panel shows the same information, only the template spectrum was different, using an undiluted M3lab star spectrum. Measured velocity dispersions span a much larger age range (note the different scales on the x axis), which serves as a criterion for the selection of a matching stellar template.

Another indication that this is the correct treatment (also explained in 5.4.4, see there for details) comes from the spectrum of the cluster that was observed with both instruments, ISAAC and UVES, since the relative contributions of B2V and M3I types to the respective wavelength ranges of the cluster match with the SED's of the stellar types.

A whole set of template star spectra, with and without diluting continuum, was fit to the cluster spectra. Best fits were achieved for the M3Iab+0.14, which is probably due to the fact that all clusters have similar ages. The results are listed in Table 5.7.

The fit for cluster [W99]-15 with the spectrum of M3Iab, diluted with 14% of continuum, is excellent (see Figures 5.18 and 5.19). The template matches well in both, the bandhead and the overtones. The residuals are small and do not show trends like for the other two clusters, where the residuals increase considerably towards the overtones of the bandhead.

The fit is worst for cluster [W99]-2, where Figure 5.18 shows again the fit with the best matching template, an M3Iab star with an additional contribution from hot main sequence stars on the level of 14%. This spectrum is the one with the lowest SNR of the three observed. This cluster, even though brightest in K, was observed only for a short integration time (see Table 5.4.1) which resulted in a SNR of $\sim$15, and the residuals show some non-white noise which is not removed for any other selection of templates currently available.

The masses were determined from the velocity dispersions, taking into account the effective radii determined by the technique described in section 5.5. All of these three clusters have dynamical masses above 10^6 $M_\odot$. A high total mass for at least some of the clusters had already been suggested by the photometric data. If these clusters are representative of the progenitors of part of the population of globular clusters in ellipticals, even taking into account the mass loss (up to $\sim 60\%$, see Chernoff & Weinberg (1990)) they would suffer during the evolution of several Gyrs would place them at the top end of the globular cluster mass distribution function. This can easily be explained as an effect of our selection, since for our first spectroscopic observations of this nature, we deliberately selected the brigtest clusters in K and I, respectively. Since they are at roughly the same ages, it is to be expected that the brightest clusters are also the most massive ones.

The last column in Table 5.7 lists the ratios of the masses determined by the two different techniques. The masses determined from the absolute K-band luminosity was for a model with the given age and the *standard parameter* set, which also constrains the slope of the IMF and $M_{\rm upper}$ and $M_{\rm lower}$. In this case, the slope was Salpeter, with $M_{\rm lower}$ of 1 $M_\odot$, and $M_{\rm upper}$ of 100 $M_\odot$. The photometrically determined masses are lower by a factor $\sim$ 20 in two cases. Even if the uncertainties are far too high to be able to constrain the slope of the IMF or $M_{\rm lower}$ from this ratio, the large value for two of the three clusters at least suggests that there are stars below 1$M_\odot$ present, which account for this extra mass, because they are too faint to contribute to the luminosity of the cluster, but are so numerous that they make up a large fraction of the total cluster mass. See also section 5.4.3.

Masses from UVES spectroscopy

Reduction of the UVES data was performed in the Echelle spectra reduction environment of the IRAF data reduction software package. The first reduction step was bias subtraction (dark subtraction was not performed. This would have meant to perform dark integrations for 4800s, and is not necessary because the dark current is subtracted together with the background determined from apertures around the object).

Flatfielding used the dome flat integrations and was performed in the standard way.

Spectra were extracted from user specified apertures. A background was fit to the neighbouring regions and subtracted. In this extraction process, bad pixels above or below a certain threshold (10σ) were detected and replaced with median values of neighbouring pixels. The full moon was fairly close to the object during the integrations, and its scattered light introduced a solar spectrum into the data. However, this contribution was removed during the background subtraction step.

Wavelength calibration requires the identification of several lines in the ThAr-spectra, a few lines in several of

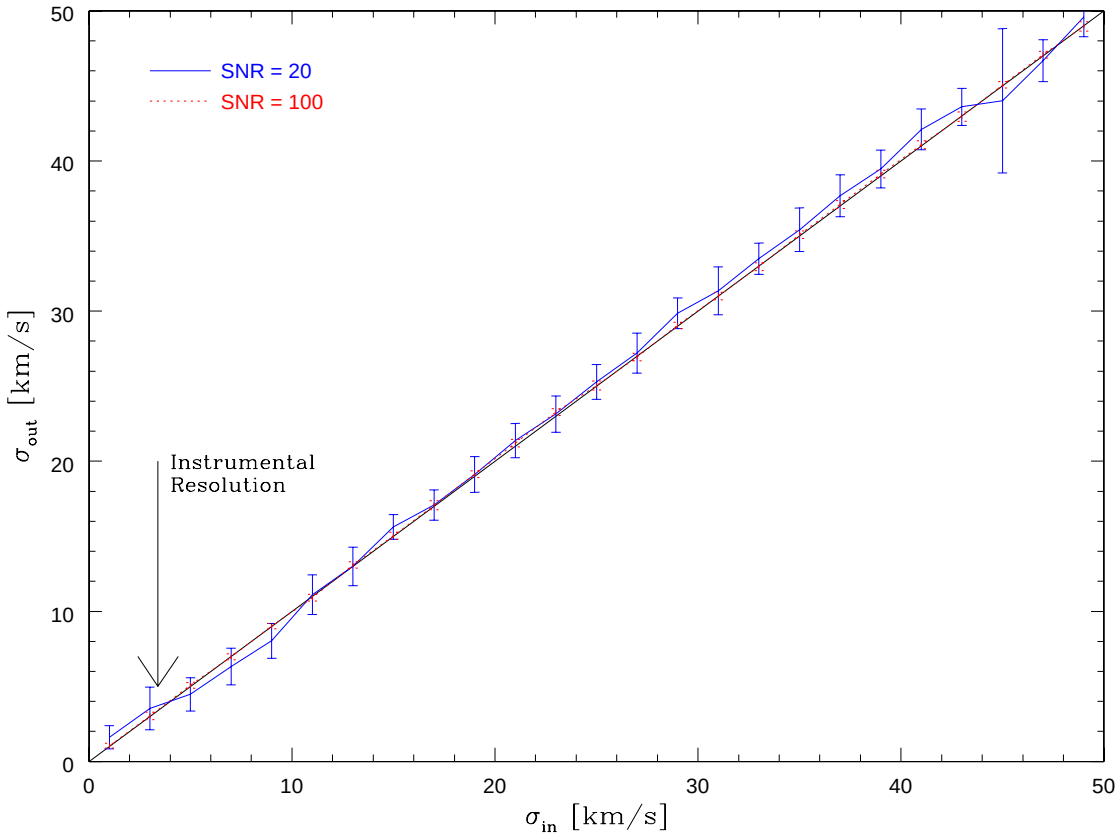

Fig. 5.21: Test of the dependence of the redetermined velocity dispertion $\sigma_{\rm out}$ on the input dispersion $\sigma_{\rm in}$ and on the SNR. The template used was the third feature of the CaT (CaII λ8662) of an M3lab star. 15 runs were performed for each $\sigma_{\rm in}$-SNR pair, the average and dispersion giving $\sigma_{\rm out}$ and the 1-σ-errorbars.

the echelle orders, with emission lines from a supplied table. A dispersion function was then fit and applied to the science data. This data set contained each order of the spectrum in a seperate channel. These pieces were combined into one final spectrum covering the total wavelength range. This involved regridding of the wavelength axis into equal wavelength bins.

UVES spectroscopy, as mentioned in previous sections, was also used to determine the velocity dispersions in the star clusters, mainly relying on the Calcium Triplet around 8500 Å, but also using, for example, the Mg absorption feature at 8800 Å and other weaker metal absorption lines.

Similar tests like for the ISAAC spectra on the reliability of the technique were performed, but only the dependence of the determined velocity dispersion on $\sigma_{\rm in}$ and SNR is reproduced here (see Figure 5.21). In essence, a similar behaviour was exhibited by the UVES data as was found for the ISAAC data.

UVES spectra, as mentioned in 5.4.4, were not only composed of a mixture of supergiant spectra, but also contain some contribution from hot main sequence stars, mainly of B2-B5V type.

This means that the spectra cannot be fit by simply broadening the stellar template, but that either the hot star contribution needs to be added to the template, as was done in the case of the ISAAC spectra, or that the contribution needs to be subtracted from the cluster spectrum.

Here, the procedure was different to that applied for ISAAC, because the hot main sequence stars were not completely flat over the analyzed wavelength range, but had some Paschen absorption features. These lay on

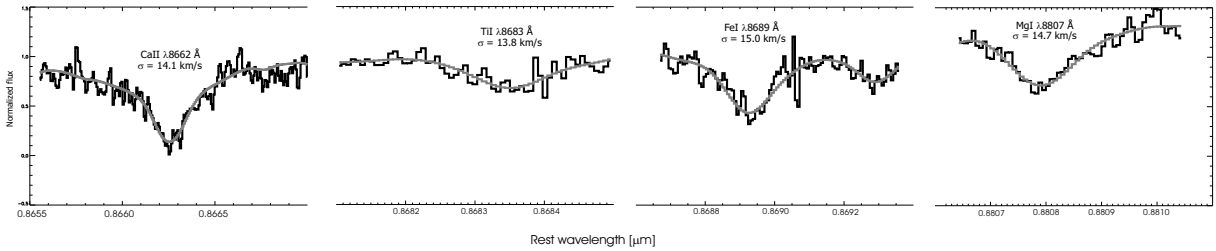

Fig. 5.22: Displayed are parts of the normalized spectrum of cluster [W99]-2 (black), which had the main sequence star contribution removed by subtracting a B2V spectrum at a level of 45%. The fit (grey) of a broadened M3Iab star spectrum is overlaid in grey. The four pieces were fit seperately, with the values for the velocity dispersion determined indicated in each piece. The average value of the velocity dispersion is $\sigma = 14.3 \pm 1.0$ km/s. It is worth noting that this is the cluster which was also observed with ISAAC, and to compare the results (12.3±1.2 km/s for ISAAC)

Cluster	Age $[10^6 \mathrm{yr}]$	Size [pc]	W_{CO} [Å]	σ [km/s]	M_{dyn} $[M_\odot]$	M_{phot} $[M_\odot]$	$\frac{M_{dyn}}{M_{phot}}$
WS95-355	8.5±0.3	4.8±0.5	16.3±0.2	20.6±0.6	4.7	0.25±0.25	20
W99-15	8.7±0.3	3.6±0.5	17.2±0.2	19.0±0.5	3.0	0.15±0.15	20
W99-2	6.6±0.3	4.6±0.5	16.2±0.2	13.3±0.3	1.9	1.9±0.3	1.0
W99-1	8.1±0.3	3.6±0.5	15.0±0.5	9.1±0.6	0.69	0.34±0.3	1.9

Tab. 5.7: The cluster masses as they were derived from ISAAC and UVES spectra in comparison with supergiant template spectra. The age was derived from the combination of $W_{Br\gamma}$,W_{CO} and W_{CaT}. Size denotes the effective radius R_{eff} as it was measured in the dithered HST images (not for [WS95]-355: R_{eff} with uncertainties was supplied by Whitmore (2000). It is so extinguished that it is only detected in I, and our technique did not result in a reasonable size estimate). W_{CO} was determined from the ISAAC spectra, and in the case of [W99]-2 compared to the value obtained from 3D integral field spectroscopy (which gave 16.1Å). M_{dyn} is the virial mass determined from equation 4.7, M_{phot} is the mass determined from the absolute, extinction corrected K-band magnitude $M_K(0)$, in comparison to that expected for a cluster of the given age and the *standard parameters* (page 27), except for [W99]-2, for which a metallicity of Z = 2 x $Z_\odot$ is assumed. The IMF for these models have Salpeter slope with M_{lower}= 1 $M_\odot$, M_{upper}= 100 $M_\odot$. The factor in the last column describes the discrepancy between the masses measured by the two techniques, indicating that the star formation parameters, namely M_{lower} and IMF slope, need to be adjusted. See the discussion in chapter 5.4.3 for details.

top of the first of the CaT absorption features, and since their dispersion is rather connected to rotation of the star itself, not the dispersion in the star cluster, they cannot be used as tracers of the velocity dispersions. And in order to not affect the results, this contribution is subtracted rather than left in for the determination.

However, tests with the other technique, fitting with a template composed from supergiants and main sequence stars, showed that it does not matter which of the two techniques is used.

The factor in the last column of Table 5.7 describes the discrepancy between the masses measured from photometry in comparison with evolutionary synthesis models and those measured dynamically.

There are large differences between those two mass estimates which would require adjustments to the model assumptions in order to be reconciled. The uncertainties involved are fairly substantial. For example the mass of [WS95]-355 would decrease if the half light radius, which could not be redetermined, was smaller. The currently assumed radius is fairly high, compared to other cluster radii, not only those listed in the table, but also other cluster radii throughout the Antennae. But for clusters [W99]-15 and [W99]-2, the radius determination worked well, and both velocity dispersions are well constrained, in the case of [W99]-15 by the quality of the fit, in case of [W99]-2 by the two independent measurements. If the standard solar metallicity was assumed for [W99]-2, that would decrease the photometric mass by a factor 1.7.

But even then there are still large differences observed which are most easily solved if variations in the IMF from cluster to cluster are assumed.

If $M_{\rm dyn}$ is identical with $M_{\rm phot}$, this means that the assumed *standard parameters* represent the correct net effect of IMF slope and mass limits. In the case of [W99]-2, this would mean that there are either indeed no stars below 1 $M_\odot$ present, as was assumed in the model, or that the IMF is flatter than Salpeter, or a combination of both.

However, cluster [W99]-15 shows 20 times the expected mass. This means that there are a lot more low mass stars present than predicted by our standard model. Going to a lower mass cutoff of 0.1 $M_\odot$ raises the photometric mass only by a factor of 2.6. It seems required to assume a steeper slope for the IMF. For example, keeping $M_{\rm lower}$ at 1 $M_\odot$, a slope of 3.3 instead of 2.35 would be consistent with the observations.

The conclusion is, that even though the type of modification required, IMF slope or lower mass cutoff, is not clear, there is evidence for variations in the IMF between different clusters in the Antennae. Some are seemingly more rich in low mass stars than others. They would certainly host enough mass in form of low mass stars to survive evolution for several Gyrs, and could evolve into globular clusters. For the clusters which seem to be deficient in low mass stars, this is rather unlikely.

Considering the small sample, it is too early to draw any conclusions about the survival of the cluster population as a whole or about IMF variations as a function of other parameters, like total cluster mass or location within the merger. An answer to that will be attempted when a bigger sample is available. The necessary observations for that are currently taken.

5.4.4 Stellar populations

As anticipated from the cluster models, young clusters have different contributors to their spectrum, with variable influence at different ages (see also 4.2) The contribution of different spectral types, largely red supergiants or hot (B-type) main sequence stars, is most obvious in the UVES spectra, but also the ISAAC spectra lead to that conclusion.

As templates for the synthesis of the cluster spectra we use the spectra observed with UVES, as listed in Table 5.6. Figure 5.23 shows the spectra of the different stellar types.

Figure 5.24 shows how the synthesis of one of the star cluster spectra was performed, requiring contributions from an M3I and from a B2V star.

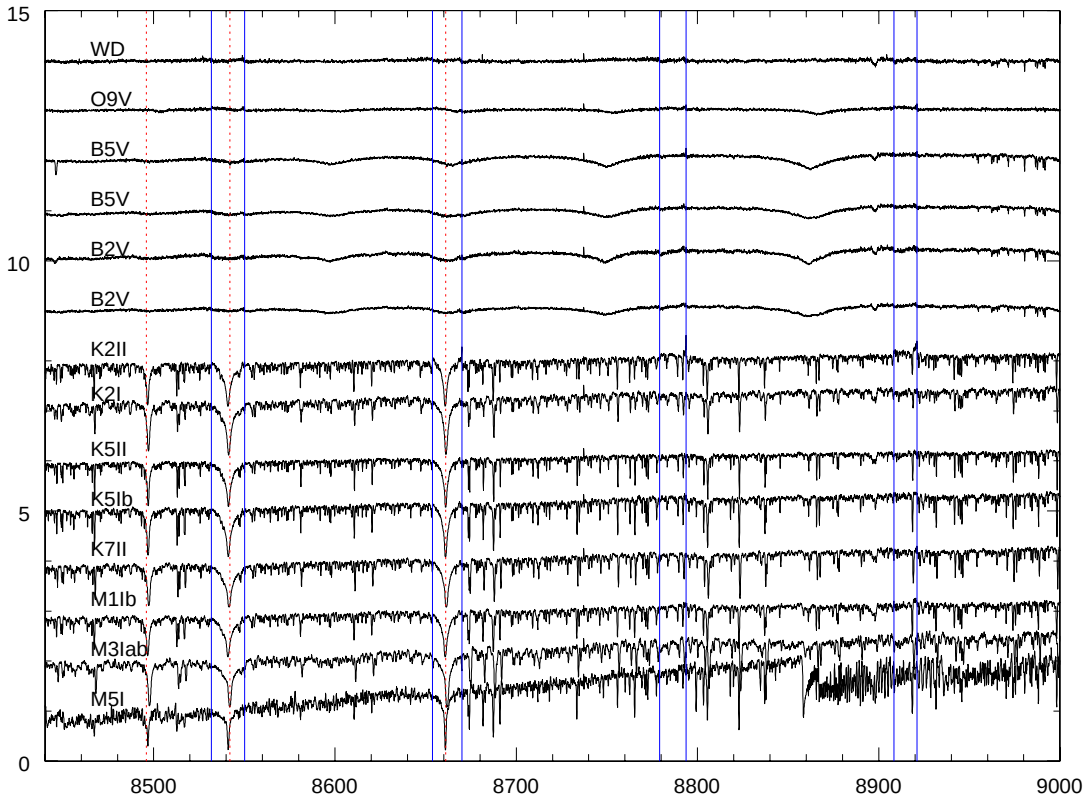

Fig. 5.23: Spectra of the stellar types observed with UVES, in the wavelength range 8400-9000 Å. The solid vertical lines indicate the locations of the order edges in the echelle spectrum, where artifacts might show up in the spectra. Dashed vertical lines indicate the positions of the CaT absorption features.

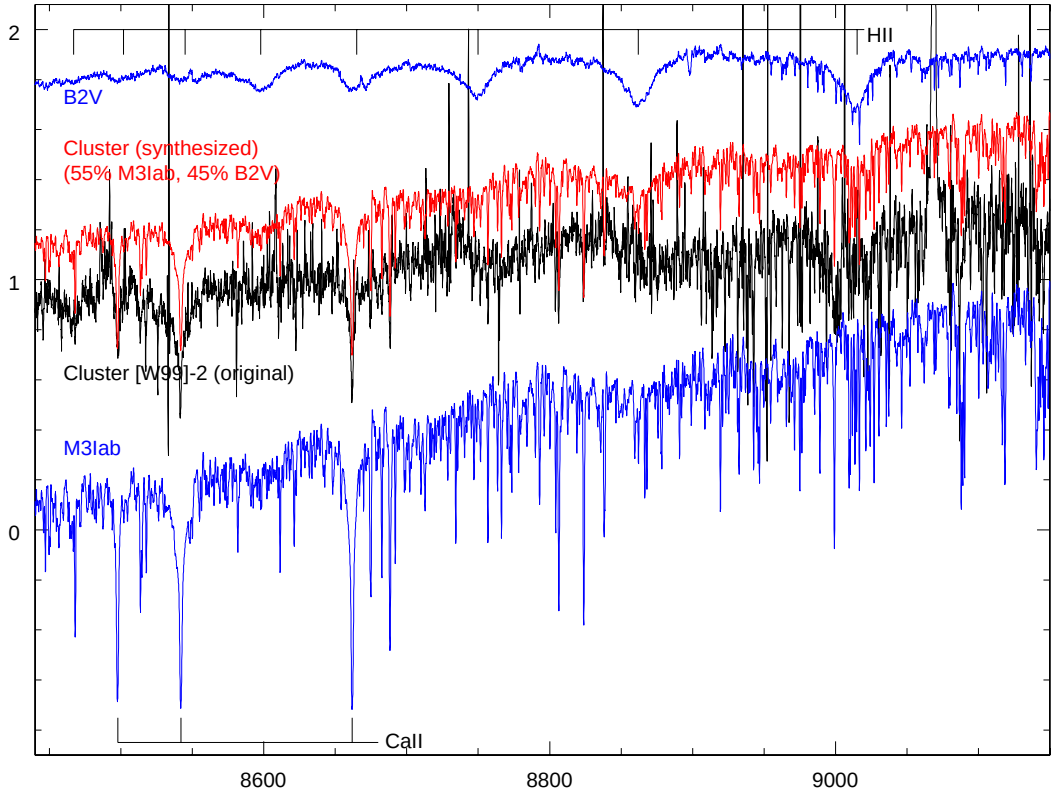

Fig. 5.24: The cluster spectrum observed with UVES (red part of the red arm) is displayed together with the spectrum of an M3Iab and a B2V star spectrum. A combination of both (in blue) simulates fairly well the cluster spectrum (black). The synthesized spectrum reproduces much better than the M3Iab star alone the slope of the continuum and the depth of the absorption features which are characteristic for the supergiant spectrum. Indicated are the locations of the CaT absorption lines, and also those of the Paschen lines, which are the dominating features in the B2V spectrum.

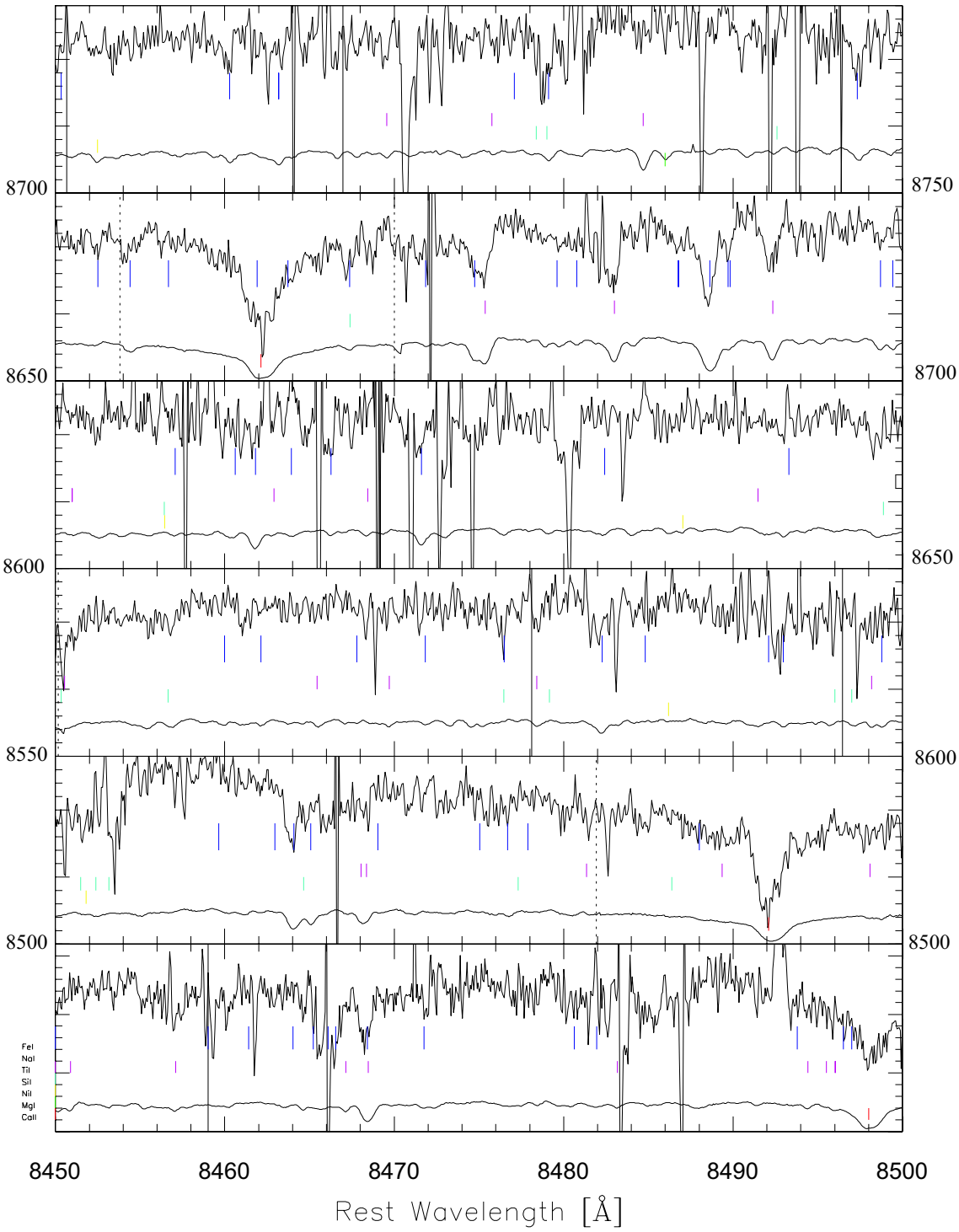
8700
8750
8650
8700
8600
8650
8550
8600
8500
8500
FeI
NaI
TiI
SiI
NiI
MgI
CaII
8450
8460
8470
8480
8490
8500
Rest Wavelength [Å]

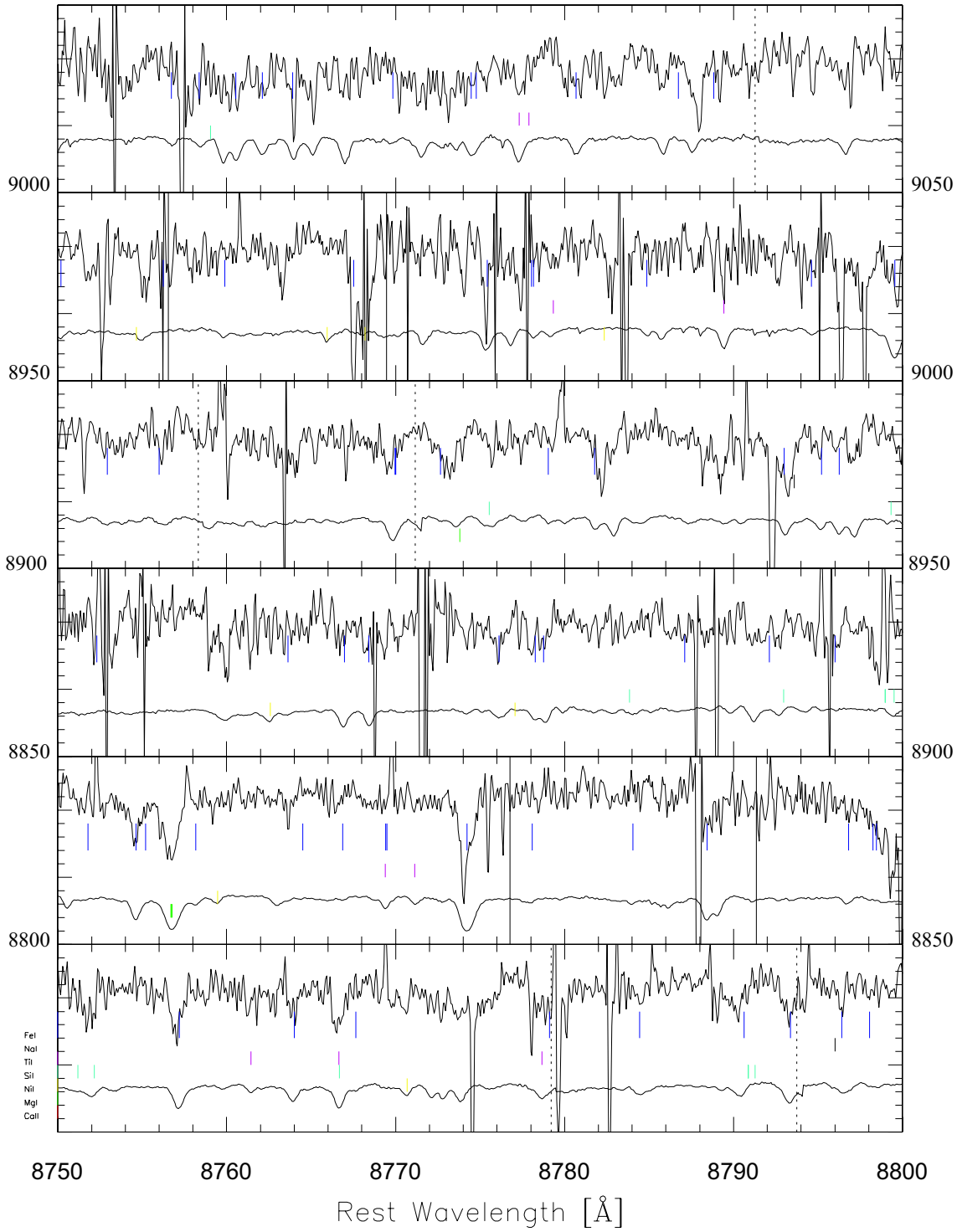

Fig. 5.25: The W99-1 cluster spectrum observed with UVES (red part of the red arm) is displayed for rest wavelengths between 8450 and 9050 Å. Spectral segments of 50 Å length were stacked in consecutive vertical panels, starting with the range 8450-8500 Å at the bottom and ending with the part 8700-8750 Å at the top. The second page displays spectral ranges 8750-8800 Å through 9000-9050 Å. For comparison, the spectrum of an M3Iab star is also shown below the cluster spectrum in each panel. Absorption lines are indicated by short vertical lines. Different metals are identified by colours and vertical positions. The vertical lines covering the whole panel indicate order borders in the echelle spectrum, where artifacts might show up. Solid vertical lines indicate the locations for the cluster spectrum, which was shifted to rest wavelength, dashed vertical lines apply to the stellar spectrum. An analysis of the MgI absorption feature at 8806 Å yielded solar metallicity for this cluster.

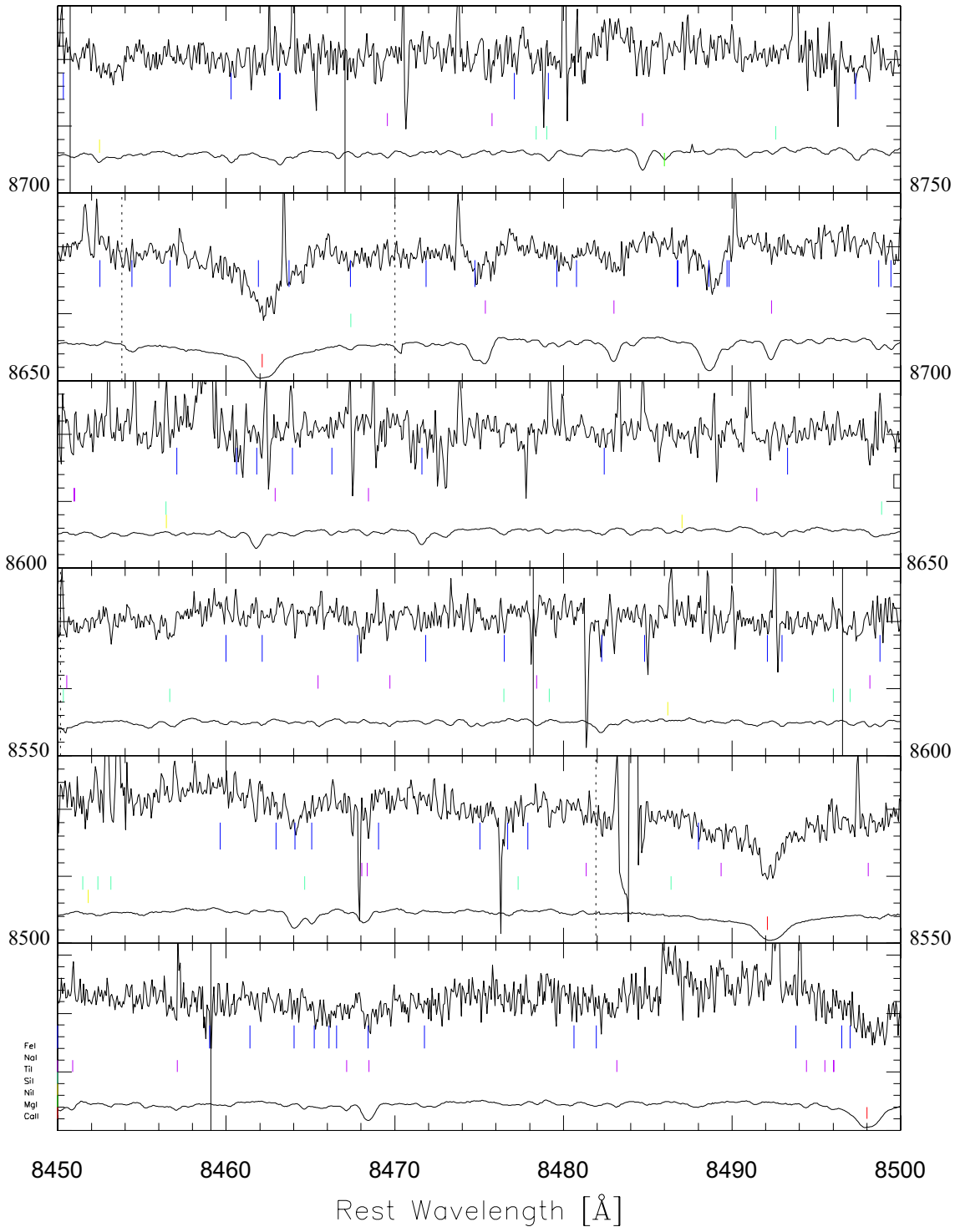
8700
8750
8650
8700
8600
8650
8550
8600
8500
8550
FeI
NaI
TiI
SiI
NiI
MgI
CaII
8450
8460
8470
8480
8490
8500
Rest Wavelength [Å]

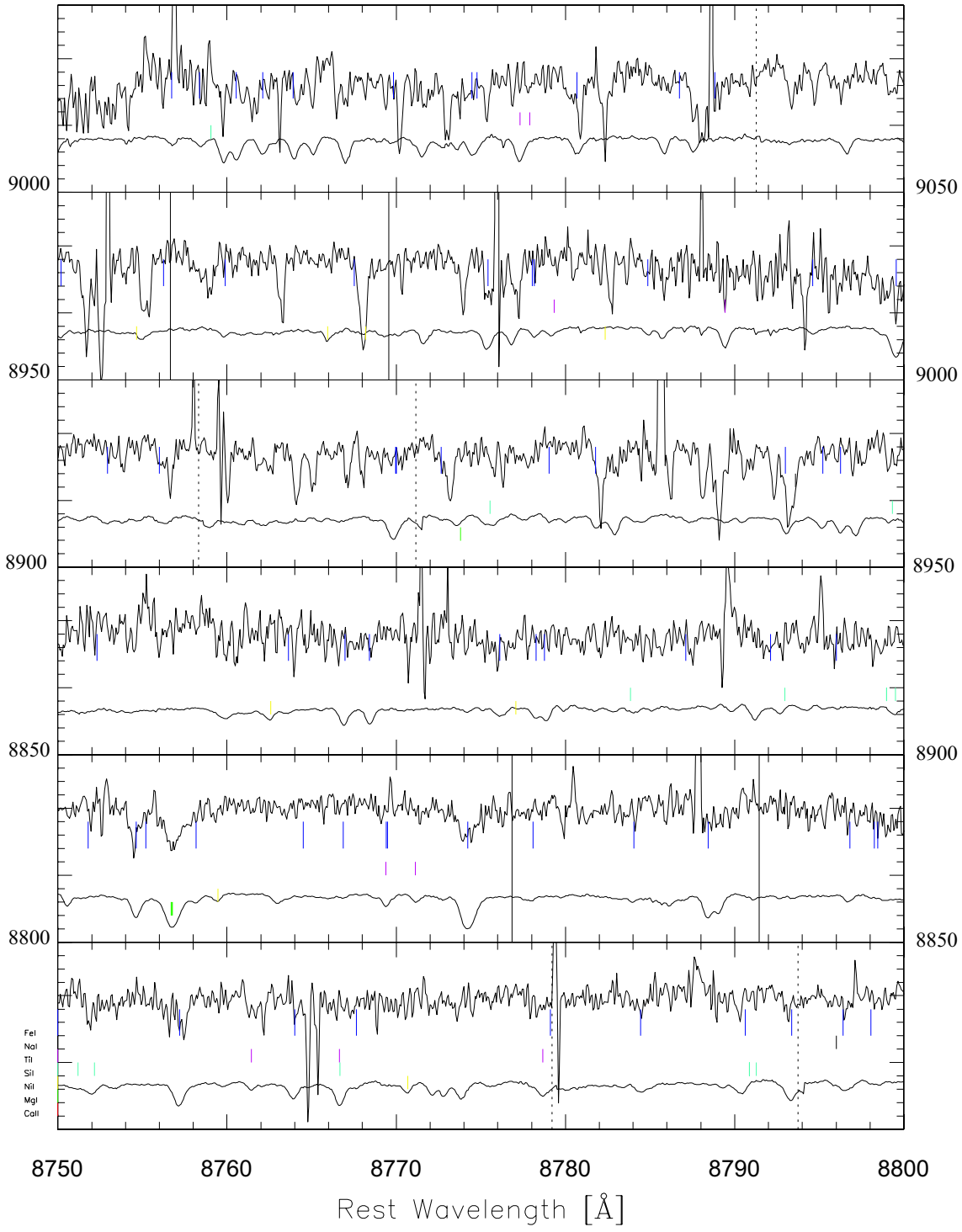

Fig. 5.26: The W99-2 cluster spectrum observed with UVES (red part of the red arm) is displayed for rest wavelengths between 8450 and 9050 Å. Spectral segments of 50 Å length were stacked in consecutive vertical panels, starting with the range 8450-8500 Å at the bottom and ending with the part 9000-9050 Å at the top. For comparison, the spectrum of an M3Iab star is also shown below the cluster spectrum in each panel. Absorption lines are indicated by short vertical lines. Different metals are identified by colours and vertical positions. An analysis of the MgI absorption feature at 8806 Å yielded supersolar metallicity for this cluster. The vertical lines covering the whole panel indicate order borders in the echelle spectrum, where artificial features might show up. Solid vertical lines indicate the locations for the cluster spectrum, which was shifted to rest wavelength, dashed vertical lines apply to the stellar spectrum.

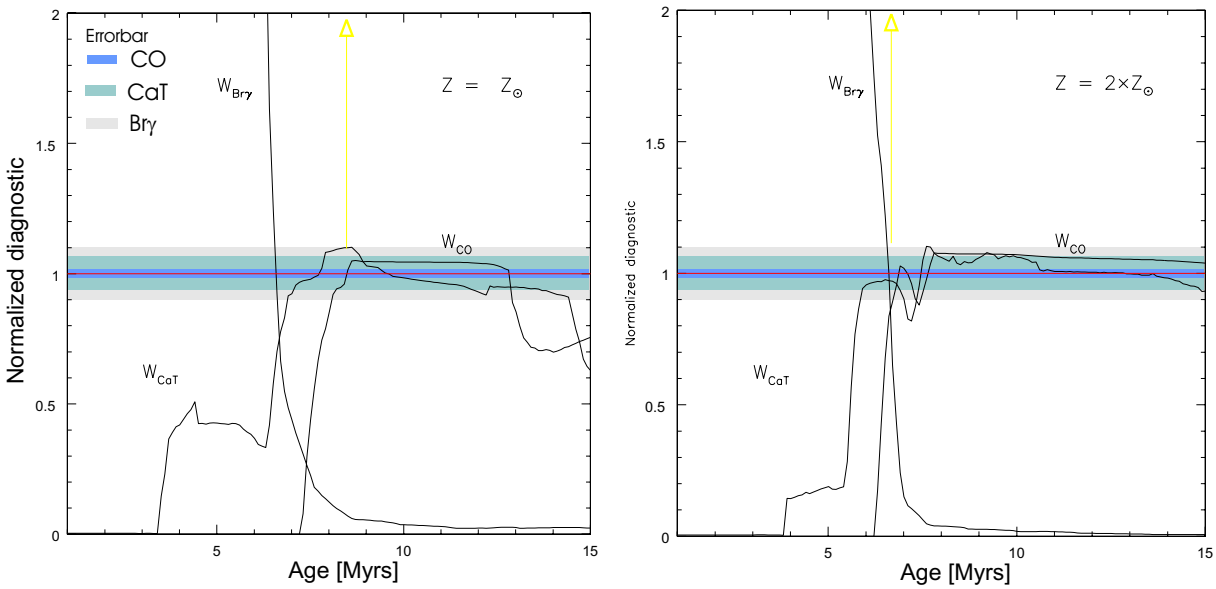

Fig. 5.27: Age determination of [W99]-2 using the three diagnostic features $W_{Br\gamma}$, W_{CO} and W_{CaT}. The measured values of 10 Å, 16.1 Å and 8.3 Å were used to normalize the y-axis of these diagrams. The assumption of solar metallicity does not provide a common age for the three diagnostics (W_{CO} was given the largest weight to derive an age of 8.1 Myrs). In the second case of Z = 2 $Z_\odot$, all diagnostic lines cross within the uncertainties at an age of 6.6 Myrs.

5.4.5 Metallicity in NGC 4038/39

In previous chapters, it was argued that it is sensible to assume solar metallicity for the young star cluster environments. The UVES spectra provide the possibility to determine the abundances of several elements, at least of Mg and Fe. See Figures 5.25 and 5.26 for a large part of the spectrum located on the chip covering the red part in the red arm of UVES.

Díaz et al. (1989) give an empirical calibration for the relation of the equivalent width of MgIλ8806Å (W_{MgI}) with metallicity. This feature was analyzed in all our UVES cluster spectra. While for cluster [W99]-1, the value for W_{MgI} of 0.75 Å is compatible with solar abundances, the corresponding value of 1.2 Å for [W99]-2 suggests that this cluster is more metal-rich. The spread is fairly large in the plot shown in Díaz et al. (1989), therefore the statement is restricted to this qualitative description. But this finding implies another possible interpretation of the discrepancy mentioned in chapter 5.2.3. [W99]-2 was found to show considerable Brγ emission *and* CO absorption, which in the case of solar metallicity is inconceivable (see Figure 5.27). Several possible interpretations were given, including the low spatial resolution of the 3D data, the size of the cluster, the possibility that shocks are present, and model uncertainties. The value of W_{CO} was given larger weight in the age determination.

Supersolar metallicity provides another possible explanation, because the equivalent widths of both, the CaT and the CO absorption reach larger values at earlier ages. Figure 5.27 shows the much better agreement of the three (normalized by the measured values) diagnostics in the case of Z = 2 $Z_\odot$. The revised cluster age then becomes 6.6 Myrs instead of 8.1 Myrs.

Only these two measurements are currently available, and no other measurements of abundances in the Antennae are published. Therefore it is unclear how many of the clusters might have supersolar or solar metallicities, or if a metallicity gradient exists.

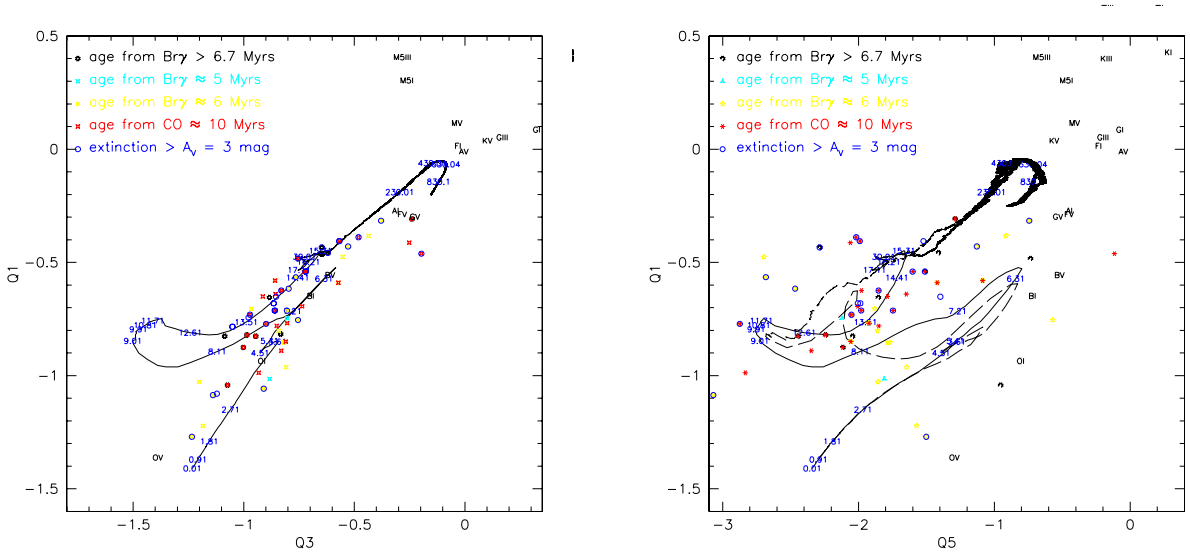

Fig. 5.28: Q-parameters Q1 = (U-B)-0.72*(B-V), Q3 = (U-B)-0.45*(V-I), Q5 = (U-B)-1.8*(J-K) for clusters selected by the criteria mentioned in the figures. They are compared with the evolutionary tracks predicted by Starburst99 (solid line: solar metallicity, dashed : Z = 2 x $Z_{\odot}$. Otherwise instantaneous burst, Salpeter IMF between 1 and 100 $M_{\odot}$). Additional line emission of Hα and Hβ was taken into account in the V filter, Brγ in K and Paβ in J. The approximate locations of various stellar types are indicated for comparison. While, in general, most clusters are located in the younger part of the evolutionary track, and some clusters are correctly placed considering their independently determined ages, even in the presence of extinction, there are also several clusters which are completely misplaced. Note for example the cluster with a Brγ-determined age of 5 Myrs, which from Q-parameters would be assigned an age of 13 Myrs. Some of these difficulties might arise from limited spatial resolution in the K-band, which leads to spectra synthesized from clusters of different ages. This is probably the explanation for discrepancies in the age determinations from Brγ and CO, visible here as overlays of red and yellow stars (see the legend for the corresponding shapes).

5.5 HST archival data

In 1999, HST was used to observe NGC 4038/4039 in UBVI broadbands and Hα narrowband for Whitmore et al. The single integrations were observed in different dithering positions to increase the spatial resolution. In section 3.2, their main results were summarized.

The data set was retrieved from the archive and reduced in a standard way by using the IRAF package. The results will here be used to determine

- the otpical magnitudes and colours of the clusters (U, B, V, R, I) and the Hα fluxes. From the colours, the extinction free Q-parameters (see following section) are determined. This is performed on both, the original images and those resampled to SOFI resolution. The Hα image is used for the determination of the extinction in comparison with the Brγ-image.

- the effective radii from the dithered images.

Colour excess E(λ1-λ2)	value [mag]
E(U-B)	0.22
E(B-V)	0.33
E(V-I)	0.52
E(J-K)	0.17

Tab. 5.8: Extinction at various wavelengths, according to the Mathis (1990) extinction law.

The Q parameter

One way to describe extinction (see also chapter 5.2) is via the *colour excess*. It is the difference in magnitude between the observed and the intrinsic colours of the object:
If the spectral dependence of the extinction, the *extinction law*, is known, the colour excess caused by extinction in one band can be compensated by the combination with a scaled different colour. Mathis (1990) gives an extinction law, and the following table is computed from his formula:
For an observed colour with intrinsic colour $(U\text{-}B)_0$, reddened by E(U-B) and a second colour $(B\text{-}V)_0$, reddened by E(B-V), a colour combination can be constructed (see, e.g., Binney & Merrifield (1998)) by setting

$$Q1 = (U-B) - \frac{E(U-B)}{E(B-V)} * (B-V) \tag{5.5}$$

$$Q1 = (U-B)_0 - E(U-B) - \frac{E(U-B)}{E(B-V)} * ((B-V)_0 + E(B-V)) \tag{5.6}$$

$$Q1 = (U-B)_0 - \frac{(U-B)}{E(B-V)_0} = Q1_0 \tag{5.7}$$

In this manner the following parameters were constructed:

Q1 = (U-B) - 0.68 (B-V)
Q2 = (B-V) - 0.63 (V-I)
Q3 = (U-B) - 0.43 (V-I)
Q4 = (U-B) - 1.12 (I-J)
Q5 = (U-B) - 1.31 (J-K)

Concerning the evolution of the Q parameters with cluster age and the possibility to discriminate between different ages, the combinations of Q1/Q3 and Q1/Q5 served best, therefore they are reproduced in Figure 5.28.

Effective radii

The images of many of the young star clusters in the Antennae taken with HST were marginally- to well-resolved. Whitmore et al. (1999) determined their effective radii using two different methods. Given the pixel sizes of the HST chips ($0\farcs101$/pix for the Wide Field Camera arrays and $0\farcs045$/pix for the Planetary Camera array), and the distance to NGC 4038/39 (implies 93 pc/arcsec), dithering the image can improve the spatial resolution by a factor of 2. Dithering in this context means that two sets of observations were performed with an uneven multiple of half a pixel offset between the two observations. This makes it possible to coadd the two sets in a frame with twice the original number of pixels in each dimension. For one of the two methods, Whitmore et al. did not use the dithered combined images, but made independent estimates of the radii for

each of the observing blocks and then averaged the results, for the second technique they used the dithered combined image. Their main aim was to determine the average radii of the clusters and to compare them to those observed in other galaxies, both to the young clusters in other mergers, where they observe comparable radii (mean R_{eff} in the Antennae is R_{eff}=4pc). Compared to those of globular clusters, these are large - the typical value for old GCs in the Milky Way is $R_{eff} \approx$ 3pc (Djorgovski, 1993).
The other purpose of determining the effective radii was to separate the stars from globular clusters, because bright single stars in the Antennae considerably contaminate the luminosity function at the faint end (below m_V ~23.5) They observed a population of faint objects with R_{eff}~2pc, which they expected to consist mainly of stars, also considering their colours. They excluded those from the further analysis of the clusters and subtracted the systematic offset of 2pc from the radii determined for the clusters (the above quoted typical R_{eff} of 4pc already took this offset into account. However, they do not list in their table in W99 the values for R_{eff} of the clusters.
For our analysis the effective radii are important for another purpose: The spatial dimensions of the clusters are a critical parameter for the determination of the dynamical mass. In priciple, also the spatial profile of the light/mass distribution is important, but difficult to obtain for clusters which are only slightly resolved. However, we fitted different cluster profiles to the observed light distribution and determined the best fitting distribution. Brad Whitmore was so kind to provide us with their estimates of the effective radii (Whitmore, 2000) for the clusters we observed with ISAAC and UVES, but we wanted to determine the cluster profile and get an independent measurement of the radii, also to get a better feeling for the uncertainties involved in fitting the light profile.
For this analysis we used the *ishape* routine described by Larsen (1999) implemented in the BAOLAB data reduction package developed by Larsen. The *ishape* routine works better than usual deconvolution routines at determining the sizes of slightly extended objects. It convolves the user provided PSF with the given cluster profile and determines the minimum χ^2 for a range of sizes using a simplex downhill algorithm to find the minimum. Cluster profiles that can be selected include Gaussian, King profiles (King, 1966) of several concentration parameters and Moffat profiles of two different concentrations. One output of the fit includes the FWHM of the profile, which for our applications needs to be converted to r_{hp}, with the conversion factors varying from profile to profile. Another output is the reduced χ^2, the absolute value of which is of significance if the noise levels were provided realistically. But even if not, the relative levels of χ^2, together with the visual inspection of the fit, allow an evaluation of the quality of the fit. This visual inspection was performed on the fits images produced by the *ishape* package, which include the artificial cluster image, the original input image, the residuals between original and fit and the weights applied to each pixel. The weighting procedure has the advantage that the code rejects outliers in the radial distribution of the cluster profile, thereby excluding, for example, neighbouring stars.
In Figure 5.29 these fits are displayed for one of the clusters. The fit is for cluster [W99]2, which was observed with both, ISAAC and UVES. Table 5.9 summarizes the results for all clusters with high resolution spectroscopy. In general, we observe that the clusters are not very well described by gaussian profiles and that a King model provides a better fit. However, the determined r_{hp} depended only weakly on the assumed concentration parameter of the profile, and a King 15 or King 30 model usually fitted best.

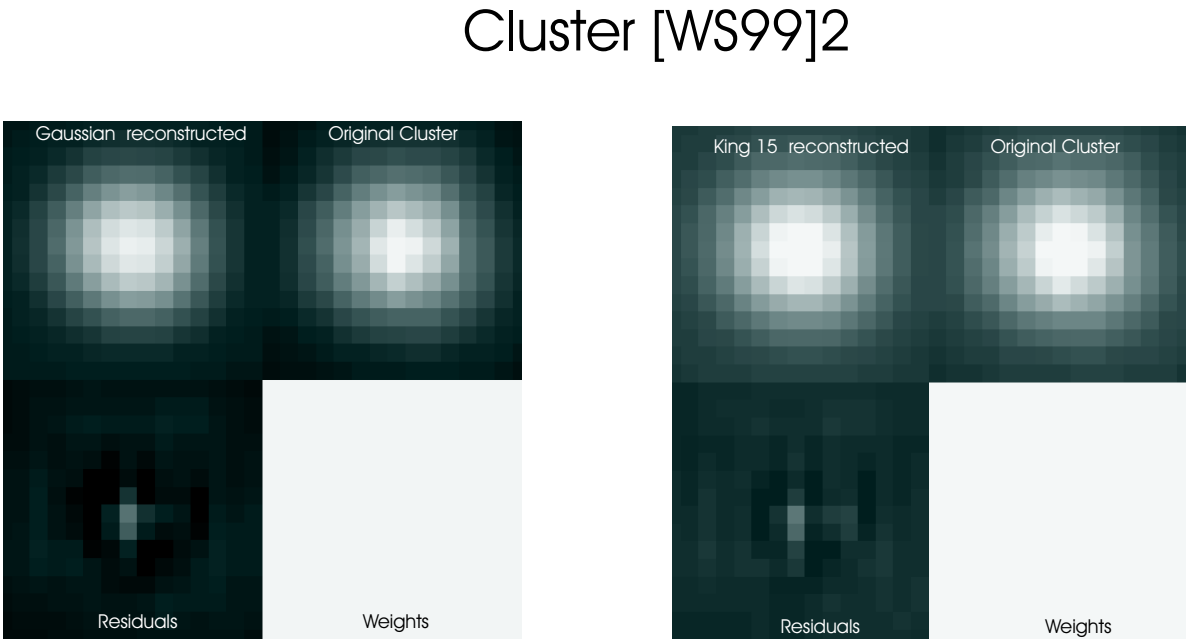

Fig. 5.29: Determination of the best fitting cluster profile of cluster [W99]-2. King profiles yield the lowest residuals and resemble most closely the original cluster profile, determined on the upper right of each panel. The effective radius determined from the fits is $R_{\rm eff}$=4.5pc. Given the intensity scales, it is difficult to demonstrate at the same time the resemblance of original and fit, and show the differences between the two fitting techniques in the residuals. But it can be detected that even though for the display of the King15 fit the intensity level is higher, the residuals are lower or comparable to the Gaussian fit, and more homogeneous (there is a low intensity ring around the peak in the residuals for the Gaussian fit which is not there for the King15 fit).

Cluster [W99]-2						
Model	FWHM [pix]	r_{hp} [pix]	r_{hp} [arcsec]	r_{hp} [pc]	χ^2_ν	Comment
Gauss	3.85	1.93	0.048	4.48	2.82	
King 5	2.68	1.90	0.048	4.42	2.07	
King 15	1.77	1.95	0.049	4.53	1.40	
King 30	1.45	2.15	0.054	4.99	1.29	
King 100	1.26	3.23	0.081	7.50	1.23	
Moffat 15	2.10	2.37	0.059	5.52	1.46	
Moffat 25	2.89	1.92	0.048	4.47	1.90	
Star						
Gauss	0.03	0.015	3.75E-4	0.035		
Cluster [WS95]-430						
Gauss	3.19	1.60	0.040	3.70	8.28	
King 5	2.15	1.53	0.034	3.19	7.27	
King 15	1.28	1.41	0.035	3.27	6.55	
King 30	0.97	1.43	0.036	3.34	6.75	
King 100	0.66	1.68	0.042	3.92	7.44	
Moffat 15	1.51	1.70	0.043	3.97	6.41	
Moffat 25	2.27	1.54	0.039	3.59	6.62	

Tab. 5.9: The effective radii of several clusters was determined by convolving the PSF with different cluster profiles. For the King models and the Moffat profiles, the numbers indicate different concentration parameters. They also determine the conversion factor to go from FWHM to r_{hp} and are 0.5, 0.71, 1.1, 1.48, 2.56, 1.13 and 0.68 for the profiles as listed.

6. SUMMARY

Merger induced star formation in NGC 4038/4039 was investigated using different types of observations, most of which were performed in the near infrared wavelength regime, due to the high extinction in parts of the galaxies. Using broad- and narrow band imaging of the whole merger and NIR integral field spectroscopy of a few selected regions, ages and extinction were determined using evolutionary synthesis models.

The striking result is that all of the detected star clusters are young, below 15 Myrs old. The youngest clusters (~ 5 Myrs) are found in the region where the two disks apparently overlap, whereas those located in the northern galaxy, espectially in the loop of star clusters towards the north-west, cluster ages are around 10 Myrs average. This timing of the burst refutes the currently believed scenario that star formation in the Antennae was triggered by the collision of the two disks during pericenter and subsequent shock waves travelling through the ISM. Models suggest that the "overlap region" is actually a bridge between NGC 4038 and 4039, and that the two galaxies are separating currently. It is a state during the merging process at which the gravitational self response of the two disks can lead to gas density enhancements accompanied by star formation.

The star formation rate was estimated based on the photometric data in combination with the ages. The total stellar mass produced in the clusters is around 1×10^8 $M_\odot$, almost all of it during the last 10 Myrs.

Only the two nuclei show an older star forming region. In both of them, star formation started 100 Myrs ago and decayed exponentially with a timescale of ~ 20 Myrs. The total mass converted to stars in the two nuclei is $\sim 8 \times 10^8$ $M_\odot$. A star formation rate of less than 20 $M_\odot$/yr makes the Antennae a mild starburster.

In order to be model independent with respect to the cluster mass estimates, high resolution spectroscopy of stellar absorption features was performed. The stellar velocity dispersions in combination with cluster size estimates yielded dynamical masses for a few clusters. The agreement between those and the model dependent photometric mass estimate varied, indicating the existence of differences in the content of low mass stars. Two of the observed four clusters host a large number of low mass stars and are therefore likely to survive the future evolution of the merger. One of the clusters seems to be deficient in low mass stars, which might, even though all the clusters are probably currently gravitationally bound, eventually lead to the disruption of the cluster. Based on the small sample it is not possible to draw conclusions on the survival of the cluster population as a whole.

But this leads the way into further investigations of the topic. Dynamical masses of a larger sample of star clusters, also including fainter ones, would allow to statistically explore the variations in the initial mass function and the cluster mass function. Only then can firmer conclusions be drawn concerning the fate of the young star clusters and their prospects to evolve into a part of the globular cluster system of an elliptical galaxy.

The star cluster ages suggest that the Antennae system was caught in a special moment of their evolution, with increased star formation throughout the two galaxies which lasts for only ~ 20 Myrs. However, short bursts of star formation have also been witnessed in other starbursters, and the question arises whether this characteristic star formation mode it is coupled to the production of star clusters, and what environmental conditions are necessary for that. Several mergers or interacting galaxies are known to host star clusters, and they and similar type objects could be explored.

Part II

THE SPIFFI NEAR INFRARED INTEGRAL FIELD SPECTROMETER

7. SPIFFI

The SPIFFI (**Sp**ectrometer for **I**nfrared **F**aint **F**ield **I**maging) near infrared integral field spectrometer will, together with the dedicated adaptive optics system MACAO (**M**ultiple **A**pplication **C**urvature **A**daptive **O**ptics), form SINFONI and be mounted to the VLT-UT4 telescope in mid-2002. It will allow diffration limited NIR integral field spectroscopy at an 8m-class telescope, and the future implementation of a laser guide star will make large regions of the sky accessible to these diffraction limited observations.
SPIFFI (Tecza, 1999) is the successor of the successful MPE-3D (Weitzel et al., 1996) integral field near infrared spectrometer. 3D has been built by MPE, started operation in 93 and is still in use. With 3D it is possible to obtain low resolution spectra ($R = \lambda/\Delta\lambda = 1000 - 2000$) of each pixel in a 16 x 16 pixel field of view (FOV) in a single integration. The spatial pixel size is between $0\farcs2$ and $0\farcs5$. Imaging a three-dimensional data set onto a two-dimensional detector is realized by placing a mirror image slicer into the focal plane of the instrument. It slices the image into strips, which are reflected at different angles onto a second set of mirrors. The purpose of the second set of mirrors is to rearrange the strips to form a long slit, which is then fed to a quasi-standard spectrograph.
Integral field spectroscopy observations are most useful for observations of extended sources, where spectral information is required for each pixel in the field of view. 3D was for example used to study the dynamics of galactic nuclei, the shocks in the star forming regions in Orion and the properties of Seyfert galaxies. Certainly the most obvious advantage of integral field observations over standard scanning techniques (like long slit spectroscopy or Fabry-Perot imaging) is the increase in observing efficiency which reduces the necessary amount of precious observing time. But there are also other advantages, related to variable observing conditions: Especially in the NIR, sky emission and atmospheric transparency vary on very short timescales, and the atmospheric seeing or the point spread function (PSF) provided by an adaptive optics (AO) system is usually not stable during observations. The conversion of the two-dimensional scan data sets into three-dimensional data cubes (by scanning a long slit across an object or scanning through a wavelength range for Fabry-Perot imaging) suffers from these varying conditions. For integral field observations, these conditions still vary, but since they affect the whole data cube simultaneously, they do not introduce inhomogeneities.
The advance in NIR detector technology, which now provides arrays of 1024 x 1024 pixels, drove the need for a new integral field spectrograph with a higher spectral *and* spatial resolution. Therefore SPIFFI was designed, with the plan to use it in combination with an adaptive optics system at an 8m telescope, to allow diffraction limited spectroscopy with very high spatial resolution. Spectral resolution was increased to $R = \lambda/\Delta\lambda = 4500$ for some observing modes to allow avoidance of the OH night sky line emission.
The observable wavelength range is 1.0 μm to 2.5 μm. The explicit inclusion of the thermal part of the K-band requires cooling to liquid nitrogen temperature (77 K). As a further improvement over 3D, SPIFFI is supposed to have a cooled integral field unit.
These are the main design goals, and the next sections will explain what they imply.

7.1 Concept of the SPIFFI spectrometer

SPIFFI being an imaging spectrometer, requires an element in the focal plane which allows to convert three-dimensional information (x, y, λ) into a two-dimensional plane which can be imaged onto the detector. This device is often referred to as the Integral Field Unit (IFU).

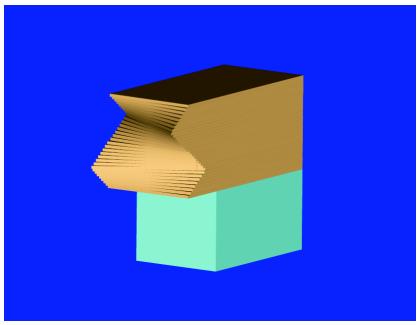

Fig. 7.1: CAD 3D view of the SPIFFI small image slicer.

The introduction briefly described the 3D IFU, two sets of plane mirror segments. Even though this concept worked very successfully in 3D, SPIFFI was first designed to incorporate an IFU consisting of an hexagonal array of flared silica fibres. This was deemed necessary for two reasons: First, because SPIFFI was supposed to be a travelling instrument, and a simple up-scaling of 3D would have resulted in a slit length of 40 cm and a correspondingly large cryostat. Second, it was not clear how the mirror slicer would react to repeated cooldowns. It was suspected that temperature variations, accompanied by differences in expansions (though very small for Zerodur) might cause the IFU to disintegrate. However, unexpected delays in the fabrication of the fibres caused a revival of the 3D concept as the "heart" of SPIFFI. Earlier concerns were solved: Forming SINFONI together with the adaptive optics system MACAO, the spectrograph has a permanent home and size and weight constraints are less tight. Nevertheless it is an advantage that by slight modifications of the slicer geometry it was possible to reduce the slit size to ∼30 cm. And finally some cooldown tests have been performed on mirror slicer test pieces, which did not show any sensitivity to even very rapid cooldowns (dumping in LN_2).

So the IFU of SPIFFI is a mirror image slicer. A drawing of the small slicer can be seen in Figure 7.1. It consists of a stack of 32 plane mirrors and is placed in the focal plane of the telescope (or rather of the adaptive optics system MACAO), reflecting the incoming light in strips into different angles onto another set of plane mirrors. The second set of mirrors serves to redirect the light to form a quasi long slit. This is then fed to an almost standard spectrograph, which disperses the light perpendicular to the slit. After passing through the collimator, reflection grating and camera, the light hits the detector, with the spatial dimension along one axis of the two-dimensional detector, the spectral dimension along the other axis. A schematic of the working principle of a mirror slicer is given in Figure 7.2. The 3D slicer is shown here, because it is easier to demonstrate the principle. The SPIFFI slicer will have a symmectric layout mirrored around the optical axis from the telescope, and the tilt angles will result in a brickwall- rather than a staircase pattern.

The detector that will be used in SPIFFI is a 1024^2 HAWAII HgCdTe detector array from Rockwell (Hodapp et al., 1996). Its layer of HgCdTe detects photons in the wavelength range between 0.8μm and 2.5μm. The foreseen working temperature is that of liquid nitrogen, 77K, which allows the use of a bath cryostat as the cooling device. At this temperature, the dark current is 0.1 e^-/s, and the readout noise is 8 e^-/(double correlated read).

The detector dimensions dictate the number of spatial pixels, 1024, which can be covered by the FOV. They are arranged in a 32 x 32 pixels square. The according 1024 spectral pixel covered for each spatial pixel are

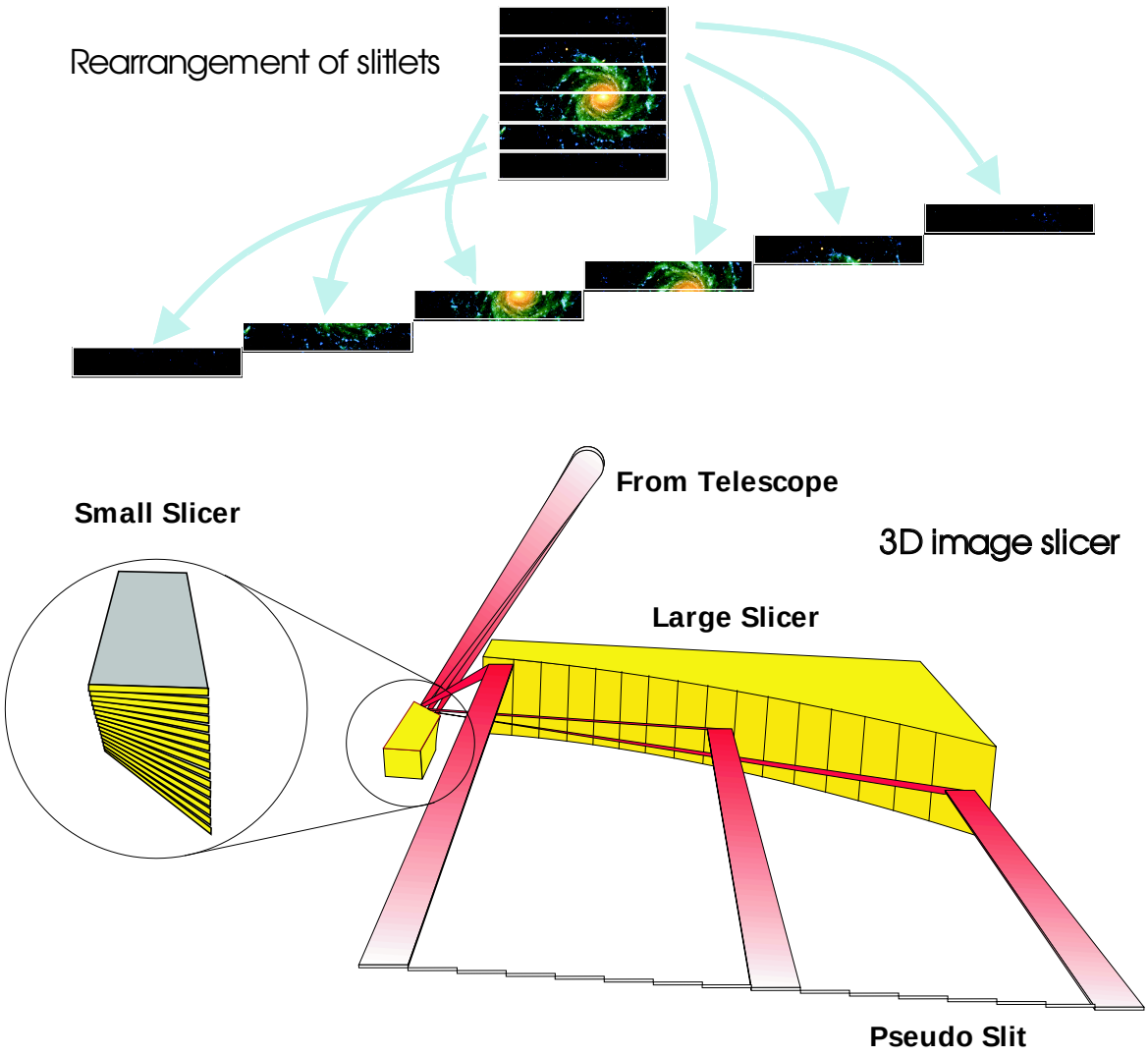

Fig. 7.2: This schematic explains the working principle of the SPIFFI mirror image slicer. The small slicer sits in the focal plane of the telescope and slices the 2-d area into 32 strips of 32 pixels each. Via the second set of mirrors, the strips are redirected to form a long slit, which is then dispersed by the grating in the spectrograph.

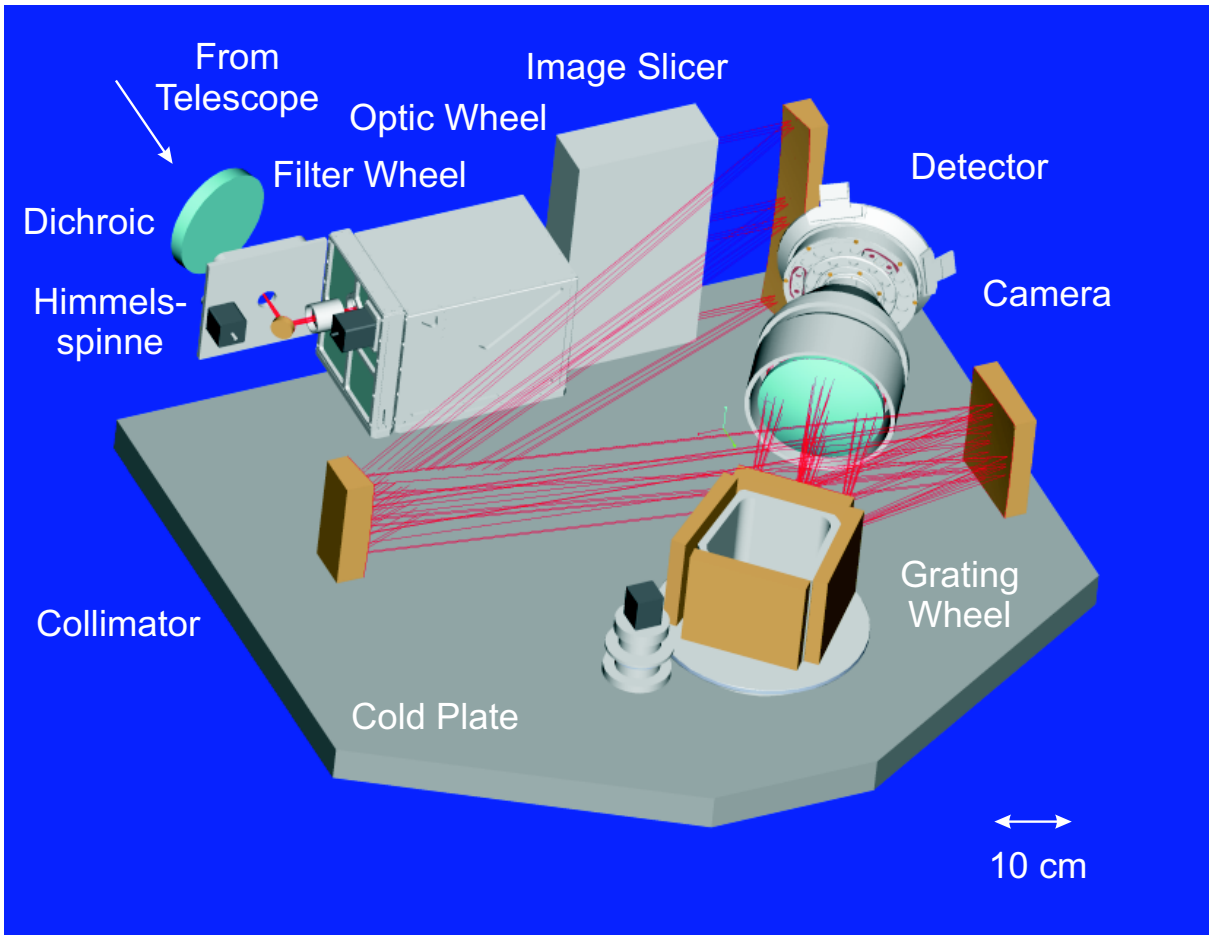

Fig. 7.3: 3d-layout of the SPIFFI instrument, with the components labelled.

required to deliver a spectral resolution of R $= \lambda/\Delta\lambda \approx 4500$ in order to allow OH avoidance (see chapter 10.2). This means that either of the three astronomical bands J, H and K can be covered in one integration. There is also a low resolution grating with R $= \lambda/\Delta\lambda \approx 2200$, which covers H and K band simultaneously. It should be noted that the spectra with this layout are not Nyquist sampled. That is achieved by interleaving two subsequent integrations, which were offset by half a pixel in the spectral domain, a technique which is also used in 3D and requires very fine-tuned movements of the reflection gratings.
The physical size of one detector pixel is 18.5μm, which leads to a total detector area of 1.9×1.9 cm. The area on the sky that is covered by the detector can be selected according to the source and to the observing conditions. In the cases where the AO cannot be used or is not wanted, two seeing limited pixel scales can be selected, 0.″25 or 0.″1 per pixel. The physical size of the detector set the maximum pixel scale in seeing mode, because it determines the design parameters for the camera. Going to the very limit of feasibility, the large pixel scale of 0.″25 could be realized.
For the AO case a pixel scale of 0.″025 is foreseen, which Nyquist samples the diffraction limit of an 8m telescope.
Figure 7.3 shows the three-dimensional layout of the instrument, with labels indicating the components.
One additional feature of SPIFFI is the so-called "Himmelsspinne" (sky spider). Its purpose is the imaging of a region of blank sky onto a corner of the detector during the source observations. This avoids the necessity to interleave object and sky observations with frequencies of a few minutes. Integration times of the order of half an hour would become possible, which is desired in the context of observing efficiency. However, this places tight tolerances on image motions introduced by e.g. flexures in the system. The total image motion within two subsequent integrations are required to amount to no more than a small fraction of a pixel, which is more difficult to achieve for longer integration times. The constraints on image motion are higher in case of the SPIFFI observations, because the interleaving of two subsequent integrations relies on a stable positioning of the object. An image drift between two spectrally dithered frames will introduce spectral ripples in the interleaved data set.

7.2 Technical specifications

Going along the light path, light enters SPIFFI through the dichroic entrance window, which is also part of the MACAO optics and reflects optical light towards the wavefront sensor. The focal plane delivered by MACAO hosts the "Himmelsspinne". It allows the selection of one of three sky positions up to 1′ away from the target. This should make it possible to find a field of blank sky for every object exept very extended ones. The filter wheel has sets of bandpass filters tuned to match the gratings: J, H, K and H+K.
The pre-optics, labelled "Optic Wheel" in Figure 7.3, allows the selection of pixel scale, either seeing limited (moderate or good seeing, corresponding to pixel sizes of 0.″25 and 0.″1) or diffraction limited, as it is delivered when adaptive optics is in use. For an 8m telescope, the pixel size of 0.″025 Nyquist samples the diffraction limited PSF. In addition to these three scale changers the pre-optics wheel includes a pupil imager. It images the telescope pupil onto the detector and thus allows for fine adjustment of the pupil alignment. Mounted in the pupil plane at the entrance of the optic wheel is the cold aperture stop, common to all image scales.
The image slicing is performed right after the scale changer and consists of the small and the big mirror slicer, built from 32 slitlets each. The mirror slicer is fabricated from Zerodur, and the single elements are stacked by optical contacting. This means that the surfaces are polished to a very high surface flatness and then pressed together. Van-der-Waals forces firmly connect the pieces. It is virtually impossible to separate two joined pieces, unless it is possible to invoke an expansion of one piece with respect to the other. Both mirror stacks are mounted, again by optical contacting, to a common base plate, which prevents relative movements.
The collimator, consisting of three mirrors, collimates the light and directs it onto the grating. They sit on a wheel which holds four gratings, allowing for an on-the-fly selection of wavelength range. It is the rotation around this axis which is also used to accomplish the half-pixel shift which is required for the spectral Nyquist

Cassegrain Instrument	Adaptive Optics system	NGS and LGS	
Input focal ratio	F = 17.5		
Operating temperature	77K		
1024 spectra	32 × 32 image pixels		
Himmelsspinne	3 mirrors for imaging	at 15″, 30″, 45″from center	
	sky field onto detector	fraction of FOV covered 0%-50%	
	+ coronograph		
Pre-optics	Lenses	Spherical	BaF_2 and IRG2
	Cold stop	6mm diameter	
	Filter	Transmission (avg.)	
	J	78%	
	H	87%	
	K	80%	
	H&K	82%	
	Pixel scales	foreseen use	
	0.″025 pix^{-1}	AO scale	
	0.″1 pix^{-1}	good seeing conditions	
	0.″25 pix^{-1}	normal seeing conditions	
	Pupil imager	pupil alignment	
Mirror Slicer	Material	Zerodur, gold coated	optically contacted
	Two sets of mirrors	32 plane mirrors each	Tilted in two angles
	Thickness small	0.3mm	
	Slit length	307.2mm	
Collimator	Description	three mirror anastigmat	
	Mirrors	1 spherical, 2 off-axis prolate ellipticals	gold coated aluminium
	Focal length	2886.5mm	
Gratings	Material	lightweighted Al	directly ruled in Au
	Size	160 x 140 mm	
	Ruling	100 lines/mm	blazed
	Wavelengths	Resolutions	Efficiency (avg.)
	J : 1.10-1.40μm	R=4170	65%
	H : 1.45-1.85μm	R=4220	70%
	K : 1.95-2.45μm	R=4500	70%
	H&K : 1.45-2.45μm	R=2000	75%
Camera	Six lenses		
	Focal length	178mm	F-number 1.4
	Material	IRG2 and BaF_2	
Detector	HAWAII 1024^2 HgCdTe		
	Pixel size	18.5μm	
	Read noise	24 e^- (ramp sampling)	
	Dark current	0.011 $e^- s^{-1}$	
	Quantum Efficiency	65% average	

Tab. 7.1: Summary of SPIFFI technical specifications. See also Tecza (1999) or Eisenhauer et al. (2000) for a more detailed description.

sampling. Motor, gears and position encoder are chosen to deliver an angular resolution of $\sim 2''$, which is required for that purpose.
The camera, consisting of six lenses, focuses the dispersed light onto the detector. Its F-number of 1.4 is on the limit of what is technically feasible, because of the small variety of near infrared lens materials.
The detector will be used at 77 K, but in order to stabilize the temperature it will be controlled and, if necessary, heated.

8. THE CRYOSTAT

The cryostat is designed to keep all of SPIFFI's optical components at liquid nitrogen temperature in an evacuated housing. It will be an improvement over the 3D spectrograph to have the image slicer cooled down to 77K, too. Extensive testing of a rapid cooldown process (repeated dumping in liquid nitrogen) proved that the optical contact of the single slitlets survives this process.
The nitrogen reservoir contains the amount of LN_2 necessary to keep the cryostat cold for at least 24h, so that a refill once a day is sufficient, which is an important requirement by the staff at ESO-Paranal foreseen to operate SPIFFI in the future. The vacuum should stay at below 10^{-5} mbar for the whole length of a run ($\sim$ 3 weeks) without the necessity to pump at the telescope.
Furthermore, the cryostat represents the mechanical connection between the SPIFFI optics and the telescope/MACAO, and also between SPIFFI's own single components. This means that the total dimensions and weight of SPIFFI must not violate the constraints set by the available space or the maximum applicable torque at the Cassegrain flange of the telescope. During the movement of the telescope, the optical alignment of all the involved components with respect to each other must not degrade above a certain limit, and the temperature across the cold plate is supposed to stay constant, which is especially critical at the detector. All the movable parts are driven by cryogenic motors, in order to avoid mechanical feedthroughs.
Additional features are supposed to ensure the safe and easy handling of the dewar.
These specifications and constraints will now be discussed in some detail.

8.1 Mechanics

The cryostat should fulfill the following requirements:

8.1.1 Minimum cold volume: Diameter 1150 mm, height 450 mm

The diameter of the cold plate is set by the arrangement of the optical components on the cold plate. A foreseen upgrade to a 2048^2 detector array was taken into account, so that the upgrade can be performed by simply exchanging the camera and the detector, without having to rearrange everything on a new, bigger cold plate in a new cryostat.
The diameter of the cold plate is essentially set by the distances between the pre-optics/Himmelsspinne, the grating wheel and one of the collimator mirrors, respectively. The height of the cold volume is determined by the length of the slit, which is arranged vertically on the cold plate. It and the mirror directly after that have a height of $\approx$40cm.

8.1.2 Maximum outer dimensions: to fit in Cassegrain volume limits of the VLT

Certainly, SPIFFI and MACAO must fit in the space available at the Cassegrain flange. With the current design of MACAO, this is not a problem, because SPIFFI basically sits vertically underneath the telescope axis, with the cold plate parallel to it. However, the small amount of space available ruled out several other designs of the AO system, including some that had one mirror less, because the cryostat then would have collided with part of the mirror support structure (see Figure 8.1).

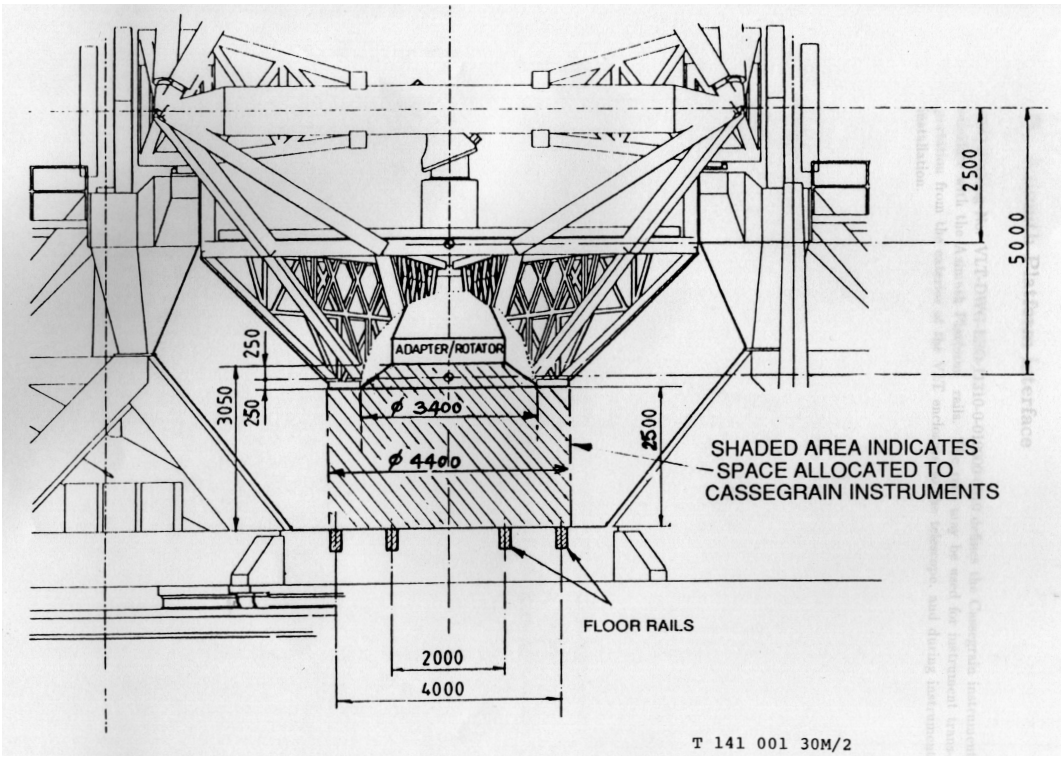

Fig. 8.1: Layout and dimensions of the Cassegrain instrument area available at the VLT telescopes. This drawing was extracted from the Document No. VLT-SPE-ESO-10000-0005, defining the VLT Observatory Requirements for Cassegrain Instruments.

8.1.3 Maximum distance outer dewar wall to focus inside SPIFFI: 131.2 mm

This constraint is imposed by the MACAO design and location, which places SPIFFI's entrance window almost directly vertically below the optical axis of the telescope. The outer wall of SPIFFI must not lie above the lowest part of the MACAO optics, which is the wavefront sensor module. The focus position provided by MACAO sits at a given distance, 131.2 mm, underneath the lower edge of the wavefront sensor. This limits the thickness of the dewar walls and constrains the location and orientation of the Himmelsspinne, the optical element in SPIFFI which sits at the focus position provided by MACAO.

8.1.4 Maximum weight: 500 kg

This specification had a large impact on the cryostat design, because it is not a trivial task to design a cryostat of these outer dimensions and the desired stability against flexure within this weight limit. The constraint is not initially a weight constraint, but rather is implied by the maximum torque that may be applied to the telescope by the weights attached to the Cassegrain adapter/rotator flange. The maximum torque around the altitude axis must not exceed 20 kN, and the torque around the Cassegrain rotator has a limit of 500 N. However, the latter specification can fairly easily be met by balancing the instrument and the electronic racks, but the first is the sum of the contributions of MACAO, SPIFFI and the electronic racks. SPIFFI has the largest distance (≈ 1.75m from SPIFFI center of gravity to the flange) and therefore contributes a large percentage of the total torque.

The first design presented by the manufacturer, using steel for the outer walls of the cryostat, was much too heavy. Including optics, the total weight would have been above 750kg. But even changing to aluminium and a cylindrical design for most of the parts did not bring down the weight considerably. It was necessary to completely change the concept of the mounting of both the cryostat to MACAO and of the cold plate to the outer wall of the dewar in order to decrease the weight significantly.

This new layout of the cryostat is displayed in Figure 8.2.

8.1.5 Flexure within limits

Tight constraints are placed on the flexures of the cryostat. This applies both to the housing, which represents the mechanical interface between MACAO and SPIFFI optics, and the mounting and internal stability of the cold plate. Special care has to be taken considering the stability of the dichroic entrance window during telescope movement and when ambient pressure changes during the night. This is critical, because the dichroic reflects the optical light (below $\sim 0.9\mu$m) towards the wavefront sensor to feed the AO system. Image motion introduced by movements of the dichroic is not compensated by the AO system. Therefore they must be limited to 0.2 pix/h, which corresponds to 0.3 mm/h at the location of the dichroic window. The first design would have violated this limit already with the expected changes of the ambient air pressure during the night, and also with the movement of the telescope, because the mounting of the cold plate to the bottom of the outer case introduced a torque at the location of the dichroic.

The new cryostat design avoids the problem by shifting the connection between cold structure and outer housing to the cylindrical part of the outer vessel. Moreover, the top plate of the housing is thicker now and has a rib structure on the outside, making it more rigid.

The cold plate, though very thick and rigid, could also be warped during pumping, when over the large diameter of the LN_2 reservoir a large pressure difference is built up. The positioning of the elements in all three dimensions has to be exact to withing 50μm to avoid a degradation of the image quality. Perpendicular to the cold plate, this is ensured by polishing the surface of the cold plate, or rather those parts of it which hold optical elements. Each of these "islands" has one sharp, accurate edge for the relative positioning in the plane of the cold plate. The angular accuracy (positioning accurate to within $1'$) is ensured by having two

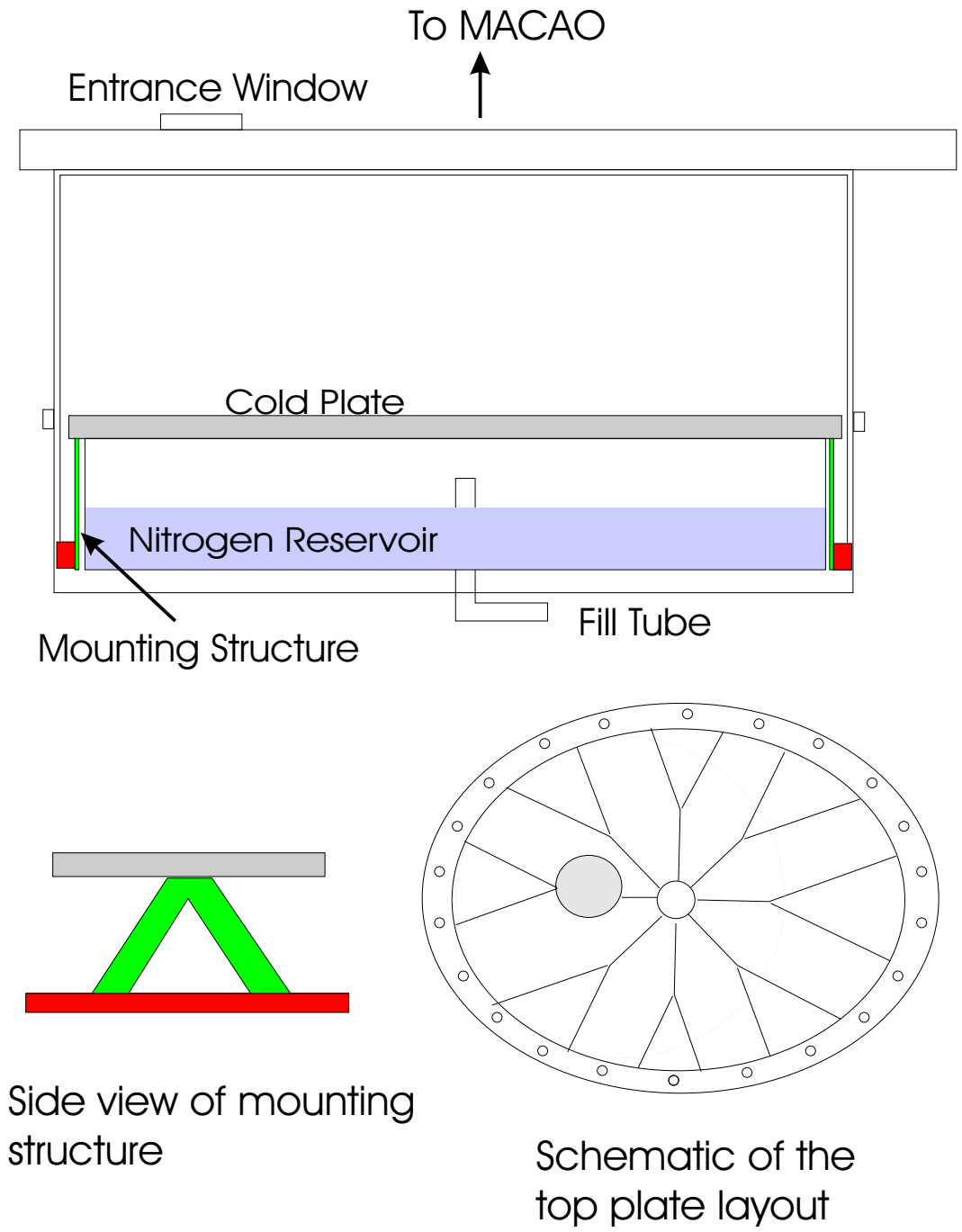

Fig. 8.2: The new layout of the cryostat with the weight within the limits ≈400 kg including optics). The design is cylindrical, and all parts except the bottom plate are Aluminium.

pins on each of the mounts of the element groups, and given their positioning accuracy and the length of the reference edges, the required tolerance can be fulfilled.

To avoid a warp of the cold plate away from the reservoir, which would exceed all of these tolerances, additional rings are placed inside the diameter of the tank, solidly connecting cold plate and bottom of the reservoir, which avoids warping. The additional functionality of this connection is the heat conduction it provides. When observations are performed at low zenith distances, probably during long periods within the night, The LN_2 rests at the bottom of the reservoir, away from the cold plate. In this case, the aluminium rings provide additional heat transport. They will have holes to allow the free flow of the liquid.

The cold structure is mounted to the outer, warm parts of the dewar via a "multiple hexapod" structure of a material with low thermal conductivity, like Glass Fibre Composite (GFC) or fiberglass. The multiple hexapod shape of the structure (it consists of nine triangles) has a double functionality. On the one hand, it is the structure that maximizes the ratio of stability over amount of material used, on the other hand the diagonal connection with respect to a straight line increases the conducting length between cold and warm structure, minimizing the heat load.

An additional functionality of the mounting structure is the foreseen adjustment mechanism. Manufacturing tolerances leading to a tilt and/or a vertical shift of the cold plate with respect to the lid/dichroic/mounting flange can be compensated by adjusting the lengths of the single elements of the mounting structure. This adjustment will be performed only once and the position then fixed. This ensures that the optical axes of SPIFFI and MACAO are aligned to within the tolerance of $1'$.

The lid is soldered to the cylindrical part of the outer vessel, and it has an eccentric shape matching the dimensions of the mounting ring provided by MACAO. The size of the connecting screws is chosen a little smaller than the corresponding holes. This allows for adjustments in the image position, necessary because the combined manufacturing tolerances could introduce a horizontal shift up to ± 2mm, with the tolerances being only ± 1mm. During first mount, adjustment screws will be attached to the cryostat to perform the small shifts required. These adjustment devices will after first mounting be replaced by pins marking the correct position.

8.2 Temperature

Quite naturally, temperature is a critical issue in a cryogenic instrument. The main issues concern the heat input into the instrument, consumption of liquid nitrogen, temperature gradients (if present) the possible temperature changes of the cold parts during operation, and baffling of the light path. These topics are discussed below.

8.2.1 Operation temperature: 77K

As mentioned earlier, all optical components of SPIFFI will be cooled down to 77K. In this SPIFFI differs from the progenitor 3D, which had the slicer decoupled from the cold plate, so that it cooled only passively via radiation. The baffle around the slicer was cooled via a copper cable connection from the cold parts of the instrument. The mirror slicer was not cooled, because it was not clear how the optical contact of the slicer segments would react to the cooldown.
The term "optical contacting", as mentioned in the introduction, describes the connection of parts by the force of Van-der-Waal's force alone. For this purpose, the parts to be joined have to be polished to a very high surface flatness ($< \lambda/10$). For parts like the little slitlets of the small mirror slicer, only the flatness on small scales (roughness) of the surface is important, because the material is so thin and flexible, that it will warp to compensate for large scale variations in the surface flatness. The two parts are then cleaned and joined by simply bringing them into contact, starting at one edge and continuing to the opposite end, so that no air will be trapped between the pieces. The pieces after that form a more or less monolithic structure, which should not break apart during cooldown. However, if the part was heated or cooled inhomogeneously, the fear was that the slicer might disintegrate.
This has been investigated for the SPIFFI slicer. A test piece consisting of 5 slitlets of the small mirror slicer was cooled down rapidly (dumping in LN_2 but sealed in a plastic bag to avoid liquid and condensed water from creeping in between the slits) and warmed up again by letting it sit at room temperature. This process was repeated $\sim$100 times and led to virtually no degradation in the contact of the slitlets. The speed of the cooldown process of the spectrograph will therefore be limited by the large lenses, especially the BaF_2 lenses, where large temperature gradients can break the crystal. However, the recommended maximum cooldown rate is not determined yet and will depend upon tests to be performed on the assembled instrument, with temperature sensors measuring the cooldown delay of the lenses.
The only test of this nature performed so far concerned the gratings on the grating wheel. They were also expected to cool slowly, due to the few contact points in the ball bearings of the drive and the steel springs in the grating mounts. It was found out that the gratings reach 100K after 20h, and will reach 80 K $\sim$ 40 h after the beginning of the cooldown. This means that they are not expected to represent the limiting element in achieving thermal equilibrium within the spectrograph.

8.2.2 Minimum hold time for LN_2 : 24h

This issue has practical reasons. The hold time certainly has to be greater than $\sim$14 hrs, otherwise it would be required to refill during an observing run, which would waste precious observing time. It would be safest to start the night with a full reservoir, therefore refilling once in 24h is foreseen, and the hold time for LN_2 should not be smaller than this. Including a safety margin of 50% we estimate the amount of LN_2 required for a hold time of 36h.
To estimate this amount of LN_2 the heat input into the cryostat has to be determined. The manufacturer of the cryostat, Cryovac, will estimate this, but we have performed a calculation of the absolute and relative contributions of the various components:
Since the cryostat is evacuated, convection is irrelevant. The pressure will be sufficiently good ($< 10^{-5}$mbar) that heat conduction between the cold structure and the outer dewar wall is negligible. So the sources of heat

input into the cryostat are radiation from the warm outer wall toward the cold shield/nitrogen reservoir and conduction through solid structures connecting cold and warm parts, like cables, mounts and filling tubes.

Radiation between outer dewar wall and cold shield/tank:
Heat transfer by radiation between two surfaces is described by

$$\text{P [W]} = 5.68 \times \epsilon_{red} \times \left[\left(\frac{T_2[\text{K}]}{100} \right)^4 - \left(\frac{T_1[\text{K}]}{100} \right)^4 \right] \times A_1[\text{m}] \tag{8.1}$$

with

$$\epsilon_{red} = \frac{1}{\frac{A_1}{A_2}\left[\frac{1}{\epsilon_2} - 1\right] + \frac{1}{\epsilon_1}} \tag{8.2}$$

where ϵ_{red} is the reduced emissivity. A_1 and A_2 are the cold and warm surface, respectively, with the temperatures T_1 and T_2.
In our case, T_2 = 293K, T_1 = 77K, the emissivities are ϵ_1 = 0.033 (Aluminium foil at 77K) and ϵ_2 = 0.07 (Aluminium, with oxide layer, at 293K). The linear dimensions of the inner parts of the cryostat measure ~85% of the outer dimensions, which means that the ratio of the areas is ~73%. This leads to a value for

$$\epsilon_{red} = \frac{1}{0.73\left[\frac{1}{0.07} - 1\right] + \frac{1}{0.033}} = 0.025$$

The surfaces of the cryostat are (approximately) the sum of the flat parts of top and bottom and the cylindrical part. This is:

$$A_{T+B} = \pi r^2 \times 2 = \pi \left[\frac{1200\text{mm}}{2}\right]^2 \times 2 = 2.262\text{m}^2$$

$$A_{Cyl} = 2\pi r * h = 2\pi \left[\frac{1200\text{mm}}{2}\right] * 750\text{mm} = 2.827\text{m}^2$$

The total outer area is therefore 5.089 m^2, the inner area 73% of this, 3.71 m^2.
Heat input by radiation from the outer to the inner wall of SPIFFI is:

$$\mathbf{P_{rad}} = 5.684 * 0.025\left[2.93^4 - 0.77^4\right] * 3.71 = \mathbf{38.8W}$$

The assumption of a temperature difference of the whole 293K-77K = 216K is a worst-case-scenario, because the radiation loss occurs between the outer wall and the cold shield. The latter will not be at 77K over its whole extent. But together with the assumed emissivity of the surfaces, which we assumed to be Aluminium of fairly high reflectivity, our estimate agreed well with that of the manufacturer, with their assumptions being based on superinsulated surfaces, and on their experience with other cryostats.

The other radiative contribution enters the cryostat through the entrance window. The same formula for radiative transfer (equation 8.1) applies, but the parameters are as follows:
Transmissive area ≈ 4 x (16mm)^2 = 1000mm^2. This is an estimate of the area of the window that is not covered by reflective coating, which are the object fields and three sky fields. For the largest pixel size, each of them has a size of roughly 16mm x 16mm at the location of the entrance window. Outside and inside the cryostat we assume blackbody behaviour, resulting in $\epsilon_{red} = 1$. This gives:

$$\mathbf{P_{win}} = 5.684 * 1\left[2.93^4 - 0.77^4\right] * 0.001* = \mathbf{0.42W}$$

The rest of the heat load on the cryostat is introduced by conduction. This is described by

$$P = \frac{\Delta T * A * \lambda}{L} \tag{8.3}$$

with ΔT being the temperature difference between the two end points, A the surface of the connecting material, λ the thermal conductivity and L the length of the connection.
In our case the temperature difference is again 293K - 77K = 216K, somewhat overestimated in case of the cables, since they will be thermally coupled to the cold shield before they reach the cold plate. But it is the worst case assumption, and certainly the correct description for the mounting structure and the filling hose.

The heat introduced by the cables is estimated as follows:
We will use cables which we have on stock at MPE, mainly custom-made vacuum proof cryogenic cables fabricated by Gore, originally designed for use on a satellite. They have copper wires and their diameters are described by the AWG parameters. We will use AWG 24, 26 and 20 cables. See the list below for the cross sections implied. The detector cables, which come in form of flexible boards with a given number of copper cables, have the total area listed in the table below. For this estimate, we took into account the (somewhat larger) number of connections required for the 2048^2 array. The thermal conductivity for Cu is $\lambda_{\mathrm{Cu}} = 4.1$ W/cmK.
The cross sections are

Cable	# strands per cable	Cross section strand [mm^2]	Cross section shield [mm^2]	Length [m]	# of strands	total cross section [mm^2]
AWG 24	2	0.24	0.70	1	44	26
AWG 26	2	0.149	0.70	1	32	16
AWG 20	2	0.62	1.8	1	2	2.4
AWG 26	4	0.149	0.78	1	8	2.8
Konstantan 38	20	0.008	0.4	1		1.84
Detector				0.615		1.9

Heat input through the detector cables is

$$\mathrm{P_{det}} = \frac{216\mathrm{K} * 0.019\mathrm{cm}^2 * 4.1\mathrm{W}}{0.615\mathrm{cm}^2\mathrm{K}} = 0.3\mathrm{W}$$

and that of the other cables sums up to

$$\mathrm{P_{Cu}} = \frac{216\mathrm{K} * 0.427\mathrm{cm}^2 * 4.1\mathrm{W}}{100\mathrm{cm}^2\mathrm{K}} = 2.79\mathrm{W}$$

$$\mathrm{P_{Konstantan}} = \frac{216\mathrm{K} * 0.018\mathrm{cm}^2 * 0.22\mathrm{W}}{100\mathrm{cm}^2\mathrm{K}} = 0.06\mathrm{W}$$

The total input by cables is the sum of P_{det}, $\mathrm{P_{Cu}}$ and $\mathrm{P_{Konstantan}}$:
$\mathbf{P}_{cables}$ = 0.3W + 2.79W + 0.06W = **3.2 W**
The cables were assumed to be only 1m long, because the stock of some varieties of cables may be just barely enough if we chose a length of between 1.5 and 2m per cable. However, if the length was indeed increased to 1.5 m, in favour of the reduced heat conduction, the total heat input through cables is decreased to 2.2 W.

The mounting structure is expected to introduce the following heat load:
Dimensions of a single "leg" of the multiple hexapod mounting structure: 0.3 cm x 3 cm x 15 cm. Material: fiberglass, thermal conductivity λ_{fg} = 0.005 W/cmK at 100K. Since there are 9 pairs of such mounting elements, this adds up to:

$$\mathbf{P_{mount}} = \frac{216\mathrm{K} * 16.2\mathrm{cm}^2 * 0.005\mathrm{W}}{15\mathrm{cm}^2\mathrm{K}} = \mathbf{1.17W}$$

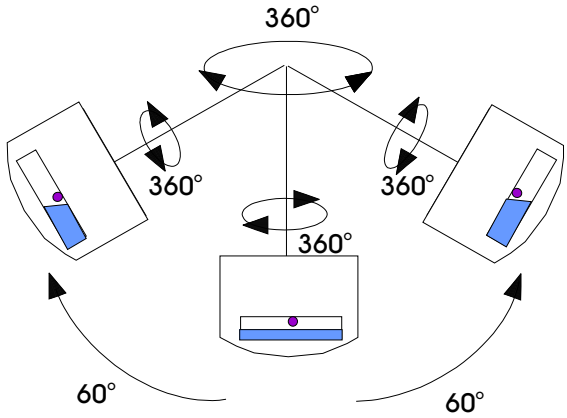

Fig. 8.3: This schematic shows the possible orientations of the cryostat at the Cassegrain focus of the telescope during observations. For maintenance, the telescope might also be moved to 90°(instead of 60°). The possible orientations limit the amount of volume available for the liquid and determine the location of the exhaust pipe (indicated by the dot inside the reservoir volume).

The last major contributor to the heat load is the filling tube. It consists of steel (λ_{Steel} = 0.123 W/cmK) and is assumed to have the following dimensions: A = T x D = 6cm x π x 0.5mm = 0.94 cm^2, L = 15 cm

$$\mathbf{P_{hose}} = \frac{216\text{K} * 0.94\text{cm}^2 * 0.123\text{W}}{15\text{cm}^2\text{K}} = \mathbf{1.7W}$$

We assume that all motors will be switched off during operation at the telescope, so that the only time they contribute to the heat load is when they actually are driving elements in the spectrograph. This will add another small amount of heat. We estimate it conservatively to be an additional 10W.
Total sum of all contributions is:

Radiation	38.8 W
Window	0.4 W
Cables	3.2 W
Mounting	1.2 W
Fill tube	1.7 W
Safety margin	10.0 W
TOTAL	55.2 W

The nitrogen heat of vaporization is 199.2 kJ/kg. During 36h of operation, 55.2W x 36h = 7.15 x 10^{6}J are introduced into the cryostat. The required amount of LN_2 is therefore:

$$\text{V}_{LN_2} = \frac{7.15 * 10^6\text{J}}{199.2\text{kJ/kg} * 0.804\text{kg/l}} = \mathbf{44.6l}$$

The reservoir can only be half filled to prevent spillover due to the movement of the telescope, so the volume of the tank should be slightly above 90 l.

This discussion shows, that the major contributor (80%, not taking into account the motors) to the heat load on the cryostat is the radiation from the outer wall to the cold structure. This makes the superinsulation of all surfaces facing warm parts essential. Nevertheless, within reasonable limits, efforts should be made to

- switch off all motors and encoders when they are not required
- have the entrance window transmissive only in the parts needed, although this may cause it to ice over more easily
- select cables with the smallest cross section possible, with the lowest thermal conductivity possible (which is not easy to achieve, since thermal and electrical conductivity are related), and as long as possible. A thermal trap should be implemented (clamping the cables to the cold shield). This increases the heat introduced into the cold structure by shortening the conductive path length, but it minimizes the heat directly introduced into the cold plate
- have the mounting structure as long as possible, but with the area as small as possible within the limits set by the stability constraints. The material should have as low a thermal conductivity as possible
- filling tube as long as possible between the warm part and the connection point to the tank

8.2.3 Temperature variations < 1K

Temperature variation could occur as two different types of variations: spatial or temporal, and should not exceed a certain limit, set to 1K somewhat arbitrarily here. The first term describes a temperature gradient across the cold plate or between cold plate and optical elements. It could be introduced by the thermal coupling of the cold plate to the nitrogen reservoir, due to the special arrangement with the LN_2 underneath the cold plate, or from bad thermal coupling of optical elements to the mounting structure, which in some cases cannot be avoided.
Temporal temperature variations describe a behaviour where for a given location on the cold plate the temperature varies with time. This could arise from the sinking level of LN_2 in the reservoir which is being used up, or from the movement of the instrument when the telescope moves during operation (see Figure 8.3 for an illustration of possible instrument orientations), causing the conductive path length to the LN_2 to vary for a given location on the cold plate. A third cause for temporal temperature variations are changes in the heat load, where the long use of a motor would have the most severe impact on its immediate surroundings.
None of these variations have a huge impact on the performance of the instrument unless the variations are large. The only critical element is the detector, which has a temperature dependent dark current. But it is foreseen to have a temperature controller that keeps the temperature constant to sub-Kelvin accuracy. Distances, radii, refractive indices and blackbody emission stay constant if temperature variations are below 1K.
The temperature gradients across the cold plate and the variations with telescope orientation were estimated as follows:

Temperature gradient across the cold plate

First the average temperature of the cold shield is determined. Incident thermal energy (29W, assumed to enter at the center of the top), thermal conductivity of Aluminium (4.5 W/cmK), the thickness of the shield (1.5mm minimum), average distance to the LN_2 (83cm) and the circumference (190cm) are required for that estimate:

$$\mathrm{T}_{shield} = \Delta\mathrm{T}/2 = \frac{PL}{2A\lambda} = \frac{29W\,83cm}{229cm^2\,4.5Wcm^{-1}K^{-1}} \approx 10\mathrm{K} \tag{8.4}$$

The temperature of the cold shield determines the radiation that is incident on the cold plate coming from the shield. It requires not only the knowledge of the different temperatures (shield vs. cold plate), areas and emissivities of the parts, but also of the geometry, which means the orientation of the radiating surfaces with respect to each other. This is important because not all the radiation emanating from one surface reaches the surface of interest, and the percentage depends on the geometry. For two parallel circular surfaces, the

angle factor is (Sparrow & Cess, 1966, p.303, 307) 45%. For radiation from the cylinder to the cold plate, this angle factor is considerably smaller, but for a worst-case-scenario assumed to be 45%, too. This makes the active surface $A^* = (1200\text{mm}/2)^2 * \pi + 1885\text{mm} * 470\text{mm} * 0.45 = 0.87\ \text{m}^2$.
The emissivities of the inner side of the cold shield and the cold plate are assumed to be 0.04 and 0.07, respectively. The latter is a fairly high value for a metal at 77K, but given the fact that a large fraction of the radiation incident on the cold plate will rather hit optical elements than the cold plate itself, this seems a reasonable assumption. This gives ϵ_{red}:

$$\epsilon_{red} = \left[1 + \left(\frac{1}{\epsilon_1} - 1\right)\frac{A^*}{A_1} + \left(\frac{1}{\epsilon_2} - 1\right)\frac{A^*}{A_2}\right]^{-1} =$$

$$= \left[1 + \left(\frac{1}{0.04} - 1\right)0.45 + \left(\frac{1}{0.07} - 1\right)\frac{0.87}{1.131}\right]^{-1} = 0.045$$

The amount of energy reaching the cold plate via radiation from the shield is:

$$P_{S\to CP} = 5.648W/m^2 * 0.045\left[0.87^4 - 0.77^4\right] * 0.865m^2 = 0.053W$$

Since this is a very low absolute value and also small (5%) compared to the heat introduced by the mounting structure (≈1W), it is interesting to compare at which temperature of the cold shield the two sources of energy input would reach comparable levels. Inverting the above equation and setting $P_{S\to CP}$ to 1W, it results that this only happens for an average temperature of the cold shield of $\mathbf{160K}$, which will certainly never be reached during operation.
To determine the temperature gradient in the cold plate which arises from the heat load and the finite thermal conductivity of the material connecting the cold plate and the LN_2 reservoir, we consider two limiting "worst case" scenarios:

- 2/3 of the nitrogen are used up (after 24h) and the zenith distance is ∼20°, so that the remaining LN_2 contacts neither the upper half of the bottom plate, nor the top plate of the tank connecting to the cold plate (see Figure 8.4, top). This means that part of the heat load on the cold shield may reach the LN_2 via the cold plate rather than directly or through the bottom plate

- Same filling status, but the telescope points to zenith. At all points, the cold shield connects directly to the LN_2, but the heat load on the cold plate needs to be channeled through the cylinder walls towards the nitrogen.

The temperature difference between two points connected by material of finite thermal conductivity λ, length L and cross section A, and with the power P transmitted through the material, is given by:

$$\Delta\text{T} = \frac{L}{A * \lambda} * P \tag{8.5}$$

In analogy to electrical current, I call the factor $L/(A*\lambda) = R$. In this picture, P represents the current I and ΔT is the voltage U. Serial and parallel combinations of resistances are consequently treated by Kirchhoff's laws.
The resistances R_{ij} of the foreseen paths of heat transfer are listed in Table 8.2.3:

All the material used here is Aluminium with a heat conduction of λ=4.5 W/cmK. The dimensions used in the calculation are:

i	j	L [cm]	B [cm]	D [cm]	R [K/W]	R_{tot} [K/W]	comments
1	1	60	1.2π*R_T^2/2L	1	0.17	0.17	for B used area/L
2	1	80	πR_T*10/$2\pi R_T$	0.5	7.2	3.6	two symmetric cylinder parts
3	1	$\pi R_T/2$	L*2*10	0.5	0.87		through cyl. to top
	2	R_T	$\pi R_T^2/2R_T$	1	0.14	1.09	through top plate
	3	7	$\pi R_T/4$	0.5	0.08		through cyl. to LN_2
4	1	1.2H+5	$2\pi R_T/(24*8)+$ $+\pi(R_T^2\text{-}R_R^2)/(5*8)$	0.5	0.23		through cylinder and top plate
	2	4	$\pi R_R/4$	5	0.0003		through the ring
	3	$2R_R$	$\pi R_R^2/2R_R$	4	0.057	0.296	through the cold plate
	4	4	$\pi R_R/4$	5	0.0003		identical to 4.2
	5	7+5	$2\pi R_T/(7*8)+$ $+\pi(R_T^2\text{-}R_R^2)/(5*8)$	0.5	0.008		through cylinder to LN_2
Mount	1	$2R_P$	$\pi R_P^2/9R_P$	4	0.035		from one leg through plate
	2	4	$\pi R_R/4$	5	0.0003	0.327	through the ring
	3	7+5	$2\pi R_T/(7*8)+$ $+\pi(R_T^2\text{-}R_R^2)/(5*8)$	0.5	0.008		through cylinder to LN_2
Radiation	1	R_P	$\pi R_P^2/2R_P$	4	0.035		from center of plate
	2	4	$\pi R_R/4$	5	0.0003	0.044	through the ring
	3	7+5	$2\pi R_T/(7*8)+$ $+\pi(R_T^2\text{-}R_R^2)/(5*8)$	0.5	0.008		through cylinder to LN_2

Property	Size	used as
Diameter Cold Plate	1200 mm	$= 2\ R_P$
Thickness Cold plate	40 mm	in column "D"
Diameter Ring[1]	850 mm	$= 2\ R_R$
Thickness Ring	50 mm	in column "D"
Height Ring	40 mm	in column "L"
Diameter Tank	1000 mm	$= 2\ R_T$
Thickness Tank bottom/top	10 mm	in column "D"
Thickness Tank cylinder	5 mm	in column "D"

The resistance of the whole system as seen from one point on the bottom circumfence of the nitrogen reservoir is

$$R = \left[\frac{1}{R_1} + \frac{1}{R_2} + \frac{1}{R_3} + \frac{1}{R_4}\right]^{-1} =$$

$$= 0.17^{-1} + 3.6^{-1} + 1.1^{-1} + 0.3^{-1} = 0.096\frac{K}{W}$$

This implies that, assuming 60% of the heat load on the cold shield (20W) enter the cold system at one point on the bottom of the reservoir, the temperature on that point will be

$$T = 77K + \Delta T = 77K + 0.1\frac{K}{W} * 20W = 77 + 2 = 79K$$

The temperature gradient over the cold plate can be estimated as follows:

$$P_{coldplate} = \Delta T_{tot}/R_4 = \frac{2K}{0.3\frac{K}{W}} = 6.7W$$

With the total energy transfered through the cold plate and the shield as the origin being 6.7W, this makes the temperature difference in the cold plate between the two connecting points to the ring in this 2d picture

$$\Delta \mathrm{T}_{coldplate} = \frac{6.7\mathrm{W}}{0.06\frac{\mathrm{K}}{\mathrm{W}}} = 0.4\mathrm{K}$$

Compared to this the other two contributions, from the mounting of the cold plate and from radiation directly onto the cold plate (from the shield and through the entrance window) are small:

$$\Delta \mathrm{T}_{coldplate} = \frac{0.13\mathrm{W}}{0.33\frac{\mathrm{K}}{\mathrm{W}}} = 0.04\mathrm{K}$$

$$\Delta \mathrm{T}_{coldplate} = \frac{0.5\mathrm{W}}{0.04\frac{\mathrm{K}}{\mathrm{W}}} = 0.02\mathrm{K}$$

For the second limiting case, the resistances combine as follows:

i	j	L [cm]	B [cm]	D [cm]	R [K/W]	R_{tot} [K/W]	comments
1	1	R_R	πR_R	5	0.014		through plate
	2	4	π*85	5	0.0007		through the ring
	3	7	$\pi(2R_T+85)/2$	1	0.005	0.044	through top
	4	17	$\pi 2R_T$	0.5	0.024		identical to 4.2

This results in a temperature difference between the center of the cold plate and the outer rim of

$$\Delta \mathrm{T}_{coldplate} = \frac{1.6\mathrm{W}}{0.04\frac{\mathrm{K}}{\mathrm{W}}} = 0.06\mathrm{K}$$

The temperature variation of 0.5K total is compared to that implied by the largest expected pressure variations during an observing night. If the latter were higher, this would mean that the temperature variations just estimated are of no concern without the necessity to argue further. However, this is not the case. The typical pressure at Paranal is 744 mbar, with maximum variations during a night ranging from 741 to 747 mbar. An empirical formula compiled from measurements by NIST (2000)

$$\mathrm{T[K]} = \frac{264.651}{3.7362 - \log(\mathrm{P[mbar]})} + 6.788 \tag{8.6}$$

The temperatures corresponding to 741 and 747mbar are 75.238K and 75.299K, respectively, with the temperature difference ΔT = 0.06K.

All the above considerations were worst case estimates, with all the energy being introduced at one point, leaving out additional conducting elements like the two Aluminium rings inside the nitrogen reservoir and the amount of LN_2 left over being that expected after 24h. Therefore, it seems safe to assume that the actual temperature differences will be lower. But with the detector heated for temperature stabilization, even the temperature variations of 0.5K are no source of worry, because they lead to an expansion of the cold plate of (-0.004+0.00392)/25K^{-1}*0.5K*1200mm=2μm, which is absolutely negligible for the relative positioning of the optics units.

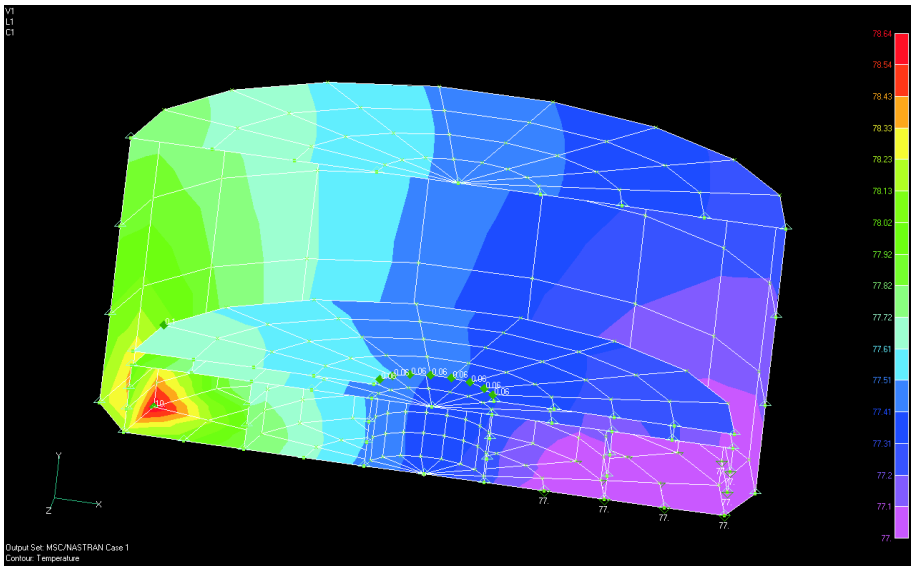

Fig. 8.4: This model of the temperature variations in the cryostat closely represents the first of the two cases considered in the by-hand-calculations. The only differences are the presence of the two additional rings connecting bottom and top of the nitrogen reservoir and the thickness of the cylinder wall, which is 1cm here, instead of 5mm in the calculations.

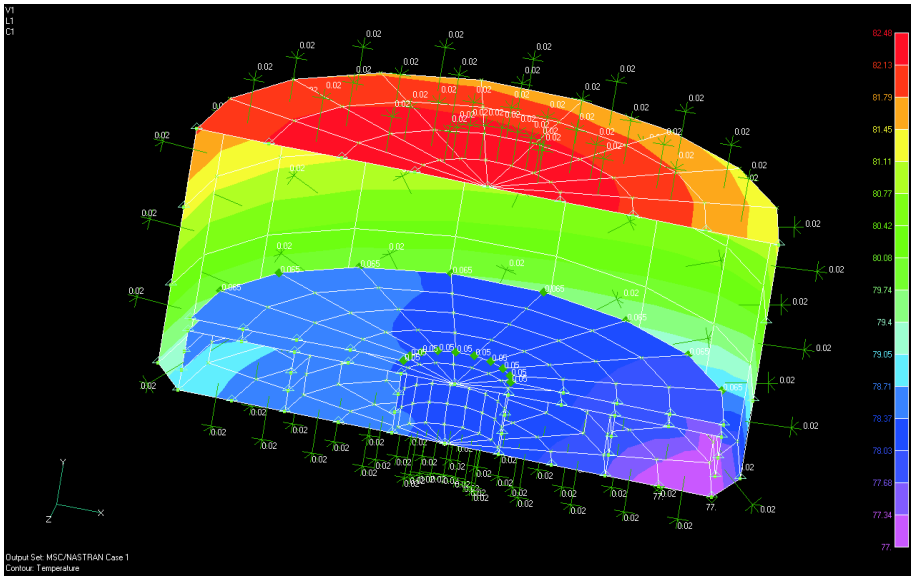

Fig. 8.5: FEM analysis of the temperature distribution in the cryostat with the reservoir almost empty. In contrast to the previous figure, the cold plate thickness is 3cm here (instead of 4cm in 8.4). It is obvious that the temperature of the far edge of the cold plate with 78.7 K is above the tolerance and therefore additional measures of reducing the cold plate temperature need to be considered.

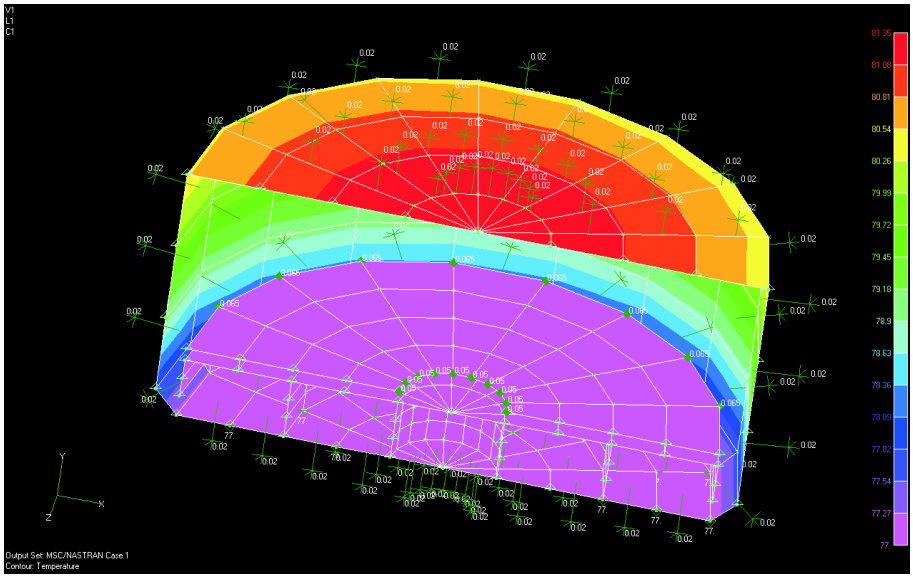

Fig. 8.6: FEM analysis of the temperature distribution in the cryostat. Most input parameters are the same as in the previous figure, only the presence of additional "pockets" on the bottom plate of the tank are simulated by setting additional points on the bottom of the grid to a fixed temperature of 77K. The result is fairly dramatic, with the cold plate and the nitrogen reservoir achieving constant temperature.

Figure 8.4 shows the output of a finite element analysis, analyzed for the temperature distribution in the cryostat. This shows that the by-hand calculations were not far off and provide a fairly realistic approximation to the actual temperature distribution.

The next figure, 8.5, shows an FEM analysis of the heat load on the cryostat, and here the heat is mainly introduced by radiation on the cold shield. This is simulated by placing the object into an environment of 297K and assigning emissivities/absorption coefficients to the surfaces. The temperature differences decrease, which was expected, because the previous case was assumed to be a worst-case-scenario, especially concerning the power input into one point.

However, the temperature difference of 1.7 K to the far side of the cold plate is still too much to be tolerated. One very effective means of reducing the temperature gradient would be to keep the bottom of the cold plate at 77K everywhere. This can be achieved if additional "pockets" are mounted on the bottom of the tank. They would stand vertical to the bottom of the tank, so that the nitrogen can be released when the telescope points to zenith, but when the zenith distance increases, they are arranged circularly on the plate with the openings pointing outward, so that the nitrogen which is flowing to the lowest point collects in these pockets and keeps these points of the cold plate at 77K.

Figure 8.6 shows that this measure has dramatic influence on the temperature gradient, keeping all of the cold structure actually at 77K.

8.3 Additional aspects

This section describes aspects that were important for the cryostat design apart from the topics mentioned above, and also explains additional functionality that usually concerns the safe and easy handling of the instrument.

- Orientation during operation: 90° from vertical, 360° rotation around Cassegrain derotator axis:
  As mentioned earlier, the spectrograph spans a large range of possible orientations (see Figure 8.3). Even though during observations the maximum zenith distance is 60°, daytime maintenance of the telescope might require a zenith distance up to 90°. This influences the total volume of the LN_2 reservoir, because it can be filled only up to the 50% level to avoid spilling and to be able to find a position for the installation of the overpressure security valve and the exhaust pipe.

- Hold time for vacuum ∼3 weeks:
  The minimum time that the cryostat can stay at high vacuum without being pumped on is required to be 3 weeks. Assuming that the dewar stays cold, this is achieved by installing an activated charcoal trap, as estimated by the manufacturer of the cryostat. The trap is regenerated by heating it multiple times after each observing cycle. The heaters have a control unit that is activated directly at the instrument, rather than at the control room. Only when the temperature inside the cryostat is close to room temperature will it be possible to activate the trap heating, because it would be disastrous if the trap was regenerated while the dewar is cold.

- Removable lid:
  The lid, even though it is very rigid, needs to be removable, because otherwise the cold plate would not be accessible for installation and maintenance of the spectrograph elements. This connection is foreseen to be at the level of the cold plate.

- Spatial separation of detector signal and instrument control:
  Several different connectors are foreseen for the detector signal and the instrument control signals, with a spatial separation of the two types of signal achieved by feeding them through different flanges.

- Nitrogen drain valve:
  This valve will be installed to ensure the possibility to empty the liquid nitrogen reservoir in nominal position. This is necessary for the test phase and for instrument maintenance. If the spectrograph failed during operation, it would take much too long to boil off the coolant in order to warm up the instrument. Even if the reservoir is emptied, it will still take 12h to warm up the cold structure to room temperature using the heater attached to the bottom of the LN_2 tank.

- Cryostat heating:
  For maintenance purposes, the cryostat is required to be warmed up from 77K to room temperature within 12h. With the amount of material in the cold structure (∼250kg) this requires an input power of ∼500W.

- Laboratory handling:
  In the lab, SPIFFI sits in a cart which will also be used to lift the cryostat up to the mounting position at the telescope. Since the operation position at the telescope is the same as in the lab, with the cold plate upwards, the cryostat does not need to be rotated for any operation.

- No dead end holes:
  Dead end holes have to be avoided in all inner parts of the cryostat, to avoid slow outgassing when the instrument is evacuated.

- Vacuum gauges at dewar and pumping device:
  Two sets of vacuum gauges are installed, one in the spectrograph and one at the pump. This ensures that the valve between the spectrograph and the pump can only be opened if the pressure inside the cryostat is above that of the pump, unless re-pressurizing is anticipated. For this latter case, a proper override system will be installed.

- Nitrogen level sensor and automated filling:
  A series of Platinum resistance (Pt100) temperature sensors will be installed in the nitrogen reservoir, sensing the LN_2 level if the telescope is near zenith (the temperature sensors can be read out in other orientations, too, but then the measurement is not easily interpreted). At a minimum level to be defined, a warning is displayed to the operator. This level sensor, or rather the upper Pt100, will also be used during the refilling procedure of the LN_2 reservoir. The refilling process is automated; the signal (I/0) from the topmost sensor will be relayed to an Omega control unit that closes a cryogenic valve on the nitrogen reservoir from which SPIFFI is filled.

- Automated cooldown
  The same type of controller is also used for the cooldown of the instrument, but the input signal used comes from a Platinum resistance thermometer on the cold plate and the resistance is used as an analog signal that is compared to the programmed cooling ramp. The valve on the nitrogen reservoir is driven by the Omega controller to reproduce the programmed ramp with the temperatures read back from the cold plate.

9. THE GRATINGS

9.1 General description

SPIFFI will incorporate four different gratings, one of which can be selected on-the-fly. Three of them deliver a medium resolution of R∼4500 (J, H, K). They are suitable for efficient OH avoidance and observations involving dynamics of galaxies (e.g. velocity dispersion measurements of galactic nuclei). For cases where such high resolution is not necessary or a large wavelength coverage is desired, a fourth grating covering the H and K bands simultaneously is foreseen. Its spectral resolution is R∼2200. All four gratings are mounted on a common grating wheel with a very high angular positioning accuracy ($< 2''$). This is required, because the data initially are not Nyquist sampled in the spectral direction, and the proper sampling is achieved by two sequential observations with a spectral offset of half a pixel. This offset specifies the positioning accuracy of the gratings. In principle, it is possible to install gratings with other properties (resolution, wavelength range), but the available space is limited to four. A maximum of five mounting positions could be provided, if the central element of the mount were to be modified.
The gratings are mounted in a so-called Ebert mount, with an angle of 45° between the incoming and diffracted beams. They are blazed for maximum efficiency.

9.2 Specifications

A grating has several important parameters determining its performance:

- The line density σ in [lines/mm], also expressed as the grating constant a in μm($a = \sigma^{-1}$). For a given instrument and a given order, this determines the dispersion. The contraction of the substrate at the operating temperature of 77K needs to be taken into account.
- The blaze angle δ_{bl}, which maximizes the efficiency in the order which will be used.
- The flatness of the grating substrate, which influences the point spread function/encircled energy on the detector.

Table 9.1 lists the specifications of the four gratings.
The line density was determined from the grating equation

$$\sin\alpha \mp \sin\beta = \frac{m\lambda}{\mathrm{a}} \tag{9.1}$$

where α is the incoming, β the diffracted beam, measured positive with respect to the grating normal. The "-"' is valid in cases where incoming and diffracted beam lie on opposite sides of the grating normal (as in our case), otherwise it is "+". The three other constraints for the determination of a were

$$\Theta = \alpha + \beta = 45^\circ; \qquad a \geq 5\lambda; \qquad a^{-1} \times 3600 = \text{integer} \tag{9.2}$$

The first constraint is determined by the angle between collimator and camera in SPIFFI the second arises from polarization effects in the grating that start lowering the efficiency roughly around that limit, the third is set by limitations of the ruling engine used by the manufacturer Hyperfine.

Band	H & K	J	H	K
Wavelength range [μm]	1.45-2.45	1.10-1.40	1.45-1.85	1.95-2.45
grating constant, 77K [μm]	9.960	5.810	7.747	9.684
Grooves/mm, 77K	100.400	172.114	129.086	103.268
Grooves/mm, 293K	100.000	171.429	128.571	102.857
Order	1	2	2	2
Blaze angle [°]	5.72	13.59	13.17	14.10
Blaze wavelength	1.82	1.25	1.62	2.16

Tab. 9.1: Specifications of the four gratings. All of them have a ruled width of 156 mm, a groove length of 136 mm and should fulfill the additional constraints: **Flatness:** a maximum error in the diffracted wavefront of $\lambda/7$ measured at 632.8 nm at normal incidence. **Efficiency:** more than 60% over the whole wavelength range, measured with our setup.

The blaze angle is given by

$$\delta_{bl} = \frac{\alpha - \beta}{2} \tag{9.3}$$

It is the angle that, in case of a flat mirror, would reflect a beam coming in at an angle α into direction β. The purpose of blazing a grating is to redirect light from other orders into the order which is of interest. The overall efficiency of a grating reacts very sensitively to changes in blaze angle. Usually, manufacturers guarantee the blaze angle accuracy to within a tolerance of 10%. For our combinations of wavelengths, orders and blaze angles, a deviation of 10% from the nominal blaze angle would have placed the blaze wavelength, which is that with the highest efficiency, outside the observed wavelength range. Maximum efficiencies would then even theoretically not have exceeded 60-70%. Therefore it was necessary to constrain the tolerances on the blaze angle to be 3%. This would imply a decrease in efficiency of 5% maximum. As will be shown in the next paragraph, the blaze angle of the delivered J-band was offset by 5%, with corresponding low efficiency (see Figure 9.1).

9.3 Properties

The first grating to be delivered was the H&K grating. It has gone through cold cycling without degradation in surface quality. The two pictures in Figures 9.3 show it shortly after delivery still in the box and mounted on the grating wheel in the test cryostat, respectively. Figure 9.4 shows parts of the construction drawings made by H. Dohnalek, and the figure caption describes the most relevant parts and adjustment mechanisms. The wavefront that is meant to be achieved on the detector places very stringent constraints on the surface parameters, and also on the gratings. It was a potential worry that the lightweighting pattern of crossed drill holes could show through in the polished and/or the ruled surface, but this is not the case: Figure 9.5 shows the interferograms of the flatness measurements for all four gratings before and after the ruling. They are all well within the specifications, since the number on the top left of each plot gives the value for the RMS wavefront error. It should be below 0.14 to fulfill the specicfications, which were derived from the tolerancing within the ZEMAX optical design program.

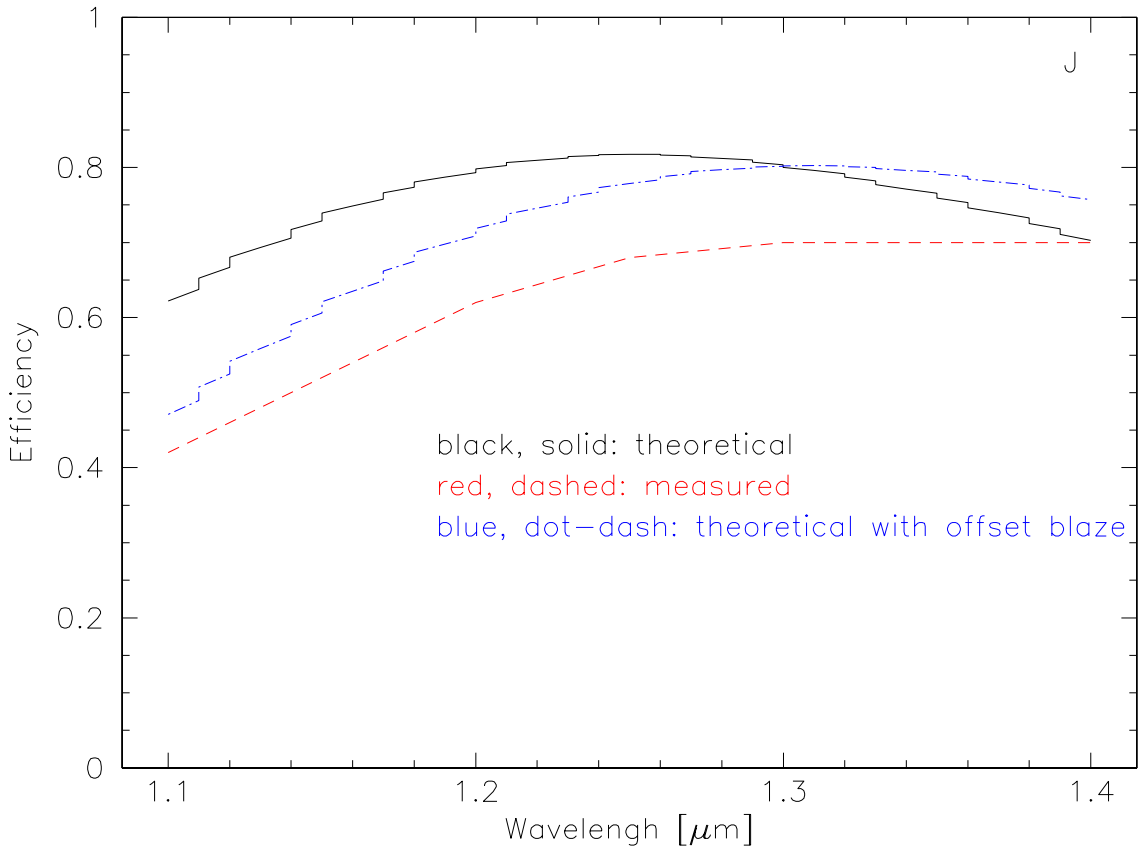

Fig. 9.1: Comparison of grating efficiencies with variation of blaze angle. The black, solid curve is the theoretical efficiency for a blazed grating with the specifications of the J-band grating as we will use it in SPIFFI. The blaze angle of 13.59° has maximum efficiency roughly in the middle of the observed wavelength range and comparable efficiencies at the borders of the band. The measured efficiency displayed as the red, dashed line shows very different spectral behaviour, and this can easily be explained by comparison with the theoretical efficiency for a blaze angle of 14.3°. The almost constant offset between that theoretical and measured curve arises from imperfections in the grating, like coating peeled off, reduced reflectivity etc.

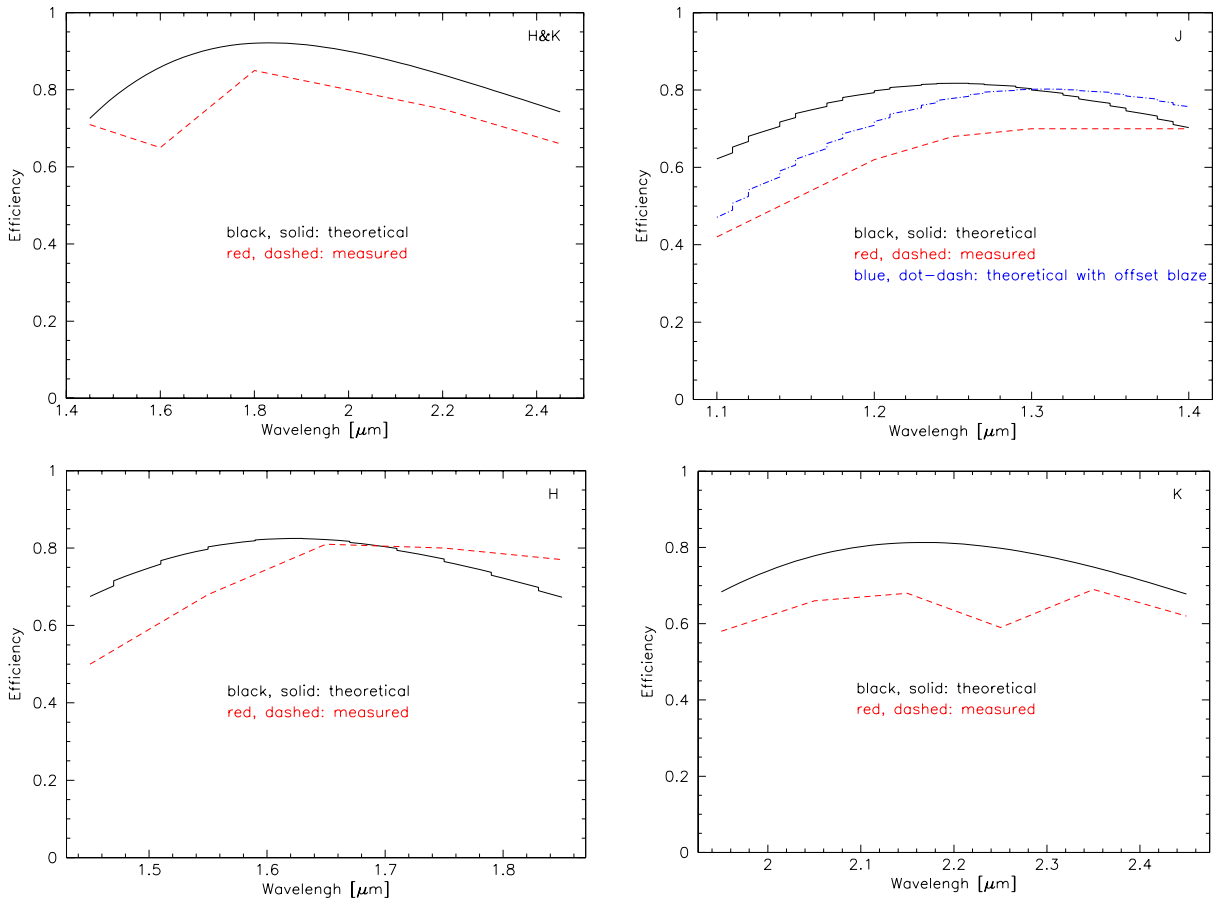

Fig. 9.2: The efficiencies of the gratings (relative to an Aluminium mirror for H&K, J and H, and relative to an Au mirror for K), as they were measured by the manufacturer. As a comparison, the theoretical efficiencies are plotted as solid lines. In the case of the J-band grating, where those two differ substantially, a theoretical plot with the blaze angle shifted to 14.3° (instead of 13.59°) is given in dash-dot. It shows that the asymmetric shape of the efficiency curve is probably caused by a wrong blaze angle.

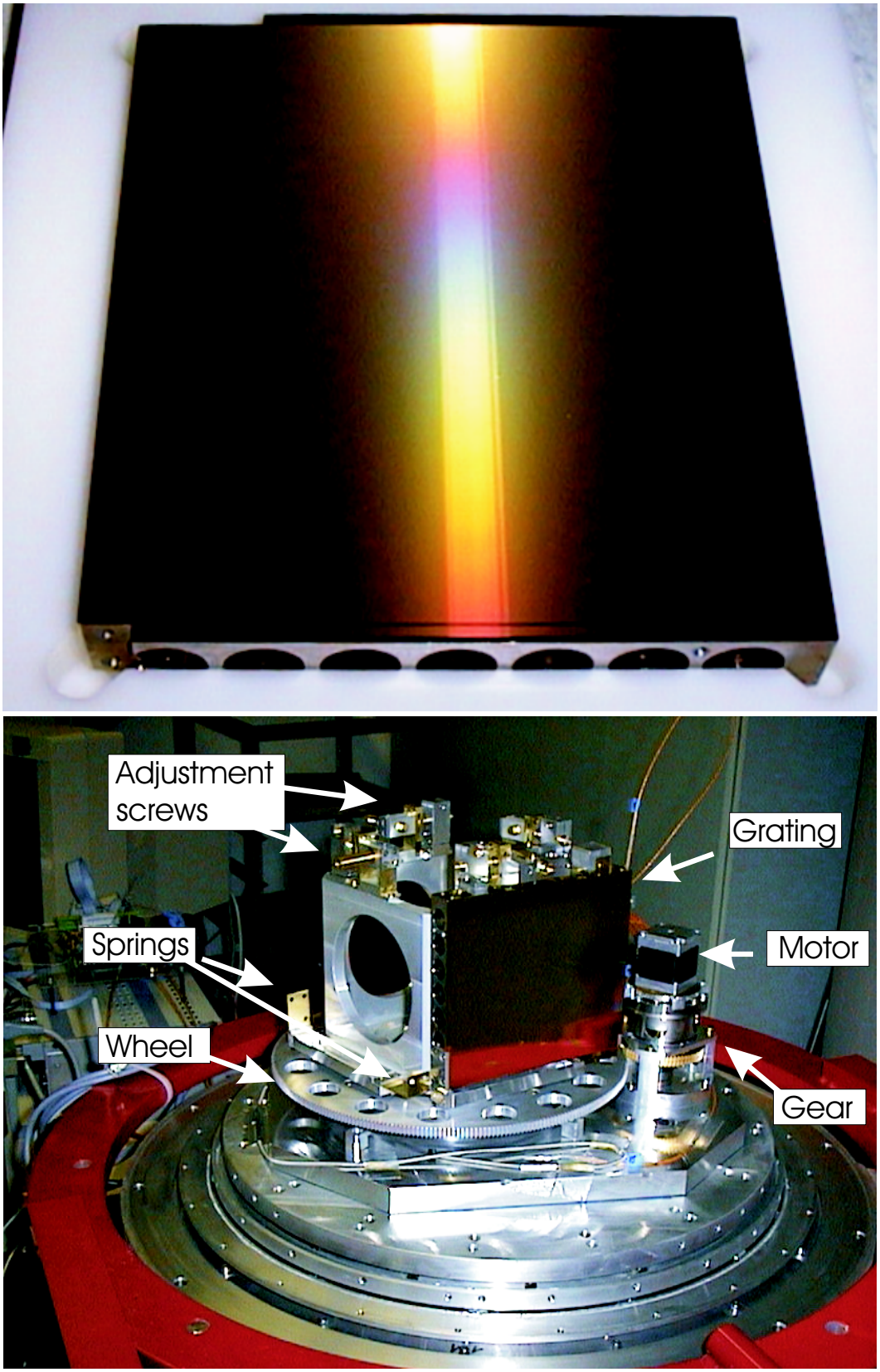

Fig. 9.3: Photograph of the H&K-grating, unmounted, on the left, and mounted on the grating wheel (right). The lightweighting structure is very well visible. The grating wheel requires the large sprocket diameter and a low gear ratio to allow for the spectral dithering. On the top of the grating mount, adjustment screws are visible which are used for the postitioning around the other two axes.

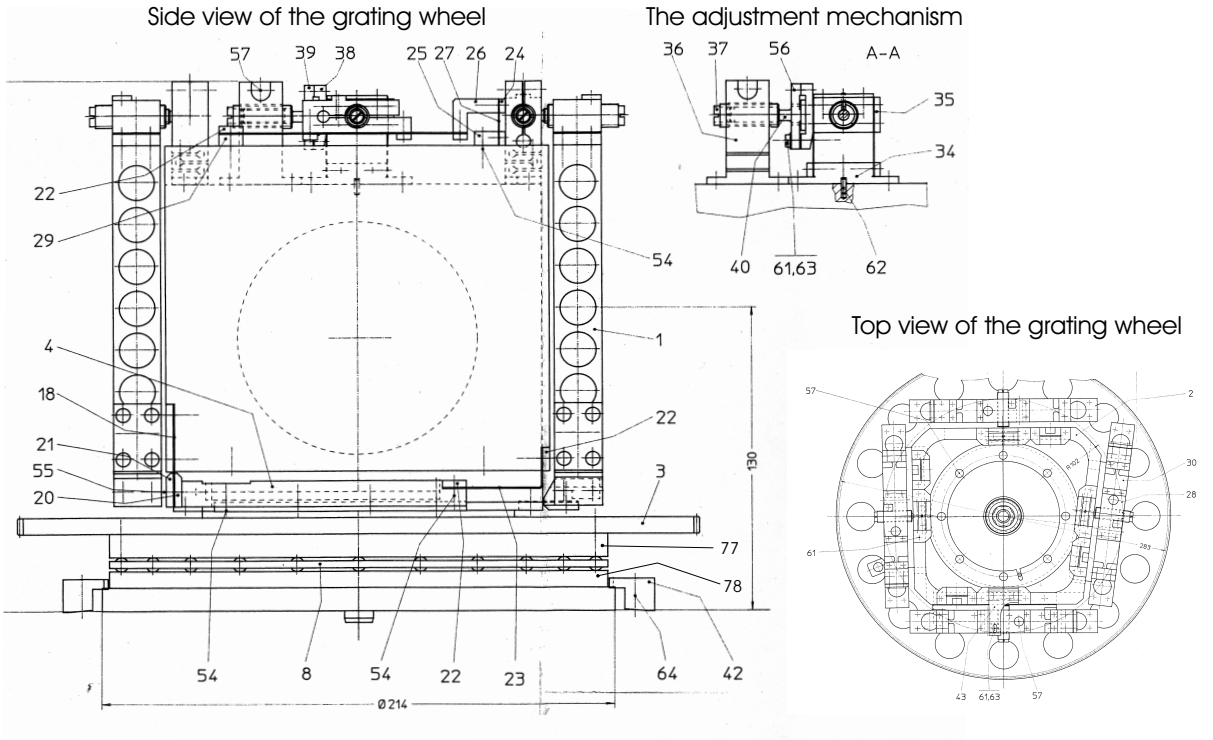

Fig. 9.4: Extraction of the construction drawings for the grating wheel. The side view shows two of the gratings (**1**) with the lightweighting holes on the mount, with the mount screwed onto the grating wheel (**3**). This is directly connected to the moving part of the position encoder (**77**), which in reference to the fixed bottom part (**78**) allows to determine the angular position of the grating wheel with a resolution of $\sim 2''$. The gratings are connected to the central part of the mount via steel plate springs and adjustment mechanisms. The springs (e.g **18, 23, 43**) allow relative movements of grating and mount during cooldown. The purpose of the adjustment mechanisms (see blow-up in top right corner and various views on top of the gratings and mount) is to position the grating very accurately with respect to the optical axis. These adjustments can only be made when the instrument is open. However, the displacement of the spectrum needs to be measured when the instrument is cold, in thermal equilibrium and operation mode. Movements around the axis parallel to the grooves are performed by rotating the whole grating wheel. Displacements concerning the axis orthogonal to the grating surface, which lead to a tilt in the spectra (not parallel to columns of array any more) are corrected by turning the differential screw on the top right corner of each grating. Displacements of the object points, caused by a wrong grating angle around the axis perpendicular to the grooves, are corrected by the adjustment mechanism connected to the top centre of each grating. Each of these displacements need to be determined by scanning a point source through the field of view and by acquiring a calibration spectrum for each grating on the wheel. These linear or angular displacements need to be converted into turns of the differential screws, which are then turned by the required amount after the instrument is warmed up again.

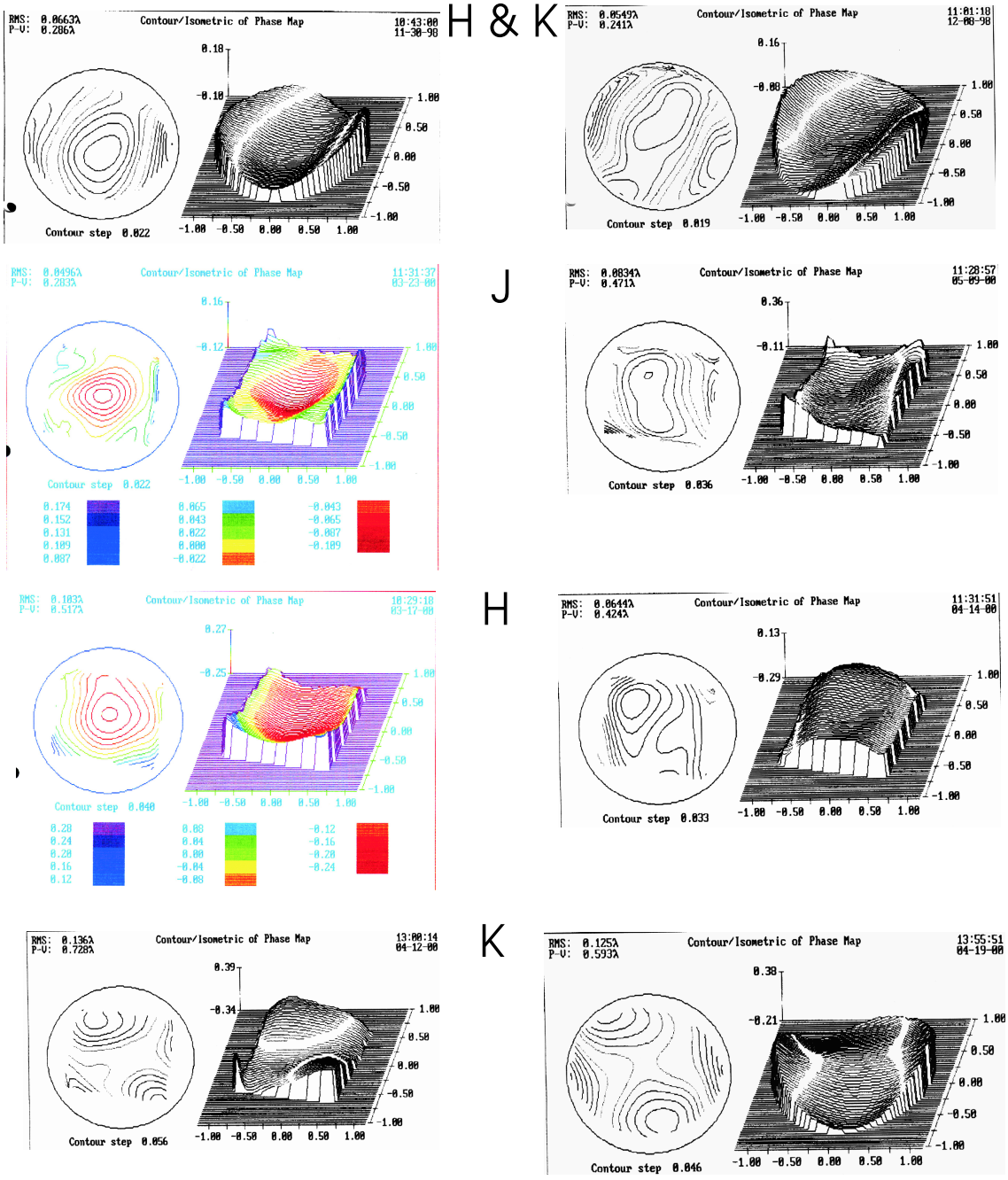

Fig. 9.5: Contour plots of the four gratings, in the left column before, on the right column after the ruling. The contours represent the wavefront error in units of λ at the wavelength of the measurement of 632.8 nm. All of them fulfill the specifications of RMS (wavefront error) $\leq \lambda/7$.

10. THE SINFONI EXPOSURE TIME CALCULATOR

10.1 Description

The IDL-based SINFONI exposure time calculator applies the basic formula

$$\mathrm{SNR} = \langle n_s \rangle / \sqrt{N + R^2} \qquad \mathrm{N} = \langle n_s \rangle + \langle n_b \rangle + \langle n_d \rangle \tag{10.1}$$

where n_i denotes the total number of generated e^- at a given pixel, the indices s, b and d indicate source, background and dark, respectively. R is the read noise in e^-/read (or rather for ramp sampling in our case). It is used via a graphical user interface, which is displayed in Figure 10.1
The parameters taken into account are:

- VLT collecting area
- Atmospheric transmission curve
- Spectrally averaged instrument transmission
- Atmospheric emission curve
- Thermal background from the telescope
- Detector quantum efficiency curve
- Pixel size in arcsec^2 on the sky
- Spectral resolution
- Application of OH avoidance and/or spectral rebinning
- Source extent (point source, extended with integrated spectrum or extended with pixel-by-pixel analysis)
- Source magnitude (in mag for point sources, mag arcsec^{-2} for extended sources), spectrum and redshift
- Seeing
- Strehl ratio in AO assisted observations

Depending on what is required, two of the following parameters need to be supplied, the third is then determined:

- Integration time
- S/N
- source strength (in mag or mag arcsec^{-2})

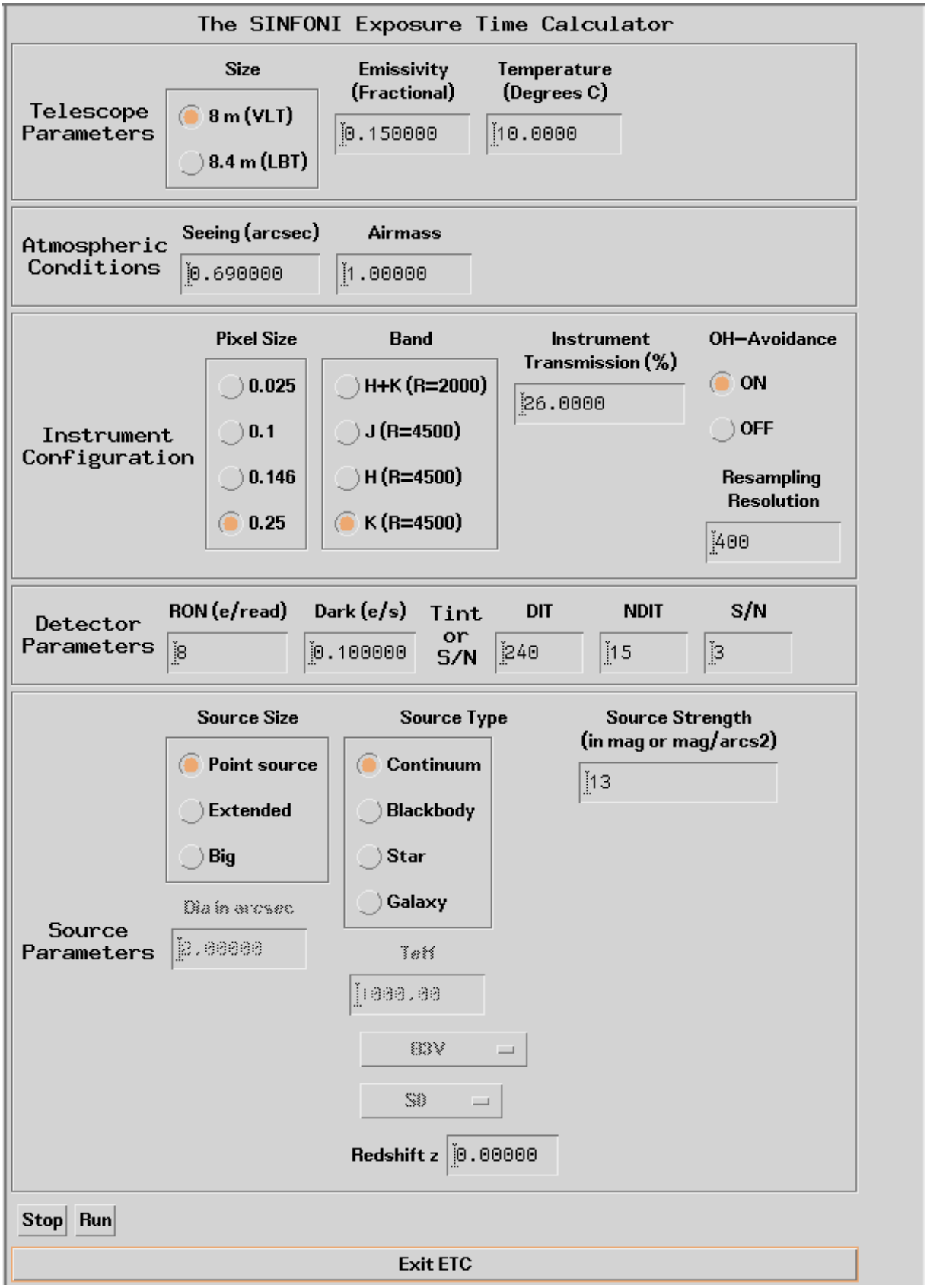

Fig. 10.1: The graphical user interface of the SINFONI exposure time calculator.

Element	Transmission [%]
Telescope and MACAO	65
Dichroic	90
Filter	80
Pre-Optics	90
IFU	88
Collimator	94
Grating	68
Camera	88
TOTAL	20

Tab. 10.1: Average transmissions for the elements in SPIFFI. The total instrument transmission, including telescope and adaptive optics, but excluding the detector, is 20%.

The SPIFFI instrument was designed to maximize the througput wherever possible and to minimize the background and the noise. The first goal will be achieved by selecting high transmission/efficiency optics, and by placing them in an evacuated environment that prevents degradation over a long period of time. The second point requires the whole spectrograph to be a cryogenic instrument, such that the thermal background contribution of the instrument itself is negligible compared to the telescope and the sky. The third point was helped by the fact that the HAWAII array we bought from Rockwell shows low read noise and dark current. The relative impact of the read noise will be minimized by selecting long integration times, made possible by the implementation of the sky spider. Moreover we will optimize the electronics and the read out modes (ramp sampling). The dark current cannot be overcome, and our estimates show that the instrument is dark current limited at AO pixel scales and high spectral resolution in the J and the H band.
Table 10.1 lists the sensitivities for a variety of cases which are of interest to the general observer. They were computed using the SINFONI exposure time calculator which allows to set explicitly almost all of the parameters below and thus can be used to derive the corresponding magnitudes for other cases of interest. The limiting magnitudes given in Table 10.1 are valid for the following constraints/specifications:

- Operation at the VLT
- S/N of 5 in 1h of integration time (6 integrations, 600s each)
- Detector characteristics: Jansen (1999) measured a read noise of 42^{-} for a single read and a dark current D = $0.01e^{-}s^{-1}$. We will use the value of $24e^{-}$ read noise which will be achieved by ramp sampling, and the measured $0.01e^{-}s^{-1}$ dark current.
- Median Paranal seeing (0.″69), airmass 1.0
- Spectrally dependent atmospheric transmission for usual Paranal conditions. The data file was obtained from the ESO webpage.
- Telescope temperature 283K, emissivity 35% (includes MACAO)
- Instrumental transmission, including telescope, MACAO and SPIFFI but excluding the detector, 20%
- Wavelength dependent detector quantum efficiency as provided by Rockwell, average 60%
- S/N per spectral channel, resampling to R=400 for case of OH suppression

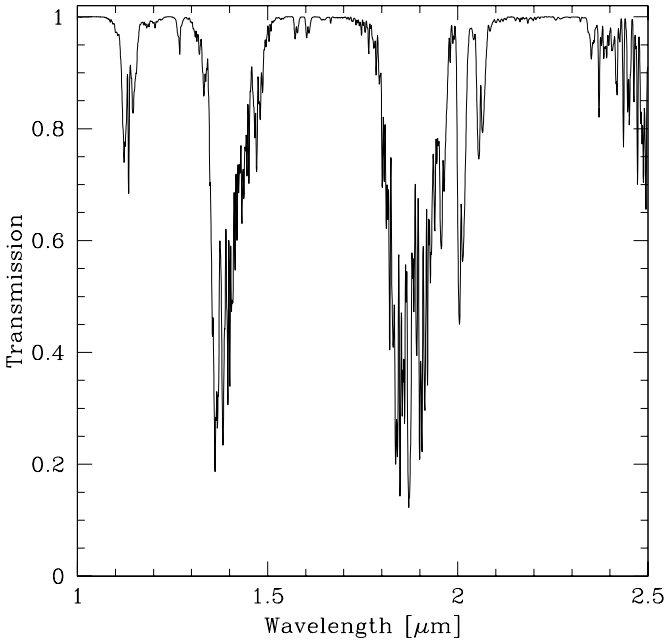

Fig. 10.2: Atmospheric transmission at Paranal for the wavelength range observed by SINFONI. The data file was obtained from the ESO web page.

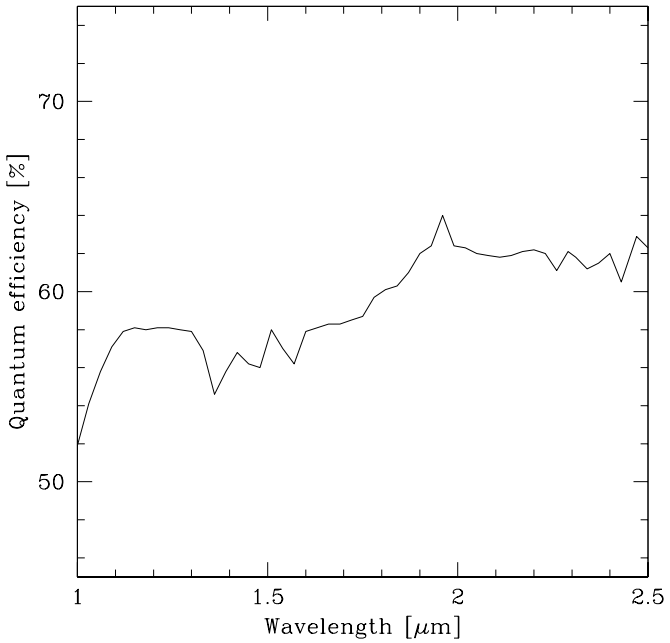

Fig. 10.3: Quantum efficiency of the Rockwell HAWAII 1024^2 array, as it was measured by the manufacturer.

- Either the integrated spectrum within the FWHM for the case "Point Source" or per spatial pixel. The last column gives the line fluxes which correspond to the per pixel/No OH-suppression case.
- Pixel size 0.″25 for the seeing limited, 0.″025 (0.5×diffraction limit of an 8m telescope) for the AO assisted case
- Strehl ratio of 0.25 for the AO case, which is achieved with a natural guide star brighter than 14.5 mag within 15″ of the object in case of K-band (Ströbele, 2000). The strehl ratio assumed for J-band is 0.15.
- Results give point source magnitudes (the average value for the whole band) in the case of "Point source" and mag arcsec^{-2} in the cases of "Extended source" and "per pixel"

If the "Himmelsspinne" indeed makes possible on-source integration times of half an hour or longer, this improves the sensitivity especially in those cases where the sky background was intrinsically low, which is for the AO scales and J band. The increase in limiting magnitude is 0.5 mag for the AO scales and between 0.1 and 0.5 mag for the seeing limited scales.

10.2 OH suppression

A large fraction of the sky background between 0.7 and 2.3μm consists of line emission (see Figure 10.4 which is mainly produced by the reaction H + O_3 $\rightarrow$ OH^* + O_2 in an atmospheric layer centered at a hight of 87km (Baker and Stair Jr., 1988). It leaves the OH molecules in excited vibrational states up to v=9. Due to the low temperatures and the small pressure broadening in their atmospheric layer, the OH lines are intrinsically very narrow, much narrower than the gaps between adjacent lines. Not only the intensity of the lines in total, but also their relative fluxes vary on short timescales of a few minutes. They show a general trend of decreasing intensity (factor 2-3) towards the end of the night, overlaid on which is a sinusoidal variation on the 10-15% level arising from gravity waves in the atmosphere (Turnbull & Lowe, 1991). Furthermore, they vary with season and location of the observatory and with the zenith distance. But few measurements have been published that would allow a derivation of a general average spectrum or one taking into account given input parameters. One of the most useful measurements was performed by Maihara et al. (1993a) using the 2.2m telescope on Mauna Kea. They detected 69 OH-lines in the H-band and 53 in J. Oliva & Origlia (1992) detected 65 lines in K. The results of both groups are summarized in Table 10.3.
Since the background is known or suspected to be extremely low inbetween the lines, it would be useful to somehow blank out the regions which are contaminated by the lines while keeping the flux from the regions inbetween the lines. However, the level of continuum background inbetween the lines is poorly known. There are two main emission sources that contribute to the near-infrared continuum at these wavelengths: Thermal emission from telescope, instrument and atmosphere, and airglow emission, which is still fairly mysterious. It was expected to show a solar spectrum decreasing from the optical towards the near infrared, but the very few measurements available (Maihara et al., 1993a; Lopez-Moreno et al., 1987) showed that this might not be the case. But since this is a very critical value when the performance of hardware OH avoidance instruments is to be estimated, further investigations of this background are crucial.
There are several ways to avoid the influence of the bright sky lines. The properties can be arranged in a table, as presented below.
The usefulness and gain that can be made by the various approaches depends on a number of factors, like the actual amount of continuum emission, the density and intensity of the lines, the characteristics of filters that can be produced and the properties of the instrument used for the OH suppression. Estimates of the possible gain of these types of instruments were discussed in a number of publications, e.g. Maihara et al. (1993b, 1994); Herbst (1994); Content (1996); Jones et al. (1996); Offer & Bland-Hawthorn (1998).

		Point Source [mag]		per pixel [mag/arcsec^2 (a^α = a * 10^α erg/cm^{2}sÅ)	
		No OH-sup.	OH-sup.	No OH-sup.	OH-sup.
J	Seeing	19.3	21.6	17.3 (1.9^{-17})	19.6
	AO	20.5	22.6	13.1 (6.7^{-16})	15.3
H	Seeing	18.9	21.3	16.8 (1.2^{-17})	19.0
	AO	20.2	22.2	12.8 (3.4^{-16})	14.8
K	Seeing	17.9	20.2	15.8 (1.3^{-17})	17.8
	AO	19.7	21.6	12.2 (2.1^{-16})	14.1
H+K	Seeing	19.0		17.0 (8.2^{-18})	
	AO	20.8		13.4 (1.3^{-16})	
K(10000)	Seeing	16.8		14.8 (3.2^{-18})	
	AO	18.6		11.2 (6.1^{-16})	

Tab. 10.2: SINFONI sensitivities for various observing modes. 1 hr integration (600s x 6) achieving S/N=5. Point source magnitudes in [mag] or surface brightnesses in [mag/arcsec^2] for the four available gratings and a foreseen upgrade grating (red half of the K-band at R=10000) at seeing- or diffraction limited resolution. When OH suppression is applied, the spectrum is resampled to a resolution of R=400. This is not feasible (too many masked pixels) for the H&K grating, and not sensible (high spectral resolution desired) for the K(10000) grating. Further assumptions were 24 e^- read noise (ramp sampling) and 0.01e^-/s dark current, seeing of 0.″69, telescope emissivity of 35% at 10° (this includes the emission of the MACAO mirrors), a total instrument transmission for SINFONI of 20%, and Strehl ratios of 0.15 (J) and 0.25 (H, K), respectively. The values are taken for one spectral pixel and are integrated within the FWHM for point sources. For the per-pixel-case, the corresponding line flux is given in parantheses. See the text for further details. The given numbers are average values over the bands.

Band	Number of Lines	Total sky counts in $\gamma s^{-1}m^{-2}arcsec^{-2}\mu m^{-1}$	Total line intensity in %	Background in $\gamma s^{-1}m^{-2}arcsec^{-2}\mu m^{-1}$	Sky in mag	Continuum in mag
J	53	17000	95-98%	320-1400	15.2	18
H	69	26000	98%	590	14.0	18.0
K	65					

Tab. 10.3: Properties of the OH line emission, taken from Maihara et al. (1993a) for J and H, and Oliva & Origlia (1992) for K.

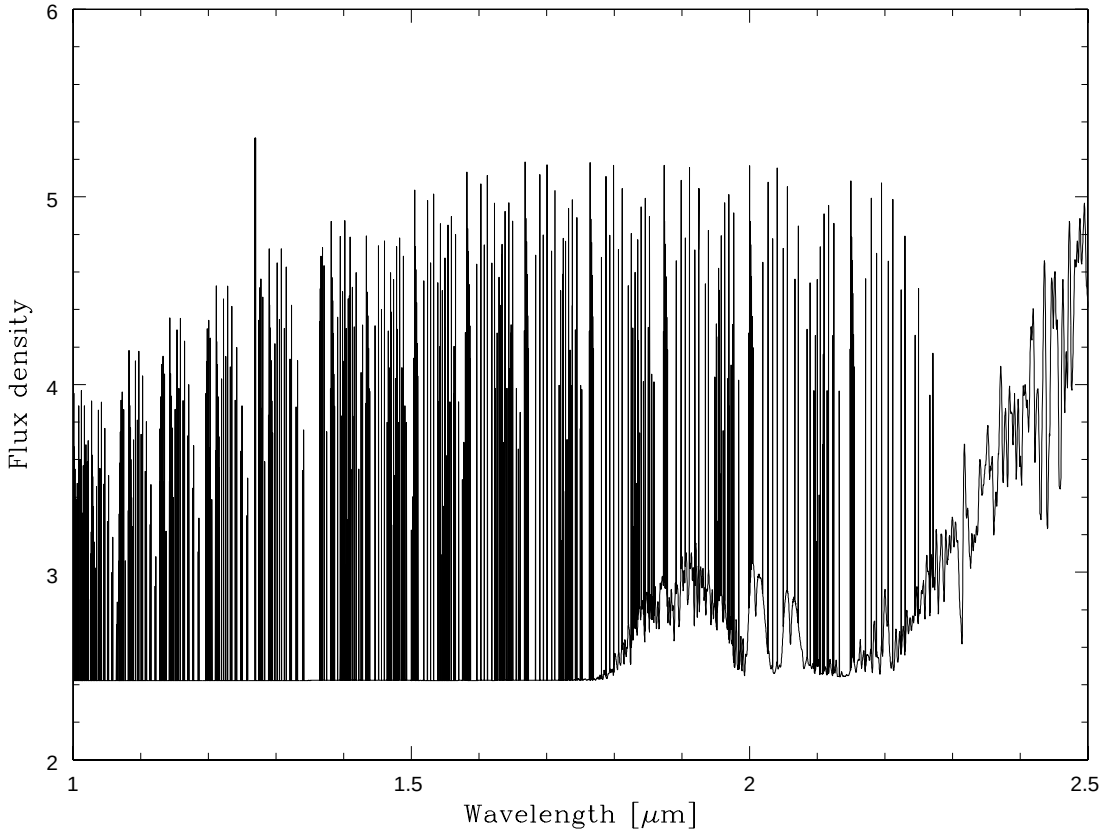

Fig. 10.4: Night sky emission in the near infrared (from Gillett (1995)). The photon flux density (given in $\log(\gamma/s/cm^2/arcsec^2/\mu m)$) varies strongly with wavelength. Main contributors in J and H band are the OH emission lines, which at the resolution of this plot almost merge, but in reality are separated by large spaces with very low continuous sky background emission.

	masked	unmasked
Filter	Bandpass or Bandblock (Notch)	Normal Filters
Dispersive	OH suppressors	OH-avoidance

Tab. 10.4: This table lists various techniques applied in order to avoid night sky OH emission lines. Bandpass/block filters show a sequence of passbands or blocks, avoiding a few very strong lines. Normal filters have just one passband, which is placed in a relatively line-free wavelength range. OH-suppressors disperse the light to a high resolution and mask out strong lines before resampling to lower resolution. OH avoidance is performed in medium to high resolution spectroscopy, where line contaminated regions are not used for data analysis.

From the background limited approximation of the definition of the SNR

$$\mathrm{SNR} = \frac{S}{\sqrt{B + S + N_B^2 + N_d^2}} \simeq \frac{S}{\sqrt{B}} \tag{10.2}$$

In background limited cases, the SNR of an image can be improved, if a filter which reduces the object flux by a factor r reduces the background flux by more than a factor r^2. As discussed by Herbst (1994), no single line is intense enough that a notch filter with an average transmission of 90% (state of the art performance) could provide an increase in SNR. For bandpass filters, in H and K bands, the line density is too high for a filter to fulfill this requirement. However, there are several possible J-band narrow bandpass filters that increase the SNR by a factor 1.6, corresponding to an increase in limiting magnitude by 0.5 mag.
However, if it is possible to produce bandblock filters with a series of irregular, sharply defined bandpasses (or -blocks) with a high transmission in the unblocked regions, this could provide a factor of two improvement in SNR in J-band.
Dispersive OH suppressors use a seperate instrument that disperses the incoming light to a fairly high spectral resolution (above ≈ 20000) and places a mask in an intermediate focus. Its transmission is usually either 1 or 0, and the number of lines blocked depends on the background/source ratio. All lines above a threshold are suppressed. After the mask, the light is recombined to a white light image and then either detected directly or dispersed again to a lower resolution than before.
In our case, the possibility for OH suppression comes "for free", because the scientific applications require a high spectral resolution. The line emission will reach the detector, but then the corresponding pixels will be rejected before the data cube is resampled to a lower resolution or an integrated image.
For the software OH suppression (OH avoidance) it is not relevant if the transmission of the mask is 1, 0, or an intermediate value. This gives the possibility to apply the optimal weight to each line, defined by:

$$\mathrm{k}_\lambda = \frac{\mathrm{S}_\lambda / \mathrm{N}_\lambda^2}{(\mathrm{S}_{\lambda_m} / \mathrm{N}_{\lambda_m}^2)_{max}} \tag{10.3}$$

where S_λ and N_λ are signal and noise at a given wavelength, and λ_m is the wavelength where the weight is maximal (k_λ=1).

10.3 Research prospects

This section describes examples of possible scientific targets of interest and the observing modes that should be chosen for their observation. Two of them are accompanied by simulated observations.

10.3.1 Faint, extended objects

For extended objects, the sensitivity of SPIFFI is not increased going to AO scales, because even though the sky background is reduced, the source is distributed over a larger number of pixels accordingly. In order to observe faint, extended objects, the larger pixel size is required to maximize the sensitivity. This is true, no matter if the integrated spectrum is taken or if the object is analyzed pixel-by-pixel.
One group of very obvious targets are high redshift galaxies, like those observed in the Hubble Deep Field (HDF) at a typical spatial extent of a few arcsec. The determination of their properties will have an impact on the theories of the formation and evolution of galaxies. Their nature can only be verified spectroscopically, and many of them show a distorted spatial structure that underlines the benefit of spatially resolved spectroscopic information. The advantage that the NIR provides for this type of objects is that the optical diagnostic lines, like Hα and [O III], are redshifted into the SINFONI observing windows for redshifts z= $0.5 - 2.7$ (Hα) and 1.0-3.9 ([O III]). Hα is a tracer for star formation and not as prone to extinction as Lyα, while [O III] serves as an excitation diagnostic.

Line	$\lambda_0[\mu m]$	J	H	K
Hα	0.6563	0.5–1.1	1.5–1.8	2.0–2.7
[OIII]5007	0.5007	1.0–1.8	2.0–2.7	3.0–3.9
Hβ	0.4861	1.1–1.9	2.1–2.8	3.1–4.0
[OII]3727	0.3727	1.7–2.8	3.0–3.9	4.4–5.5
Lyα	0.1215	7.2–10	11–14	15–19

Tab. 10.5: Redshift ranges in which the lines in column 1 are observable in the SINFONI windows J, H and K.

To identify and measure those lines, a low spectral resolution is sufficient (e.g., R=400), which means that the observations are performed at a high spectral resolution and after OH avoidance are rebinned along the spectral axis to result in a lower spectral resolution, thereby increasing the SNR.
The spectra in Figures 10.5 and 10.6 show the simulated observations of a spectrum with a strong emission line (initially an Ultra Luminous Infrared Galaxy (ULIRG) spectrum redshifted to z=0.25, where the Paα line is shifted into the K-band). The simulated performance is calculated for a single pixel in 1h integration time for a source of 16 mag arcsec^{-2} surface brightness. The top spectrum shows the input spectrum, the result at the initial resolution of R$\sim$4500 without OH-suppression is displayed in the middle spectrum. The lower right spectrum was created by resampling (R$\sim$1300) with software OH suppression. For comparison, a spectrum derived at a point source magnitude of 20mag is plotted in Figure 10.6. In all spectra, the Paα line can be clearly identified and used as a diagnostic for star formation.

10.3.2 Faint point sources

In the case of point sources, the sensitivity is increased going to the AO pixel scales, because the sky background is reduced and the number of pixels covered by the source stays the same. So for maximum sensitivity, the AO pixel scale will be chosen. In the case of very faint targets, it is possible to convolve the spectrum down to a lower resolution, for example if the detection of emission lines is the goal.
Typical objects for this case are QSOs. Their central objects are unresolved, just like many questions concerning their nature. Even if for some of them their hosts were detected which would make them targets for the previous category, others are too faint to detect the host and provide excellent targets for a study of their strong emission lines, which are redshifted into the SINFONI windows at various redshifts (see Table 10.3.1). They can provide clues about the nature of these objects.

10.3.3 Bright extended objects

The objects in this group are expected to be observed at high spectral and spatial resolution. The targets are for example interacting galaxies, the narrow line regions of AGN or near-by ULIRGS as extragalactic targets, jets and disks around young stars or planetary nebulae in our Galaxy. Those objects will profit from the spatial coverage of SINFONI, and their spectra can be studied pixel-by-pixel.
One group of targets where already SINFONI's precursor MPE 3D (Weitzel et al., 1996) has been proven to deliver valuable data is the centres of external galaxies. MPE 3D's spectral resolution of 2000 is sufficient to determine the stellar dynamics in these targets, and it was shown that the three-dimensional information is required for the determination of a central mass, because only then can anisotropy effects be accounted for

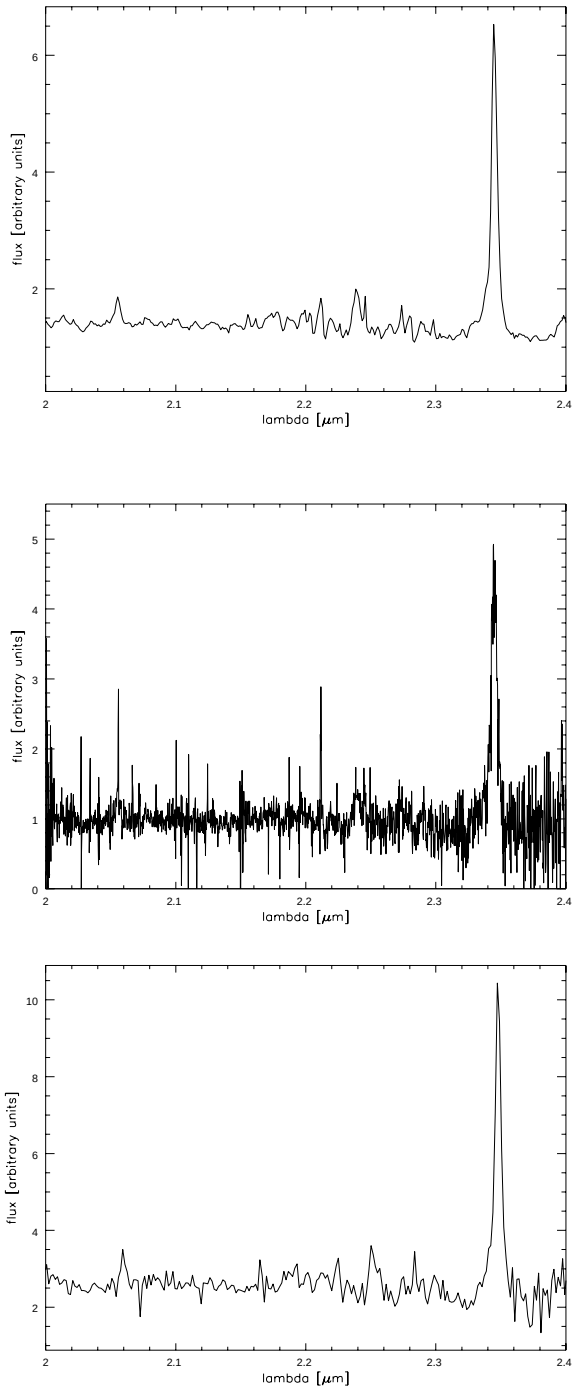

Fig. 10.5: Simulation of SINFONI observations of an object with a bright emission line (a ULIRG spectrum redshifted to z=0.25, kindly provided by H. Dannerbauer). The input spectrum is displayed at the top. The output spectra were achieved at one hour integration time, and show the spectra for a single pixel (0.″25). The surface brightness is 16 mag arcsec^{-2}. The middle spectrum has the original K-band resolution of R~ 4500, for the lower plot it was resampled to R~ 1300, with software OH suppression applied. The Paα line at $\sim 2.35\mu$m can be identified in both spectra, providing information about the star formation history of these objects.

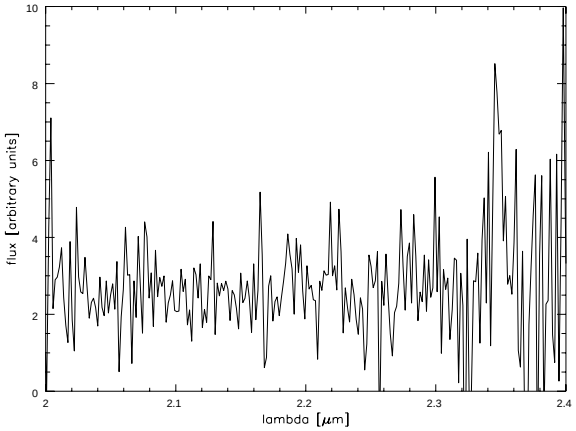

Fig. 10.6: Same as Figure 10.5, but now for a point source of 20 mag. Spectral resampling to R~ 1300 was applied. The line can be fairly well identified (S/N$\sim$5 in the continuum).

(Anders, 1999).

10.3.4 Bright point sources

For bright point sources, using the AO scales has advantages and the high spectral resolution can be exploited, too. Possible targets are the cores of globular or young stellar clusters, close binary star systems or star clusters in external galaxies. In cases where the star clusters are so close that they are resolved into single stars, it is possible to determine their spectral type and thus to place them on the Hertzsprung-Russell diagram. This will then allow conclusions on the stellar content of these clusters and thereby the Initial Mass Function (IMF), which is still an open question.
However, distant clusters show a spectrum which is the combination of the single contributor spectra and will be dominated by very luminous constituents during some phases of their evolution, like it was explained in Part I of this thesis. The following simulation (Figure 10.7) shows a spectrum of an M supergiant (M2Iab-Ib). This kind of spectrum is observed in clusters with an age in the 10 Myr regime, which are dominated by this type of stars. They can for example be observed in interacting galaxies, or can be the central cluster in a galaxy. If the velocity dispersion is high enough ($\sigma >\sim 50$km/s) in the cluster, it can be determined at the spectral resolution of SPIFFI. Since the SPIFFI spectral resolution is too low to determine the velocity dispersion typically observed in star clusters outside the centers of galaxies ($\sim$15 km/s), it was suggested to implement an additional grating with a spectral resolution of R = 10,000. This is considered to be implemented together with the larger detector array.
The input parameters for the simulation with the usual resolution grating (R = 4,400) were the standard parameters again, the object was assumed to be a point source of 17th mag and 15th mag, respectively. The input spectrum is displayed at the top. No spectral rebinning was applied. In the first case, the presence of CO absorption features can clearly be verified, which can serve to age date the population. In the second case, the SNR is high enough ($\sim$30) to determine a broadening of the feature due to a velocity dispersion in the cluster.

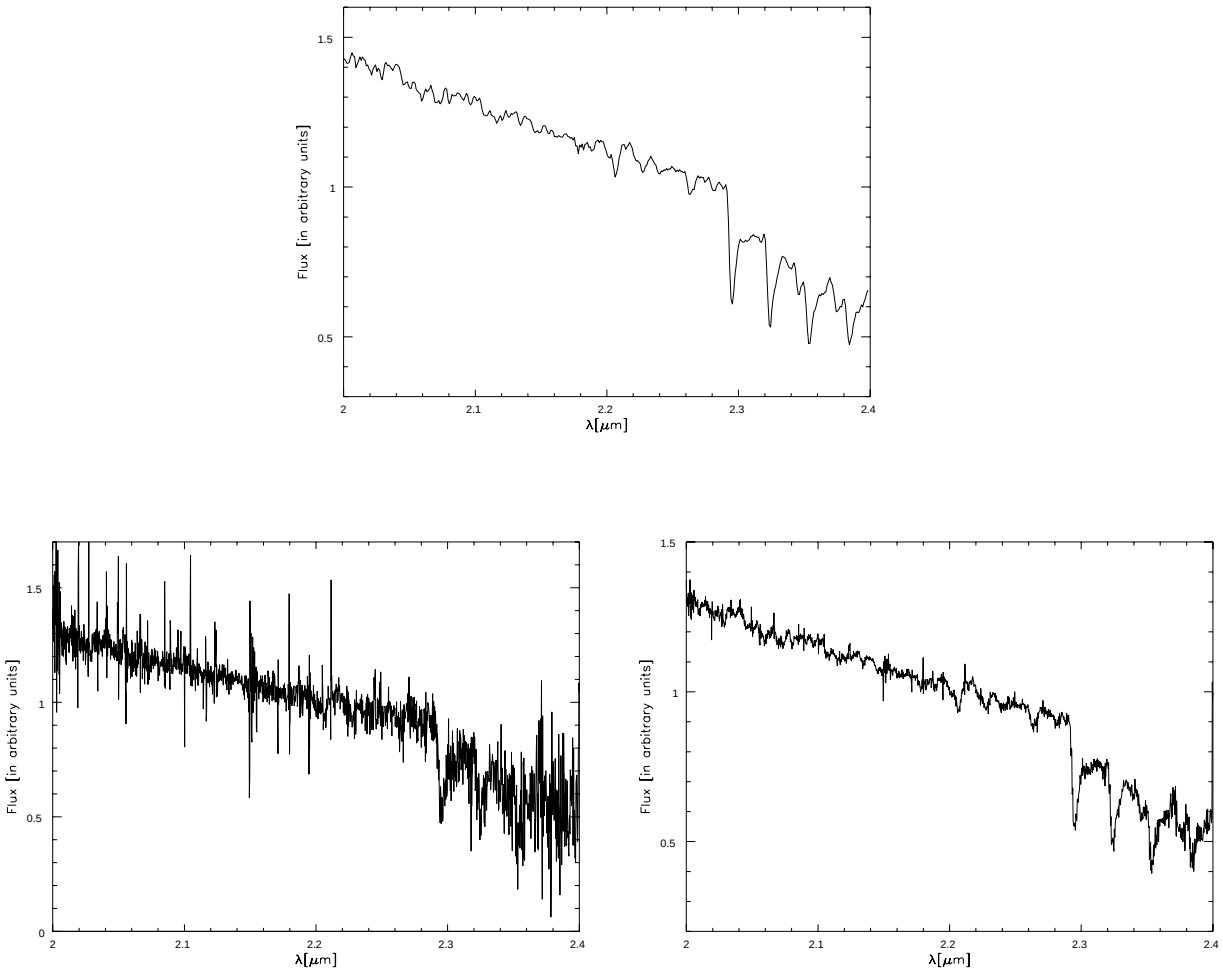

Fig. 10.7: Simulation of SINFONI observations of a stellar cluster dominated by light from M2Iab-Ib supergiants. The input spectrum is displayed at the top, the object is assumed to be a point source of 17th mag (lower left) and 15th mag (lower right). The integration time was one hour (AO pixel scale), no spectral rebinning was applied. In the left hand spectrum, the presence of absorption can be verified, in the high SNR case the obtained SNR (∼50) is more than sufficient to derive a velocity dispersion.

APPENDIX

A. TABLE WITH RESULTS FROM 3D AND SOFI

This table includes the results from the analysis of SOFI and 3D data. The first two columns give the cluster position (as difference in arcseconds in RA and Dec) in relation to a star cluster taken as reference position by WS95: R.A. = $12^{\rm h}01^{\rm m}52\overset{\rm s}{.}97$, Dec. = -18°52′08″.29. It is located close to the northern nucleus. Relative observed magnitudes are given for the broad bands V, J, H and K. V-band magnitudes do not match exactly with numbers given by W99, because they were derived from an image smoothed to the same resolution as the K-band image. Therefore, usually more than one of the clusters detected by W99 is covered by the broadened PSF. $A_{\rm V}$ is the extinction which was derived using the comparison of Brγ/Hα to theoretically expected values. Age is the age which was determined from a combination of $W_{\rm Br\gamma}$, $W_{\rm CO}$ and broadband colours in combination with evolutionary synthesis models for an instantaneous burst, Salpeter IMF slope between 1 and 100 $M_\odot$ and solar metallicity (except for [W99]2: Metallicity twice solar). $M_{\rm phot}$ is the mass which is derived from the extinction corrected K-band magnitude in comparison with that expected from the models for the determined age. Identifications list corresponding numbers in W99, where applicable.

ΔR.A. arcsec	Δ Dec arcsec	m_V mag	m_J mag	m_H mag	m_K mag	A_V mag	Age Myrs	M_{phot} 10^6 $M_\odot$	Identifications
62.0	33.3	*	18.3	17.1	16.3	0.0	10.0	0.1	
48.3	-29.9	18.8	16.5	16.0	15.4	-1.4	10.0	0.3	
46.4	-35.4	20.6	15.8	15.2	15.1	5.3	7.3	0.0	Star
45.9	-11.0	19.4	17.0	16.1	15.8	6.3	7.0	0.5	
45.5	-9.3	19.1	16.4	15.9	15.7	6.4	7.2	0.5	
45.9	-11.0	19.2	16.4	15.9	15.5	5.5	6.6	0.9	
43.6	1.7	20.9	19.1	17.5	16.9	6.1	*	0.0	[W99] Interm. 1
43.1	-1.9	17.9	15.2	14.6	14.2	0.2	10.0	0.9	[W99]-10
42.9	-1.9	17.9	15.1	14.5	14.2	0.2	10.0	0.9	[W99]-16
43.0	-10.5	19.2	16.4	16.1	15.5	4.9	10.0	0.4	
42.9	-23.2	19.4	17.1	16.8	16.1	2.5	6.7	0.4	
43.0	-10.5	19.2	16.4	16.1	15.5	4.6	10.0	0.4	
41.9	-13.0	19.2	16.3	16.3	15.6	0.0	10.0	0.3	[W99]-48
40.4	1.9	19.2	16.6	16.2	16.2	4.8	10.0	0.2	
40.2	-33.3	17.5	16.1	15.9	15.3	0.2	7.4	0.5	[W99]-5
39.4	-4.8	17.8	15.7	15.0	14.7	2.1	8.0	0.7	
39.4	-9.0	19.2	16.7	16.8	16.4	4.6	*	0.0	[W99]-37
39.4	-4.7	17.8	16.1	15.0	14.7	-0.5	10.0	0.5	
38.6	-19.6	19.6	16.4	15.8	15.4	2.1	10.0	0.3	
38.8	-5.9	17.8	16.0	15.3	15.1	1.1	6.3	1.8	
37.7	-13.7	17.6	15.0	14.5	14.0	3.9	6.3	6.6	[W99]-35
37.0	-19.6	19.6	16.2	15.6	15.4	4.2	6.4	0.9	
36.2	-10.1	*	16.9	15.9	15.4	4.1	7.0	0.6	
36.6	-33.5	17.5	18.4	17.3	17.4	0.9	7.0	0.1	
37.8	-36.6	18.8	*	*	15.7	2.8	5.8	1.8	
35.7	-0.9	19.6	17.2	16.7	16.3	7.8	*	0.0	
35.8	-14.8	17.6	15.2	14.7	14.2	1.5	7.0	1.4	
35.2	2.6	22.4	18.2	17.0	16.9	0.0	6.7	0.2	
35.8	-13.8	17.6	15.3	14.7	14.3	1.0	7.2	1.2	
34.9	-19.9	19.3	15.6	14.9	14.6	6.2	6.6	2.3	
35.0	-28.0	19.8	16.6	16.2	15.8	0.9	6.5	0.5	
35.0	-40.2	17.1	15.3	15.3	14.4	1.3	5.5	5.3	[W99]-17+19
34.7	-8.7	19.3	17.6	16.6	16.1	1.7	8.7	0.1	[W99]-15
34.2	3.5	20.3	17.4	16.6	16.6	3.6	10.0	0.1	
35.7	-0.9	19.7	17.2	16.2	16.2	4.2	10.0	0.2	
33.5	-20.8	19.0	15.4	14.8	14.3	4.0	6.5	2.4	

ΔR.A. arcsec	Δ Dec arcsec	m_V mag	m_J mag	m_H mag	m_K mag	A_V mag	Age Myrs	M_{phot} 10^6 $M_\odot$	Identifications
34.1	-35.9	21.9	16.9	15.9	15.6	0.0	6.3	1.1	
32.3	-5.6	19.6	16.0	15.2	15.5	2.8	8.5	0.3	WS95-355
32.5	-38.3	19.6	16.5	15.7	14.9	1.3	6.2	2.3	
32.6	-9.3	18.6	15.8	15.0	14.5	4.2	10.4	1.0	
31.9	0.9	21.7	18.2	16.6	16.4	0.0	*	0.0	
32.5	-9.3	19.6	15.9	14.7	14.2	0.0	10.0	0.9	
30.7	-2.6	18.7	16.0	15.2	14.6	3.7	8.5	0.7	
31.5	-7.6	19.6	17.2	14.7	14.2	3.4	10.0	1.2	
30.7	-2.6	18.6	15.8	15.3	14.6	4.1	9.0	0.7	
29.5	-4.1	19.6	15.8	15.5	14.9	1.0	10.0	0.5	
29.5	-65.5	20.2	16.8	16.1	15.3	6.4	*	0.0	
28.9	-45.6	22.7	17.1	16.5	15.3	6.3	9.0	0.4	
29.2	-56.9	20.8	15.7	15.1	14.8	4.3	5.5	4.2	WS95-80
28.9	-24.1	19.8	18.4	16.8	17.4	0.0	*	0.0	
27.2	22.4	19.7	16.7	16.3	15.9	2.5	*	0.0	Star
27.2	-4.5	17.9	16.0	15.7	15.0	0.5	8.0	0.5	[W99]-18
27.0	-24.0	19.8	17.1	16.9	16.7	0.0	10.0	0.1	
26.4	-22.3	20.6	17.2	16.2	15.8	2.1	7.3	0.4	
26.2	-42.1	18.9	16.1	15.0	14.0	6.8	6.4	4.1	
25.8	0.1	18.6	16.5	16.0	15.9	0.7	10.0	0.2	
25.4	8.9	20.2	17.7	17.2	17.4	3.8	*	0.0	
24.9	-2.2	17.6	16.4	15.9	15.5	0.5	8.0	0.3	[W99]-7
25.0	-27.2	20.2	16.9	16.2	16.4	3.2	6.9	0.2	
24.2	-48.0	18.8	18.3	17.0	16.0	1.7	6.9	0.3	
23.9	2.5	18.7	16.7	16.6	15.7	-0.9	10.0	0.2	
23.1	1.1	18.8	*	18.3	15.8	-0.6	10.0	0.2	
24.2	-88.7	*	15.6	15.0	14.8	0.0	10.0	0.5	
23.4	12.9	19.0	17.6	16.8	15.6	1.1	8.0	0.3	
23.5	-54.4	16.4	14.2	13.9	14.5	1.3	3.7	3.0	9+11+20+26+30+33+39
23.5	-38.3	20.9	17.8	16.7	16.0	5.1	6.7	0.5	[W99]-14
23.1	1.1	18.8	17.9	17.9	15.7	-1.5	6.5	0.4	[W99]-13
21.7	-3.2	20.0	18.1	17.1	16.9	-0.9	6.9	0.1	
21.6	0.3	18.6	18.5	17.5	15.7	-0.5	10.0	0.2	[W99]-41
19.6	10.6	20.0	16.8	16.3	15.7	0.0	20.0	1.2	[W99]-21
17.4	0.9	19.9	18.0	17.6	16.7	2.2	15.0	0.4	

ΔR.A. arcsec	Δ Dec arcsec	m_V mag	m_J mag	m_H mag	m_K mag	A_V mag	Age Myrs	M_{phot} 10^6 $M_\odot$	Identifications
18.6	13.9	19.3	16.8	16.1	15.8	2.1	9.0	0.2	[W99]-24
17.1	6.1	19.3	17.5	16.9	16.4	2.4	6.7	0.3	
8.5	-61.4	17.3	14.6	12.1	11.8	3.3	6.8	0.0	
8.6	-6.0	20.7	16.9	16.7	16.7	6.5	*	0.0	
8.5	-61.4	16.5	12.7	12.1	11.8	4.2	5.8	0.0	
7.3	-58.2	17.5	15.1	12.1	11.8	-2.0	*	0.0	
7.0	-58.4	18.8	14.8	12.1	11.8	0.2	6.3	0.0	[W99]-45
4.7	1.7	18.2	14.9	13.2	12.8	3.6	6.5	0.0	
5.4	8.1	19.4	15.6	13.2	12.8	5.1	6.5	0.0	
4.4	22.0	19.3	16.8	16.4	16.4	0.0	10.0	0.1	
3.4	14.3	18.7	15.8	15.2	15.3	3.7	10.0	0.4	
3.6	10.2	20.1	15.6	13.2	14.7	4.6	7.3	1.2	
3.4	14.3	18.7	16.1	15.2	15.4	2.9	10.0	0.4	[W99]-42
2.6	-58.7	18.7	15.7	15.3	14.9	1.8	6.5	1.1	[W99]-35
2.2	1.7	17.8	14.8	13.2	13.4	1.4	10.0	2.1	
1.9	-15.0	18.9	16.5	15.9	15.6	4.6	10.0	0.4	
1.2	6.3	17.0	13.8	13.2	12.8	2.3	6.7	0.0	[W99]-34+38
1.0	5.2	17.0	13.8	13.2	12.8	2.6	6.6	0.0	
0.9	20.4	19.6	17.8	17.2	17.1	-0.6	10.0	0.1	
0.5	9.4	19.8	14.9	13.2	12.7	3.9	6.7	0.0	
0.3	0.2	17.0	14.8	14.3	13.7	0.8	7.2	0.0	
0.8	5.2	17.0	14.2	13.2	12.7	1.5	6.7	0.0	
-0.5	-62.0	19.1	16.5	16.1	15.6	4.7	5.8	2.2	
-2.5	33.0	19.8	17.1	16.7	16.0	-0.9	10.0	0.2	
-2.8	-64.8	19.7	17.2	16.7	16.5	3.3	6.3	0.6	
-4.8	29.7	19.3	17.7	17.2	16.3	0.0	*	0.0	
0.8	5.1	18.1	15.4	13.1	12.7	2.2	15.0	0.0	[W99]-32
-6.6	-2.1	18.9	16.1	16.0	16.0	3.1	*	0.0	
0.0	-8.7	19.1	16.8	16.7	16.0	1.2	10.0	0.2	
-7.5	-69.9	19.3	16.8	16.4	16.4	3.9	5.8	1.0	
-8.2	13.0	19.5	16.3	15.9	15.3	0.0	*	0.0	
-8.8	13.7	19.5	16.4	15.8	15.4	-1.1	7.3	0.4	
-9.5	-10.3	17.8	16.1	15.7	15.1	0.3	10.0	0.4	
-10.8	-11.3	17.8	16.2	15.8	15.1	-0.5	25.0	2.1	[W99]-28
-12.7	3.3	20.3	17.2	16.9	16.7	3.8	*	0.0	
-13.2	37.0	19.6	17.5	17.0	17.1	0.0	25.0	0.3	

ΔR.A. arcsec	Δ Dec arcsec	m_V mag	m_J mag	m_H mag	m_K mag	A_V mag	Age Myrs	M_{phot} 10^6 $M_\odot$	Identifications
-13.6	-18.3	17.7	15.9	15.2	14.9	0.0	7.5	0.7	
-13.4	-21.4	17.7	15.8	15.4	15.1	1.0	10.0	0.4	[W99]-23
-14.0	31.0	20.3	17.5	16.8	16.4	2.3	25.0	0.8	
-14.1	-17.8	17.9	15.6	15.0	14.6	0.8	8.0	0.7	[W99]-25
-14.7	-23.3	17.7	16.4	15.8	15.6	0.8	25.0	1.4	
-15.7	-17.6	17.9	15.5	15.2	14.7	0.6	9.0	0.5	
-15.6	-18.8	17.9	16.4	15.2	14.7	1.4	10.0	0.6	[W99]-27
-15.6	-18.8	18.0	16.8	16.6	16.2	-0.5	*	0.0	
-18.4	34.8	18.0	14.1	13.7	13.6	3.9	6.6	4.6	
-19.2	-17.9	19.2	16.5	16.0	15.5	2.5	*	0.0	
-20.3	27.2	19.6	16.7	16.3	15.6	1.3	*	0.0	
-22.9	25.2	17.6	15.2	14.4	14.3	2.7	10.0	1.0	
-22.9	23.2	17.6	14.8	14.3	13.9	4.3	9.0	1.3	[W99]-43
-22.9	-15.9	19.3	17.6	17.8	16.5	-0.5	10.0	0.1	[W99]-49
-23.2	-25.2	19.6	16.9	16.4	15.6	1.6	10.0	0.3	
-23.2	19.6	17.9	15.4	14.9	14.5	2.4	10.0	0.9	[W99]-44
-22.9	23.2	17.5	15.9	14.3	13.9	2.1	8.1	1.4	[W99]-1
-26.2	-20.3	18.5	16.4	15.8	15.5	2.5	10.0	0.3	[W99]-8
-26.1	-23.5	18.8	17.5	16.3	16.0	1.7	10.0	0.2	
-27.7	0.5	20.5	17.5	16.7	16.1	0.0	10.0	0.2	
-29.3	-6.6	18.8	16.5	15.8	15.4	-0.2	10.0	0.3	
-34.1	4.8	17.4	15.6	15.1	14.8	1.8	10.0	0.6	
-34.8	-1.7	17.3	14.8	14.4	14.0	1.1	10.0	1.2	[W99]-6
-35.4	-8.9	17.8	15.8	14.7	14.3	0.9	6.3	3.9	
-35.1	-12.1	17.1	15.0	14.6	14.1	0.6	7.3	1.4	[W99]-22
-35.4	3.9	17.3	15.2	14.7	14.4	0.1	7.3	1.1	[W99]-12+47+50
-36.2	-3.3	16.7	14.2	13.7	13.9	0.0	6.6	1.9	[W99]-2
-36.9	-10.4	17.1	15.2	14.7	14.3	-2.4	8.2	0.5	
-37.5	-9.3	17.1	15.1	14.5	14.2	-0.6	10.0	0.9	[W99]-31+40+46
-45.0	49.3	19.4	17.2	17.2	17.0	0.0	*	0.0	Star
-44.5	-26.8	*	18.5	17.5	16.8	16.0	*	0.0	
-52.9	-57.0	22.9	17.1	16.6	16.4	7.2	*	0.0	

Tab. A.1: Photometric results for the star clusters detected in K-band with SOFI.

BIBLIOGRAPHY

Abraham R.G., 1999, *Galaxy Interactions at Low and High Redshift*, eds. J.E. Barnes & D.B. Sanders (Kluwer, Dordrecht), p. 11

Amram P., Marcelin M., Bouleseix J., and le Coarer E., 1992, A&A, 266, 1992

Anders S., *Beugungsbegrenzte Nahinfrarot-Feldspektroskopie und Stellare Kinematik in der Galaxie NGC 3115*, 1999, Thesis Ludwig-Maximilians-Universität, München, Germany

Baker D.J. & Stair A.T. Jr., 1988, Phys. Scripta, 37, 611

Barger A.J., Cowie L.L., Sanders D.B., Fulton E., Hu E.M., Songaila A., & Hall D., 1999, AJ, 117, 102

Barnes J.E. & Hernquist L.E., 1991, ApJ, 370, L65

Barnes J.E., 1988, ApJ, 331, 699

Barnes J.E., 1999, astro-ph, 9903234

Bernardi M., Renzini A., da Costa L.N., Wegner G., Alonso M.V., Pellegrini P.S., Rité C., Willmer C.N.A., 1998, ApJ, 508, L43

Binney J. & Merrifield M., 1998, *Galactic Astronomy*, Princeton University Press, p. 187

Blumenthal G.R., Faber S.M., Primack J.R., Rees M.J., 1984, Nature, 311, 517

Böker T., van der Marel R.P., Vacca W.D., 1999, AJ, 118, 831

Bonaccini D., Rigaut F., Dudziak G., and Monnet G., "Curvature adaptive optics at ESO", 1998, Proc. SPIE, 3353, 553

Brandl B., Sams B.J., Bertoldi F., Eckart A., Genzel R., Drapatz S., Hofmann R., Loewe M., and Quirrenbach A., 1996, ApJ, 466, 254

Brandl B., Brandner W., Eisenhauer F., Moffat A.F.J., Palla F., Zinnecker H., 1999, A&A, 352, 69

Bruzual A.G., 1983, ApJ 273, 105

Bushouse H.A. & Stanford S.A., 1992, ApJS, 79, 213

Césarsky C.J. et al., A&A, 315, 32

Cerviño M. & Mas-Hesse J.M., 1994, A&A, 284, 749

Charlot S., & Bruzual G.A., 1991, ApJ, 367, 126

Chernoff D.F., and Weinberg M.D., 1990, ApJ, 351, 121

Clegg P.E., Ade P.A.R. et al., 1996, A&A, 315, 38

Content R., 1996, ApJ, 464, 412

de Carvalho R.R & Djorgovski S., 1992, ApJ, 389, L49

de Graauw T. et al., 1996, , A&A, 315, 49

Díaz A.I., Terlevich E. & Terlevich R., 1989, MNRAS, 239, 325

Djorgovski S., 1993, *Structure and Dynamics of Globular Clusters*, ASP Conf. Series, Vol. 50, eds. S.G. Djorgovski & G. Meylan (ASP, San Francisco), p. 373

Draine B.T. 1989, in Proc. of the 22^{nd} ESLAB Symposium on Infrared Spectroscopy in Astronomy, ed. B. H. Kaldeich (ESA SP-290), P. 93

Efremov Y. & Elmegreen B. 1998, MNRAS, 299, 588

Eisenhauer F., Tecza M., Mengel S., Thatte N.A., Roehrle C., Bickert K., Schreiber J., 2000, Proc. SPIE, 4008, 289

Eisenhauer F., Quirrenbach A., Zinnecker H., Genzel R., 1998, ApJ, 498, 278

Elmegreen B. & Efremov Y. 1997, ApJ, 480, 235

Englmaier P., Rigopoulou D., and Mengel S., 2000, Eds. J.E. Hibbard, M., Rupen, J.H. van Gorkom. ASP Conference Series, San Francisco, California, 1

Englmaier P., private communication

Ferland G.J., Korista K.T., Verner D.A., Ferguson J.W., Kingdon J.B., Verner E.M., 1998, PASP, 110, 761

Fischer J. et al. 1996, A&A, 315, 97

Fioc M. & Rocca-Volmerange B., 1997, A&A, 326

Förster-Schreiber, N. M. 1998, Ph. D. thesis, der Ludwig-Maximilians-Universität München

Gerhard O., 2000, ASP Conference Series 211, *Massive Stellar Clusters*, eds. A. Lançon and C. Boily (San Francisco: ASP), 12

Gerritsen J.P.E., 1997, PhD thesis, University of Groningen

Gilbert A.M., Graham J.R., McLean I.S., Becklin E.E., Figer D.F., Larkin J.E., Levenson N.A., Teplitz H.I., and Wilcox M.K., 2000, ApJ, 533, 57

Gillett F.C., 1995, SPIE Proceedings, 2475, 2

González Delgado R.M. & Leitherer C., 1999, ApJS, 125, 479

Harris W.E. & Racine R., 1979, ARA&A, 17, 241

Harris W.E. & van den Bergh S., 1981, AJ, 86, 1627

Herbst T., 1994, PASP, 106, 1298

Herzberg G., 1950, *Molecular Spectra and Molecular Structure*, D. van Nostrand Company, Inc.

Ho, L. & Filippenko, A. 1996, ApJ, 472, 600

Hodapp K.-W., Hora J.L., Hall D.N.B., Cowie L.L., Metzger M., Irwin E., Vural K., Kozlowski L.J., Cabelli S.A., Chen C.Y., Cooper D.E., Bostrup G.L., Bailey R.B. and Kleinhans W.E., 1996, New Astronomy, 1, 177

Holtzman, J. A. et al. 1992, AJ, 103, 691

Huchra J.P., 1977, ApJ, 217, 928

Hughes D.H., Serjeant S., Dunlop J., Rowan-Robinson M., Blain A., Mann R.G., Ivison R., Peacock J., Efstathiou A., Gear W., Oliver S., Lawrence A., Longair M., Goldschmidt P., & Jenness T., 1998, Nature, 394, 241

Hummel E. & Van der Hulst J.M. 1986, A&A, 155, 151

Hummer D.G. & Storey P.J. 1987, MNRAS, 224, 801

Jansen J., 1999, *Inbetriebnahme und Charakterisierung des HAWAII Nahinfrarot-Arrays für das abbildende Spektrometer SINFONI am ESO VLT*, Master Thesis, Technische Universität München

Jones J.E., Alloin D.M., Jones B.J.T., 1984, ApJ, 283, 457

Jones D.H., Bland-Hawthorn J., Burton M.G., 1996, PASP, 108, 929

Kaufmann G., Charlot S., and White S.D.M, 1996, MNRAS, 283, L117

Keel W.C., Kennicutt Jr., R.C., Hummel E., van der Hulst J.M., 1985, AJ, 90, 708

Kennicutt Jr. R.C., 1998, ApJ, 498, 541

Kessler M.F. et al., 1996, A&A, 315, L27

King I.R., 1966, AJ, 71, 64

Kleinmann S.G. & Hall D.N.B., 1986, ApJS, 62, 501

Kovo O., Sternberg A., & Alexander T. 1998, private communication

Krabbe A., et al. 1995, ApJ, 447, 95

Kunze D. et al. 1996, A&A, 315, 101

Lançon A. & Rocca-Volmerange B., 1992, A&AS, 96, 593

Larsen S.S., 1999, A&AS, 139, 393

Layzer D., 1954, AJ, 59, 170

Leitherer, C., et al. 1999, ApJS, 123, 3

Lejeune T., Buser R. & Cuisinier F., 1997, A&AS, 125, 229

Lopez-Moreno J.J., Rodrigo R., Moreno F., Lopez-Puertas M. & Monila A., 1987, Planet Space Sci., 35,1029

Lutz D., A&A, 245, 31

Maihara T., Iwamuro F., Yamashita T., Hall D.N.B., Cowie L.L., Tokunaga A.T. & Pickles A., 1993, PASP, 105, 940

Maihara T., Iwamuro F., Hall D.N.B., Cowie L.L., Tokunaga A.T. & Pickles A., 1993, SPIE, 1946, 581

Maihara T., Iwamuro F., Oya S., Tsukamoto H., Hall D.N.B., Cowie L.L., Tokunaga A.T. & Pickles A., 1994, SPIE, 2198, 194

Mandushev G., Spassova N. & Staneva A., 1991, AAP, 252, 94

Mas-Hesse J.M. & Kunth D., 1999, A&A, 349, 765

Mathis J.S., Rumpl W. & Nordsieck K.H., 1977, ApJ, 217, 425

Mathis J.S., 1990, ARA&A, 28, 37

McWilliam A. & Lambert D.L., 1984, PASP, 96, 882

Meylan G., 2000, ASP Conference Series 211, *Massive Stellar Clusters*, eds. A. Lançon and C. Boily (San Francisco: ASP), 215

Meynet G., Maeder A., Schaller G., Schaerer D., & Charbonnel C., 1994, A&AS, 103, 97

Mihos J.C., 1999, Astrophysics and Space Science, 266, 195

Mihos J.C. and Hernquist L., 1996, ApJ, 464, 641

Mirabel I.F., et al. 1998, A&A, 333, 1

Nikola T., Genzel R., Herrmann F., Madden S.C., Poglitsch A., Geis N., Townes C.H., and Stacey G.J., 1998, ApJ, 504, 749

National Institute of Standards and Technology, 2000, based on data by Edejer & Thodos, 1967

Offer A. and Bland-Hawthorn J., 1998, MNRAS, 299, 176

Oliva E. and Origlia L., 1992, A&A, 254, 466

Origlia L., Moorwood A.K.M, & Oliva E., 1993, A&A, 280, 536

Oliva E., Origlia L., Kotilainen J.K., and Moorwood A.F.M., 1995, A&A, 301, 550

Origlia L., and Oliva E., 2000, A&A, 357, 610

Osterbrock D.E., 1974, *Astrophysics of Gaseous Nebulae*, W.H. Freeman and Company

Portegies Zwart S.F., 2000, ASP Conference Series 211, *Massive Stellar Clusters*, eds. A. Lançon and C. Boily (San Francisco: ASP), 181

Persson S.E. et al., 1983, ApJ, 266, 105

Rubin V. et al. 1970, ApJ, 160, 801

Salpeter E.E., 1955, ApJ, 121, 161

Schade D., Lilly S.J., Crampton D., Ellis R.S., Le Fèvre O., Hammer F., Brinchmann J., Abraham R., Colless M., Glazebrook K., Tresse L., & Broadhurst T., 1999, ApJ, 525, 31

Schmutz W., Leitherer C. & Gruenwald R., 1992, PASP, 104, 1164

Schaerer D. & Vacca W.D. 1998, ApJ, 497, 618

Schweizer F., 1997, *The nature of elliptical galaxies*, ASP conference Series, Vol. 116, eds. M. Arnaboldi, G.S. Da Costa, P. Saha, p. 447

Schweizer F., and Seitzer P., 1992, AJ, 104, 1039

Schweizer F., and Seitzer P., 1993, ApJL, 417, L29

Schweizer F., and Seitzer P., 1998, AJ, 116, 2006

Shields J. 1993, ApJ, 419, 181

Smits D.P., 1991, MNRAS, 248, 193

Sparrow E.M. & Cess R.D., 1966, *Radiation Heat Transfer*, Belmont, CA: Brooks/Cole, Thermal Science Series, p. 322

Spitzer L. 1978, *Physical Processes in the Interstellar Medium* (New York: Wiley)

Spitzer L. & Hart M.H., 1971, ApJ, 164, 399

Stanford S.A., Sargent A.I., Sanders D.B., and Scoville N.Z., 1990, ApJ, 349, 492

Sternberg A., 1998, ApJ, 506, 721

Storey, P. J. & Hummer, D. G. 1995, 272, 41

Ströbele S. (ESO, MACAO project), 2000, private communication

Tecza M., 1999, PhD thesis, Ludwig-Maximilians-Universität, München, Germany

Tecza M., Thatte N., Krabbe A., and Tacconi-Garman L.E., 1998, SPIE proc., 3354, 394

Tecza M., Thatte N., Eisenhauer F., Mengel S., Röhrle C., Bickert K., and Schreiber J., 2000, SPIE proc., in press

Thatte, N. A., Kroker, H., Weitzel, L., Tacconi-Garman, L. E., Tecza, M., Krabbe, A., & Genzel, R. 1995, SPIE, 247, 228.

Thatte N., Tecza M., Eisenhauer F., Mengel S., Krabbe A., Pak S., Genzel R., Bonaccini D., Emsellem E., Rigaut F., Delabre B., and Monnet G., 1998, SPIE proc., 3353, 704

Thatte N., Anders S., Eisenhauer F., Tecza M., Mengel S., Eckart A., Genzel R., Monnet G., and Bonaccini D., 2000, *Imaging the Universe in Three Dimensions*, ASP Conference Series 195, eds. W. van Breugel and J. Bland-Hawthorn, p.206

Tinsley B.M., 1972, A&A, 20, 383

Toomre A. & Toomre J., 1972, ApJ, 179, 623

Turnbull D.N. & Lowe R.P., 1991, Geophys. Res. Lett., 18, 1345

Vanbeveren D., Van Bever J., & de Donder E., 1997, A&A, 317, 487

van den Bergh S., Abraham R.G., Ellis R.R., Tanvir N.R., Santiago B.X., and Glazebrook K.G., 1996, AJ, 112, 359

van der Hulst J.M., 1979, A&A, 71, 131

van der Hulst J.M., Terlouw J.P., Begeman K., Zwister W., & Roelfsema, 1992, *Astrophysical Data Analysis Software and Systems I*, eds. D. M. Worall, C. Biemesderfer, and J. Barnes, ASP Conference Series 25, p. 131

Vigroux L. et al. 1996, A&A, 315, L93

Weitzel L., et al. 1996, A&AS, 119, 531

Whitmore B.C., Schweizer F. Leitherer C., Borne K., & Robert C. 1993, AJ, 106, 1354

Whitmore, B. & Schweizer, F. 1995, AJ, 109, 960

Whitmore B C., Miller B.W., Schweizer F., & Fall S.M., 1997, AJ, 114, 2381

Whitmore B.C., Zhang Q., Leitherer C. Fall S.M., Schweizer F., & Miller B.W. 1999, AJ, 118, 1551

Whitmore B.C., 2000, private communication

Wilson C.D., Scoville N., Madden S.C. & Charmandaris V., 2000, ApJ, 542, 120

Zepf S.E., Carter D., Sharples R.M. & Ashman K.M., 1995, ApJL, 445, L19

Zepf S.E., and Koo D.C., 1989, ApJ, 337, 34

Zhang Q. & Fall S.M., 1999, ApJ, 527, 81